Stellar Models with Magnetism and Rotation: Mixing Length Theories and Convection Simulations

Lewis George Ireland

Submitted by Lewis George Ireland to the University of Exeter as a thesis for the degree of Doctor of Philosophy in Physics, June, 2018.

I certify that all material in this thesis which is not my own work has been identified and that no material has previously been submitted and approved for the award of a degree by this or any other University.

Signed: .....

Lewis George Ireland

Date: .....

Abstract

1st Supervisor: Prof. Matthew Browning 2nd Supervisor: Prof. Sean Matt

Some low-mass stars appear to have larger radii than predicted by standard 1D structure models; prior work has suggested that inefficient convective heat transport, due to rotation and/or magnetism, may ultimately be responsible. In this thesis, we explore this possibility using a combination of 1D stellar models, 2D and 3D simulations, and analytical theory. First, we examine this issue using 1D stellar models constructed using the Modules for Experiments in Stellar Astrophysics (MESA) code. We begin by considering standard models that do not explicitly include rotational/magnetic effects, with convective inhibition modelled by decreasing a depth-independent mixing length theory (MLT) parameter $\alpha_{\rm MLT}$. We provide formulae linking changes in $\alpha_{\rm MLT}$ to changes in the interior specific entropy, and hence to the stellar radius. Next, we modify the MLT formulation in MESA to mimic explicitly the influence of rotation and magnetism, using formulations suggested by Stevenson (1979) and MacDonald and Mullan (2014) respectively. We find rapid rotation in these models has a negligible impact on stellar structure, primarily because a star's adiabat, and hence its radius, is predominantly affected by layers near the surface; convection is rapid and largely uninfluenced by rotation there. Magnetic fields, if they influenced convective transport in the manner described by MacDonald and Mullan (2014), could lead to more noticeable radius inflation. Finally, we show that these non-standard effects on stellar structure can be fabricated using a depth-dependent $\alpha_{\rm MLT}$: a non-magnetic, non-rotating model can be produced that is virtually indistinguishable from one that explicitly parameterises rotation and/or magnetism using the two formulations above. We provide formulae linking the radially-variable $\alpha_{\rm MLT}$ to these putative MLT reformulations.

We make further comparisons between MLT and simulations of convection, to establish how heat transport and stellar structure are influenced by rotation and magnetism, by looking at the entropy content of 2D local and 3D global convective calculations. Using 2D "box in a star" simulations, created using the convection code Dedalus, we investigate

changes in bulk properties of the specific entropy for increasingly stratified domains. We observe regions stable against convection near the bottom boundary, resulting in the specific entropy in the bulk of the domain exceeding the bottom boundary value: this could be a result of physical effects, such as increased amounts of viscous dissipation for more supercritical, highly stratified cases, but may also be influenced by the artificial boundary conditions imposed by these local simulations. We then turn to 3D global simulations, created using the convection code *Rayleigh*, and investigate these same properties as a function of rotation rate. We find the average of the shell-averaged specific entropy gradient in the middle third of the domain to scale with rotation rate in a similar fashion to the scaling law derived via MLT arguments in Barker et al. (2014), i.e., $|\langle ds/dr \rangle| \propto \Omega^{4/5}$.

Contents

List of Figures

List of Tables

Declaration

The majority of work presented in this thesis was performed by the author, with guidance from their supervisor. Chapter 3 contains much of the work outlined in Ireland and Browning (2018). Chapter 4 contains analysis by the author, using local 2D simulations of convection performed by Currie and Browning (2017), and global 3D simulations of convection performed by Sainsbury-Martinez et al. (In preparation).

Acknowledgements

Firstly, I thank my supervisor, Matthew Browning, for the continuous support and encouragement he has provided me during my project. The guidance and constant feedback he provided, including the many afternoons we spent crafting our first paper, were vital in the completion of my PhD. I thank the other members of our group, Felix, Laura, and Lucia, for their helpful discussions during weekly group meetings, and for also investing their own time to help me complete my thesis. I thank the ERC for funding my PhD, and allowing me to travel to conferences both nationally and internationally.

I thank my mother and father, Julia and Bernie, for their constant support throughout my life. They nurtured my interest in science and mathematics from a very young age, and without them, I would not have been as dedicated or hard-working throughout my academic career so far. Also, I thank my sisters, Frances and Alexandra, for their support over the years. I thank my friend, Chris, who I sat next to in the open office: our shared love of quoting The Simpsons, powerlifting, and other forms of procrastination, were probably the reason why this took four years instead of three. I also thank him, along with the morning gym crew and the University of Exeter Powerlifting Society, for their encouragement during training and competitions, helping me let off some steam.

Last, and most importantly, I thank my wife, Holly Ireland, for her patience, her love, and support during the last four years. Without her motivation throughout our relationship, I may never have come this far academically.

Lewis George Ireland

Exeter, U.K.

June 2018

Chapter 1

Motivation and Background

This chapter highlights some of the background and motivations for the work in this thesis. Firstly, Section 1.1 discusses properties of convection and magnetism in the stellar interior, their interaction with one another, and the resulting dynamical behaviour of stars. Section 1.2 describes the motivation behind the focus on low-mass stars throughout this thesis, and Section 1.3 looks at the observational evidence for radius inflation, and possible correlation with rotation and magnetism, of these objects. Section 1.4 introduces convective simulations and the modelling of stars, and the impact they have made on the understanding and modelling of astrophysical objects. Section 1.5 gives a brief overview of the history of magnetic and rotating stellar simulations, including those for low-mass fully convective stars. Finally, Section 1.6 gives a brief overview of this thesis.

1.1 Stellar Convection and Magnetism

The structure of a star depends on its age and mass. Within the stellar interior, heat is transported predominantly via convection and radiation, carrying energy from the core up to the surface. Convection is universally present in stars, with high-temperature, low-density fluid parcels near-adiabatically rising through a stratified temperature gradient. These convective motions help transfer the heat produced from nuclear fusion occurring in the stellar core. The structure of the stellar interior is highly mass-dependent, due

to changes in heat flux, opacity, and ionisation. Main-sequence solar-mass stars (0.35 $M_\odot < M_* < 1.8\ M_\odot$) have radiative cores and convective envelopes, more-massive "hot" stars ($M_* > 1.8\ M_\odot$) have convective cores and radiative envelopes, and low-mass stars ($M_* < 0.35\ M_\odot$) are fully convective (Kippenhahn et al. 2012; Chabrier and Baraffe 1997).

Significant insight into the nature of convection and magnetism in stars has come from studying the Sun. The solar structure consists of a core from the centre up to $\approx 0.25\,R_\odot$, where $R_\odot$ is the solar radius ($R_\odot = 695,508$ km), a radiative zone from the core up to $\approx 0.70\,R_\odot$, and a convective envelope from the top of the radiative core up to near the surface. At the solar surface, a vast scale of convective motions are observed. These include granulation (diameter: ~ 1 Mm, lifetime: $\sim 5-10$ minutes), mesogranulation (diameter: ~ 5 Mm, lifetime: ~ 3 hours), and supergranulation (diameter: ~ 30 Mm, lifetime: ~ 1 day). In Figure 1.1, we show observations of granulation and supergranulation, from the Swedish 1 m Solar Telescope and the SDO/HMI instrument, respectively. These structures arise from a variety of competing processes, as discussed, for example, in Rast (2003), and reviewed in Nordlund et al. (2009).

These convective structures transport both heat and angular momentum, resulting in differential rotation, defined as a state in which the rotation rate is dependent on both depth and latitude. The differential rotation of the Sun has been extensively investigated using helioseismology: the study of the solar structure and dynamics through the oscillation of pressure modes (p-modes), internal gravity waves (g-modes), and surface gravity waves (f-modes). Modes travelling through the Sun are affected by the stellar interior, giving insight into its structure, which can be used to infer the profile of the solar internal differential rotation (Christensen-Dalsgaard et al. 1996). Figure 1.2 illustrates how p-modes and g-modes oscillate in the solar interior, whilst Figure 1.3 shows the internal rotation and differential rotation profiles of the Sun determined using helioseismic inversion. One of the most striking findings of this analysis is the transition from solid body to differential rotation at radii $> 0.7\,R_\odot$. This region of strong shear is called the tachocline.

Asteroseismology is a closely related study for the oscillations of other stars, which can be used to infer details of their stellar structure. However, the resolution is limited by the size of data sets and poor frequency resolution of measurements (e.g., Aerts et al. 2010).

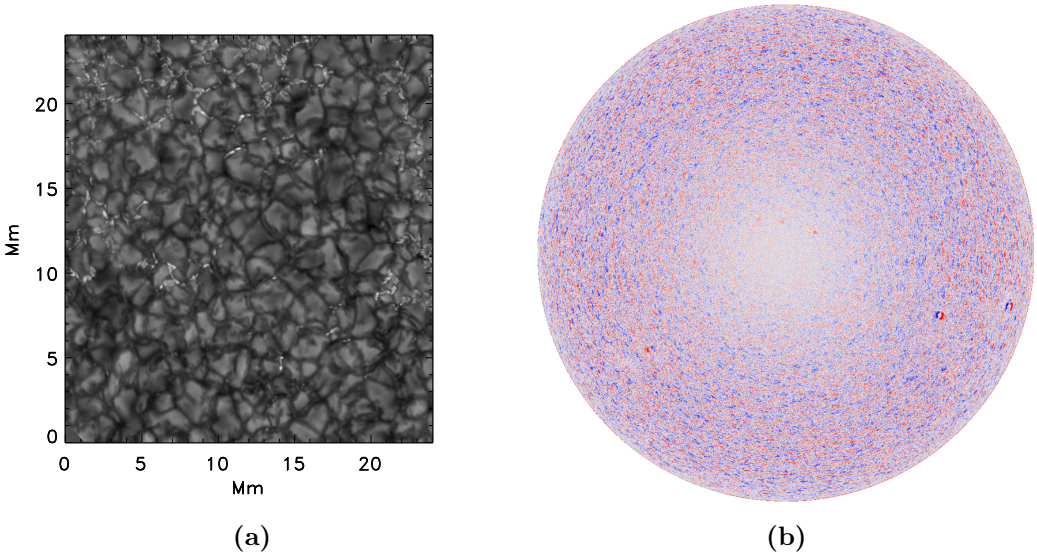

Figure 1.1: (a) Solar granulation (Swedish 1 m Solar Telescope and Institute of Theoretical Astrophysics, Oslo): features at the top of convective cells, which are ~ 1 Mm diameter and have a lifetime of $\sim 5-10$ minutes. This pattern is seen across the solar surface (excluding areas covered by sunspots), and is constantly evolving as the convective fluid rises up from the interior, spreads across the surface, and sinks downward along the thin dark inter-granular lanes. Image credit: Nordlund et al. (2009). (b) Solar supergranulation (SDO/HMI instrument at 5:00UT 1 November 2012): much larger features of convection (~ 30 Mm diameter), with a longer lifetime of ~ 1 day. These are observed via measurements of the Doppler shift, capturing the dynamics of the line-of-sight component of the convective flow. Image credit: Hathaway et al. (2015).

The Kepler mission helped obtain asteroseismic data for thousands of stars over several years (Gilliland et al. 2010), capturing differential rotation signatures in some stars (e.g., Deheuvels et al. 2012), and also demonstrating age discrepancies when compared to other methods such as period-age relations (e.g., Davies et al. 2015; van Saders et al. 2016). Nevertheless, relative to our understanding of the Sun, our knowledge of other stellar interiors is still highly incomplete.

Magnetic fields can have an impact on the differential rotation profile of a star. It has been found in previous studies (e.g., Gilman 1983; Browning et al. 2004; Browning 2008) that the torque of these strong magnetic fields can indeed suppress the differential rotation of a star. Most stars harbour magnetic fields somewhere in their interiors, and these fields likely play a role in nearly every phase of stellar evolution, as the presence of a magnetic field can influence the convective flow, which in turn can modify the strength and behaviour of the magnetic field itself. It is suggested via observations that these two phenomena are linked, such as the correlation between rotation rates and magnetic activity in stars throughout the Hertzsprung-Russell diagram (e.g., Pizzolato et al. 2003;

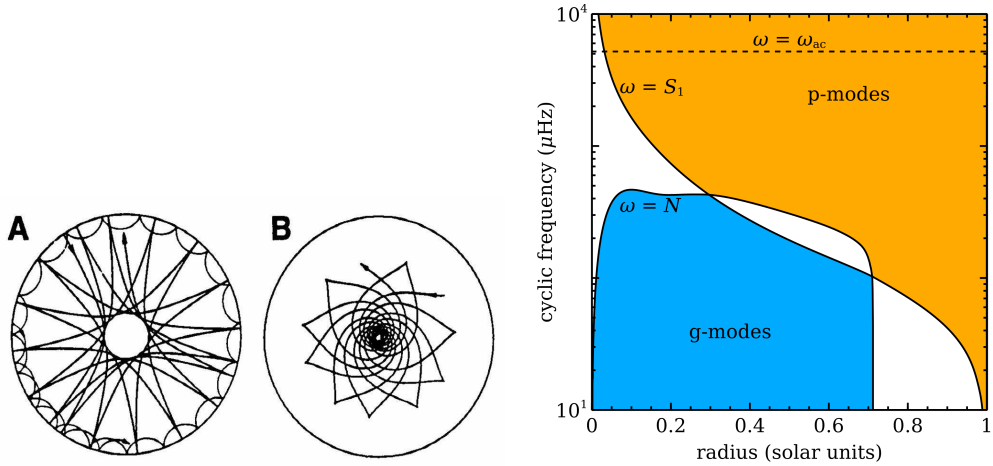

(a) (b)

Figure 1.2: (a) A diagram illustrating how the behaviour of different oscillation modes depend on different parts of the solar interior: (A) p-modes propagate in the radiative and convective zone of the Sun, (B) g-modes propagate in the radiative zone. Image credit: Gough et al. (1996). (b) A diagram showing the propagation of g-modes and p-modes in a standard solar model, and how the modes probe different parts of the solar interior. There is an overlap in approximately the middle third of the interior, which contains mixed-mode oscillations. Image credit: Christensen-Dalsgaard et al. (1996).

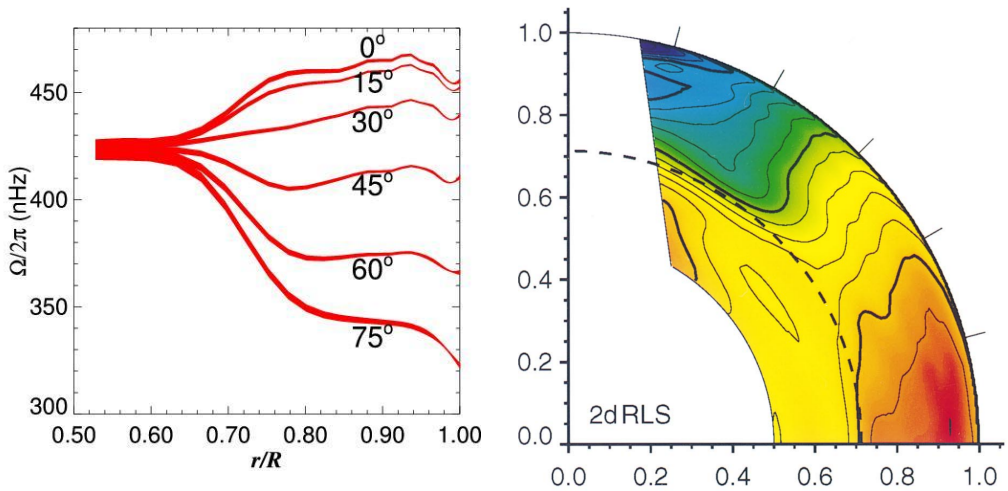

(a) (b)

Figure 1.3: (a) Internal rotation rate as a function of solar radius, for differing latitudes, from helioseismic inversion of GONG observations. Image credit: Harvey et al. (1996). (b) Differential rotation contour map of the Sun recovered from helioseismic inversion of GONG observations. Image credit: Schou et al. (1998). Both figures illustrate the solar transition from solid body rotation to differential rotation at $\approx 0.7\,R_\odot$.

Wright et al. 2011). However, we lack an exact theoretical understanding of the influence both convection and magnetism have on one another, and the resulting effect this has on the stellar structure.

These strong stellar magnetic fields are theorised to originate from a dynamo: a mechanism by which a star, or a planet, generates a magnetic field from a weak seed field, converting kinetic energy into magnetic energy (Moffatt 1978), which can be sustained over a long timescale. An electrically conducting fluid, and its associated motion, drives dynamo action. For a perfectly conducting fluid, magnetic field lines are "frozen" into the fluid, thus convective flow will stretch field lines, resulting in the amplification of a magnetic field. Rotation provides a level of symmetry-breaking in the flow, allowing the possibility of large-scale dynamo action, rather than simply fields structured on the scale of the convective eddies. Furthermore, differential rotation, and its resulting zonal flows, stretches and advects fields and thus is a primary factor of the stellar dynamo. Helioseismic data has helped refine our understanding of how the solar dynamo operates (e.g., Parker 1993; Ossendrijver 2003). A more in-depth description of dynamo action can be found in reviews, such as Brandenburg and Subramanian (2005), Charbonneau (2010), and Brun and Browning (2017).

The Sun exhibits magnetic structures on differing scales, ranging from small scale fields existing in the inter-granular lanes of convective flow, to large sunspots. Sunspots are a visible result of the solar dynamo on the surface: they are home to strong magnetic fields with strengths ~ 3 kG, and appear darker on the surface, as they become a window into the cooler interior, due to the resulting inhibition of convection. Figure 1.4 shows an observation of a sunspot from the Swedish 1 m Solar Telescope. Sunspots follow an approximate 11-year cycle, with the flux emergence visible initially at $\pm 30°$ latitude, slowly converging towards the equator as the cycle progresses. The eruption of magnetic flux tubes produces sunspot pairs of opposite magnetic polarities, which reverse after each cycle (Hale's law, Hale et al. 1919) simultaneously with the weaker solar magnetic dipole (Babcock 1961; Ossendrijver 2003); thus a full magnetic (dynamo) cycle is roughly 22 years. Also, sunspots appear slightly tilted (tilt angle increases with latitude), with the leading member of the pair appearing closer to the equator (Joy's law, Hale et al. 1919).

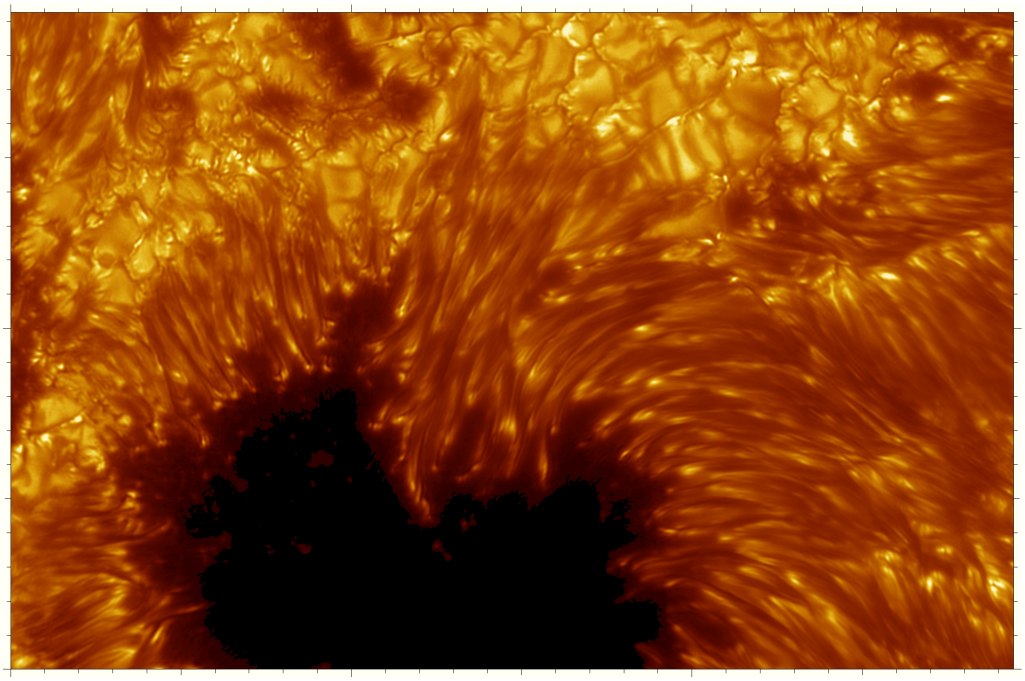

Figure 1.4: An observation of a sunspot using the Swedish 1 m Solar Telescope. The umbra (centre of the sunspot) is darker due to the inhibition of convection via strong magnetic fields. The penumbra is made up of thread-like structures surrounding the umbra. Tick mark distance: 1 Mm. Image credit: Scharmer et al. (2002).

Figure 1.5 is the solar magnetic butterfly diagram, showing how the surface latitudinal magnetic field strength varies with time.

For more distant stars, the detection of stellar magnetic fields is more indirect. These fields have been largely observed via photometry. This technique has a long history of measuring stellar variability, dating back to at least the 17th century (see, e.g., review in Strassmeier 2009). Magnetic fields can be inferred either from starspots, or through the measurement of chromospheric or coronal heating, revealing the prevalence of magnetic activity across the Hertzsprung-Russell diagram. Also used is the Zeeman-Doppler Imaging (ZDI) technique: the combination of the Zeeman effect (Zeeman 1897), where magnetic fields split the energy levels of spectral lines formed in the atmosphere of the star, and the periodic modulation of Zeeman signatures as the star rotates, i.e, the Doppler effect, which can reconstruct the surface vectorial magnetic field.

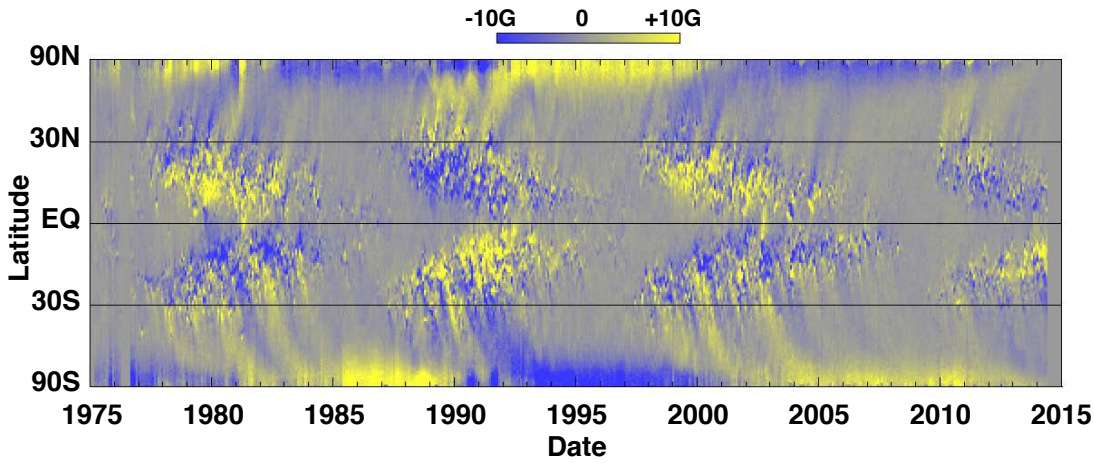

Figure 1.5: The solar magnetic butterfly diagram, showing the surface magnetic field strength varying as a function of latitude and time. This illustrates the approximate 22-year magnetic dynamo cycle, the convergence of sunspots towards the equator with each half-cycle, the switching of polarity at every 11-year half-cycle (Hale's law), and the observed tilt of sunspot pairs (Joy's law). Image credit: Hathaway (2015).

1.2 Low-mass Stars

This section gives a brief overview of the importance of low-mass stars, which is drawn largely from the review of Brun and Browning (2017). A majority of stars are smaller than the Sun (e.g., Chabrier 2003), with some 70% of our galaxy's stellar population consisting of M-dwarfs with masses $0.08-0.5\ M_\odot$, and luminosities ranging from $10^{-3}-10^{-1}\ L_\odot$ (e.g., Chabrier and Baraffe 1997; Reid and Hawley 2005). These objects are targets in regards to searching for Earth-like exoplanets (e.g., Tarter et al. 2007; Scalo et al. 2007; Berta et al. 2012), and there is major interest in their magnetic activity, due to the potential effect it would have on the environment of exoplanets orbiting in the relatively close "habitable zones" of these low-mass stars (e.g., Lammer et al. 2007; Walkowicz et al. 2008).

The interiors of these low-mass stars differ greatly from the Sun, becoming fully-convective between spectral types M3-M4, at masses $\lesssim 0.35\ M_\odot$ (e.g., Chabrier and Baraffe 1997). Thus, it could be expected that the magnetic field strength, structure, and generation in such a star is different to that in the Sun, where magnetism and its properties are influenced by the tachocline, i.e., the interface between the radiative core and the convective envelope, where there are strong regions of internal shear; differences are reviewed

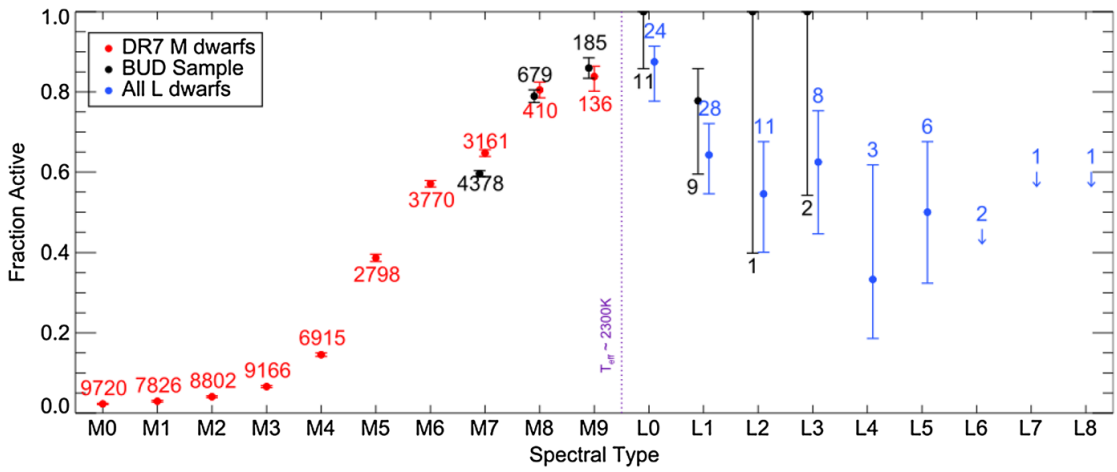

Figure 1.6: The fraction of stars of spectral type M0-L8 with observed chromospheric activity. It is found to be very common in fully convective stars, with spectral types in the mid-M regime. Image credit: Schmidt et al. (2015).

below. Many of these stars are highly active: Figure 1.6 shows the fraction of stars of spectral type M0-L8 that have measurable magnetic activity (Schmidt et al. 2015), with observations suggesting that chromospheric emission is evident and very common in the fully convective M-dwarf regime. Furthermore, many authors have attempted to understand whether there is a correlation between rotation rate and magnetic activity, similar to that found for solar-like objects, for fully convective M-dwarfs, helping to further constrain dynamo models (e.g., Mohanty and Basri 2003; Reiners and Basri 2008; Reiners et al. 2009; Browning et al. 2010; McLean et al. 2012). For example, in Figure 1.7, the chromospheric activity (determined using the Hα line) increases with rotation rate in the slowly rotating regime, and remains constant with more rapid rotation rates (Newton et al. 2017).

Due to the structural differences between low-mass and solar-like stars, the spatial distribution of magnetic fields of these objects is of great interest. Zeeman broadening measurements suggest average surface magnetic field strengths of $\sim$ kG for some fully convective low-mass stars (e.g., Reiners and Basri 2009). The structure appears to be mostly poloidal and axisymmetric, with ZDI observations depicting a transition from toroidal to poloidal fields at a similar spectral type range in which the transition to a fully convective interior occurs. In larger stellar objects, the field geometry determined by ZDI has apparent dependence on the stellar mass and the rotation rate. However, this does not

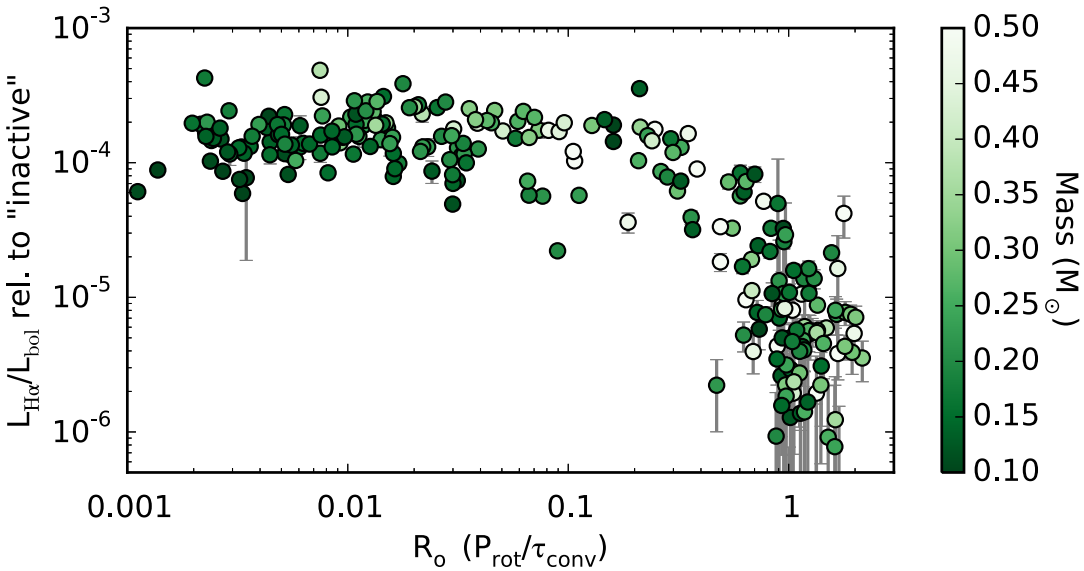

Figure 1.7: A measure of chromospheric activity as a function of the Rossby number Ro (ratio of inertial and Coriolis forces), showing an increase in activity with increasing rotation rates in the slowly rotating regime, before plateauing in the rapidly rotating regime. Ro is used as an estimation of the rotation rate, where $P_{\rm rot}$ is the rotation period and $\tau_{\rm conv}$ is the convective turnover time (increasing rotation right to left). Image credit: Newton et al. (2017).

appear to be a valid assumption for low-mass stars: it has been found that some late-M dwarfs have strong, axisymmetric dipolar fields (Morin et al. 2010), and some have weaker, nonaxisymmetric fields; this may either be a result of cycles between weak and strong field states (Kitchatinov et al. 2014), or a possible "bistability" in the dynamo process (see, e.g., Morin et al. 2011; Gastine et al. 2013).

1.3 Observational Background: Radius Inflation, Rotation, and Magnetic Activity

Some authors suggest that strong magnetic fields and rotation have a possible impact on the stellar structure of low-mass stars. It appears, using observations of eclipsing binaries, that some active M-dwarfs have radii that are greater than those predicted by 1D stellar structure models (e.g., Torres and Ribas 2002; López-Morales 2007; Morales et al. 2008; Stassun et al. 2012; Torres 2013), which can have an effect on the estimated ages of stars in the main sequence. Several authors have suggested that the convective heat transport

in the stellar interior is impacted by strong magnetic fields and/or rotation (e.g., Cox et al. 1981; Chabrier et al. 2007), and different mixing-length prescriptions have been adopted in 1D stellar structure models (e.g., MacDonald and Mullan 2014; Feiden and Chaboyer 2014) to investigate this issue further. See Section 3.1 for a more detailed introduction into the possible impact of magnetism and/or rotation on the structure of low-mass stars. In this section, we briefly discuss some of the observational background in regards to radius inflation and its possible correlation with rotation and magnetic activity.

Previous studies have found large discrepancies in stellar parameters between photometric observational data and those predicted by models. For example, using the Pleiades as a fiducial cluster, Bell et al. (2012) set up a benchmark test for pre-main-sequence isochrones, due to the cluster's significant number of pre-main-sequence objects, its distance and age values independent of the colour-magnitude diagram, and its low extinction. An isochrone is created via a spline fit to the Pleiades objects, which is then compared to model isochrones (Baraffe et al. 1998; Siess et al. 2000; D'Antona and Mazzitelli 1997; Dotter et al. 2008). The model isochrones appear to systematically overestimate the flux by a factor of 2 at 0.5 µm, which in optical colours results in a 2-3 factor age underestimation for stars younger than 10 Myr. These discrepancies were also found by Stauffer et al. (2007) in the V band, whereas Bell et al. (2012) show that this is the case for all optical bands.

Mann et al. (2015) used spectroscopic calibrations to derive effective temperatures ($T_{\rm eff}$), metallicities, and bolometric fluxes, and, using the Stefan-Boltzmann law, derived stellar radii for 183 late-type K7-M7 objects, allowing them to develop model-independent relations between $T_{\rm eff}$ and radius. To test the precision of these stellar radii, Mann et al. (2015) used the Dartmouth stellar evolution code to produce models with identical $T_{\rm eff}$ and bolometric fluxes to observations, in order to determine the stellar mass and age. From these masses, a semi-empirical mass-absolute magnitude relation is derived; it is found that the best models predict stellar radii to be $\sim 5\%$ (on average) lower than the observationally determined radii. Regardless of this, they find no correlation between radius inflation and magnetic activity: radius discrepancies between observations and models appear to be independent of magnetic activity signatures, such as observed Hα

activity measures and the ratio of coronal X-ray flux to the bolometric flux. This suggests that there are possible issues with underlying model assumptions, such as the convective mixing length or opacities used.

Jackson et al. (2018) combined rotation period measurements from the *Kepler* K2 survey of the Pleiades with measurements of rotational broadening from the WIYN 3.5 m telescope to estimate the radii of several hundred stellar objects in this cluster. For low-mass ($0.1 \leq M/M_{\odot} \leq 0.8$) rapidly-rotating ($\lesssim 2$ days) stars in this sample, the average radius is $14 \pm 2\%$ higher at a specific luminosity than what is predicted by the evolutionary models (at 120 Myr) of Dotter et al. (2008) and Baraffe et al. (2015). They considered unresolved binarity, differential rotation, and measurement bias to only have a $1 - 2\%$ effect on their results. Standard models predict radii that match interferometric observations of old, magnetically inactive low-mass stars, inferring that magnetic activity or rotation may be responsible for the inflation of young, more active objects.

MacDonald and Mullan (2017a) created 15 low-mass star magneto-convective models where magnetic fields affect the structure of the stellar interior, causing the stellar radius become inflated compared to the equivalent standard models. The magnetic field strength is capped at 10 kG, which is based on 3D numerical models of turbulent dynamos. A majority of these models replicate empirical radii measurements from low-mass star observations (Dittmann et al. 2017; Lubin et al. 2017; Gillen et al. 2017; Kraus et al. 2017) when using independent age estimates. Thus, it appears that interior magnetic fields on the order of 10 kG are responsible for the inflation of stellar radii in low-mass active stellar objects.

Kesseli et al. (2018) test whether single, rapidly rotating, fully convective stars are inflated by using measured rotational broadening and photometric rotation periods to determine the stellar radius. Radius inflation for objects in the range of the convective boundary (0.35 $M_{\odot}$) are consistent with that observed in partially convective eclipsing binaries, thus radius inflation is not necessarily due to a star's binarity. Furthermore, a few single, slowly rotating M-dwarfs have radii larger than standard models predict, thus it appears that neither binarity or rotation are responsible for fully convective M-dwarf radius inflation. However, their data is consistent with the stellar models of MacDonald

and Mullan (2017a), where magnetic fields of ~ 10 kG inhibit convection and inflate the stellar radii on the order of $\sim 10\%$.

The above observational background demonstrates the likelihood that the physics of standard stellar models should be reconsidered, in order to incorporate potential mechanisms that alter the stellar structure, and hence the stellar radius.

1.4 Convective Simulations and Stellar Modelling

Describing the structure and evolution of a star is complex. In order to understand these dynamical objects, one must consider many fields of physics: nuclear physics, to explain the nuclear fusion occurring in the core; fluid dynamics, thermodynamics and energy transfer, to understand how the resulting heat from the core is transferred through the interior via convective or radiative heat transport; magnetism, to understand how a magnetic field influences convection; even quantum mechanics, to understand degeneracy. Simulating convection is also challenging: convection and magnetism influence one another, but also depend on rotation (solid body or differential) and structural effects (stratification or surface properties). This makes it impossible to correctly model all detailed aspects of convection and magnetism analytically. Thus, it is necessary to use numerical simulations in order to gain an understanding of the dynamical behaviour within the stellar interior.

Due to the advancement of computational capabilities, numerical simulations are continually becoming more refined, allowing for more in-depth modelling of astrophysical objects and fluids. However, resolving all relevant scales is not an option with today's or any foreseeable computing capabilities. Convection is incredibly turbulent in stars, where the Reynolds number Re (the ratio of inertial to viscous forces) in stellar objects is substantially larger than simulations can run. This is primarily a result of the large range of scales present in the stellar interior. It is necessary to operate outside astrophysical parameter regimes in 3D simulations, thus it is impossible to fully capture the turbulence of the convective flow in these simulations. Approximations are made to achieve the highest resolution of small-scale turbulent flow possible, including modifying the Euler or Navier-Stokes equations to filter out sound waves (see the anelastic approximation in

Section 2.6.1), using more simple geometries for certain problems (e.g., "box in a star" calculations), using 2D simulations, or limiting the number of modes used in the spectral method (see Section 2.7.2) for the modelling of full spheres or spherical shells (see, e.g., discussion in Kupka and Muthsam 2017).

Due to the high turbulence of convective fluid flow in stellar interiors, it is not an option to simulate convection over stellar evolutionary timescales. Typically, 2D/3D simulations are capable of modelling convection over a multiple of the convective turnover timescale, which can be on the order of weeks, whereas the nuclear timescale of a star can be on the order of 10^9 years or more. Because of this, the stellar structure equations (see Section 2.2) are solved using 1D stellar structure models, in order to get an approximation of how a star's interior evolves, from the pre-main-sequence through to the main-sequence, with minimal difficulty. One of these approximations involves mixing length theory (MLT), which is widely used to model convection in a simplified way (Vitense 1953; Böhm-Vitense 1958). Briefly, it assumes a convective fluid parcel to rise a characteristic *mixing* length ℓ_{MLT} before giving up its heat to the surroundings, where ℓ_{MLT} is proportional to the pressure scale height at that point multiplied by a given MLT parameter α_{MLT}, i.e., $\ell_{\mathrm{MLT}} = \alpha_{\mathrm{MLT}} H_p$. An appropriate value of α_{MLT} is dependent on the MLT formulation, but in practice, is typically on the order of unity and calibrated via observation. However, this mechanism of convective modelling is limited by the lack of insight into the structure of the convective turbulent flow it provides.

Regardless of the above limitations, 2D/3D simulations are useful when it comes to investigating the effects of convective fluid flow, providing information on convective and magnetic behaviour, and their effects on the stellar interior. They can be used in conjunction with 1D stellar structure models, allowing α_{MLT} to be calibrated using results from 2D/3D simulations of convection (see, e.g., Abbett et al. 1997; Trampedach et al. 2014). Typical prescriptions of MLT do not consider rotation or magnetic fields, but this is being explored in recent studies (e.g., Chabrier et al. 2007; Feiden and Chaboyer 2014; MacDonald and Mullan 2014).

1.5 A History of Magnetic and Rotating Stellar Simulations

We briefly review the history of magnetic and rotating stellar simulations, which closely follows the more in-depth discussion in Brun and Browning (2017). Global simulations of stellar convection were first performed in the 1970s by Gilman and collaborators (Gilman 1975; Gilman 1977; Gilman and Glatzmaier 1981; Gilman 1983; Glatzmaier 1985). These models were laminar, linear, and relied on the Boussinesq approximation, which assumes that motion-induced density fluctuations are neglected, except when coupled to the gravitational acceleration in the buoyancy force. As more computing power became available, calculations, starting with those by Glatzmaier (1984), were performed using the anelastic approximation (Ogura and Phillips 1962; Gough 1969a), which filters out sound waves to avoid time step limitations (see Section 2.6.1). These simulations were still quite laminar, but started to encompass more complex and time-dependent calculations, thus it became increasingly possible to model more turbulent flow within strongly stratified regions, which were also less dominated by viscosity, thermal, and magnetic diffusivities.

Using a similar approach to Gilman and Glatzmaier, many codes have been produced and used in recent literature of stellar convection; examples include the Anelastic Spherical Harmonics (ASH) code (Clune et al. 1999; Miesch et al. 2000; Brun et al. 2004), and the recent *Rayleigh* code (see Featherstone and Hindman 2016). These various codes produce simulations that agree with one another in regards to the transportation of angular momentum, and also the solutions to the dynamo, whether cyclical or steady state; this led to a benchmark simulation described in Jones et al. (2011).

In comparison to solar-like stars, literature on stellar dynamos for low-mass stars is limited. The first 3D magnetohydrodynamic convective simulations of fully convective spheres were performed by Dobler et al. (2006) using the Cartesian grid-based finite-difference code PENCIL. These calculations were weakly stratified, and the rotational influence was low, but had established "anti-solar" differential rotation profiles, i.e., where the poles rotate slower than the equator. Also, dynamo action with magnetic field strengths of the order of equipartition with surface flows was generated, possessing a great range of spatial scales with a dominating large-scale component.

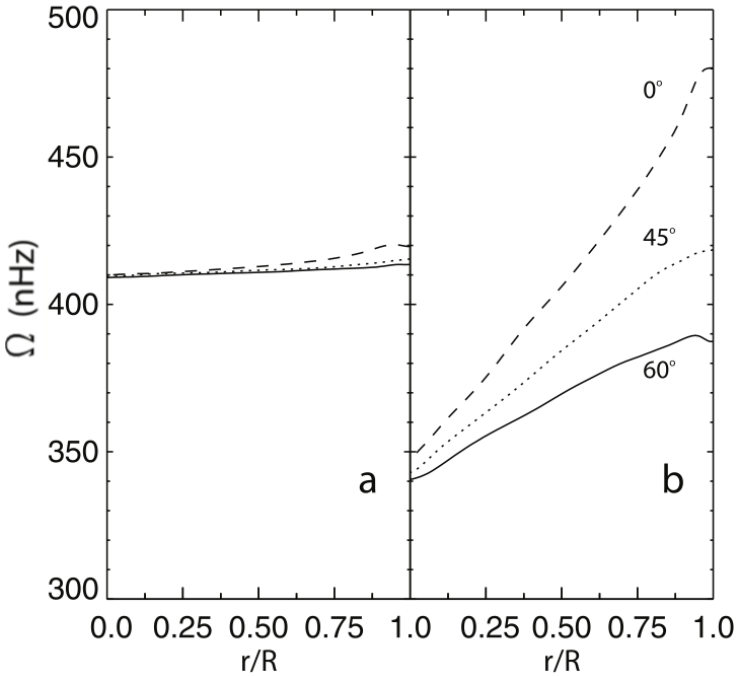

Figure 1.8: Angular velocity as a function of radius for multiple latitudes, for both the (a) magnetohydrodynamic and (b) hydrodynamic cases in Browning (2008). This demonstrates that differential rotation is suppressed in the magnetohydrodynamic simulation, where the star is essentially rotating as a solid body. Image credit: Browning (2008).

Anelastic simulations of a 0.3 $M_\odot$ M-dwarf were performed by Browning (2008), with a much stronger density stratification and for a range of different resolutions and turbulent diffusivities. Dynamo generation again achieved magnetic fields of ∼kG-strength, which is on the order of equipartition. It was also found that solar-like differential rotation was attained in hydrodynamic simulations, but disappeared in magnetohydrodynamic simulations due to strong Maxwell stresses as a result of the magnetic fields, as demonstrated in Figure 1.8. These simulations demonstrate that rotation has a strong influence on the dynamics within the stellar interior: the Rossby number Ro (ratio of inertial and Coriolis forces) was $\ll 1$ for models at the solar rotation rate, implying that rotation in these low-mass stars has a stronger influence compared to solar-like stars (where Ro $\sim 0.1 - 1$).

Yadav et al. (2015) performed simulations at lower diffusivities and even lower density stratifications, reaching lower values of Ekman number Ek (ratio of viscosity and Coriolis forces) compared to prior literature, and as a result, increased the influence of rotation. The model produced a dipole-dominated surface magnetic field, with a magnetic field strength comparable to observations. Small-scale fields carrying a majority of the

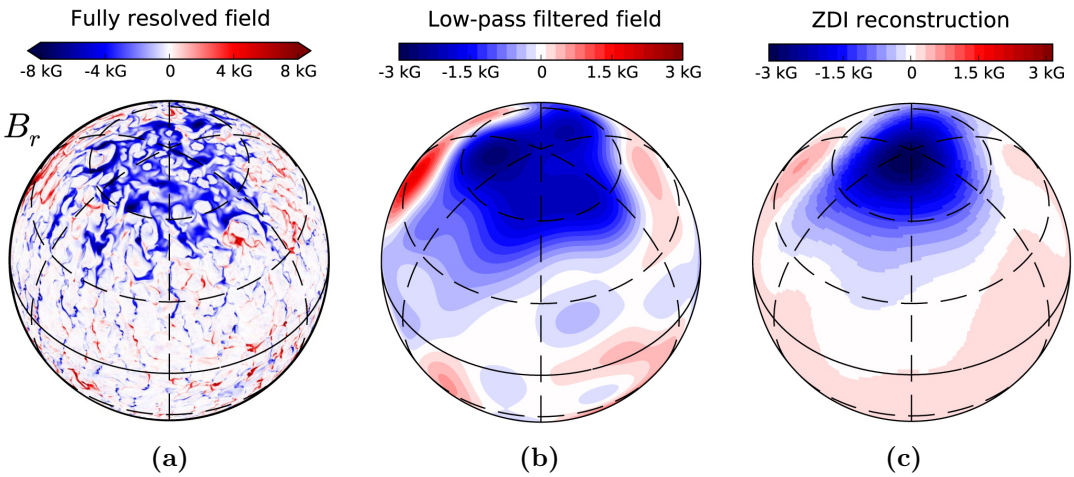

Figure 1.9: Radial component of the magnetic field in Yadav et al. (2015): (a) Orthographic projection, (b) Orthographic projection with a low-pass filter ($\ell \leq 10$), (c) Magnetic field map using the ZDI technique on synthetic observational data. Image credit: Yadav et al. (2015).

magnetic flux were produced via the interaction of the magnetic field with turbulent convection in the outer layers, as shown in the orthographic projection of the radial magnetic field component in Figure 1.9a. The ZDI technique was applied to synthetic spectropolarimetric data from their model, which reproduces a majority of the large scale field in their calculations; see Figures 1.9b and 1.9c for a comparison between a low-pass filtered orthographic projection of the radial magnetic field strength and the recreated magnetic field map from using the ZDI technique. The morphology and magnitude of both the large-scale and small-scale fields are also comparable to observations of low-mass fully convective stars.

Overall, these recent simulations have shown that fully convective stars drive differential rotation in some cases, and that convection can be influenced by magnetic fields generated by the stellar dynamo.

1.6 This Thesis

Rotation and magnetism are both known to influence convection: reduced horizontal lengthscales and convective speeds in rapidly rotating systems, and Lorentz forces in magnetised objects, are expected to impact the convective heat transport in the stellar interior (see Section 3.1). The specific entropy content of a star is linked to the stellar structure

and heat transport, thus any influence that rotation and magnetism have on convection will also modify the structure of specific entropy in the interior. This specific entropy structure—and in particular the adiabat on which much of the star lies—may in turn be calibrated using observations. Thus, it is the aim of this thesis to further our understanding of how rotation and magnetic fields influence the heat transport and structure of a star. Below is a brief overview of the two core projects of this thesis.

Firstly, Chapter 2 gives a brief overview of the computational tools and numerical methods used in 1D stellar structure and evolution models, and in 2D/3D simulations of convection. The stellar structure equations are presented, as well as an introduction into convection and MLT, used to model convection in 1D stellar models. For convective simulations, numerical approximations and an introduction into the magnetohydrodynamic equations, and their approximations, are listed. The codes used for our investigations in stellar modelling (MESA) and convective simulations (Dedalus and *Rayleigh*) are also described briefly in this chapter.

Chapter 3 looks at how the radius and specific entropy of a fully convective star is affected by rotation and magnetism, using 1D stellar structure models. Reformulations of MLT, namely those of Stevenson (1979) and MacDonald and Mullan (2014), are used to mimic the inhibition of convective heat transport in 1D stellar models, arising from rotation and magnetism, respectively. We examine changes in the entropy content of the star, and consequent changes in the stellar radius. Furthermore, an expression for a depth-dependent α_{MLT} parameter is constructed to produce nonstandard 1D stellar models, i.e., involving the effects of rotation and magnetism.

Chapter 4 looks at comparisons between MLT and simulations of stellar convection, in order to get an understanding of how rotation and magnetic fields can influence the transport of heat and the stellar structure in these calculations. We investigate this by examining changes in both the specific entropy and its gradient, firstly in 2D local simulations as a function of the density stratification, and secondly in 3D global simulations as a function of rotation rate, comparing our findings from the latter to the "rotating" MLT reformulation of Stevenson (1979) (supported by the local layer simulations of Barker et al. 2014).

Finally, Chapter 5 provides concluding remarks and discusses relevant future work.

Chapter 2

Computational Tools and Numerical Methods

2.1 Introduction: The Magnetohydrodynamic Equations

This chapter discusses the analytical and numerical tools used to perform theoretical modelling of the internal flows within a star or planet, allowing us to explore the dynamical behaviour of these astrophysical objects. In general, one can describe the macroscopic behaviour of astrophysical phenomena using the magnetohydrodynamic (MHD) equations, which are essentially the equations of fluid dynamics together with Maxwell's equations. For a fully compressible fluid, the conservation of mass can be expressed via the continuity equation:

$$\boldsymbol{\nabla} \cdot (\rho \boldsymbol{v}) = -\frac{\partial \rho}{\partial t}, \tag{2.1}$$

where ρ is density, $\boldsymbol{v}$ is the vector velocity, and t is time. The conservation of momentum, which describes the force balance of the fluid, is described by

$$\rho\left(\frac{\partial \boldsymbol{v}}{\partial t} + (\boldsymbol{v}\cdot\boldsymbol{\nabla})\boldsymbol{v} + 2\boldsymbol{\Omega}\times\boldsymbol{v}\right) = -\boldsymbol{\nabla}p + \rho\boldsymbol{g} - \boldsymbol{\nabla}\cdot\boldsymbol{\mathcal{D}} + \frac{1}{4\pi}(\boldsymbol{\nabla}\times\boldsymbol{B})\times\boldsymbol{B}, \tag{2.2}$$

where $\boldsymbol{\Omega}$ is the vector angular velocity, p is pressure, $\boldsymbol{g}$ is the vector gravitational acceleration, and $\boldsymbol{B}$ is the vector magnetic field. $\boldsymbol{\mathcal{D}}$ is the vector viscous stress tensor, defined by

$$\mathcal{D}_{ij} = -2\rho\nu\left(e_{ij} - \frac{1}{3}(\boldsymbol{\nabla}\cdot\boldsymbol{v})\right), \tag{2.3}$$

where e_{ij} is the strain rate tensor and ν is the kinematic viscosity. One form of the energy equation, which describes the conservation of energy in the system, is

$$\rho T\left(\frac{\partial s}{\partial t} + (\boldsymbol{v}\cdot\boldsymbol{\nabla})s\right) = \boldsymbol{\nabla}\cdot(\kappa\rho T\boldsymbol{\nabla}s) + Q + \Phi + \frac{\eta}{4\pi}[\boldsymbol{\nabla}\times\boldsymbol{B}]^2, \tag{2.4}$$

where T is temperature, s is specific entropy, κ is thermal diffusivity, Q is a heating function (representing, for example, the effects of nuclear energy generation), and η is magnetic diffusivity. The viscous heating term Φ is defined by

$$\Phi = 2\rho\nu\left(e_{ij}e_{ij} - \frac{1}{3}(\boldsymbol{\nabla}\cdot\boldsymbol{v})^2\right). \tag{2.5}$$

Finally, the induction equation, which describes how field lines are stretched by advection and how they decay due to ohmic resistivity, is

$$\frac{\partial \boldsymbol{B}}{\partial t} = \boldsymbol{\nabla}\times(\boldsymbol{v}\times\boldsymbol{B}) - \boldsymbol{\nabla}\times(\eta\boldsymbol{\nabla}\times\boldsymbol{B}). \tag{2.6}$$

In this chapter, we explore different ways to solve this set of equations. In Section 2.2, we assume there to be spherical symmetry, hydrostatic equilibrium, and no magnetic fields ($B = 0$), in order to express the 1D stellar structure equations. To solve these equations, we require a description of convection in stellar modelling: Section 2.3 discusses the criterion for the onset of convection, and Section 2.4 introduces and derives

the mixing length theory of convection. Section 2.5 discusses how the 1D stellar evolution code MESA solves these stellar structure equations to produce 1D stellar models. We then consider the full set of MHD equations for simulations of convection in both 2D and 3D. Section 2.6 covers approximations used to make simplifications to the full MHD equations, and Section 2.7 discusses the methods of numerical approximation used to convert continuous equations into solvable algebraic expressions. There is also a discussion of the codes used to model convection throughout this project, starting with a simple 2D convection code, in Section 2.8, and then the codes used to investigate convection in the stellar context in Sections 2.9 and 2.10, covering *Rayleigh* and Dedalus, respectively.

2.2 1D Stellar Structure Equations

The structure of a star can be described via a set of differential equations, which, assuming spherical symmetry, considers the pressure $p(r)$, density $\rho(r)$, temperature $T(r)$, specific energy generation rate $\epsilon(r)$, and luminosity $L(r)$ at a shell of thickness dr, at a distance r from the centre. One constraint is the equation of mass continuity, which relates the (cumulative) mass m and radius coordinates of a shell at distance r to the density at that point:

$$\frac{dr}{dm} = 4\pi r^2 \rho. \tag{2.7}$$

Another is the equation of momentum continuity, which relates the pressure and mass at a given point by balancing opposing forces due to gravity and pressure:

$$\frac{dp}{dm} = -\frac{1}{4\pi r^2}\left(\frac{Gm}{r^2} - \frac{d^2r}{dt^2}\right), \tag{2.8}$$

where G is the gravitational constant, and d^2r/dt^2 represents the acceleration of mass at that point if these forces are in imbalance. However, if the star is in hydrostatic equilibrium, the acceleration term is neglected, giving the equation of hydrostatic balance:

$$\frac{dp}{dm} = -\frac{Gm}{4\pi r^4}. \tag{2.9}$$

An additional constraint is the equation of energy conservation, which is derived by considering the specific energy generation rate ϵ (per unit mass) at a given point of the stellar interior, giving

$$\frac{dL}{dr} = 4\pi r^2 \rho \epsilon. \tag{2.10}$$

The specific energy generation rate can be expressed as the following power law:

$$\epsilon = \epsilon_0 \rho^\lambda T^\nu, \tag{2.11}$$

where ϵ_0 is the constant of proportionality, and λ and ν represent the density and temperature exponents of ϵ, respectively. Finally, we require an equation describing the energy transport, relating the luminosity (or flux) and temperature. In practice, this equation is expressed as

$$\frac{dT}{dm} = -\frac{Gm}{4\pi r^4}\frac{T}{p}\nabla, \tag{2.12}$$

where $\nabla = d\log T/d\log p$ is the logarithmic run of temperature with pressure. In the simple case where the sole method of heat transfer is radiation, $\nabla = \nabla_{\mathrm{rad}}$, which provides us with an analytical expression for the radiative energy transport:

$$\frac{dT}{dm} = -\frac{3}{64\pi^2 ac}\frac{\kappa L}{r^4 T^3}, \tag{2.13}$$

where a is the radiation constant, c is the speed of light, and κ is opacity. The opacity is typically expressed as a power law:

$$\kappa = \kappa_0 \rho^\alpha T^\beta, \tag{2.14}$$

where κ_0 is the constant of proportionality, and α and β represent the density and temperature exponents of κ, respectively. These four differential equations govern the stellar structure, in the absence of convection. If convection is the method of heat transport in a region, the full equation of energy transport generally cannot be expressed analytically, and must be solved using mixing length theory (see Section 2.4) or an equivalent.

To close this set of equations, we employ the equation of state (EOS): an expression used to relate thermodynamic variables, typically pressure, density, temperature and composition. The stellar interior consists of gas (ions and electrons) and radiation (photons). Assuming a general equation of state $\rho = \rho(p, T, \mu)$, where μ is the mean molecular weight, one can write

$$\frac{\partial \rho}{\rho} = \alpha \frac{\partial p}{p} - \delta \frac{\partial T}{T} + \varphi \frac{\partial \mu}{\mu}, \tag{2.15}$$

where

$$\alpha = \left(\frac{\partial \log \rho}{\partial \log p} \right)_{T,\mu}, \tag{2.16}$$

$$\delta = - \left(\frac{\partial \log \rho}{\partial \log T} \right)_{p,\mu}, \tag{2.17}$$

and

$$\varphi = \left(\frac{\partial \log \rho}{\partial \log \mu} \right)_{p,T}. \tag{2.18}$$

An ideal gas equation of state ($\alpha = \delta = \varphi = 1$), including the radiation pressure contribution, is given by

$$p = \frac{\mathcal{R}}{\mu} \rho T + \frac{1}{3} a T^4, \tag{2.19}$$

where $\mathcal{R}$ is the ideal gas constant.

Various simplifications to the EOS have proven useful in studying stellar interiors. Chief among these are polytropic models, in which the pressure scales with density in the following manner:

$$p = K\rho^{(n+1)/n}, \tag{2.20}$$

where K is the polytropic constant, and n is the polytropic index. The density exponent can also be expressed as the adiabatic exponent $\gamma = (n+1)/n$. For example, a $n = 1.5$ ($\gamma = 5/3$) polytrope is a good approximation for a fully convective star, which results in a constant specific entropy gas, i.e., $s \sim \ln(p/\rho^{5/3}) \sim const$, whereas a $n = 3$ polytrope is typically used to model main sequence stars similar to the Sun, also known as the Eddington Standard Model. Both of these polytropes must be computed numerically, as they have no analytical solutions.

2.3 Convection in 1D Stellar Models

Convection is a method of heat transport in which fluid parcels carry heat by physical motion. Consider a fluid parcel in a gravitational field at an initial position with density ρ and pressure p, with the surroundings at identical ρ and p. For a sensible EOS, if a parcel temperature increases, its density will decrease. If the parcel is less dense than its surroundings, it will experience a buoyancy force by Archimedes' principle, and it will begin to rise. For a parcel displaced vertically upward by a small distance Δr, the density change of the fluid element is

$$\Delta\rho' = \left(\frac{\partial\rho'}{\partial r}\right)\Delta r, \tag{2.21}$$

whilst the density change of the surroundings is

$$\Delta\rho = \left(\frac{\partial\rho}{\partial r}\right)\Delta r. \tag{2.22}$$

We assume it is in pressure equilibrium as it rises, consistent with the argument that the velocity of the parcel is much smaller than the local sound speed.

Depending on the thermal stratification of the stellar interior, thermal buoyancy forces can produce either thermal convection flows or internal gravity waves, determined by the temperature gradient. To assess the treatment of convection in these stellar models, one must consider the convective stability of a region. For a parcel to be unstable against convection, the density of the parcel must be less than its surroundings:

$$\left(\frac{\partial \log \rho'}{\partial r}\right) < \left(\frac{\partial \log \rho}{\partial r}\right). \tag{2.23}$$

However, if the density of the parcel is larger than the density of its surroundings, it is stable against convection, thus it will eventually halt and become "anti-buoyant", falling until its density is less than its surroundings, becoming buoyant once more. This oscillation about an equilibrium point results in internal gravity waves.

To derive a criterion of convection, we first differentiate the EOS in Equation (2.15) with respect to radius:

$$\frac{\partial \log \rho}{\partial r} = \alpha \frac{\partial \log p}{\partial r} - \delta \frac{\partial \log T}{\partial r} + \varphi \frac{\partial \log \mu}{\partial r}. \tag{2.24}$$

Assuming that the fluid element's composition is uniform with depth, i.e., $(\partial \log \mu'/\partial \log p) = 0$, and multiplying by the pressure scale height $H_p = -\partial r/\partial \log p$, gives the criterion for convection instability as

$$\nabla' - \nabla < -\frac{\varphi}{\delta}\nabla_\mu, \tag{2.25}$$

where

$$\nabla' = \left(\frac{\partial \log T'}{\partial \log p}\right), \tag{2.26}$$

$$\nabla = \left(\frac{\partial \log T}{\partial \log p}\right), \tag{2.27}$$

and

$$\nabla_\mu = \left(\frac{\partial \log T}{\partial \log \mu}\right). \tag{2.28}$$

When a region is convectively unstable, it is said to be superadiabatic, i.e., the adiabatic temperature decreases slower than the surrounding temperature over an equivalent distance, whereas a region that is convectively stable is said to be subadiabatic, i.e., the parcel (adiabatic) temperature decreases faster than the surrounding temperature over an equivalent distance (see Figure 2.1b).

In a region of high efficiency convection, such as the bulk of a convective stellar interior, the element temperature gradient is approximately the adiabatic temperature gradient, i.e., $\nabla' = \nabla_{\rm ad}$. Therefore, one arrives at the *Ledoux criterion*, which shows a region to be convectively unstable if

$$\nabla > \nabla_{\rm ad} + \frac{\varphi}{\delta}\nabla_\mu, \tag{2.29}$$

reducing to

$$\nabla > \nabla_{\rm ad} + \nabla_\mu \tag{2.30}$$

for an ideal gas. If the region is of uniform composition, the stability criterion reduces to the more simple *Schwarzschild criterion*:

$$\nabla > \nabla_{\rm ad}. \tag{2.31}$$

The extent to which the temperature gradient exceeds the adiabatic is typically defined as the superadiabatic gradient $\nabla_{\rm s}$:

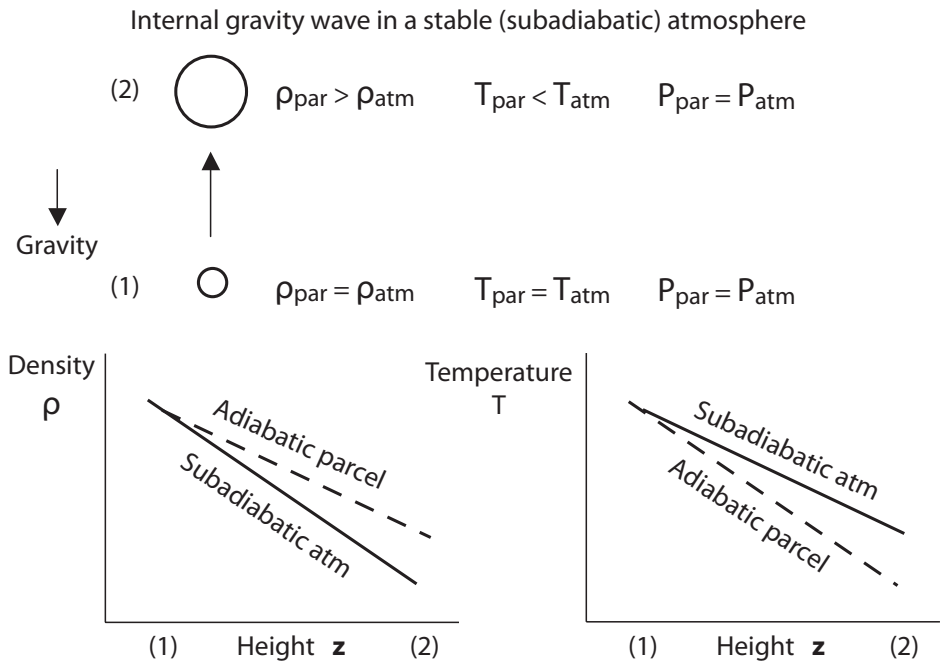

(a)

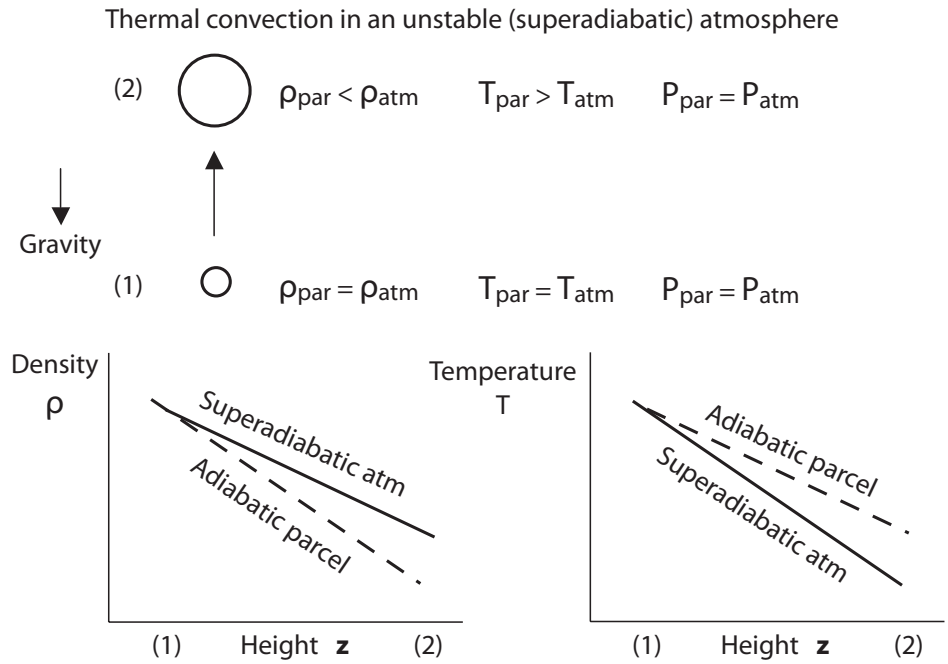

(b)

Figure 2.1: A fluid parcel travelling vertically upward in a region with (a) subadiabatic, (b) superadiabatic temperature and density profiles, where $\rho_{\rm par}$ and $\rho_{\rm atm}$ are the density of the parcel and its surroundings, respectively, and $T_{\rm par}$ and $T_{\rm atm}$ are the temperature of the parcel and its surroundings, respectively. In (a), the adiabatic parcel temperature decreases faster than its surrounding temperature with height, resulting in gravity waves. In (b), the adiabatic parcel temperature decreases slower than its surrounding temperature with height, resulting in thermal convection. Image credit: Glatzmaier (2013, p. 5).

$$\nabla_{\rm s} = \nabla - \nabla_{\rm ad}. \tag{2.32}$$

In regions of highly efficient convection, the temperature gradient need only be slightly larger than the adiabatic, i.e., $\nabla_{\rm s} \lesssim 10^{-5}$, in order to transfer the given heat flux. The entropy gradient is related to the superadiabatic gradient:

$$\frac{ds}{dr} = -\frac{c_p}{H_p}\nabla_{\rm s}, \tag{2.33}$$

therefore the fluid is unstable to convection if $ds/dr < 0$. Due to the small superadiabaticity of high efficiency convective regions, the specific entropy profile is near constant throughout the convective region of a stellar interior (see Section 3.2 for an in-depth discussion of the role of specific entropy in 1D stellar models).

If a stellar model has nonuniform composition, e.g., due to nuclear burning, it is possible for the region to be unstable against convection by the Schwarzschild criterion, yet stable by the Ledoux criterion, or vice versa. If the mean molecular weight increases with radius in a region where it is convectively stable by the Schwarzschild criterion, convective instability can still be caused by ∇_μ alone: this is known as thermohaline mixing. On the other hand, if the mean molecular weight increases with radius in a region which is convectively unstable by the Schwarzschild criterion, convective stability could occur due to ∇_μ: this is known as semi-convection. However, for the 1D stellar model work in Chapter 3, a uniform mean molecular weight is assumed for simplicity, neglecting the Ledoux criterion for convection.

2.4 Mixing Length Theory of Convection

Convection is a complex phenomenon: it is not possible to simulate the 3D dynamical behaviour of convection over stellar evolutionary timescales. Therefore, 1D stellar models are used to describe the changes in stellar structure over millions of years, where the effects of convection are typically modelled by employing the *mixing length theory* (MLT). This treatment considers the convection process as consisting of discrete parcels of fluid that

retain their temperature and density, until they have travelled a characteristic length called the "mixing length" ($\ell_{\rm MLT}$). The parcels then disperse into the atmosphere and share their energy with their surroundings. MLT assumes pressure equilibrium and symmetric flow, where there are equal numbers of warm buoyant upflows and cool sinking downflows. The mixing length $\ell_{\rm MLT}$ is expressed as a multiple of the MLT parameter $\alpha_{\rm MLT}$ and the pressure scale height H_p, i.e.,

$$\ell_{\rm MLT} = \alpha_{\rm MLT} H_p. \tag{2.34}$$

It was first introduced by Vitense (1953) and Böhm-Vitense (1958), and is still the most widely used model for convection in stellar interiors due to its fast calculation, its model simplicity with just one free parameter, and also its success in matching various stellar observations. The value of $\alpha_{\rm MLT}$ is typically of order unity, and determines the stellar radius (and the adiabat) of the model; this value is typically calibrated through comparison with observations.

MLT is useful in describing the thermal structure of convection zones, as mass mixing occurs in convection for stratified atmospheres. The rate of heat transport can be determined by the formation rate of the parcel, velocity of the parcel, the mixing length $\ell_{\rm MLT}$, the temperature gradient of the star and how much heat parcels "leak" radiatively (see, e.g., Hansen et al. 2004, p. 242). Most versions of MLT are local theories, because convective heat flux is computed at single radii. MLT calculates the local temperature gradient in the convective zone of a stellar model, permitting solution of the equation of energy transport (Equation (2.12)) in these convectively unstable regions.

The purpose of MLT is to relate luminosity (or flux) to the temperature for regions undergoing convective heat transport. One starts by expressing the fictitious radiative temperature gradient $\nabla_{\rm rad}$ as that required to transfer all the flux by radiative heat transfer:

$$\begin{aligned} F_{\rm tot} &= F_{\rm conv} + F_{\rm rad} \\ &= \frac{4ac}{3}\frac{T^4}{\kappa\rho H_p}\nabla_{\rm rad}. \end{aligned} \tag{2.35}$$

The radiative flux is actually defined as

$$F_{\rm rad} = \frac{4ac}{3}\frac{T^4}{\kappa\rho H_p}\nabla, \tag{2.36}$$

where the temperature gradient ∇ needs to be determined. The convective flux transported by these elements is

$$F_{\rm conv} = \rho\bar{v}c_p\Delta T, \tag{2.37}$$

where ρ, $\bar{v}$, c_p, and ΔT are the average density, convective velocity, specific heat capacity (at constant pressure), and temperature excess, respectively. In MLT, it is assumed that a fluid element rises (in pressure equilibrium) and travels a characteristic mixing length $\ell_{\rm MLT}$ before giving up its heat to its surroundings. At first order, a fluid parcel rising an average distance $\ell_{\rm MLT}/2$ has an average temperature excess over the surrounding region of

$$\Delta T = \frac{\ell_{\rm MLT}}{2}\left(\frac{dT'}{dr} - \frac{dT}{dr}\right). \tag{2.38}$$

In terms of the temperature gradient ∇ and ∇', using H_p, this can be expressed as

$$\Delta T = T\frac{\ell_{\rm MLT}}{2H_p}(\nabla - \nabla'), \tag{2.39}$$

thus the convective flux can be defined as

$$F_{\rm conv} = \frac{1}{2}\rho\bar{v}c_pT\frac{\ell_{\rm MLT}}{H_p}(\nabla - \nabla'). \tag{2.40}$$

The buoyancy force experienced by a fluid element is

$$\begin{aligned} f_{\rm b} &= -g\Delta\rho \\ &= g\rho\delta\frac{\Delta T}{T}, \end{aligned} \tag{2.41}$$

where $\Delta\rho/\rho = -\delta\Delta T/T$ for a uniform composition ideal gas in pressure equilibrium (see Equation (2.23)). The average work done (assuming half of the work is acting on the fluid element over a distance $\ell_{\rm MLT}/2$) is therefore

$$\begin{aligned} W &= \frac{1}{2}\frac{\ell_{\rm MLT}}{2}g\rho\delta\frac{\Delta T}{T} \\ &= \frac{1}{8}\frac{\ell_{\rm MLT}^2}{H_p}g\rho\delta(\nabla - \nabla'). \end{aligned} \tag{2.42}$$

Typical versions of MLT assume that half of this work done is transferred into kinetic energy ($(1/2)\rho\bar{v}^2$), thus the average convective velocity can be expressed as

$$\bar{v} = \left(\frac{1}{8}\frac{\ell_{\rm MLT}^2}{H_p}g\delta(\nabla - \nabla')\right)^{1/2}. \tag{2.43}$$

Therefore, one can rewrite the convective flux as

$$F_{\rm conv} = \frac{1}{4\sqrt{2}}\rho c_pT(g\delta H_p)^{1/2}(\nabla - \nabla')^{3/2}\left(\frac{\ell_{\rm MLT}}{H_p}\right)^2. \tag{2.44}$$

We now require an expression for the fluid element temperature gradient ∇'. A fluid element rising not only loses heat adiabatically, but also via radiative losses to its surroundings. Assuming that these elements are optically thick, the equation of radiative

transfer for optically thick turbulence elements is

$$F = -\frac{4ac}{3}\frac{T^3}{\kappa\rho}\frac{\Delta T}{\ell_{\rm MLT}/2}. \tag{2.45}$$

This flux is lost to the surroundings across the surface area S of the fluid element, thus the radiative losses per unit time λ can be expressed as

$$\lambda = SF = -\frac{4ac}{3}\frac{T^3}{\kappa\rho}\Delta T\frac{S}{\ell_{\rm MLT}/2}. \tag{2.46}$$

This becomes a correction to ∇':

$$\nabla' = \nabla_{\rm ad} - \frac{\lambda H_p}{\rho V c_p \bar{v} T}, \tag{2.47}$$

where V is the volume of the fluid element. Using Equation (2.39), and setting $S\ell_{\rm MLT}/V = 9/2$ to obtain numerical agreement with the results of Böhm-Vitense (1958) (Weiss et al. 2004, p. 393), we can derive the following expression:

$$\frac{\nabla' - \nabla_{\rm ad}}{\nabla - \nabla'} = \frac{6acT^3}{\kappa\rho^2 c_p \bar{v}\ell_{\rm MLT}}. \tag{2.48}$$

We now have five equations: Equations (2.35), (2.36), (2.43), (2.44), (2.48), and five unknowns: $F_{\rm rad}$, $F_{\rm conv}$, $\bar{v}$, ∇', ∇. The mixing length $\ell_{\rm MLT}$ is set to be a multiple of the pressure scale height, as discussed above. To solve for these analytically, the following are defined:

$$U = \frac{3acT^3}{\kappa\rho^2 c_p \ell_{\rm MLT}^2}\left(\frac{8H_p}{g\delta}\right)^{1/2}, \tag{2.49}$$

$$W = \nabla_{\rm rad} - \nabla_{\rm ad}, \tag{2.50}$$

$$\zeta^2 = \nabla - \nabla_{\rm ad} + U^2. \tag{2.51}$$

Using Equations (2.43) and (2.48), one can eliminate $\bar{v}$:

$$\nabla' - \nabla_{\rm ad} = 2U(\nabla - \nabla')^{1/2}. \tag{2.52}$$

Using Equations (2.35), (2.36), and (2.44), it is possible to define:

$$(\nabla - \nabla')^{3/2} = \frac{8}{9}U(\nabla_{\rm rad} - \nabla). \tag{2.53}$$

By expressing $(\nabla' - \nabla_{\rm ad}) = (\nabla - \nabla_{\rm ad}) - (\nabla - \nabla')$, one can write

$$(\nabla - \nabla')^{1/2} = \zeta - U, \tag{2.54}$$

which when combined with Equation (2.53), gives the following cubic equation that can be solved for ζ:

$$(\zeta - U)^3 + \frac{8}{9}U(\zeta^2 - U^2 - W) = 0, \tag{2.55}$$

providing a solution for the temperature gradient ∇.

2.5 1D Modelling of Stars with MESA

The Modules for Experiments in Stellar Astrophysics (MESA) code[1] (Paxton et al. 2011; Paxton et al. 2013; Paxton et al. 2015; Paxton et al. 2017) is a suite of libraries that includes the 1D stellar evolution module `MESA star`, combining numerical and physical modules for simulations of stellar structure and evolution. It is open source, and is capable of modelling various objects, from planets to massive stars, in a variety of environments and advanced evolutionary phases. `MESA star` simultaneously solves the fully coupled structure and composition equations, and allows for modules (written independently in Fortran 95) to implement the equation of state (EOS), opacity, nuclear reaction rates, at-

1. http://mesa.sourceforge.net, accessed June 2018

mosphere boundary conditions, and element diffusion. Modern numerical methods, such as high-order interpolation schemes, and advanced adaptive mesh refinement, are supported, taking advantage of its shared memory parallelisation (Paxton et al. 2011). The stellar models used in Chapter 3 were calculated using the MESA 10108 release. A more in-depth discussion of MESA and its capabilities can be found in Paxton et al. (2011), but a brief description of how MESA solves for stellar structure and evolves a model can be found below.

Section 2.5.1 describes the initial checks that MESA makes before producing a model, and also the MLT calculations performed. Section 2.5.2 demonstrates how the stellar structure and composition equations must be written in order for them to be solvable, how the EOS is determined, and gives a brief overview of how cells work in MESA. Section 2.5.3 shows how the Newton-Raphson solver is used to iterate over these equations and converge to a final solution at each time step, and Section 2.5.4 shows how time step selection is determined during the evolution of a stellar model.

2.5.1 Initialising Model and MLT Calculations

Firstly, `MESA star` reads the user input files in order to initialise the appropriate physics modules. This input specifies properties of the input model, such as the type of evolution calculation, the EOS and opacity data, chemical composition, and the nuclear network required. A pre-main-sequence model is created from a user inputted mass, a uniform composition, a luminosity, and a low central temperature. Using an $n = 1.5$ polytrope, an initial guess for the central density ρ_c is made, which is used by the `mlt`, `eos`, and `num` (Newton solver) modules to find a value of ρ_c that is consistent with the mass. This model is then entered into the evolution loop.

At the beginning of each time step, `MESA star` checks the structure and composition of the model. The adaptive mesh algorithm checks how changes in temperature, density, and the helium mass fraction between two adjacent cells compare to user inputted thresholds for each parameter; if these changes are less than the threshold, these adjacent cells are merged. The splitting of cells will occur in areas where higher resolution is required,

such as convective zone boundaries, or in the vicinity of nuclear burning, where changes in the nuclear energy generation are large compared to changes in pressure.

The `mlt` module calculates the convective diffusion coefficients via MLT (see Section 2.4). However, MLT fails to account for mixing in the boundary between regions of convection and radiative layers. In MESA, this is modelled as a diffusive process with a diffusion coefficient D that decays exponentially past this (Schwarzschild) boundary:

$$D = D_{\mathrm{conv},0} \exp\left(-\frac{2z}{f H_{p,0}}\right), \tag{2.56}$$

where $D_{\mathrm{conv},0}$ is the MLT derived diffusion coefficient at a point in the convection zone near the Schwarzschild boundary, $H_{p,0}$ is the pressure scale height at this point, z is the distance from this point, and f is a free parameter that is used to describe the efficiency of the extra diffusive mixing (see Herwig 2000). This allows a user to limit the regions of a star where this overshoot mixing is considered.

2.5.2 Solving the Structure and Composition Equations

The module then solves the stellar structure and composition equations over all the cells. Each cell consists of face variables and mass-averaged variables, as shown in Figure 2.2, due to the finite volume of these cells. Hereafter, subscripts $k-1$, k, and $k+1$ represent the variable at those particular grid cells. In MESA, the stellar structure equations are reformulated in order to improve numerical stability and to minimise potential round-off errors; these reformulations are given below. By considering the density evolution of a given cell k:

$$\rho_k = \frac{dm_k}{(4/3)\pi(r_k^3 - r_{k+1}^3)}, \tag{2.57}$$

where dm_k is the finite element of mass interior to the face, the reformulation of the mass continuity equation (Equation (2.7)) is

$$\log(r_k) = \frac{1}{3}\left(r_{k+1}^3 + \frac{3}{4\pi}\frac{dm_k}{\rho_k}\right). \tag{2.58}$$

r_{k+1} is replaced by the inner boundary condition (typically zero) at the innermost cell. The full equation of hydrostatic balance (Equation (2.8)), which includes the hydrodynamic term, is rewritten to give the pressure p_k:

$$p_{k-1} - p_k = \frac{1}{2}\frac{(dm_{k-1} + dm_k)}{4\pi r_k^2}\left(\frac{-Gm_k}{r_k^2} - a_k\right), \tag{2.59}$$

where a_k is the Lagrangian acceleration at the cell face, which is calculated by considering the change in velocity at the cell face over time step δt ($a_k = 0$ if hydrostatic). The equation of energy transport (Equation (2.12)) is written as

$$T_{k-1} - T_k = \frac{1}{2}\frac{(dm_{k-1} + dm_k)}{4\pi r_k^2}\left(-\nabla_k \frac{Gm_k}{r_k^2}\frac{\bar{T}_k}{\bar{p}_k}\right), \tag{2.60}$$

where ∇_k is the face value determined via the `mlt` module, and $\bar{T}_k = (T_{k-1}dm_k + T_k dm_{k-1})/(dm_k + dm_{k-1})$ and $\bar{p}_k = (p_{k-1}dm_k + p_k dm_{k-1})/(dm_k + dm_{k-1})$ are the temperature and pressure interpolated by mass, respectively. For numerical stability, Equations (2.59) and (2.60) are divided by $\bar{p}_k$ and $\bar{T}_k$, respectively. Finally, the equation of energy conservation (Equation (2.10)) becomes

$$L_k - L_{k+1} = dm_k(\epsilon_{\rm nuc} - \epsilon_{\nu,\rm thermal} + \epsilon_{\rm grav}), \tag{2.61}$$

where $\epsilon_{\rm nuc}$ is the nuclear energy generation rate, $\epsilon_{\nu,\rm thermal}$ is the specific thermal neutrino-loss rate, and $\epsilon_{\rm grav} = -Tds/dt$ is the specific rate of change of gravitational energy due to expansion/contraction. The rate of change of specific entropy s is determined using the EOS. The EOS is determined by the `eos` module, using ρ and T as independent variables. This ρ-T EOS data is stored in tables, and is dependent on the density and temperature range of the model. MESA tables are based on the OPAL EOS tables (Rogers and Nayfonov 2002) and SCVH tables for lower values of T and ρ (Saumon et al. 1995);

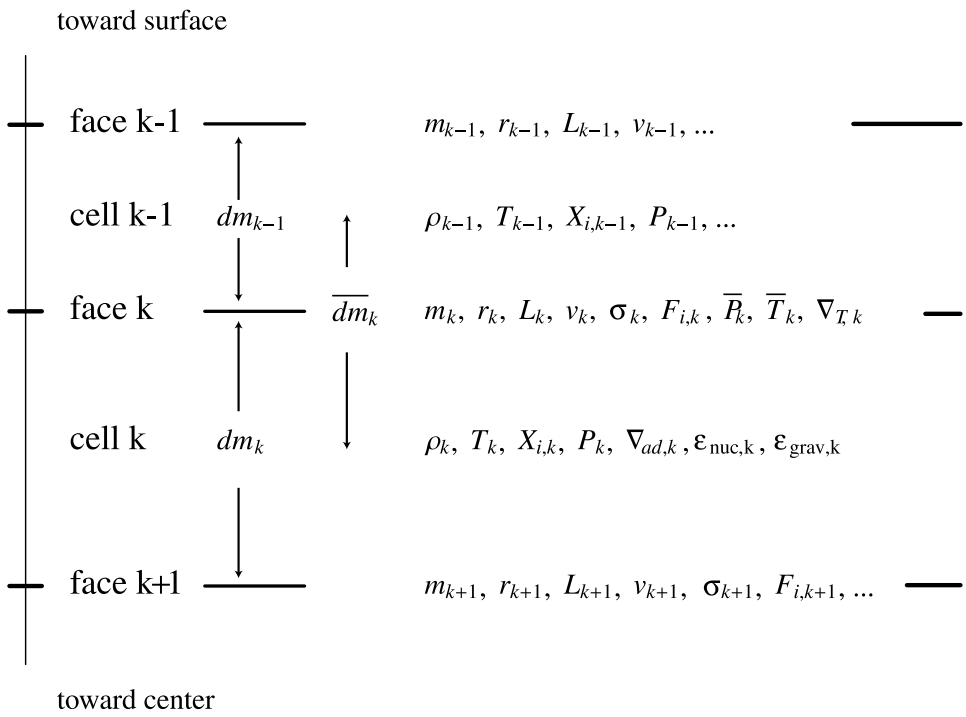

Figure 2.2: A schematic demonstrating the cell structure in MESA, and how they consist of face variables and mass-averaged variables. Image credit: Paxton et al. (2011).

a smooth transition is constructed between these. Figure 2.3 shows the EOS coverage for metallicity $Z \leq 0.04$, showing which EOS tables are used for particular regions of ρ and T. Tables are provided for hydrogen mass fractions $X = 0 - 1.0$ ($\Delta 0.2$) and $Z = 0 - 0.04$ ($\Delta 0.02$). Outside the OPAL/SCVH regime, HELM (Timmes and Swesty 2000) and PC (Potekhin and Chabrier 2010) EOS tables are used (for $Z > 0.04$), which both assume complete ionisation. Custom EOS tables can also be used in MESA.

Finally, the equation for the mass fraction $X_{i,k}$ of species i is

$$X_{i,k}(t + \delta t) - X_{i,k}(t) = \frac{dX_{i,k}}{dt}\delta t + (F_{i,k+1} - F_{i,k})\frac{\delta t}{dm_k}, \tag{2.62}$$

where

$$F_{i,k} = 2(X_{i,k} - X_{i,k-1})\frac{\sigma_k}{(dm_{k-1} + dm_k)} \tag{2.63}$$

is the mass of species i across the face of k, where σ_k is the Lagrangian diffusion coefficient that captures the effects of convection and overshoot mixing. The rate of change of $X_{i,k}$

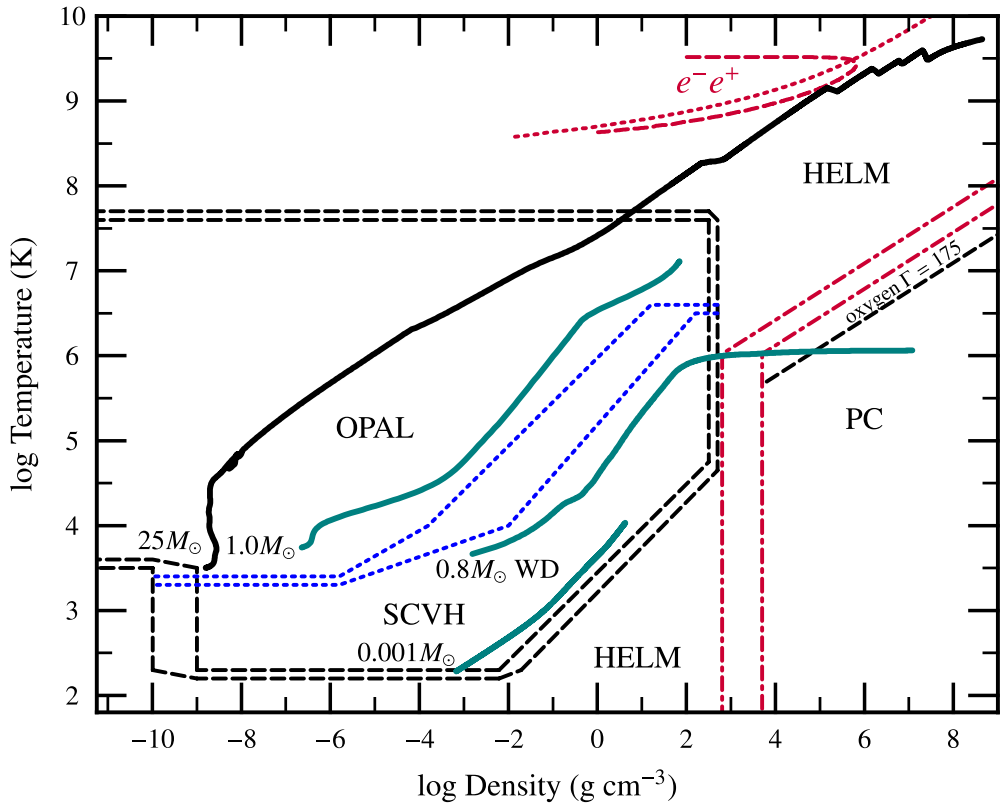

Figure 2.3: The EOS (ρ-T) coverage used by the MESA module `eos`, for metallicity $Z \leq 0.04$. MESA EOS tables, constructed from OPAL and SCVH, are used for the region within the black dashed lines, which are blended in the region within the blue lines. Outside the MESA EOS regime, HELM AND PC EOS tables are used (regions outside of the black dashed lines), which cover electron-positron pairing (at high T) and crystallisation (at low T), respectively. The red dotted line shows where the number of electrons per baryon doubles due to pair production, and $\Gamma_1 < 4/3$ ($\equiv (d\log p/d\log\rho)_s$) to the left of the red dashed line. The red dot-dashed line depicts where the PC and HELM EOS tables are blended, and below the black dashed line, labelled $\Gamma = 175$ (the Coulomb coupling parameter), represents where a plasma of pure oxygen becomes fully crystallised. Green lines indicate profiles for a main-sequence 1 $M_\odot$, a contracting 0.001 $M_\odot$, and a cooling 0.8 $M_\odot$ white dwarf model, whereas the thick black line shows the profile of an evolved 25 $M_\odot$ star, with an infalling speed ≤ 1000 km s^{-1}. Image credit: Paxton et al. (2011).

is determined by the `net` or `jina` module.

2.5.3 Convergence to Solution

In MESA, a Newton-Raphson solver is used to integrate the equations from the previous section, in order to solve for the structure and composition of the stellar model. These equations are rewritten in terms of the following expression:

$$\begin{aligned} 0 = \boldsymbol{F}(\boldsymbol{y}) &= \boldsymbol{F}(\boldsymbol{y_i} + \delta \boldsymbol{y_i}) \\ &= \boldsymbol{F}(\boldsymbol{y_i}) + \left(\frac{d\boldsymbol{F}}{d\boldsymbol{y}}\right)_i \delta \boldsymbol{y_i} + O(\delta \boldsymbol{y_i}^2), \end{aligned} \tag{2.64}$$

where y_i is the first iteration (or the trial solution using the previous model), $\boldsymbol{F}(\boldsymbol{y_i})$ is the residual, and $(d\boldsymbol{F}/d\boldsymbol{y})_i$ is the Jacobian matrix, which is calculated analytically. This equation produces δy_i, which is a correction that is made to the trial solution. At each time step, the trial solution is iterated until it converges to a final solution (typically in a few iterations), which is accepted when the corrections and residuals are small enough (not quite zero, due to nonlinear behaviour). Upon failing convergence, a reduced time step will be tried; this is repeated upon retry failures until termination, due to either model convergence or if the time step hits a user inputted minimum.

2.5.4 Time Step Selection

The time steps selected should be large enough to evolve a model efficiently, but be small enough to capture important changes in structure of composition, and converge without an unnecessary quantity of iterations. `MESA star` first estimates a new time step using a scheme based on "digital control theory" (Soderlind and Wang 2006), before attempting to reduce this time step by checking whether a control variable representing the unweighted average of relative changes in the logarithmic density, temperature, and radius across all the cells, is less than a user inputted target value. To improve numerical stability, the following time step for the next step $k+1$, δt_{k+1}, is a function of the time steps at the

previous step $k-1$, δt_{k-1}, and the current step k, δt_k:

$$\delta t_{k+1} = \delta t_k f \left(\frac{f(v_\mathrm{t}/v_{\mathrm{c},i}) f(v_\mathrm{t}/v_{\mathrm{c},i-1})}{f(dt_i/dt_{i-1})} \right)^{1/4}, \tag{2.65}$$

where v_c is the control variable, v_t is the target value, and $f(x) = 1 + 2\arctan[0.5(x-1)]$.

2.6 Approximations to the MHD Equations

In Chapter 4, we use numerical simulations of convection to investigate the interior of fully convective stars further. In this section, we look at different approximations that are used to reduce the full MHD equations into a more tractable form. Section 2.6.1 looks at the anelastic approximation, and Section 2.6.2 discusses the large-eddy formalism.

2.6.1 Anelastic Approximation

When dealing with stellar convection zones, one must consider the high density stratification of such regions. However, the effects of compressibility in such convective simulations can be computationally challenging. In the Sun, for example, the density contrast between the base of the convection zone and the atmosphere ($r = 0.99\,R_\odot$) is $\sim 10^5$ (Nordlund et al. 2009); M-dwarfs have even larger density stratifications. Variations in density across the region may influence dynamo processes (Ossendrijver 2003) and break symmetry between upflows and downflows of convective fluid (Brummell et al. 1996). However, the effects of compressibility introduces sound waves, which are much faster than convective motions in the stellar interior. Thus, in a fully compressible code, the inclusion of these sound waves is computationally expensive and inefficient, as smaller time steps would be required to resolve the motion of the convective fluid. Assuming that these acoustic perturbations have little direct role in the dynamics of the convective fluid, one can use the anelastic approximation (Gough 1969a; Gilman and Glatzmaier 1981) to filter out sound waves, and avoid these time step limitations.

Filtering requires setting $\partial\rho/\partial t = 0$ in the mass continuity equation (Equation (2.1)),

which is equivalent to requiring the vector momentum to be solenoidal (i.e., $\boldsymbol{\nabla}\cdot(\rho\boldsymbol{v})=0$). This is valid when convective velocities are subsonic, i.e., when the radial entropy gradient driving convection is only slightly superadiabatic. If this is the case, changes in thermodynamic variables due to convection are treated as small perturbations to the spherically-symmetric mean. Hence, thermodynamic variables, namely pressure p, density ρ, temperature T, and specific entropy s, can be separated into two components: their mean values $\bar{p}$, $\bar{\rho}$, $\bar{T}$, and $\bar{s}$, respectively, and their respective perturbations p', ρ', T', and s', respectively, i.e.,

$$p(r,\theta,\phi,t)=\bar{p}(r,t)+p'(r,\theta,\phi,t) \tag{2.66}$$

$$\rho(r,\theta,\phi,t)=\bar{\rho}(r,t)+\rho'(r,\theta,\phi,t) \tag{2.67}$$

$$T(r,\theta,\phi,t)=\bar{T}(r,t)+T'(r,\theta,\phi,t) \tag{2.68}$$

$$s(r,\theta,\phi,t)=\bar{s}(r,t)+s'(r,\theta,\phi,t). \tag{2.69}$$

These can be linearised with respect to an evolving spherically symmetric mean state; equations remain nonlinear in velocity and magnetic field.

The simulations in Chapter 4 use anelastic MHD equations under the Lantz-Braginsky-Roberts (LBR) approximation (Lantz 1992; Braginsky and Roberts 1995), which is valid when the reference state is nearly adiabatic and flow is subsonic (Ogura and Phillips 1962; Gough 1969a; Lantz and Fan 1999). Under this approximation, equations for the conservation of mass, momentum, and energy, along with the induction equation and the requirement of a divergence free magnetic field, in a rotating spherical shell, are as follows:

$$\boldsymbol{\nabla}\cdot(\bar{\rho}\boldsymbol{v})=0 \tag{2.70}$$

$$\bar{\rho}\left(\frac{\partial\boldsymbol{v}}{\partial t}+(\boldsymbol{v}\cdot\boldsymbol{\nabla})\boldsymbol{v}+2\boldsymbol{\Omega}\times\boldsymbol{v}\right)=-\boldsymbol{\nabla}p'+\frac{s}{c_p}\bar{\rho}\boldsymbol{g}-\boldsymbol{\nabla}\cdot\boldsymbol{\mathcal{D}}+\frac{1}{4\pi}(\boldsymbol{\nabla}\times\boldsymbol{B})\times\boldsymbol{B} \tag{2.71}$$

$$\bar{\rho}\bar{T}\left(\frac{\partial s}{\partial t}+(\boldsymbol{v}\cdot\boldsymbol{\nabla})s\right)=\boldsymbol{\nabla}\cdot(\kappa\bar{\rho}\bar{T}\boldsymbol{\nabla}s)+Q+\Phi+\frac{\eta}{4\pi}[\boldsymbol{\nabla}\times\boldsymbol{B}]^2 \tag{2.72}$$

$$\frac{\partial\boldsymbol{B}}{\partial t}=\boldsymbol{\nabla}\times(\boldsymbol{v}\times\boldsymbol{B})-\boldsymbol{\nabla}\times(\eta\boldsymbol{\nabla}\times\boldsymbol{B}) \tag{2.73}$$

$$\boldsymbol{\nabla} \cdot \boldsymbol{B} = 0, \tag{2.74}$$

where $\boldsymbol{v}$ is the vector velocity, $\boldsymbol{\Omega}$ is the vector angular velocity, $\boldsymbol{B}$ is the vector magnetic field, c_p is the specific heat capacity (at constant pressure), κ is the effective thermal diffusivity, Q is the heating profile, and η is the effective magnetic diffusivity. $\boldsymbol{\mathcal{D}}$ is the vector viscous stress tensor, defined by

$$\mathcal{D}_{ij} = -2\bar{\rho}\nu \left(e_{ij} - \frac{1}{3}(\boldsymbol{\nabla} \cdot \boldsymbol{v}) \right), \tag{2.75}$$

and

$$\Phi = 2\bar{\rho}\nu \left(e_{ij}e_{ij} - \frac{1}{3}(\boldsymbol{\nabla} \cdot \boldsymbol{v})^2 \right) \tag{2.76}$$

is the viscous heating term, where e_{ij} is the strain rate tensor and ν is the effective kinematic viscosity.

To close Equations (2.70)–(2.73), the perturbations in the aforementioned thermodynamic variables must satisfy the following linearised relations:

$$\frac{\rho'}{\bar{\rho}} = \frac{p'}{\bar{p}} - \frac{T'}{\bar{T}} = \frac{1}{\gamma}\frac{p'}{\bar{p}} - \frac{s'}{c_p}, \tag{2.77}$$

assuming the ideal gas law, i.e.,

$$\bar{p} = \mathcal{R}\bar{\rho}\bar{T}. \tag{2.78}$$

To satisfy these conditions, the mass flux $\bar{\rho}\boldsymbol{v}$ and magnetic field $\boldsymbol{B}$ are decomposed into toroidal and poloidal components:

$$\bar{\rho}\boldsymbol{v} = \boldsymbol{\nabla} \times \boldsymbol{\nabla} \times (W\hat{\boldsymbol{r}}) + \boldsymbol{\nabla} \times (Z\hat{\boldsymbol{r}}) \tag{2.79}$$

$$\boldsymbol{B} = \boldsymbol{\nabla} \times \boldsymbol{\nabla} \times (C\hat{\boldsymbol{r}}) + \boldsymbol{\nabla} \times (A\hat{\boldsymbol{r}}), \tag{2.80}$$

where W and Z are poloidal and toroidal streamfunctions, respectively, and C and A

are magnetic potentials. This ensures that these both remain divergence free, satisfying Equations (2.70) and (2.74).

2.6.2 Large-eddy Formalism

The spatial scales of stellar convection and magnetic fields span across a large order of magnitudes, and are impossible to simulate numerically. Codes are typically chosen to resolve only the largest scales of convective flows and magnetic fields, which are likely candidates for generating mean properties of the convection, such as differential rotation and zonal flows. Our simulations, which fall under the large-eddy formalism, use sub-grid-scale (SGS) descriptions of the unresolved small turbulent motions. These SGS motions are implemented as enhancements to the thermal and magnetic diffusivities (κ and η, respectively), and the kinematic viscosity (ν), thus becoming effective eddy viscosities/diffusivities. For example, the 3D global simulations of convection in Chapter 4 have $\nu \sim 10^{11}$ cm^2 s^{-1} and $\kappa \sim 10^{12}$ cm^2 s^{-1}, whereas typical values in the upper solar convection zone are $\nu \sim 1$ cm^2 s^{-1} and $\kappa \sim 10^5$ cm^2 s^{-1} (Miesch 2005). Regardless of these large differences between physical and eddy values, dynamical behaviour in simulations may not differ as much as expected when compared to real stars; as we will show later (Chapter 4), some aspects of the flow become nearly independent of ν and κ in appropriate regimes.

This approach is chosen for simplicity, where larger resolved motions are assumed to have a negligible impact on small scale motions. In recent studies (e.g., Featherstone and Miesch 2015; O'Mara et al. 2016), viscosities and diffusivities are held constant, thus any unresolved motion effects are uniform across the simulation. However, past studies have used depth-dependent eddy transport coefficients that increase near the surface, motivated by the view that SGS eddies dissipate more energy due to small density scale heights near the surface, favouring small-scale motion driving that cannot be resolved (e.g., Browning 2008; Browning et al. 2016).

2.7 Methods of Numerical Approximation for Fluid Flows

In general, fluid simulations use numerical approximations in order to convert continuous equations used to describe the dynamics of numerical simulations into solvable algebraic expressions via a discretisation method. A good approximation is one that represents the underlying equations consistently and converges with increasing resolution. Sections 2.7.1 and 2.7.2 describe the finite-difference and spectral methods, respectively.

2.7.1 Finite-difference Method

The finite-difference method is used to replace continuous partial differential equations with analytical formulae that relate values of a given variable at neighbouring locations to derivatives for the same variable at each grid point, which can be solved using linear algebra. We illustrate this for the most simple case: a central difference first-order scheme for a uniform grid. For a function $f(z)$, on a uniform discrete set of grid points with spacings $\Delta z = 1/(N_z - 1)$, where N_z is the total number of grid points, one can use a Taylor expansion to express a neighbouring point $f_{k\pm1}$ (either side) in terms of the first and second derivative of a given point f_k (neglecting terms $> O(\Delta z^2)$):

$$f_{k\pm1} \simeq f_k \pm \left(\frac{\partial f}{dz}\right)_k \Delta z + \frac{1}{2}\left(\frac{\partial^2 f}{dz^2}\right)_k \Delta z^2, \tag{2.81}$$

which allows us to determine both the first and second derivative of f_k:

$$\left(\frac{\partial f}{dz}\right)_k = \frac{f_{k+1} - f_{k-1}}{2\Delta z}, \tag{2.82}$$

and

$$\left(\frac{\partial^2 f}{dz^2}\right)_k = \frac{f_{k+1} - 2f_k + f_{k-1}}{(\Delta z)^2}, \tag{2.83}$$

respectively. This particular example is straightforward to implement, and only requires the two nearest neighbours to approximate the first and second derivatives. There are forward and backward difference forms, which only consider terms either side of the given point.

This method works for both linear and nonlinear partial differential equations, and can be used with simulations of large spatial scale ranges using nonuniform grids. However, this method is restricted by slow convergence as resolution is increased; the type of convergence depends on the order of the scheme, but in general the convergence scales with resolution to some power. It can also struggle in spherical coordinate systems, where coordinate singularities on uniform grids, i.e., the poles, can limit the time steps due to the enhanced resolution there. This is in accordance with the Courant–Friedrichs–Lewy (CFL) condition, which states that the time step taken must be less than the time it takes for a fluid parcel to flow through one grid point to another (Courant et al. 1928).

2.7.2 The Spectral Method

The spectral method is another discretisation method, where quantities are expressed in terms of orthogonal basis functions. Unlike the finite-difference method, the spectral method does not depend just on neighbouring points, but on the entire domain. As a result, the convergence of this method scales exponentially with resolution. Spectral methods have been used in examples of turbulent flow (e.g., Arakawa 1966; Gottlieb and Orszag 1977; Canuto 1988; Zang et al. 1989; Ferziger and Peric 2003), improving the capturing of dynamical behaviour in such simulations.

For spherical geometry, the expansion is typically made in terms of spherical harmonics $Y_{lm}(\theta, \phi)$, i.e., the eigenfunctions of the horizontal Laplacian operator. A time-dependent variable f with a radial component r, and spherical components θ and ϕ, can be expanded in terms of these spherical harmonics:

$$f(r, \theta, \phi, t) = \sum_{m=-m_{\max}}^{m_{\max}} \sum_{l=|m|}^{l_{\max}(m)} f_l^m(r, t) Y_{lm}(\theta, \phi), \tag{2.84}$$

where

$$Y_{lm}(\theta,\phi) = \sqrt{\frac{2l+1}{4\pi}\frac{(l-m)!}{(l+m)!}}P_l^m(\cos\theta)e^{im\phi} \tag{2.85}$$

represents a spherical harmonic function of degree l and order m, with $P_l^m(\cos\theta)$ representing the associated Legendre polynomials of order m. Using triangular truncation, Equation (2.84) can be reduced by taking $l_{\max}(m) = l_{\max} = m_{\max}$; this gives properties that are rotation invariant, and has equal resolution throughout the sphere (Boyd 1989). Triangular truncations also allow for the elimination of aliasing errors arising from quadratically nonlinear terms, provided that the number of latitudinal and longitudinal points on the grid satisfy

$$N_\phi \geq 3l_{\max} + 1 \tag{2.86}$$

and

$$N_\theta \geq \frac{3l_{\max}+1}{2}, \tag{2.87}$$

respectively.

In the spectral method, variables must be transformed between physical and spectral space. Considering the conversion to occur over the collocation points (θ_i, ϕ_j), the spherical harmonic transform is the following:

$$f_l^m(r,t) = \sum_{i=1}^{N_\theta}\sum_{j=1}^{N_\phi} w_i w_j Y_{lm}(\theta,\phi) f(r,\theta,\phi,t), \tag{2.88}$$

with the weightings

$$w_i = \frac{2}{\left(\sin^2(\theta_i)P'_{N_\theta}(\cos(\theta_i))\right)^2}, \tag{2.89}$$

and

$$w_j = N_\phi^{-1}, \tag{2.90}$$

where P'_{N_θ} are the derivatives (with respect to $\cos(\theta)$) of $P_l(\cos(\theta))$, the associated Legendre polynomial of the first kind. The physical grid points are given by $\phi_j = 2\pi j/N_\phi$ in ϕ, i.e., Gaussian abscissae, and by zeros of the Legendre polynomials of degree N_θ in θ. The radial component can be expanded using the Chebyshev expansion, using Chebyshev polynomials

$$T_n(x) = \cos(n \arccos(x)), \tag{2.91}$$

which is evaluated at each Chebyshev collocation point

$$x_k = \cos\left(\frac{(k-1)\pi}{N_r - 1}\right), \tag{2.92}$$

where N_r is the number of grid points associated with the Chebyshev domain. We then transform from physical to spectral space using the Chebyshev transform, which gives the radial Chebyshev expansion as

$$f_l^m(r_k, t) = \frac{2}{N_r - 1} \sum_{n=1}^{N_r} N_r \epsilon_k f_{ln}^m(t) T_{n-1}(x_k), \tag{2.93}$$

where f_{ln}^m, i.e., the spectral coefficients, are given by

$$f_{ln}^m = \sum_{k=1}^{N_r} N_r w_k T_{n-1}(x_k) f_l^m(x_k, t), \tag{2.94}$$

with the weighting

$$w_k = \frac{\epsilon_k \pi}{N_r - 1}, \tag{2.95}$$

where $\epsilon_k = 1$ for $k = 2 \to N_r - 1$, and $\epsilon_k = 1/2$ for $k = 1$ and N_r.

The equation of temporal evolution of the system can be expressed in terms of

$f_l^m(r_k, t)$, split into its linear and nonlinear components:

$$\frac{\partial f_l^m(r_k, t)}{\partial t} = L_{lmk}(t) + N_{lmk}(t), \tag{2.96}$$

where $L_{lmk}(t)$ and $N_{lmk}(t)$ represent the linear and nonlinear terms, respectively (full forms of these terms can be found in, e.g., Brun et al. 2004); the purpose of this is to enable us to solve each term in a numerically optimal manner. Nonlinear terms are computationally expensive to evaluate in spectral space, due to becoming convolution sums, where the time it takes for a code to perform n nonlinear calculations scales as n^2. Thus, it is preferable to reduce the computational cost by computing nonlinear terms in physical space, using the Fast Fourier Transform (FFT) to transform from spectral into physical space, where time taken for the FFT transformation into linear space scales as $n \log(n)$, and the time taken for the calculations themselves scales as n. This is called the *pseudo-spectral method*, where linear terms are solved in spectral space, and nonlinear terms in physical space, which can reduce the computational cost by up to three orders of magnitude (Falgarone and Passot 2003).

2.8 Simple Modelling of 2D Rayleigh-Bénard Convection

To illustrate some of the ideas and what occurs in a time-dependent convective field, we built a simple 2D convection code in the Fortran programming language, following theory and discussion in Glatzmaier (2013). The code models Rayleigh-Bénard convection, where buoyant fluid is heated by the bottom boundary and cooled by the top boundary. This is under the Boussinesq approximation, which assumes that motion-induced density fluctuations are neglected, except when coupled to the gravitational acceleration in the buoyancy force. A constant background density is assumed, hence it deals with incompressible flow. The fluid domain is defined as a 2D rectangular region, with top and bottom boundaries maintained at constant temperatures, differing by ΔT, and periodic side boundaries. The code solves for temperature T, vorticity $\boldsymbol{\omega} \equiv \boldsymbol{\nabla} \times \boldsymbol{v}$, and the streamfunction ϕ. It is convenient to update $\boldsymbol{\omega}$ and then solve for fluid velocity, $\boldsymbol{v}$, at each time step by using ϕ, recognising that $\boldsymbol{v} \equiv \boldsymbol{\nabla} \times \phi\hat{\boldsymbol{y}}$, as $v_y = 0$ and $\partial/\partial y = 0$ in this 2D problem.

The following Boussinesq equations are solved for, which are nondimensionalised by the depth of the box (D), the thermal diffusion time (D^2/κ), where κ is the thermal diffusivity, and temperature drop across the depth (ΔT) (with gravitational acceleration $\boldsymbol{g} = -g_0\hat{\boldsymbol{z}}$ pointing downward):

$$\boldsymbol{\nabla} \cdot \boldsymbol{v} = 0 \tag{2.97}$$

$$\frac{\partial \boldsymbol{v}}{\partial t} = -(\boldsymbol{v} \cdot \boldsymbol{\nabla})\boldsymbol{v} - \boldsymbol{\nabla} p + \mathrm{RaPr}T\hat{\boldsymbol{z}} + \mathrm{Pr}\nabla^2\boldsymbol{v} \tag{2.98}$$

$$\frac{\partial T}{\partial t} = -(\boldsymbol{v} \cdot \boldsymbol{\nabla})T + \kappa\nabla^2 T, \tag{2.99}$$

where

$$\mathrm{Ra} = \frac{g_0\alpha\Delta T D^3}{\nu\kappa} \tag{2.100}$$

is the Rayleigh number, i.e., the measure of convective driving, where α is the thermal expansion coefficient, and ν is the kinematic viscosity. The Prandtl number, i.e., the ratio of viscous to thermal diffusivity, is defined as

$$\mathrm{Pr} = \frac{\nu}{\kappa}. \tag{2.101}$$

Instead of solving for time-dependent values on a finite set of grid points in x, horizontal spectral decomposition based on Fourier expansions in x can expand T, ω and ϕ as a finite series of sines or cosines and solve for time-dependent and z-dependent coefficients of these. This allows the following set of equations to be expressed for each individual mode n:

$$\frac{\partial T_n}{\partial t} = -[(\boldsymbol{v} \cdot \boldsymbol{\nabla})T]_n + \left(\frac{\partial^2 T_n}{\partial z^2} - \left(\frac{n\pi}{a}\right)^2 T_n\right) \tag{2.102}$$

$$\frac{\partial \omega_n}{\partial t} = -[(\boldsymbol{v} \cdot \boldsymbol{\nabla})\omega]_n + \mathrm{RaPr}\left(\frac{n\pi}{a}\right)T_n + \mathrm{Pr}\left(\frac{\partial^2 \omega_n}{\partial z^2} - \left(\frac{n\pi}{a}\right)^2 \omega_n\right) \tag{2.103}$$

$$\omega_n = -\left(\frac{\partial^2 \phi_n}{\partial z^2} - \left(\frac{n\pi}{a}\right)^2 \phi_n\right), \tag{2.104}$$

where a is the aspect ratio of the boxed region. For the $n = 0$ mode, the background temperature follows a linear gradient in z: $T_0(z) = 1 - z$, and for $n > 0$ modes, the initial temperature perturbation is set to be sinusoidal: $T_n = sin(\pi z)$ at $t = 0$, with the initial fluid velocity set to zero for each mode along z: $\omega_n = \psi_n = 0$ at $t = 0$. Boundary conditions for $n > 0$ at the top ($z = 1$) and bottom ($z = 0$) boundaries are set to zero: $T_n = \omega_n = \psi_n = 0$.

The linear parts of the time derivatives in Equations (2.102) and (2.103) are calculated, where second order derivatives for a function f with respect to z and t on a discrete set of grid points, $z_k = (k-1)\Delta z$, are computed using the vertical finite-difference method (see Section 2.7.1). The spectral-transform method is used to calculate the nonlinear terms of the temperature and vorticity time derivatives. The aim is to separately transform the two variables of the nonlinear term, e.g., v and T in Equation (2.102), from spectral space into real space using the Fast Fourier transform (FFT), multiply them together, then transform the product back into spectral space.

The semi-implicit scheme is used to compute T and ω for the next time step. Nonlinear terms are treated explicitly using the second-order Adams-Bashforth time integration scheme, which uses current (t) and previous ($t - \Delta t$) time steps to update a given variable y at a new time step ($t + \Delta t$):

$$y_{t+\Delta t} = y_t + \frac{\Delta t}{2}[3y'(t) - y'(t - \Delta t)]. \tag{2.105}$$

Linear terms are treated implicitly using the Crank-Nicolson time integration scheme:

$$y_{t+\Delta t} - \frac{1}{2}y'(t + \Delta t)\Delta t = y_t + \frac{1}{2}y'(t)\Delta t. \tag{2.106}$$

Using these, Equation (2.102), for example, in the semi-implicit scheme is

$$\left[1-\frac{1}{2}\Delta t\left(\frac{\partial^2}{\partial z^2}-\left(\frac{n\pi}{a}\right)^2\right)\right]T_n(z,t+\Delta t)=\left[1+\frac{1}{2}\Delta t\left(\frac{\partial^2}{\partial z^2}-\left(\frac{n\pi}{a}\right)^2\right)\right]T_n(z,t)$$
$$+\frac{\Delta t}{2}\left[3(-(\boldsymbol{v}\cdot\boldsymbol{\nabla})T)_{n,z,t}-(-(\boldsymbol{v}\cdot\boldsymbol{\nabla})T)_{n,z,t-\Delta t}\right] \tag{2.107}$$

(Glatzmaier 2013, p. 94). The implicit part of Equation (2.107) needs to be constructed as a matrix operator, as the vertical Laplacian couples all z-levels. ψ is computed for the next time step by constructing Equation (2.104) as a matrix operator.

Figure 2.4 illustrates the temperature profiles of an example multi-cell Rayleigh-Bénard convective simulation at different time steps, evolved from a linear temperature gradient with an initialised $n = 1$ mode temperature perturbation. The simulation eventually reaches a steady state in this case, because nonlinear amplitudes initially grow exponentially, before becoming large enough to inhibit this growth. Whilst useful for developing knowledge of convective modelling, this simple 2D convection code is not suitable for our main investigation, due to both physical (using the Boussinesq approximation) and computational (single threaded) limitations. Any 2D/3D convective simulations to investigate stellar interiors require more complex, parallelised codes. We describe two such codes used for the investigations detailed in Chapter 4 below.

2.9 *Rayleigh*: Spherical-harmonic-based Code

Rayleigh[2] is a 3D convection code that evolves incompressible and anelastic MHD equations in a rotating spherical geometry using the pseudo-spectral approach, in order to study dynamo behaviour (Featherstone and Hindman 2016). It uses spherical harmonics and Chebyshev polynomials for the horizontal and radial directions, respectively. As it uses the pseudo-spectral approach (see Section 2.7.2), linear terms are calculated in spectral space, and nonlinear terms are calculated in physical space. Linear term time stepping uses the semi-implicit second-order Crank-Nicolson method, whereas nonlinear terms use the second-order Adams-Bashforth method. *Rayleigh* parallelises efficiently on

2. https://github.com/geodynamics/Rayleigh, accessed June 2018

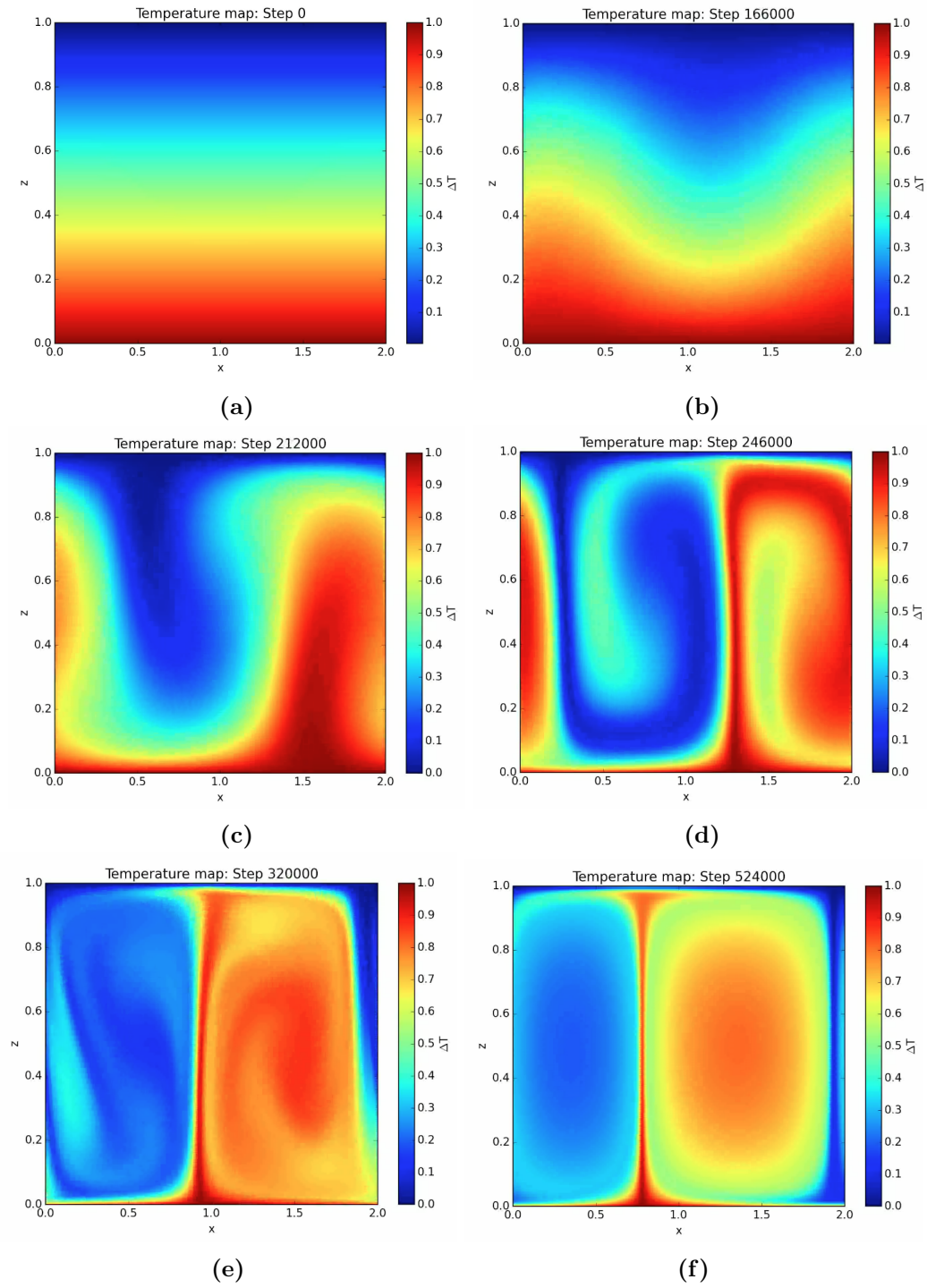

Figure 2.4: 2D temperature profiles of a multi-cell Rayleigh-Bénard convective simulation ran for over 10^6 time steps, plotted on a real space (x, z) grid. Parameters: Ra $= 10^6$, Pr $= 1$, $a = 2$, $dt = 10^{-7}$. (a) The simulation begins as a linear temperature gradient with an initialised $n = 1$ mode temperature perturbation; (b)-(c) Convective flows begin to rise from the bottom to the top boundary; (d)-(e) Convective flows begin to overturn into neighbouring downward flows before reaching the top boundary, due to mass conservation; (f) The simulation converges to a steady-state solution of one convective circulation cell.

up to $O(10^5)$ cores (Featherstone and Hindman 2016; Matsui et al. 2016). To do this, work is distributed by assigning the calculation of a set of m-modes to different groups of processes, or ranks. Each value of m requires different periods of computational time to be calculated, as they will have different numbers of l-modes due to triangular truncation, i.e., $0 \leq m \leq l$, $0 \leq l \leq l_{\max}$. Initially, *Rayleigh* will limit the number of ranks to $N_{\max} = (l_{\max} + 1)/2$, to ensure that each rank is assigned m-modes with approximately an equal number of l-modes; these are evenly distributed to individual processes for each rank. We describe the process of performing simulations of convection in *Rayleigh* (such as those used in Chapter 4), closely following the *Rayleigh* user guide[3]. In Section 2.9.1, we describe the resolution and domain bounds, and in Section 2.9.2, we discuss the time stepping/run length controls. In Section 2.9.3, we discuss how *Rayleigh* solves the MHD equations and specify the physical controls used, and in Section 2.9.4, the boundary conditions are mentioned. The initialisation of a model is discussed in Section 2.9.5. A more detailed description of the numerical set up behind the *Rayleigh* simulations used in Chapter 4 can be found in Section 4.3.1, including the background state, boundary conditions, and input parameters used.

2.9.1 Resolution and Domain Bounds

First, the resolution and domain bounds are defined by the user. The number of radial and θ grid points, N_r and N_θ, respectively, are inputted, and the number of ϕ grid points $N_\phi = 2N_\theta$. Alternatively, one can specify the maximal spherical harmonic degree $\ell_{\max} \equiv N_\ell - 1$, rather than N_θ. The radial domain is then defined by either inputting an inner and an outer radial boundary, r_i and r_o, respectively, or specifying a shell depth $r_o - r_i$ and aspect ratio r_i/r_o. These domain parameters are interpreted differently for dimensional and nondimensional simulations.

3. https://geodynamics.org/cig/software/rayleigh/user_guide_0.9.0.pdf, accessed June 2018

2.9.2 Time Stepping and Run Length

The temporal input controls are then specified: these include the maximum time a simulation is allowed to run, the maximum number of time steps allowed, and the time step size. The simulation will complete when either the maximum time or the maximum time step number are met, depending on which constraint occurs first. The size of time steps is determined by the Courant-Friedrichs-Lewy condition (CFL), where a time step must be smaller than the time taken for a parcel of fluid to flow between two grid points. To control this, there are two safety factor inputs that can be defined: the first is applied to the maximum time step determined by the CFL condition ($\mathrm{cfl}_{\mathrm{max}}$), and the second is used to determine whether the time step should be increased ($\mathrm{cfl}_{\mathrm{min}}$). A minimum and maximum time step size can also be defined, t_{min} and t_{max}, respectively; if the CFL condition is less than the minimum value, the simulation will end. When calculating the time step size, *Rayleigh* employs the following logic:

- IF $\{\Delta t \geq \mathrm{cfl}_{\mathrm{max}} \times t_{\mathrm{CFL}}\}$ THEN $\{\Delta t = \mathrm{cfl}_{\mathrm{max}} \times t_{\mathrm{CFL}}\}$,
- IF $\{\Delta t \leq \mathrm{cfl}_{\mathrm{min}} \times t_{\mathrm{CFL}}\}$ THEN $\{\Delta t = \mathrm{cfl}_{\mathrm{max}} \times t_{\mathrm{CFL}}\}$,
- IF $\{\mathrm{cfl}_{\mathrm{max}} \geq t_{\mathrm{min}}\}$ THEN $\{\Delta t = t_{\mathrm{max}}\}$,
- IF $\{\Delta t \leq t_{\mathrm{min}}\}$ THEN {Exit *Rayleigh*},

where Δt is the current time step size, and t_{CFL} is the maximum time step as described by the CFL limit.

2.9.3 Physical Controls

The MHD equations that *Rayleigh* solves, and the diagnostics, can be dimensionalised or nondimensionalised. *Rayleigh* includes the nondimensional Boussinesq, and dimensional or nondimensional anelastic formulations. For the simulations in Chapter 4, the anelastic MHD equations (as shown in Section 2.6.1) are solved for. The perturbations to the thermodynamic variables satisfy the linearised equation of state (Equation (2.77)). The kinematic viscosity ν, thermal diffusivity κ, and magnetic diffusivity η (if magnetism is

enabled) are inputted by the user: in our case, we define these variables at the upper boundary, and they are considered to be eddy viscosities/diffusivities (see Section 2.6.2). Magnetism, rotation, Lorentz forces, viscous heating, and ohmic heating are all logical variables that can be enabled or disabled. For this dimensional anelastic case, the background polytropic state is defined, identical to the benchmark described in Jones et al. (2011), and inputs include the polytropic index n (where $P \propto \rho^n$), the number of density scale heights, the mass and density interior to the defined inner radial boundary, the specific heat capacity (at constant pressure), and the angular velocity of the simulation.

2.9.4 Boundary Conditions

Boundary conditions are then set: *Rayleigh* simulations have impenetrable boundaries, which may either be no-slip or stress-free. It is possible to set magnetic boundary conditions, to match a potential field at both the inner and upper boundary. It is possible to either fix a thermal anomaly Θ value to each boundary, or specify a constant $\partial\Theta/\partial r$ at each boundary. In Chapter 4, a fixed specific entropy is defined at the upper boundary, and a fixed specific entropy gradient at the inner boundary. An internal heating function $Q(r)$ also needs to be specified (see Equations (4.28)-(4.29) in Section 4.3.1).

2.9.5 Initialising a Model

A simulation in *Rayleigh* can be started by using a random thermal initialisation (and/or a magnetic field initialisation for magnetic simulations). The thermal options include: reading velocity and thermal fields from a checkpoint file, a temperature mode initialisation that follows the case 0 benchmark in Christensen et al. (2001), an entropy mode initialisation for the steady anelastic benchmark in Jones et al. (2011), or a random temperature/entropy perturbation. Initialising a random thermal field requires all spherical harmonic modes to be independently initialised with a random amplitude, where the maximum value can be defined. This random initialisation can be expressed as

$$T(r,\theta,\phi) = \sum_{\ell}\sum_{m} c_l^m f(r) g(\ell) Y_l^m(\theta,\phi), \tag{2.108}$$

where c_l^m represents complex random amplitudes in the range defined by the user, $f(r)$ is the radial amplitude that is given by

$$f(r) = \frac{1}{2}\left[1 - \cos\left(2\pi \frac{r - r_{\min}}{r_{\max} - r_{\min}}\right)\right], \tag{2.109}$$

which goes to zero at the inner and outer boundaries, and $g(\ell)$ is a random amplitude function that concentrates power in the central band of spherical harmonic modes, given by

$$g(\ell) = \exp\left[-9\left(\frac{2\ell - \ell_{\max}}{\ell_{\max}}\right)\right]. \tag{2.110}$$

2.10 Dedalus: Pseudo-spectral Code

Dedalus[4] is an open source pseudo-spectral code used to solve partial differential equations using spectral methods, dealing with both astrophysical and geophysical fluid dynamical problems (Burns et al. 2016). It is predominantly written in Python, and includes an interface that accepts symbolic equation entry, allowing differential equations and algebraic constraints to be entered in plain text. Any linear terms are solved using sparse matrix systems, whereas nonlinear terms are solved using the pseudo-spectral method. The first $(N-1)$ dimensions are parallelised using MPI, thus Dedalus is capable of scaling to thousands of processes. In this section, we describe the process of performing simulations of convection in Dedalus, such as those used in Chapter 4, closely following the Dedalus tutorial notebooks[5]. Section 2.10.1 discusses bases and domains available in Dedalus, and Section 2.10.2 discusses fields and operators. Section 2.10.3 covers the different types of problems and their corresponding solvers. A more detailed description of the numerical set up behind the Dedalus simulations used in Chapter 4 can be found in Section 4.2.1,

4. http://dedalus-project.org, accessed June 2018
5. http://dedalus-project.readthedocs.io/en/latest/getting_started.html, accessed June 2018

including the background state, boundary conditions, and input parameters used.

2.10.1 Bases and Domains

Bases are represented as separate classes: when declaring a basis to use, a user inputs the name of the basis, the number of modes required, and specify a dealiasing scaling factor to pad the tracked modes when performing transformations into grid space. Typically, a scaling factor $\geq 3/2$ is required to properly dealias quadratic nonlinearities. These basis objects have corresponding transformation and operation methods, which are covered in Section 2.10.2. One must specify a basis for each dimension of the simulation, e.g., x, y and z for a 3D calculation, and then create a physical domain, in the form of a domain object, from these. Dedalus is capable of solving over domains that can be expressed in terms of the direct product of spectral bases; separable bases currently include the Fourier and sine/cosine series, whereas coupled bases currently include Chebyshev polynomials. It supports domains of N-dimensions, with the first $(N-1)$ dimensions being discretised by separable bases, and the last being discretised by either a separable (where derivatives do not couple modes, allowing for parallelisation) or coupled (where derivatives do couple modes, requiring a local solve for each transverse mode) basis.

2.10.2 Fields and Operators

Field objects represent scalar fields over the domain, in which field data can be assigned. In Chapter 4, a field object is used to initialise the density stratification over the domain, which is set to be $1-\beta z$, where β is the inverse temperature scale height, and z represents a given point on the vertical scale (Currie and Browning 2017). Operators are then used to perform mathematical operations on fields. Arithmetic operations between fields, or fields and scalars, can be produced simply using Python's operators for arithmetic. Other operators, such as differentiation, integration, and interpolation, are possible using factories from the `operators` module. The differentiation operator allows for higher-order and mixed derivatives involving different bases. In addition, the integration and interpolation operators allow these to be performed along multiple axes.

2.10.3 Problems and Solvers

In Dedalus, differential equations are represented in the following form:

$$\mathcal{M} \cdot \delta_t \mathcal{X} + \mathcal{L} \cdot \mathcal{X} = \mathcal{F}, \tag{2.111}$$

where $\mathcal{M}$ and $\mathcal{L}$ are linear differential operator matrices, $\mathcal{X}$ is a state-vector of fields, and $\mathcal{F}$ represents nonlinear expressions. Equations and boundary conditions can be inputted in plain text in Python, using Dedalus' symbolic parser, which are then manipulated into the matrix form of Equation (2.111). Equations are written so that left-hand terms are implicitly evaluated (linear terms only), and right-hand terms explicitly (nonlinear/linear terms that couple modes). Short aliases can be defined prior to this, to simplify equation entry. In Chapter 4, anelastic equations under the Lantz-Braginsky-Roberts (LBR) approximation are used (Lantz 1992; Braginsky and Roberts 1995), which is valid when the reference state is near-adiabatic and flow is subsonic (Ogura and Phillips 1962; Gough 1969b; Lantz and Fan 1999).

We first define input parameters that stay fixed in the simulation (see Tables 4.1 and 4.2 in Chapter 4 for our case). Then, we add any parameters, which can be either fields or scalars, that are used in the equations. Depending on the problem type, a corresponding solver is used to iterate over the solution. The Dedalus simulations of Chapter 4 are initial value problems (IVP), i.e., where an ordinary differential equation (ODE) with an initial condition evolves with time, which can be solved by spectrally discretising the spatial domain, and evolving coefficients via coupled ODEs. Implicit time stepping of linear terms and explicit time stepping of nonlinear terms is performed using a range of ODE integrators, including the implicit-explicit Runge-Kutta regime, which is used in our case.

An initial condition is then set, by directly modifying state variable data, before the simulation is run. In Chapter 4, a small perturbation is made to the specific entropy. Dedalus then enters the main-loop of the simulation: here, the evolution loop can be stopped if any specified stopping criteria is met, i.e., if the solver hits a user-specified maximum simulation time (seconds), "wall" time (seconds since the solver was initialised),

or a maximum number of iterations; all three can be set, and the simulation will end with whichever occurs first.

Chapter 3

The Radius and Entropy of a Magnetised, Rotating, Fully Convective Star: Analysis with Depth-dependent Mixing Length Theories

3.1 Introduction

All main-sequence stars are convective somewhere in their interior: low-density, high-temperature fluid parcels rise or fall through the stratified medium, transporting heat by their motion. In high-mass stars this convective transport occurs primarily in the innermost regions, whereas low-mass stars like the Sun have convection occurring in an envelope; stars of sufficiently low mass ($\lesssim 0.35\,M_\odot$) are convective throughout their interiors (e.g., Chabrier and Baraffe 1997). Pre-main-sequence stars on the Hayashi track are likewise fully convective (e.g., Hayashi 1961). Variations in the opacity, energy generation rate, or adiabatic index determine where and when this convection occurs: broadly,

it happens whenever the temperature gradient required to carry a star's flux by radiative processes alone is too steep (e.g., Böhm-Vitense 1992). This may be encapsulated via the Schwarzschild criterion, which states that convection occurs whenever the dimensionless temperature gradient $\nabla = d\log T/d\log p$ is greater than the adiabatic gradient $\nabla_{\rm ad} = (d\log T/d\log p)_{\rm ad}$.

In the interior of a star, modest convective velocities and temperature gradients very close to the adiabatic value are usually sufficient to carry a star's flux outward (e.g., Kippenhahn et al. 2012), owing mainly to the high density and heat capacity of these regions. For fully convective stars, this implies that most of the interior lies at nearly constant specific entropy. However, larger entropy gradients are established near the surface (as discussed in Section 3.2). The interaction between convection and radiative transfer in the region of the surface layer thus creates a specific entropy jump Δs between the nearly constant specific entropy in the deep interior, conventionally labelled $s_{\rm ad}$, and the specific entropy at the stellar photosphere $s_{\rm ph}$ (e.g., Trampedach et al. 2014).

The gross structure of a star is linked to its entropy (see, e.g., discussions in Stahler 1988; Hansen et al. 2004, pp. 370-373). In particular, for isentropic stars, knowledge of $s_{\rm ad}$, i.e., knowledge of which adiabat the star is on, is enough to specify the entire structure. As emphasised by Gough and Weiss (1976), a complete theory of convection would specify the adiabat but, in practice, this is typically calibrated by comparison to observations. In standard 1D stellar models employing the mixing length theory (MLT) of convection, fluid parcels are assumed to travel some characteristic mixing length $\ell_{\rm MLT} = \alpha_{\rm MLT} H_p$ before transferring their heat to their surroundings, where $\alpha_{\rm MLT}$ is conventionally a depth-independent dimensionless parameter and H_p is the pressure scale height (Böhm-Vitense 1958). In typical models of fully convective stars, $\alpha_{\rm MLT}$ effectively specifies the entropy contrast Δs, and so fixes the adiabat and the overall stellar structure.

Observations have suggested that some low-mass stars have radii that are $5-15\%$ larger than standard 1D models would predict (e.g., Torres and Ribas 2002; Ribas 2006; Morales et al. 2008; Torres et al. 2010; Terrien et al. 2012). These "inflated" radii could in turn lead to erroneous age estimates of stars on the pre-main sequence (see, e.g., Feiden 2016). Several authors have argued that the inhibition of convection by some mechanism

could explain these modifications to the structure, with rotation and/or magnetic fields both invoked as possible culprits (e.g., Cox et al. 1981; Chabrier et al. 2007).

Rotation is well known to influence convection. For example, in classic linear stability analysis, the onset of convection is impeded by the presence of rotation: the critical Rayleigh number for convective instability (measuring, roughly, how great buoyancy driving must be relative to viscous and thermal dissipation) increases with rotation rate Ω (Chandrasekhar 1961), scaling as $\Omega^{4/3}$ in appropriate circumstances. The horizontal scale of the most unstable modes likewise diminishes with more rapid rotation. The nonlinear effects of rotation on the convection are less clear. Broadly, the reduction of horizontal lengthscales and convective speeds in rapidly rotating systems is expected to inhibit the heat transport somewhat, leading to higher values of the temperature (or in a stratified system, entropy) gradient (Stevenson 1979; Julien et al. 2012; Barker et al. 2014). Rotation also breaks the spherical symmetry, with motions increasingly aligned with the rotation axis at rapid rotation rates, in keeping with the Taylor–Proudman constraint (Proudman 1916; Taylor 1917). Other aspects of the nonlinear impact of rotation, such as its effect on heat transport and on the establishment of zonal flows, have also been extensively explored using theory and simulation (e.g., Bassom and Zhang 1994; Julien and Knobloch 1998; Sprague et al. 2006; Gastine et al. 2012; Gastine et al. 2016; Julien et al. 2012; Julien et al. 2016; King et al. 2012; Stellmach et al. 2014; Aurnou et al. 2015; Calkins et al. 2015; Grooms 2015; Aubert et al. 2017).

A reformulation of MLT to treat rapidly rotating cases was proposed for example by Stevenson (1979), who argued following Malkus (1954) that the nonlinear state was likely to be dominated by the modes that transport the most heat. Julien et al. (2012) also examined the transport in rapidly rotating systems, by scaling to the state of marginal stability; they argue that, in contrast to classical non-rotating convection, in which heat transport is “throttled” in narrow boundary layers, the heat transport of rapidly rotating systems is limited by the efficiency of turbulent motion in the bulk of the fluid. Recently, Barker et al. (2014) derived a version of rotating MLT equivalent to Stevenson (1979) in a different way and tested it using 3D simulations in Cartesian domains. Broadly, several methods of analysis suggest that the temperature gradient in the middle of the

rotating convective layer ($d\langle T\rangle/dz$) increases with rotation rate Ω. In particular, Barker et al. (2014) have argued specifically that $-d\langle T\rangle/dz \propto \Omega^{4/5}$ in the rapidly rotating limit. Their simulations support this scaling, though it must be noted that their models encompass only a single latitude (namely the pole); extensions to other latitudes are under way (L. Currie et al. 2018 personal communication).

Magnetic fields are likewise known to influence convection in some manner, but it is not clear how this affects the heat transport in the stellar context. Magnetic fields can inhibit convection in the stellar interior via the Lorentz force, hindering fluid flow perpendicular to the field (e.g., Stein 2012). Like rotation, magnetic fields influence the linear stability of the fluid to convective motions: in the absence of rotation, magnetism is stabilising (Chandrasekhar 1961; Gough and Tayler 1966). When rotation is present, the linear stability is more complex, and in fact the critical Rayleigh number for convection with *both* rotation and magnetism can be lower than in the presence of either rotation or magnetism alone (Chandrasekhar 1961; Stevenson 1979). Again, the nonlinear impact of the magnetism is much less clear. Stevenson (1979) also fashioned a "magnetic" version of MLT, but (to our knowledge) this has not been incorporated into 1D stellar structure models. Mullan and MacDonald (2001), drawing on the linear stability analysis of Gough and Tayler (1966), argued that the effects of magnetism in a 1D stellar model could be mimicked simply by modifying the adiabatic gradient $\nabla_{\rm ad}$ (wherever it appears in the MLT prescription) to include a perturbation term proportional to the magnetic pressure (relative to the gas pressure). Physically, this amounts to asserting that the end-state of magnetised convection is to approach a state of marginal stability, where this stability now depends on the strength of the magnetism, in much the same way that non-magnetic convection might be taken to approach an isentropic state.

Chabrier et al. (2007), noting that even fairly modest magnetic fields might strongly feed back on the flows through Lorentz forces, modelled rotational and magnetic effects simply by varying the depth-independent $\alpha_{\rm MLT}$; they also briefly considered the effects of near-surface spots, taken to be regions of cool effective temperature covering some fraction of the surface. Feiden and Chaboyer (2012), drawing on Lydon and Sofia (1995), have implemented a more complex magnetic MLT model into the Dartmouth stellar evolution

code, with properties of the resulting structure dependent on the strength and (imposed) spatial distribution of the magnetism. Broadly, these authors have argued that magnetic fields can affect the radius of a star, either by inhibiting convection or through the effects of near-surface spots (e.g., Cox et al. 1981; Mullan and MacDonald 2001; Chabrier et al. 2007; Feiden and Chaboyer 2012, 2014; MacDonald and Mullan 2012, 2013, 2014, 2017a; Feiden 2016).

In this chapter, we examine the effects of rotation and magnetic fields on the structure of fully convective stars via 1D stellar structure models, using the Modules for Experiments in Stellar Astrophysics (MESA) code (Paxton et al. 2011; Paxton et al. 2013; Paxton et al. 2015). All the reformulations of MLT noted above can modify the adiabat of the star, by changing the efficiency of convective heat transport in the stellar interior. Thus, in Section 3.2, we begin by giving an overview of the role of entropy in standard 1D stellar structure models; in particular, we recall how the stellar radius is sensitive to changes in the specific entropy, which is itself sensitive to differing levels of convective inhibition via changes in $\alpha_{\rm MLT}$. We give an explicit relationship between specific entropy, stellar radius, and $\alpha_{\rm MLT}$ for these "standard" models with a depth-independent $\alpha_{\rm MLT}$.

We then examine the "rotating" and "magnetic" MLT reformulations by Stevenson (1979) and MacDonald and Mullan (2014), respectively, in Sections 3.3 and 3.4 to determine how these mechanisms inhibit convection, and so influence the stellar radius, compared to solely changing $\alpha_{\rm MLT}$. We set aside for now the question of whether these formulations correctly capture the complex interaction between rotation, convection, and magnetism in a star; here, we simply examine the consequences of these prescriptions for the entropy and radius of the star. We also investigate the influence on stellar structure as a result of combining these "rotating" and "magnetic" MLT reformulations in Section 3.5.

In Section 3.6, we show that these reformulations to MLT may be precisely duplicated in a standard (non-magnetic, non-rotating) 1D model by the introduction of a depth-dependent $\alpha_{\rm MLT}$. We provide formulae for depth-dependent $\alpha_{\rm MLT}$ profiles that can be used to mimic the effects of rotation or magnetism on the stellar superadiabaticity, and hence on the stellar radius (assuming these are captured by the Stevenson (1979) and MacDonald and Mullan (2014) formulations, respectively), providing a simple way for

users to model these non-standard effects. Finally, we discuss our results in Section 3.7.

3.2 Entropy, Convection, and the Radii of Standard 1D Stellar Structure Models

3.2.1 Role of Specific Entropy in Standard MLT

Heat transport, entropy, and the stellar structure are tightly linked in fully convective objects. Here, we briefly review these links, outlining how changes in the convective efficiency of classical MLT modify the internal entropy structure and hence the stellar radius. The material in this section largely duplicates standard results found elsewhere (see e.g., Hansen et al. 2004, pp. 370-373), but we include it here as background for our studies in Sections 3.3-3.6.

For an ideal gas without radiation pressure, the specific entropy (i.e., the entropy per unit mass) s is

$$s \simeq s_0 + \frac{N_{\rm A} k_{\rm B}}{\mu} \log\left(\frac{T^{1/(\gamma-1)}}{\rho}\right), \tag{3.1}$$

where s_0 is a constant, $N_{\rm A}$ is Avogadro's constant, $k_{\rm B}$ is Boltzmann's constant, μ is the mean molecular weight, T is temperature, ρ is density, and γ is the adiabatic exponent.

To examine how the specific entropy changes in response to variations in the convective efficiency, we first constructed a series of standard 1D stellar structure models using MESA. Here, we simply use the default setup provided by `MESA star`: the MLT prescription is that of Cox and Giuli (1968); the atmospheric boundary conditions are MESA's "simple" option, in which the photosphere is located at optical depth $\tau = 2/3$, the surface temperature is given by the Eddington $T(\tau)$ relation, and the opacity is calculated in an iterative fashion (see Paxton et al. (2011) for details); the metallicity is fixed at $Z = 0.02$. We model stars only at a fixed mass of $0.3\,M_\odot$, evolving each model from the pre-main sequence up to an age of 4 Gyr. Models of this mass are convective throughout their interiors.

We vary the mixing length parameter $\alpha_{\rm MLT}$ to vary the convective efficiency, effectively reducing the distance travelled by convective elements (Trampedach et al. 2014). Taken together, these choices imply that our models are somewhat more idealised depictions of a $0.3\,M_\odot$ star than the most sophisticated ones in use today (e.g., Baraffe et al. 2015). For example, in reality (and in more complete models) convection extends well into the optically thin regime, mainly because the formation of H_2 decreases the adiabatic gradient, favouring convection (Chabrier and Baraffe 1997). Values of the effective temperature in models including this effect will generally differ from those reported here (which simply assume the Eddington $T(\tau)$ relation). We choose this simpler boundary condition partly because it allows us to compare more directly with analytical theory below, and because we are interested mainly in *changes* between models with differing $\alpha_{\rm MLT}$ rather than in the absolute values of $T_{\rm eff}$, R, etc.

We turn first to consideration of the superadiabatic gradient $\nabla_{\rm s} \equiv (\nabla - \nabla_{\rm ad})$, which is a dimensionless measure of the entropy gradient. In Figure 3.1, we plot $\log_{10}(\nabla_{\rm s})$ as a function of logarithmic density $\log_{10}(\rho)$ for $0.3\,M_\odot$, 10 Myr pre-main-sequence and 1 Gyr main-sequence stellar models with $\alpha_{\rm MLT} = 0.5 - 2.0$ ($\Delta 0.5$). Vertical dotted lines in this figure and onward indicate average radial positions in the region of the surface layer. A few key features are readily apparent: first, in the bulk of the convection zone, $\nabla_{\rm s}$ reaches negligible values due to highly efficient convective transport, where the temperature gradient is nearly adiabatic. Nearer the surface, $\nabla_{\rm s}$ increases, driven by the continuous decline in the density and temperature of the plasma. Convection carries nearly all the flux until radii of greater than $0.995\,R$, where R is the radius of a given model, and is highly efficient over most of that region; radiative diffusion begins to carry a non-negligible amount of flux only above $0.9995\,R$. Comparing the top and bottom panels of Figure 3.1, we see that $\nabla_{\rm s}$ is somewhat lower in the main-sequence models (bottom panel) than on the pre-main-sequence models. In both sets of models, at all depths $\nabla_{\rm s}$ depends on the convective efficiency: less efficient convection, which in these models corresponds simply to a smaller value of $\alpha_{\rm MLT}$, means that a higher $\nabla_{\rm s}$ is required to carry the same heat flux.

To quantify how changing $\alpha_{\rm MLT}$ influences the run of $\nabla_{\rm s}$, and so explain the trends visible in Figure 3.1, we consider the convective flux $F_{\rm conv}$ as defined in the classic MLT

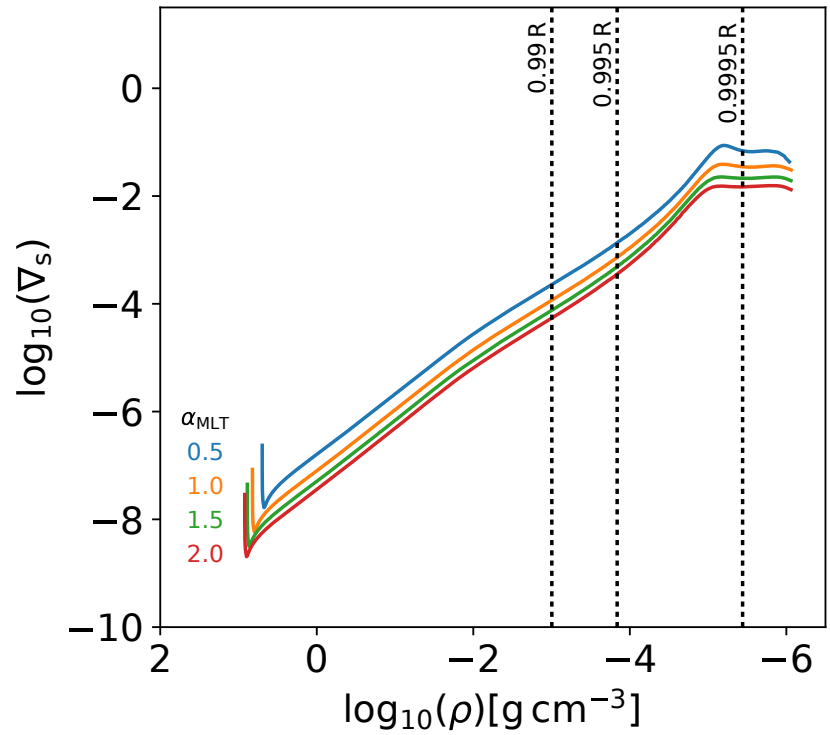

(a)

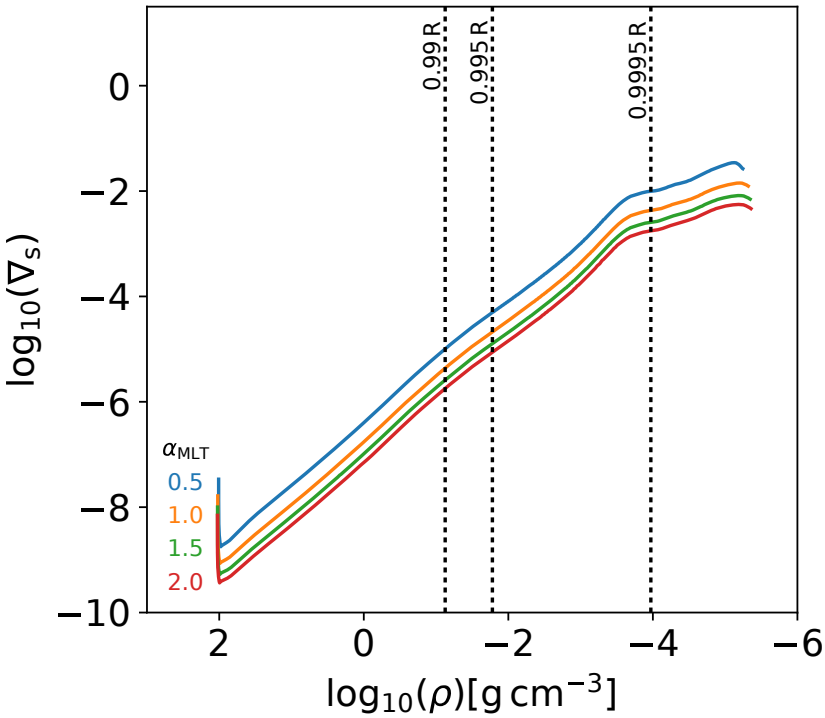

(b)

Figure 3.1: $\log_{10}(\nabla_s)$ as a function of $\log_{10}(\rho)$, for $0.3\,M_\odot$, (a) 10 Myr or (b) 1 Gyr stellar models at $\alpha_{\rm MLT} = 0.5 - 2.0$ ($\Delta 0.5$). As $\alpha_{\rm MLT}$ decreases, the superadiabaticity ∇_s increases throughout the stellar interior, but ∇_s is inherently lower in main-sequence models.

prescription of Böhm-Vitense (1958), as implemented in MESA:

$$F_{\rm conv} = \frac{1}{4\sqrt{2}} c_p (p\rho Q)^{1/2} T (\nabla - \nabla')^{3/2} \alpha_{\rm MLT}^2, \tag{3.2}$$

where c_p is the specific heat capacity (at constant pressure), p is pressure, $Q = -(\partial \log \rho / \partial \log T)_p$ is the isobaric expansion coefficient, and $\nabla' = (d \log T / d \log p)'$ is the temperature gradient of the rising element (Cox and Giuli 1968). Following Cox and Giuli (1968), we can solve for the convective efficiency $\Gamma = A(\nabla - \nabla')^{1/2}$, which is the ratio of energy successfully transported and that which is lost by a convective element, in terms of $\nabla_{\rm s}$, and express $\nabla - \nabla'$ as a function of $\nabla_{\rm s}$:

$$\begin{aligned} \nabla - \nabla' &= \left(\frac{\Gamma}{A}\right)^2 \\ &= \frac{1}{4A^2}\left(\sqrt{1 + 4A^2 \nabla_{\rm s}} - 1\right)^2, \end{aligned} \tag{3.3}$$

where

$$\begin{aligned} A &= \frac{Q^{1/2} c_p \kappa g \rho^{5/2} H_p^2}{12\sqrt{2} a c p^{1/2} T^3} \alpha_{\rm MLT}^2 \\ &\equiv A_{\rm other} \alpha_{\rm MLT}^2 \end{aligned} \tag{3.4}$$

is the ratio of convective and radiative conductivities, where κ is opacity, g is gravitational acceleration, a is the radiation constant, and c is the speed of light.

Using Equations (3.2) and (3.3), we express $\nabla_{\rm s}$ as a function of $\alpha_{\rm MLT}$:

$$\nabla_{\rm s} = \left(\frac{4\sqrt{2} F_{\rm conv}}{c_p (p\rho Q)^{1/2} T}\right)^{2/3} \alpha_{\rm MLT}^{-4/3} + \frac{1}{A_{\rm other}} \left(\frac{4\sqrt{2} F_{\rm conv}}{c_p (p\rho Q)^{1/2} T}\right)^{1/3} \alpha_{\rm MLT}^{-8/3}. \tag{3.5}$$

Equation (3.5) reflects the fact that there are two regimes of convective efficiency $\Gamma \sim A \nabla_{\rm s}^{1/2}$. As noted by Gough and Weiss (1976), stellar convection theories tend asymptotically toward two regimes: high ($\Gamma \gg 1$, left term) and low ($\Gamma \ll 1$, right term) convective

efficiency. The connection between these two asymptotic limits is very thin, so the structure of this transition is typically not significant in the astrophysical context.

For homologous stellar models of highly efficient convection, where luminosity (hence convective flux) is fixed throughout the radial distribution in the bulk of the stellar interior,

$$\nabla_{\rm s} \propto \alpha_{\rm MLT}^{-4/3}, \tag{3.6}$$

demonstrating that, in this regime, a decrease in $\alpha_{\rm MLT}$ corresponds to an monotonic increase of $\nabla_{\rm s}$ in the bulk of the convection zone (e.g., Christensen-Dalsgaard 1997).

From Equation (3.6), it is possible to reproduce a majority of a model's $\nabla_{\rm s}$ profile using the model's $\alpha_{\rm MLT}$, and an unperturbed, or reference, model's $\alpha_{\rm MLT}$ and $\nabla_{\rm s}$, via

$$\nabla_{\rm s} \simeq \nabla_{\rm s_0} \left(\frac{\alpha_{\rm MLT}}{\alpha_{\rm MLT_0}} \right)^{-4/3}, \tag{3.7}$$

where zero subscripts denote values from the unperturbed model. This is valid only for models where the convective flux remains roughly the same as in our fiducial model. In Figure 3.2, we plot the outputted $\nabla_{\rm s}$ and those reproduced using Equation (3.7) as a function of $\log_{10}(\rho)$ for $0.3\,M_\odot$, 10 Myr, and 1 Gyr stellar models with $\alpha_{\rm MLT} = 0.8 - 1.7$ (in $\Delta 0.3$ increments). We choose $\alpha_{\rm MLT} = 1.7$ to be our unperturbed model and the lower limit $\alpha_{\rm MLT} = 0.8$ corresponds to the lowest $\alpha_{\rm MLT}$ for which the convective flux is similar to the unperturbed model. We plot $\nabla_{\rm s}$ linearly to show the surface layers more clearly. Small deviations are increasingly evident right near the photosphere in the 10 Myr models with decreasing $\alpha_{\rm MLT}$, as the "low efficiency" regime (ignored in Equation (3.7)) begins to come into play. However, the approximation of Equation (3.7) captures the behaviour of $\nabla_{\rm s}$ up to $\approx 0.9995\,R$.

We turn next to an analysis of the specific entropy in the same models. In Figure 3.3, we plot s as a function of $\log_{10}(\rho)$ for these models. We obtain s as a function of the radial distribution r in our stellar models by taking the outputted central specific entropy $s_{\rm c}$ and integrating the specific entropy gradient ds/dr up to a radial point r':

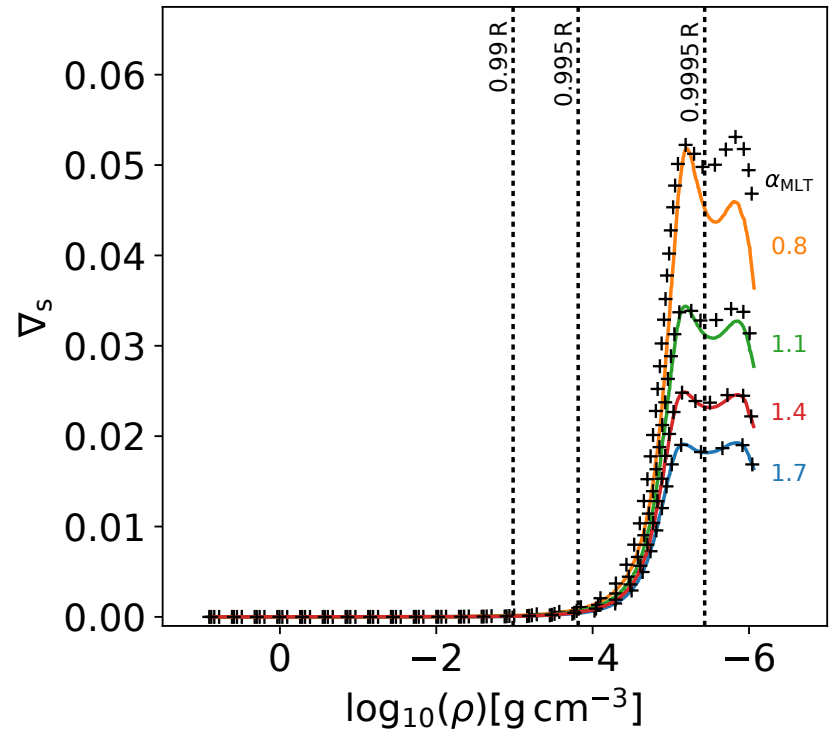

(a)

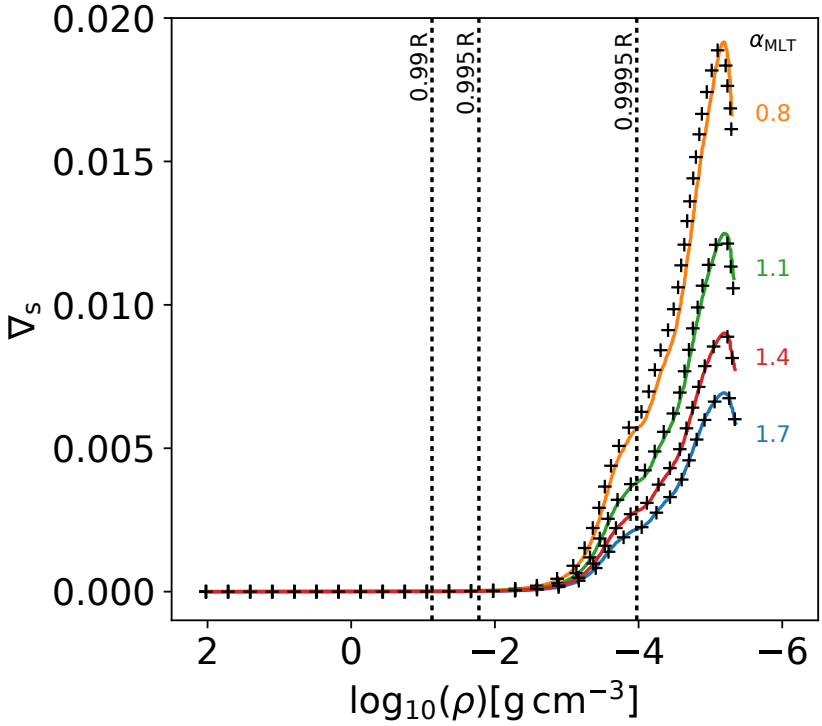

(b)

Figure 3.2: ∇_s as a function of $\log_{10}(\rho)$, comparing the outputted values and those reproduced using Equation (3.7) (plus markers), for a selection of $0.3\,M_\odot$, (a) 10 Myr or (b) 1 Gyr stellar models at $\alpha_{\rm MLT} = 0.8 - 1.7$ ($\Delta 0.3$). $\alpha_{\rm MLT} = 1.7$ is chosen to be the "unperturbed" model. As $\alpha_{\rm MLT}$ decreases, the 10 Myr model's reproduced ∇_s increasingly diverges right at the photosphere, due to the non-negligible low efficiency regime.

$$s(r') = s_{\rm c} + \int_0^{r'} \frac{ds}{dr}\, dr. \tag{3.8}$$

ds/dr is related to the superadiabaticity $\nabla_{\rm s}$ through the first and second laws of thermodynamics:

$$\frac{ds}{dr} = -\frac{c_p}{H_p}\nabla_{\rm s}. \tag{3.9}$$

In the bulk of the convection zone, specific entropy asymptotically converges with depth toward a nearly constant specific entropy value $s_{\rm ad}$. The value of $s_{\rm ad}$ largely determines the stellar structure, including the stellar radius. As noted by Gough and Weiss (1976), a perfect theory of convection would specify this adiabat (i.e., fix $s_{\rm ad}$), but, in practice, it must be calibrated via observations. To be specific, note that for a fully convective isentropic star (with $\gamma = 5/3$), we would have $s \propto \log\left(T^{3/2}/\rho\right) = const$. In this case, properties at the centre 'c' and the photosphere 'ph' would be directly linked, with $(T_{\rm c}^{3/2}/\rho_{\rm c}) = (T_{\rm ph}^{3/2}/\rho_{\rm ph})$, where $T_{\rm ph} \equiv T_{\rm eff}$. Specifying the surface properties and the adiabat would, in this case, clearly suffice to determine the properties of the star everywhere in its interior.

However, standard stellar structure models are not perfectly isentropic. Ascending into the surface layers, specific entropy decreases: although $\nabla_{\rm s}$ is nearly constant there (Figure 3.1), the entropy gradient (Equation (3.9)) is increasingly negative. This arises because, although c_p remains high even near the surface (in fact, in these models it is higher at $0.9995\,R$ than at $0.99\,R$), H_p declines monotonically, implying that ds/dr increases in magnitude near the surface. This non-zero ds/dr implies that there is an entropy jump Δs between the interior adiabat and the surface value. If this is the only region where ds/dr is non-zero, then the ratio of the central and photospheric properties, from the logarithmic argument of Equation (3.1), is now a function of Δs:

$$\frac{T_{\rm c}^{1/(\gamma-1)}/\rho_{\rm c}}{T_{\rm ph}^{1/(\gamma-1)}/\rho_{\rm ph}} = \exp\left(\frac{\mu \Delta s}{N_{\rm A} k_{\rm B}}\right), \tag{3.10}$$

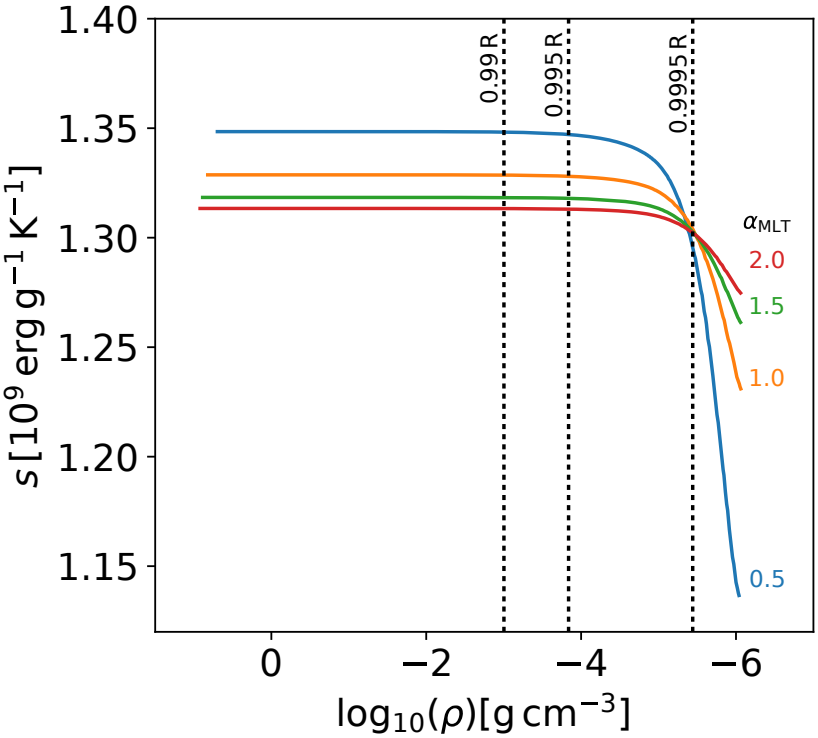

(a)

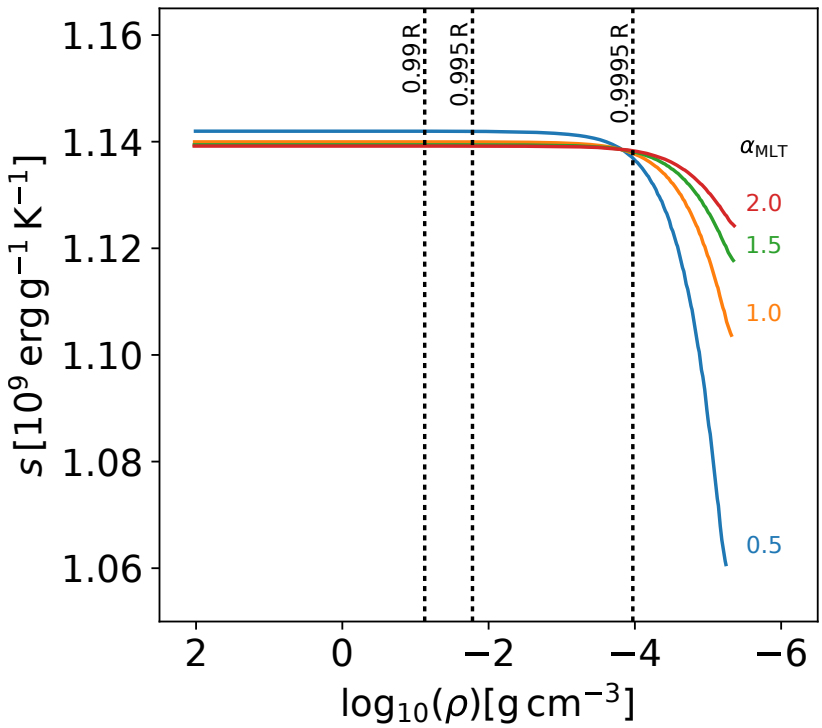

(b)

Figure 3.3: s as a function of $\log_{10}(\rho)$ for $0.3\,M_\odot$, (a) 10 Myr or (b) 1 Gyr stellar models at $\alpha_{\mathrm{MLT}} = 0.5 - 2.0$ ($\Delta 0.5$). Decreasing α_{MLT} increases s_{ad}, i.e., the asymptotic value of specific entropy in the bulk of the convection zone, but to a lesser extent for main-sequence models.

demonstrating explicitly how noticeable values of Δs may influence the stellar properties of fully convective models.

Examining the variation of specific entropy in Figure 3.3, a few key trends are clear. At both 10 Myr and 1 Gyr, models with lower $\alpha_{\rm MLT}$ always have a larger contrast Δs between the photosphere and the deep interior. The lower-$\alpha_{\rm MLT}$ models also have a lower specific entropy at the photosphere $s_{\rm ph}$. In the pre-main-sequence models, models at lower $\alpha_{\rm MLT}$ also possess a higher internal entropy $s_{\rm ad}$, but by an age of 1 Gyr this variation has largely vanished, with only the very lowest $\alpha_{\rm MLT}$ model here ($\alpha_{\rm MLT} = 0.5$) possessing a noticeably higher $s_{\rm ad}$. These features can be understood as discussed below.

First, consider the overall entropy contrast Δs in the near-surface layers. To quantify how the profile of specific entropy varies with $\alpha_{\rm MLT}$, we first consider Δs expressed in terms of $\nabla_{\rm s}$ via Equation (3.9):

$$\begin{aligned}\Delta s &= -\int_0^R \frac{ds}{dr}\,dr \\ &= \int_0^R \frac{c_p}{H_p}\nabla_{\rm s}\,dr.\end{aligned} \tag{3.11}$$

Using Equation (3.5), it can be shown that Δs increases with decreasing $\alpha_{\rm MLT}$:

$$\Delta s = \alpha_{\rm MLT}^{-4/3}\int_0^R \frac{c_p}{H_p}\left(\frac{4\sqrt{2}F_{\rm conv}}{c_p(p\rho Q)^{1/2}T}\right)^{2/3} dr + \alpha_{\rm MLT}^{-8/3}\int_0^R \frac{c_p}{H_p}\frac{1}{A_{\rm other}}\left(\frac{4\sqrt{2}F_{\rm conv}}{c_p(p\rho Q)^{1/2}T}\right)^{1/3} dr, \tag{3.12}$$

where $\alpha_{\rm MLT}$ is taken out of the integrands due to being depth independent. As we are able to reproduce a majority of $\nabla_{\rm s}$ via the high efficiency regime using Equation (3.7), it follows that for models where the convective flux remains roughly the same as in our unperturbed model that

$$\Delta s \propto \alpha_{\rm MLT}^{-4/3}. \tag{3.13}$$

Next, consider the photospheric entropy in the models. For an ideal gas with $\gamma = 5/3$,

$$\begin{aligned} s_{\rm ph} &\simeq \frac{N_{\rm A} k_{\rm B}}{\mu} \log \frac{T_{\rm eff}^{5/2}}{p_{\rm ph}} \\ &\propto \frac{N_{\rm A} k_{\rm B}}{\mu} \log (T_{\rm eff}^{23/2} \rho_{\rm ph}^{1/2} R^2), \end{aligned} \tag{3.14}$$

where R is the stellar radius, and the proportionality assumes that the photosphere occurs at a pressure $p_{\rm ph} \propto g/\kappa_{\rm ph}$, with the surface opacity $\kappa_{\rm ph}$ taken for simplicity to be dominated by H- opacity (Stahler 1988), which is proportional to $\rho_{\rm ph}^{1/2} T_{\rm eff}^9$. Note that in actuality, molecules also contribute substantially to the near-surface opacity in objects of this mass (Ferguson et al. 2005), and become more dominant at lower masses. The photospheric entropy is thus tightly linked to variations in the effective temperature, and this in turn is tightly constrained to lie within a narrow range: if the temperature were suddenly made much higher, for example, the opacity would sharply increase, increasing the optical depth at a given pressure level and hence driving the photosphere upward (i.e., to lower pressure and hence to lower temperatures). Conversely, much lower temperatures would lead to much lower opacities, requiring that the photosphere (at fixed optical depth) move inward (to higher pressures and higher temperatures). This behaviour is well known, and is essentially the basis for the "forbidden region" of cool temperatures in pre-main-sequence evolution (Hayashi 1961). In the present context, only modest variations in $T_{\rm eff}$ are therefore allowed. Within this allowed range, models with lower $\alpha_{\rm MLT}$ have a lower $T_{\rm eff}$: for the same initial interior conditions, steeper entropy (and temperature) gradients are, per our discussion of Δs above, required to carry out the same surface luminosity and this leads to slightly lower surface temperatures (the subsequent evolution of $T_{\rm eff}$ is somewhat more involved, as we will discuss more below, but the tendency to have lower $T_{\rm eff}$ at lower $\alpha_{\rm MLT}$ is robust). The strong dependence of $s_{\rm ph}$ on $T_{\rm eff}$ dominates over changes in $\rho_{\rm ph}$ and stellar radii between models at a given age, implying (finally) that $s_{\rm ph}$ is lower in models with lower $\alpha_{\rm MLT}$.

Finally, we turn to discussion of the nearly constant specific entropy $s_{\rm ad}$ in the deep interior of the models. This exhibits different behaviour on the main sequence than during the pre-main-sequence contraction phase. Recall that, during this phase, stars descend

along a Hayashi track at nearly constant $T_{\rm eff}$; they contract because they are losing total energy (via radiative losses from the surface), so the contraction rate depends on the star's luminosity. From the virial theorem, the internal temperature of the star increases as its radius decreases ($T \propto R^{-1}$), but the increasing density ($\rho \propto R^{-3}$) results in a net loss of entropy. During this phase, it is clear from Figure 3.3 that $s_{\rm ad}$ is higher at a given age in models with lower $\alpha_{\rm MLT}$. This mostly reflects the fact that these low-$\alpha_{\rm MLT}$ models have had a slightly lower effective temperature during their contraction, and have ultimately lost somewhat less entropy at any fixed time; they therefore have a somewhat greater specific entropy at the time sampled in this figure. At these ages, the enhanced entropy contrast associated with lower $\alpha_{\rm MLT}$ (per our discussion above) is thus not entirely confined to the near-surface layers: though the photospheric entropy is lower for low-$\alpha_{\rm MLT}$ models, $s_{\rm ad}$ is also higher.

The pre-main-sequence contraction eventually ends because the interior temperature and density have increased enough for nuclear fusion in the core (rather than gravitational contraction) to provide the energy needed to offset the star's radiative losses at the surface. On the main sequence, then, the value of $s_{\rm ad}$ is not merely determined by the star's initial entropy and by its passive cooling (which was mediated by the near-surface layers); rather, it is bounded from below by the entropy production associated with nuclear fusion occurring in a steady state. Of course this also is informed by the near-surface layers to some degree, but only insofar as these affect the entropy production rate by nuclear reactions. For the depth-independent $\alpha_{\rm MLT}$ values probed here, these changes are modest, and so the deep interior entropy $s_{\rm ad}$ is largely constant across models with varying $\alpha_{\rm MLT}$ (at even smaller values of $\alpha_{\rm MLT}$, $s_{\rm ad}$ would be altered, as explored for example in Chabrier et al. 2007). Thus in these models the higher Δs associated with less efficient convection is almost entirely confined to the near-surface layers: the decrease in photospheric entropy with decreasing $\alpha_{\rm MLT}$ compensates almost exactly for the increasing Δs.

3.2.2 Scaling of Stellar Radius with $s_{\rm ad}$ and $\alpha_{\rm MLT}$

It has long been realised that a star's radius is sensitive to changes in its entropy (see, e.g. Stahler 1988; Hansen et al. 2004, pp. 370-373). For example, for a star with constant

specific entropy, well-described by a polytropic model $p = K\rho^\gamma$, where K is the polytropic constant, straightforward rearrangement gives

$$s = \frac{N_\mathrm{A} k_\mathrm{B}}{\mu} \log(K). \tag{3.15}$$

It can be shown that $K \propto M^{2-\gamma} R^{3\gamma-4}$ (see Equation (7.40) in Hansen et al. 2004, p. 336), where M is the stellar mass. By substituting this into Equation (3.15) and integrating over the mass distribution of the stellar model, yielding the total entropy $S_\mathrm{tot} \sim sM$ for a star of uniform composition, it can be shown that the stellar radius increases with the exponent of S_tot for fixed mass:

$$R \propto \exp\left(\frac{\gamma-1}{3\gamma-4}\frac{\mu S_\mathrm{tot}}{N_\mathrm{A} k_\mathrm{B} M}\right), \tag{3.16}$$

as noted for example in Hansen et al. (2004, p. 372) (their Equation (7.150)). More precise relations between R, S_tot, and other variables can be derived in some specific cases, and these figure prominently in the classic theory of stellar structure (e.g., Eddington 1926; Hayashi and Hoshi 1961). For example, for a star in hydrostatic equilibrium, the assumption of a perfectly isentropic interior allows relation of the central temperature, pressure, and density to the values of these quantities at the surface, following standard polytropic theory. If the nuclear energy generation ϵ is provided by fusion, it is further possible to solve for the radius of the star from first principles (by equating the luminosity produced by fusion, $L_\mathrm{fusion} \propto R^3\epsilon \propto R^3\rho_\mathrm{c}^2 T_\mathrm{c}^6$ for the pp-chain, to the surface luminosity $L_\mathrm{surf} = 4\pi R^2 T_\mathrm{eff}^4$, and adopting a closed-form expression for the surface opacity).

However, the structure models calculated by MESA (or any other stellar structure code) are not isentropic. The level of departure from isentropy depends on details of the models, and in particular on the convective mixing length. In practice, as discussed in Section 3.2.1, most of the entropy resides in the deep interior with nearly constant specific entropy s_ad, so that $S_\mathrm{tot} \simeq s_\mathrm{ad} M$ and Equation (3.16) simplifies to

$$R \propto \exp\left(\frac{\gamma-1}{3\gamma-4}\frac{\mu s_\mathrm{ad}}{N_\mathrm{A} k_\mathrm{B}}\right). \tag{3.17}$$

Thus, we can relate the ratio of two stellar radii and the change in $s_{\rm ad}$ between two fixed mass models:

$$\frac{R_2}{R_1} \simeq \exp\left(\frac{\gamma-1}{3\gamma-4}\frac{\mu\Delta s_{\rm ad}}{N_{\rm A}k_{\rm B}}\right). \tag{3.18}$$

where R_1 and R_2 are the radii of the first and second model, respectively, assuming a uniform $\gamma = 5/3$ for simplicity. This illustrates how an increase in $s_{\rm ad}$ "inflates" the stellar radius of these stellar models. Choosing $\alpha_{\rm MLT} = 1.7$ to be our unperturbed model, we determine an unperturbed stellar radius $R_0 = 0.683\,R_\odot$ and $0.286\,R_\odot$, for 10 Myr and 1 Gyr, respectively.

Models with different $\alpha_{\rm MLT}$ have somewhat different radii. For example, at 10 Myr, "perturbing" our standard model by considering $\alpha_{\rm MLT}$ in the range 0.5-1.7 results in radius inflation $\Delta R/R_0 \lesssim 17.5\%$ ($R \lesssim 0.803\,R_\odot$). However, for 1 Gyr models with the same range of $\alpha_{\rm MLT}$, we only find $\Delta R/R_0 \lesssim 1.5\%$ ($R \lesssim 0.289\,R_\odot$); we analyse this important difference in the radius inflation between pre-main-sequence and main-sequence models in more detail below but, for now, note that it stems partly from the lower superadiabaticity of these main-sequence models. This in turn implies that the properties of fixed mass fully convective main-sequence stars are relatively insensitive to $\alpha_{\rm MLT}$ in standard stellar structure models (as noted previously by, e.g., Chabrier et al. 2007; Feiden and Chaboyer 2014).

In Figure 3.4, we examine the ratio of two outputted stellar radii as a function of $\Delta s_{\rm ad}$ via Equation (3.18), for $0.3\,M_\odot$ stellar models at both 10 Myr and 1 Gyr for all possible model comparisons between $\alpha_{\rm MLT} = 0.5 - 1.7$ ($\Delta 0.05$). The line $y = x$, which would indicate perfect agreement with Equation (3.18), is over-plotted (orange line) for ease of comparison. At 10 Myr (top panel), the variations in stellar radii are captured extremely well by this expression; at 1 Gyr (bottom panel), they deviate from it slightly. The small deviations from Equation (3.18) arise partly from departures from the ideal equation of state assumed in our derivation of this equation. In particular, the central temperature for stars of this mass on the main sequence deviates slightly from the virial expectation that $T \propto M/R$ (owing partly to the fact that these interiors are somewhat

degenerate). Further deviations from Equation (3.18) arise due to our assumption of a uniform $\gamma = 5/3$ in deriving this expression; in our models, γ is indeed roughly uniform (and $= 5/3$) in the interiors of our pre-main-sequence models, but deviates from this slightly on the main sequence. (These deviations in turn arise partly from Coulomb interactions, which, though small, are not entirely negligible.) Note, further, that the overall range in stellar radii across all models, and likewise the variation in $s_{\rm ad}$ across these models, is much smaller than on the pre-main-sequence.

The changes in $s_{\rm ad}$, and hence in the stellar radius, are linked to changes in $\alpha_{\rm MLT}$. To examine this quantitatively, we must find how the value of the adiabat is linked to Δs. For example, if all the changes in Δs between models were reflected simply in changes to the photospheric entropy $s_{\rm ph}$, this would imply an $s_{\rm ad}$ that is nearly uniform across models; meanwhile if $s_{\rm ph}$ were instead somehow held constant across all models, changes in Δs would translate directly to changes in $s_{\rm ad}$. The true relation between $s_{\rm ph}$ and $s_{\rm ad}$ (and hence Δs) is more complex than either of these simple examples. Overall, though, as established previously, a decrease in $\alpha_{\rm MLT}$ decreases $s_{\rm ph}$ and (on the pre-main sequence in particular) increases $s_{\rm ad}$.

To see roughly why this is so, note that, in general, the surface luminosity $L_{\rm surf} \propto R^2 T_{\rm eff}^4$, which (using Equation (3.14)) can be written as

$$L_{\rm surf} \propto \exp\left(\frac{\mu s_{\rm ph}}{N_{\rm A} k_{\rm B}}\right) / (\rho_{\rm ph}^{1/2} T_{\rm eff}^{15/2}). \tag{3.19}$$

On the pre-main sequence, the luminosity is ultimately derived from gravitational contraction, with $L_{\rm surf} \propto R^{-2}(dR/dt)$. Equating the two, and noting how R scales with $s_{\rm ad}$ (Equation (3.17)), implies that for contraction at nearly constant effective temperature, we must have

$$\exp\left(-\frac{\gamma - 1}{3\gamma - 4}\frac{\mu s_{\rm ad}}{N_{\rm A} k_{\rm B}}\right) \propto \exp\left(\frac{\mu s_{\rm ph}}{N_{\rm A} k_{\rm B}}\right) / (\rho_{\rm ph}^{1/2} T_{\rm eff}^{15/2}). \tag{3.20}$$

This in turn implies that $s_{\rm ad} \propto -s_{\rm ph}$ on the pre-main sequence (plus additional smaller terms). A similar proportionality holds on the main sequence, where now the interior

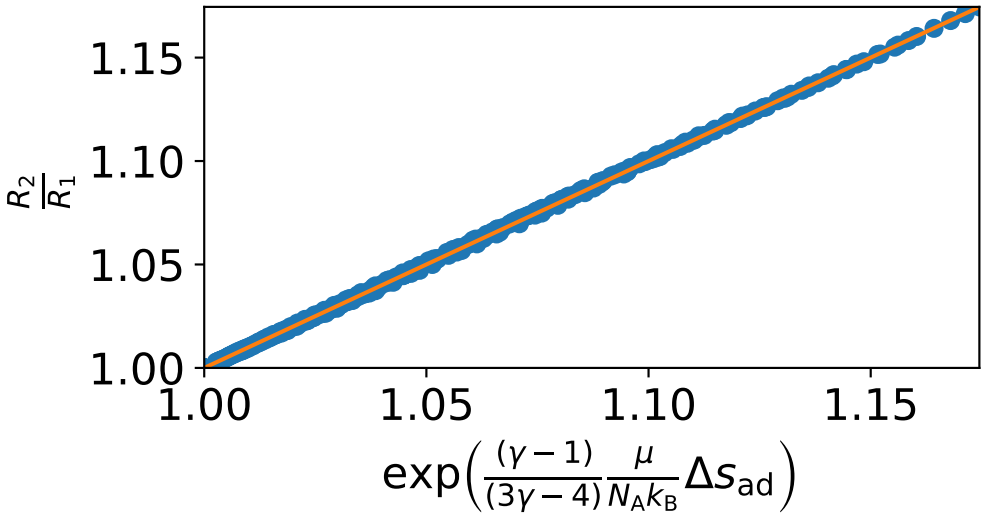

(a)

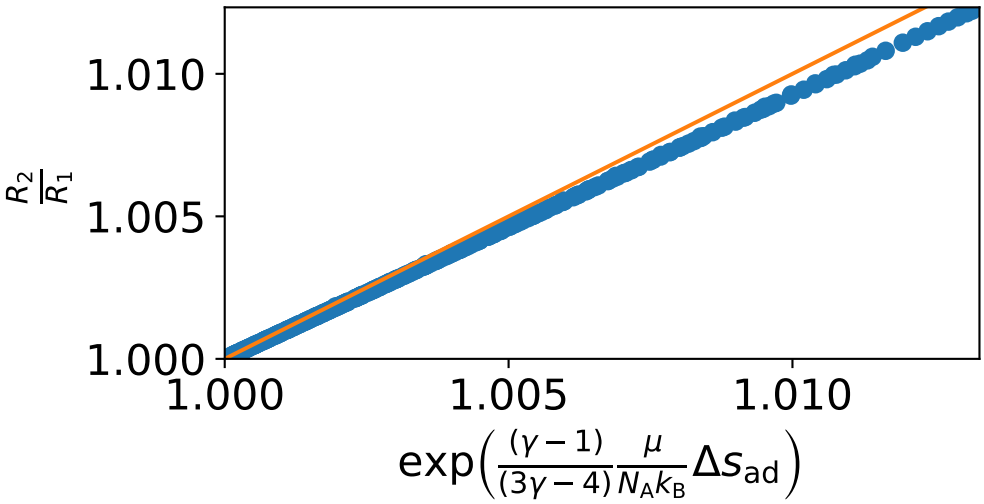

(b)

Figure 3.4: The ratio of stellar radii R_2/R_1 as a function $\Delta s_{\rm ad}$ via Equation (3.18), for $0.3\,M_\odot$, (a) 10 Myr or (b) 1 Gyr stellar models at $\alpha_{\rm MLT} = 0.5 - 1.7$ ($\Delta 0.05$). We see a divergence at 1 Gyr, which arise from deviations from the ideal equation of state. $y = x$ (orange) is plotted for ease of comparison.

luminosity is generated by fusion, with $L \propto R^3\epsilon \propto R^2\rho_c^2 T_c^6 \propto R^{-9}$ for stars in virial equilibrium. This again implies $s_{\rm ad} \propto -s_{\rm ph}$, but with a different (and in fact significantly smaller) constant of proportionality. Thus in both cases, in comparing models of similar total convective flux ($\alpha_{\rm MLT} = 0.8 - 1.7$), we have that $s_{\rm ad} \propto \Delta s$, hence

$$s_{\rm ad} \propto \alpha_{\rm MLT}^{-4/3}. \tag{3.21}$$

The constant of proportionality decreases with the age of the model—as discussed previously, the interior adiabat in pre-main-sequence models is more sensitive to variations in $\alpha_{\rm MLT}$—but the proportionality holds true even for main-sequence models.

In Figure 3.5, we examine $s_{\rm ad}$ as a function of $\alpha_{\rm MLT}^{-4/3}$ for $0.3\,M_\odot$ stellar models at $\alpha_{\rm MLT} = 0.8 - 1.7$ ($\Delta 0.05$) for both 10 Myr and 1 Gyr, where the proportionality in Equation (3.21) holds for both ages here. We extrapolate to find $s_{{\rm ad}(\alpha_{\rm MLT}\to\infty)}$, i.e., the value corresponding to an isentropic model, which gives the constant of proportionality in Equation (3.21) as

$$\frac{ds_{\rm ad}}{d\alpha_{\rm MLT}^{-4/3}} \approx \frac{s_{\rm ad} - s_{{\rm ad}(\alpha_{\rm MLT}\to\infty)}}{\alpha_{\rm MLT}^{-4/3}}. \tag{3.22}$$

Thus, for fully convective stellar models of similar total convective flux, one can predict the radius inflation between two models of known $\alpha_{\rm MLT}$ without having to determine a perturbed model's $s_{\rm ad}$, solely using the unperturbed model's $s_{\rm ad}$, and $s_{{\rm ad}(\alpha_{\rm MLT}\to\infty)}$ at a given age:

$$\frac{R_2}{R_1} \approx \exp\left(\frac{\gamma-1}{3\gamma-4}\frac{\mu}{N_{\rm A}k_{\rm B}}\frac{s_{{\rm ad}_1} - s_{{\rm ad}(\alpha_{\rm MLT}\to\infty)}}{\alpha_{{\rm MLT}_1}^{-4/3}}\Delta\left(\alpha_{\rm MLT}^{-4/3}\right)\right). \tag{3.23}$$

In Figure 3.6, we examine the ratio of two outputted stellar radii as a function of $\Delta\left(\alpha_{\rm MLT}^{-4/3}\right)$ at different ages between 10 Myr and 1 Gyr. Models at all $\alpha_{\rm MLT}$ contract on the pre-main sequence, with $dR/dt \propto R^4$, implying in turn that $R \propto t^{-1/3}$ if the effective temperature remains constant. In our models, the radius inflation between two models of differing $\alpha_{\rm MLT}$ decreases with age, becoming almost negligible during the main sequence

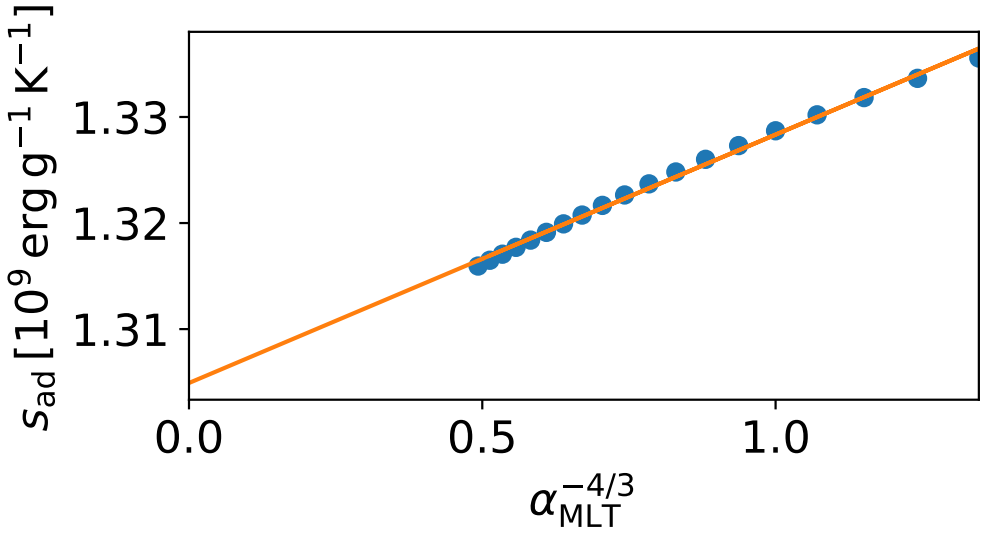

(a)

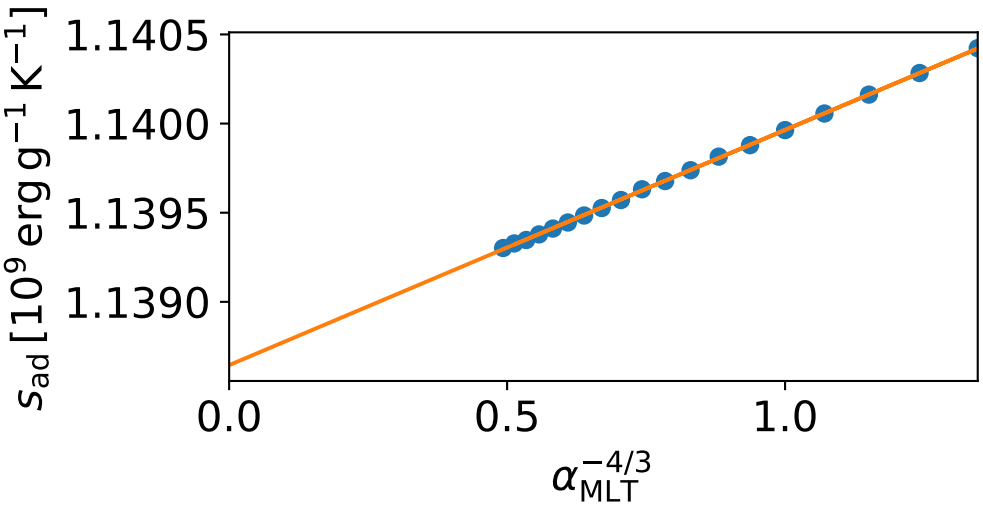

(b)

Figure 3.5: $s_{\rm ad}$ as a function of $\alpha_{\rm MLT}^{-4/3}$ for $0.3\,M_\odot$, (a) 10 Myr or (b) 1 Gyr stellar models at $\alpha_{\rm MLT} = 0.8{-}1.7$ ($\Delta 0.05$). We extrapolate to the isentropic value of $s_{\rm ad}$ at that given age, which drops as a function of age in the pre-main sequence, settling in the main sequence. The trend between $s_{\rm ad}$ and $\alpha_{\rm MLT}^{-4/3}$ also decreases with age.

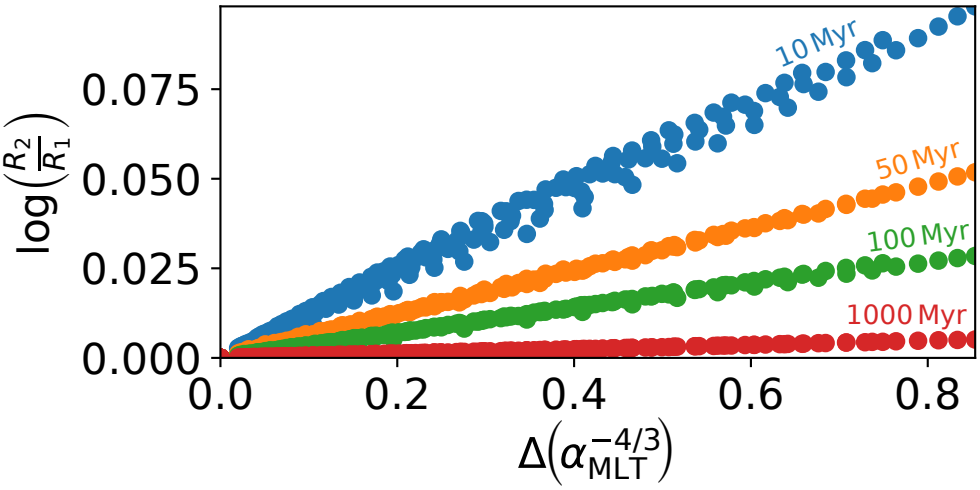

Figure 3.6: $\log(R_2/R_1)$ as a function of $\Delta\left(\alpha_{\rm MLT}^{-4/3}\right)$ at various ages for $0.3\,M_\odot$ stellar models at $\alpha_{\rm MLT} = 0.8 - 1.7$ ($\Delta 0.05$). During the pre-main-sequence, the trend decreases with age (see Equation (3.24)), eventually reaching levels of negligible radius inflation in the main-sequence.

(1 Gyr). This time dependence ultimately reflects the fact that (as shown in Figure 3.5) $ds_{\rm ad}/d\alpha_{\rm MLT}^{-4/3}$ (Equation (3.22)) changes with time, becoming much shallower on the main sequence; referring to Equation (3.23), this means a less pronounced radius inflation for a given change in $\alpha_{\rm MLT}$. Empirically, we find that

$$\frac{R_2}{R_1} \propto t^{-0.03\Delta\left(\alpha_{\rm MLT}^{-4/3}\right)}, \tag{3.24}$$

demonstrating that a larger change in $\alpha_{\rm MLT}$ between two models does indeed result in the model contracting more rapidly with time.

As previously discussed, during the main sequence, $s_{\rm ad}$ is predominantly bounded by the entropy production via nuclear fusion, thus any changes in $s_{\rm ph}$ in our models fail to produce noticeable changes in $s_{\rm ad}$. Hence, for our range of main-sequence models, where $\Delta s_{\rm ph} \lesssim 10^7\,{\rm erg\,g^{-1}\,K^{-1}}$, we find that $R_2 \approx R_1$, as demonstrated by the trend at 1 Gyr in Figure 3.6.

Note that our lowest-efficiency models in Figures 3.1 and 3.3 have $\alpha_{\rm MLT} = 0.5$; at even lower values, radius inflation is possible even on the main sequence, as demonstrated for example by Chabrier et al. (2007). In this regime, however, the convective flux is not the same as at higher values of $\alpha_{\rm MLT}$ (that is, the nuclear energy generation in the interior

is affected), breaking the assumptions made in our analysis. Indeed, Chabrier et al. (2007) show that at $\alpha_{\rm MLT} \approx 0.05$ a radiative (stable) core begins to form in the interior, violating our assumption that the star is fully convective. We defer analysis of such cases to other work.

3.3 Rotational Inhibition of Convection: Stevenson (1979) Formulation

3.3.1 Theory: Rotational Modification to MLT

As noted in Section 3.1, rotation generally acts to inhibit convection. In linear theory, this inhibition manifests itself as an increase in the critical Rayleigh number required to drive convection (Chandrasekhar 1961). The effects of rotation in the nonlinear regime are more difficult to gauge, but many authors have argued that ultimately the temperature gradient required to transport a given heat flux by convection must increase somewhat if the rotation is sufficiently rapid. Stevenson (1979) (S79, hereafter), for example, derived a mixing length prescription for rotating convection through consideration of the growth of linear, Boussinesq convective modes, constructing a finite amplitude theory by assuming that nonlinearities, such as shear instabilities, limit the amplitude of the flow. Following Malkus (1954), S79 argued that the convective flow is dominated by the modes that transport the most heat. S79 use this model to relate $\nabla_{\rm s}$ in a "perturbed" model (at rotation rate Ω) to the unperturbed (non-rotating) model's:

$$\begin{aligned}\left(\frac{\nabla_{\rm s}}{\nabla_{\rm s_0}}\right)^{5/2} - \frac{\nabla_{\rm s}}{\nabla_{\rm s_0}} &= \frac{1}{41}{\rm Ro}^{-2} \\ &\equiv \frac{4}{41}\tau_{\rm c_0}^2\Omega^2,\end{aligned} \tag{3.25}$$

where $\tau_{\rm c_0}$ is the convective turnover time of the unperturbed model, and ${\rm Ro} \equiv (2\tau_{\rm c_0}\Omega)^{-1}$ is the Rossby number.

In the slow regime, i.e., ${\rm Ro} \gg 1$,

$$\begin{aligned}\nabla_{\rm s} &\simeq \nabla_{\rm s_0}\left(1+\frac{1}{62}{\rm Ro}^{-2}\right)\\ &\equiv \nabla_{\rm s_0}\left(1+\frac{4}{62}\tau_{\rm c_0}^2\Omega^2\right),\end{aligned} \tag{3.26}$$

converging toward the non-rotating model. In the rapid regime, i.e., Ro $\ll 1$,

$$\begin{aligned}\nabla_{\rm s} &\simeq 0.23\nabla_{\rm s_0}{\rm Ro}^{-4/5}\\ &\equiv 0.92\nabla_{\rm s_0}\tau_{\rm c_0}^{4/5}\Omega^{4/5}.\end{aligned} \tag{3.27}$$

As $\nabla_{\rm s} \propto ds/dr$, this mechanism modifies the gradient of the specific entropy, i.e., specific entropy asymptotically converges to a different adiabat in the presence of rotation.

We are motivated to explore this reformulation of MLT partly because more recent investigations have suggested similar scalings for the temperature gradient and/or velocity in rapidly rotating convection. For example, as noted in Section 3.1, Barker et al. (2014) derive a rotating MLT equivalent to that of S79 via simplified physical arguments, achieving the same scaling between $\nabla_{\rm s}$ (dT/dz in their case) and Ω when in the rapidly rotating regime. To test their relationship, they take an average of dT/dz from the middle third of the convection zone in a series of 3D hydrodynamical simulations of Boussinesq convection in a Cartesian box. They find that dT/dz in the simulations does indeed scale with Ω as dictated by Equation (3.27), and likewise that the typical velocities and spatial structures amidst the flow also scale with Ω in the manner predicted by the theory. Previously, Julien et al. (2012) also examined the transport in rapidly rotating convection using a set of asymptotically reduced equations. They likewise find that heat transport in the rapidly rotating regime is "throttled" by convection in the bulk of the domain—in marked contrast to the non-rotating case, which is controlled mainly by the boundary layers. Overall, their theoretical model yields scalings of dT/dz as a function of Ω that are arguably compatible with those in S79 and Barker et al. (2014). The broad concordance between these different theoretical models suggest that the MLT formulation adopted in S79, though undoubtedly a simplified description of the complex flows occurring in actual

stars, may nonetheless adequately capture how the primary quantity of interest for stellar convection—namely the temperature or entropy gradient as a function of the flux—varies with rotation rate.

We therefore incorporate rotational effects into our 1D stellar structure models by implementing the modified MLT formulation of S79 into MESA. Observations and simulations of fully convective stars have indicated that they are likely to rotate mostly as solid bodies, supporting our choice of using a fixed Ω to model rotation inhibition. Barnes et al. (2005) shows surface differential rotation diminishes with increasing convective depth in low-mass stellar observations, and magnetohydrodynamical (MHD) simulations performed by, e.g., Browning (2008) and Yadav et al. (2015) and Yadav et al. (2016), suggest that magnetic fields react strongly on flows, helping to enforce solid-body rotation.

3.3.2 Radius Inflation: S79 Models

Some active low-mass stars are fast rotators, with rotation velocities $v_{\rm rot} \gtrsim 10\,{\rm km\ s^{-1}}$ (e.g., Reid et al. 2002; Mohanty and Basri 2003) in some cases. We test $\Omega = 5 - 20\,\Omega_\odot$ ($\Delta 5\,\Omega_\odot$), which is $\lesssim 10\%$ of the breakup velocity at 10 Myr, and $\lesssim 3\%$ at 1 Gyr, of our unperturbed $0.3\,M_\odot$, $\alpha_{\rm MLT} = 1.7$ stellar model. These produce typical rotation velocities of $v_{\rm rot} \simeq 7 - 27\,{\rm km\ s^{-1}}$ and $v_{\rm rot} \simeq 3 - 11\,{\rm km\ s^{-1}}$ for 10 Myr and 1 Gyr, respectively. We have not attempted to account for changes in the effective gravity as Ω increases; since the angular velocity in all cases is only a small fraction of the breakup velocity, these effects probably play only a minor role. At each Ω, we calculate a new value of $\nabla_{\rm s}$ at each point in the mass distribution, by modifying the non-rotating $\nabla_{\rm s}$ according to Equation (3.25), representing a "rotating" version of the 1D stellar structure model. The depth dependence of $\nabla_{\rm s}$ is then determined by the profile of Ro, which, in turn, depends on the convective overturning time at every depth in the model. Here, we take this overturning time simply to be $\tau_{\rm c_0}$ from the *unperturbed* model, that is, we neglect the small changes in overturning time associated with changes in the convective velocity at rapid rotation. This simplification has the consequence that our models slightly underestimate the influence of rotation at any fixed Ω (compared to a fully self-consistent model), but we will see in a moment that this effect is utterly negligible for the overall structure.

In Figure 3.7, we plot $\log_{10}(\nabla_{\rm s})$ as a function of $\log_{10}(\rho)$ for $0.3\,M_\odot$, $\alpha_{\rm MLT} = 1.7$ stellar models, at both 10 Myr and 1 Gyr, for $\Omega = 0 - 20\,\Omega_\odot$ ($\Delta 5\,\Omega_\odot$). In the bulk of the convection zone, convective velocities are low, i.e., Ro $\ll 1$, hence this region becomes more superadiabatic than the unperturbed model by a few orders of magnitude. However, due to the already near-adiabaticity in this region, this perturbation in $\nabla_{\rm s}$ does not influence the stellar structure noticeably. In the surface layers, where convective velocities become increasingly rapid, Ro remains $\gg 1$ at all the Ω values sampled, resulting in negligible changes in the superadiabaticity there, i.e., $\nabla_{\rm s} \simeq \nabla_{\rm s_0}$.

The near equivalence of $\nabla_{\rm s}$ in the surface layers of all these models, and their near-adiabaticity in the bulk of the convection zone, together imply that there are negligible differences between the specific entropy profiles of models at varying rotation rates. As discussed in Section 3.2, the radius of the star is determined primarily by the interior adiabat (i.e., $s_{\rm ad}$), which in turn is largely established by the near-surface layers. Because the near-surface layers have Ro $\gg 1$ and thus are almost totally uninfluenced by convection, the entropy jump in all our rotating models is nearly identical to that in the non-rotating case. This in turn means that the specific entropy of the deep interior $s_{\rm ad}$ is unchanged by rotation, even though the deep layers of the star are strongly influenced by Coriolis forces (Ro $\ll 1$), and $\nabla_{\rm s}$ varies considerably between models there. This, following the discussion in Section 3.2.2, finally implies that rotation will lead only to negligible structural changes that concern us here, i.e., those that influence the radius of the star.

This expectation is confirmed in our models. We measured $\Delta R/R_0 \sim 10^{-2}\%$ and $\sim 10^{-4}\%$ for $\Omega = 5 - 20\,\Omega_\odot$ models at 10 Myr and 1 Gyr, respectively. Thus, implementing rotational inhibition of convection using this modified formulation of MLT does not produce noticeable changes in the stellar radius. This is, again, due mainly to the depth dependence of the convective velocities and hence of the Rossby number: if the star were instead well characterised by a single depth-independent Rossby number, radius inflation would be much more noticeable (for low enough values of Ro).

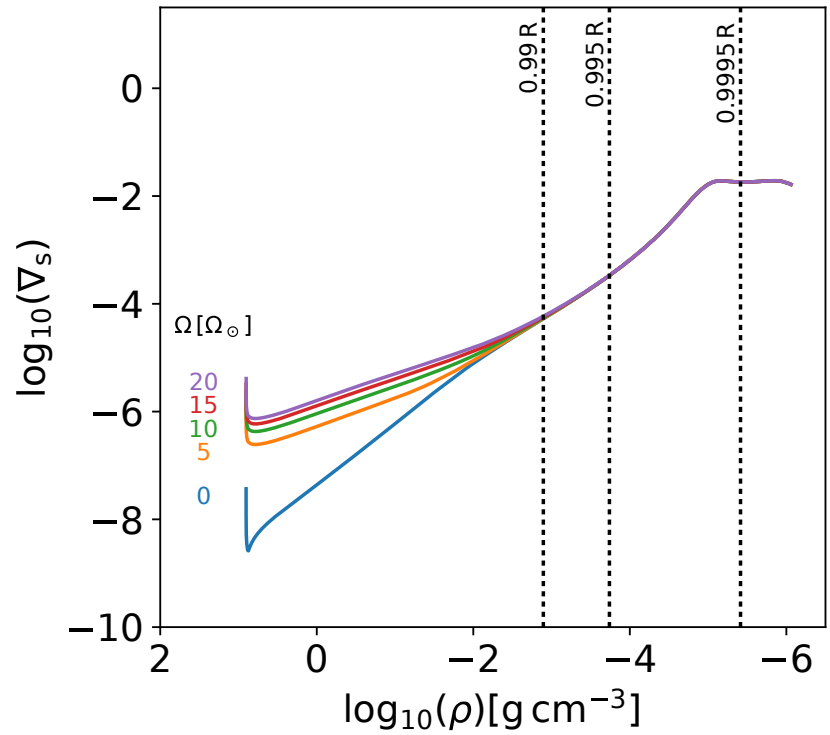

(a)

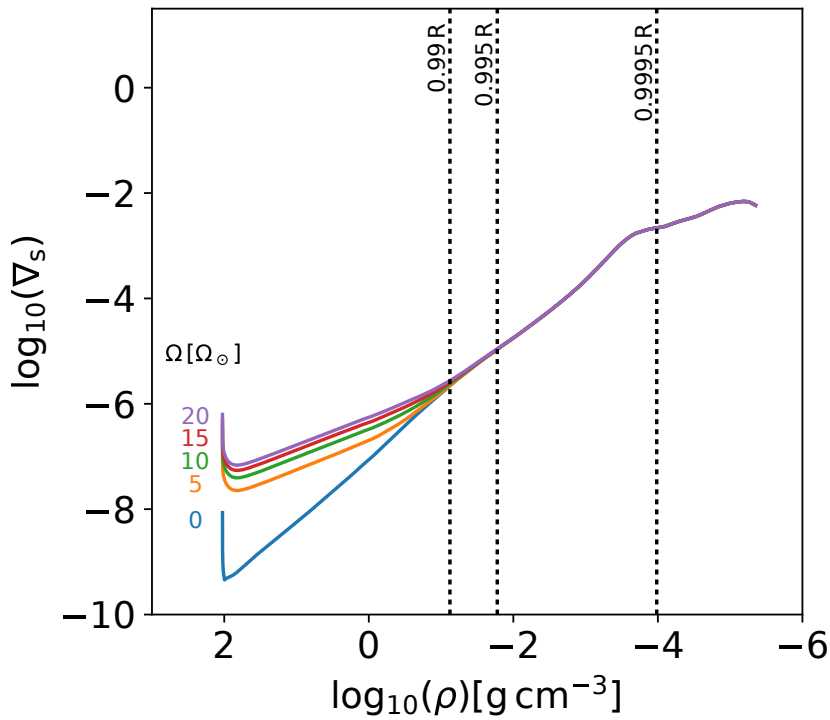

(b)

Figure 3.7: $\log_{10}(\nabla_s)$ as a function of $\log_{10}(\rho)$, for $0.3\,M_\odot$, (a) 10 Myr or (b) 1 Gyr, $\alpha_{\rm MLT} = 1.7$ stellar models at $\Omega = 0 - 20\,\Omega_\odot$ ($\Delta 5\,\Omega_\odot$). As Ω increases, ∇_s increases throughout the bulk of the stellar interior (Ro $\ll 1$), but becomes comparable to the unperturbed model in the near-surface layers (Ro $\gg 1$).

3.4 Magnetic Inhibition of Convection: MacDonald & Mullan (2014) Formulation

3.4.1 Theory: Magnetic Modification to MLT

It is not clear how best to encapsulate the influence of magnetism on convection in 1D stellar structure models. Clearly magnetic fields can inhibit flows via the Lorentz force. However, in the presence of rotation, the effects of magnetism can be more complex, with magnetised rotating fluids sometimes *more* amenable to convection than their non-magnetic equivalents (see Section 3.1). As with rotation, the impact of magnetism in the nonlinear regime is much less clear. Various authors have turned to different prescriptions for encapsulating these effects in 1D models, motivated by physical arguments and results from linear theory, as summarised also in Section 3.1. Here, we have chosen to focus our attention on one such model, namely that proposed by MacDonald and Mullan (2014) (MM14, hereafter), which is a slightly modified form of Mullan and MacDonald 2001); we have chosen this model not because it is necessarily superior to others (e.g., Feiden and Chaboyer 2012, or the reduced-$\alpha_{\rm MLT}$ models of Chabrier et al. 2007), but because its physical motivation is clear, it has been employed in a series of follow-on papers (see, e.g., MacDonald and Mullan 2015, 2017a, 2017b), and it is straightforward to implement in a 1D stellar evolution code. In this section, we briefly describe this prescription, its physical motivation, and then discuss its implementation into MESA models. We aim here to examine whether the mechanism by which radii are inflated in these "magnetic" models is substantially the same as in the non-magnetic cases discussed in Sections 3.2 and 3.3; that is, we examine how the radii, specific entropy, and adopted magnetic prescription are linked. We show that radius inflation in the MM14 models is, as in their non-magnetic cousins, associated with changes in the specific entropy of the deep interior, which in turn is linked to the entropy contrast in the near-surface layers.

The models of MM14 are based partly on the linear stability work of Gough and Tayler (1966), who derived a criterion for convective instability onset due to a magnetic field in certain circumstances. In non-magnetic models, the criterion of convective onset is

purely local; magnetic fields connect parcels of fluid at different levels, so such a criterion is not generally obtainable (Gough and Tayler 1966). However, simple local stability criteria exist for particularly elementary magnetic field configurations. In practice, MM14 modify the Schwarzschild criterion due to the presence of a magnetic field:

$$\nabla_{\rm rad} > \nabla_{\rm ad} + \frac{\delta}{Q}, \tag{3.28}$$

where

$$\delta = \frac{B_{\rm v}^2}{B_{\rm v}^2 + 4\pi\gamma P_{\rm g}} \tag{3.29}$$

is a magnetic inhibition parameter, and $Q = -(\partial \log \rho / \partial \log T)_p$ is the isobaric expansion coefficient. In this expression, $P_{\rm g}$ is the gas pressure and $B_{\rm v}$ is taken by MM14 to represent the vertical component of the magnetic field, on the grounds that this component figures prominently in the linear stability analysis of Gough and Tayler (1966). More generally, we might take $B_{\rm v}$ as a crude proxy encompassing both the strength of the field at a point and some aspects of its spatial morphology. This parameter (δ/Q) is added to every instance of $\nabla_{\rm ad}$ in the MLT prescription, in order to determine the perturbed temperature gradient at a given convective energy flux (or vice versa). Physically, this amounts to asserting that the dimensionless temperature gradient in nonlinear convection tends not toward $\nabla_{\rm ad}$, as it would for efficient non-magnetised, non-rotating convection at sufficiently high Rayleigh number, but to $\nabla_{\rm ad} + \delta/Q$. We have not attempted to take into consideration other effects arising from the presence of a magnetic field (e.g., magnetic pressure). At each time step, the model evolves self-consistently using the perturbed structure. The criterion expressed in Equation (3.28) differs from that used in Mullan and MacDonald (2001) by a factor Q, which was adopted in MM14 onward to account for non-ideal thermodynamic behaviour.

Higher values of $B_{\rm v}$ inhibit convection, requiring a steeper temperature gradient to transport an equivalent heat flux; hence, increasing δ will increase the superadiabaticity of the stellar interior. The choice of radial profile for δ is, in these models, somewhat arbitrary. MM14 choose $\delta = \text{const}$ from the surface downward to some radius $r_{\rm max}$, where $B_{\rm v}$ reaches its critical strength $B_{\text{v-max}}$; thus, δ rapidly decreases with depth for $r < r_{\rm max}$.

Best-fit magneto-convection models performed by this reformulation of MLT are more sensitive to δ than to the chosen $B_{\text{v-max}}$. The range of vertical surface magnetic field strengths $B_{\text{v-surf}}$ in the models is not dictated by the large range of uncertainty in $B_{\text{v-max}}$, i.e., deep interior field strengths, but rather to the range of δ considered.

3.4.2 Radius Inflation: MM14 Models

We implement this magnetic inhibition of convection into MESA, producing "magnetic" $0.3\,M_\odot$, $\alpha_{\text{MLT}} = 1.7$ stellar models at both 10 Myr and 1 Gyr. For ease of comparison with prior work, we adopt the same strategy as MM14 by assuming δ is constant down to some radius r_{max} at which $B = B_{\text{v-max}}$; below this point, δ decreases rapidly in accord with the rising gas pressure. It must be noted at the outset that this assumption amounts to asserting that the magnetic pressure remains a constant fraction of the gas pressure at depths between the surface and r_{max}. In nonlinear 3D simulations of turbulent stellar dynamos, the field strength is typically not directly related to the gas pressure at any given depth, but is set by the dynamics of the convection coupled to rotation and shear (e.g., Dobler et al. 2006; Browning 2008; Yadav et al. 2016). But once this choice of δ profile is made, the model is specified fully by the choice of surface δ and by the value of $B_{\text{v-max}}$.

The total gas pressure increases rapidly with depth, so if no $B_{\text{v-max}}$ is specified, the magnetic field strengths implied by a $\delta = \text{const}$ profile would quickly become enormous. Some of the first studies along these lines, for example, allowed for fields of sufficient strength that the formation of a radiative core would result (e.g., Mullan and MacDonald 2001). Some later models adopted a maximum field strength of order 1 MG, (MacDonald and Mullan 2012; Mullan et al. 2015). Recently, Browning et al. (2016) suggested $B_{\text{v-max}} \sim 10^5$ G to be an extreme upper limit for the maximum field strengths found in these fully convective low-mass stars. They argue that, at a given magnetic field strength, large-scale field configurations are subject to the constraints of magnetic buoyancy instabilities, whilst Ohmic dissipation associated with small-scale field configurations was enough to exceed the stellar luminosity in some cases. Combining these constraints produced an upper limit on the maximum field strength of $B_{\text{v-max}} \leq 800$ kG, for models of particularly

simple magnetic field spatial structure. Additional, stronger constraints come again from 3D simulations of dynamo action in these objects. For example, Yadav et al. (2015) found $B_{\text{v-max}} \approx 14\,\text{kG}$ for a fully convective M dwarf with a rotation period of 20 days, and likewise the simulations of Browning (2008) found fields of order the equipartition strength (with the turbulent convective energy density). Broadly, we think models in which the field does not greatly exceed values of order 10^4 G are most realistic (as also studied recently, for example, by MacDonald and Mullan 2017b). Note that as $B_{\text{v-max}}$ approaches the value of the surface field, the profile assumed for δ becomes increasingly irrelevant; in that limit, the field strength throughout the interior is just the constant $B_{\text{v-max}} \approx B_{\text{surf}}$.

Motivated by these considerations, we test $B_{\text{v-max}} = 10^3 - 10^5$ G ($\Delta 1 \log_{10}(\text{G})$) at both ages. Note that we include 10^5 G for comparison with prior work and to demonstrate the utility of our mechanism even in the extreme field cases, even though we think, as noted above, that 10^4 G is a reasonable upper limit. We use $\delta = 0.01 - 0.03$ ($\Delta 0.005$) for our 10 Myr models, giving $B_{\text{v-surf}} \lesssim 0.3\,\text{kG}$. We use an extended range of $\delta = 0.01 - 0.06$ ($\Delta 0.005$) for our 1 Gyr models, to counteract the suppression of radius inflation in main-sequence models, producing $B_{\text{v-surf}} \lesssim 0.9\,\text{kG}$.

In Figure 3.8, we plot $\log_{10}(\nabla_{\text{s}})$ as a function of $\log_{10}(\rho)$ for $0.3\,M_\odot$, $\alpha_{\text{MLT}} = 1.7$ stellar models, for some combinations of $B_{\text{v-max}} = 10^3 - 10^5$ G, with $\delta = 0.01 - 0.03$ for 10 Myr models and $\delta = 0.04 - 0.06$ for 1 Gyr models, which we compare with the unperturbed model. In accord with Equation (3.28), $\nabla_{\text{s}} \simeq \nabla_{\text{s}_0} + \delta/Q_0$ at all depths. Changes in Q are negligible between models, hence we used the unperturbed value. In the bulk of the convection zone, where $B_{\text{v}} = B_{\text{v-max}}$, $\nabla_{\text{s}} \sim B^2_{\text{v-max}}/Q_0 \gamma P_{\text{gas}} \gg \nabla_{\text{s}_0}$, thus a factor of 10 increase in $B_{\text{v-max}}$ results in a factor of ~ 100 increase in superadiabaticity. As δ increases, ∇_{s} increases in the surface layers. The point at which ∇_s transitions—from a nearly constant value near the surface to a steeply declining profile in the interior—is mediated by the point at which the vertical surface magnetic field (here set by δ) reaches $B_{\text{v-max}}$, because interior to that point the gas pressure begins to exceed the magnetic pressure by an increasingly large amount.

In Figure 3.9, we plot s as a function of $\log_{10}(\rho)$ for the same stellar models. At fixed

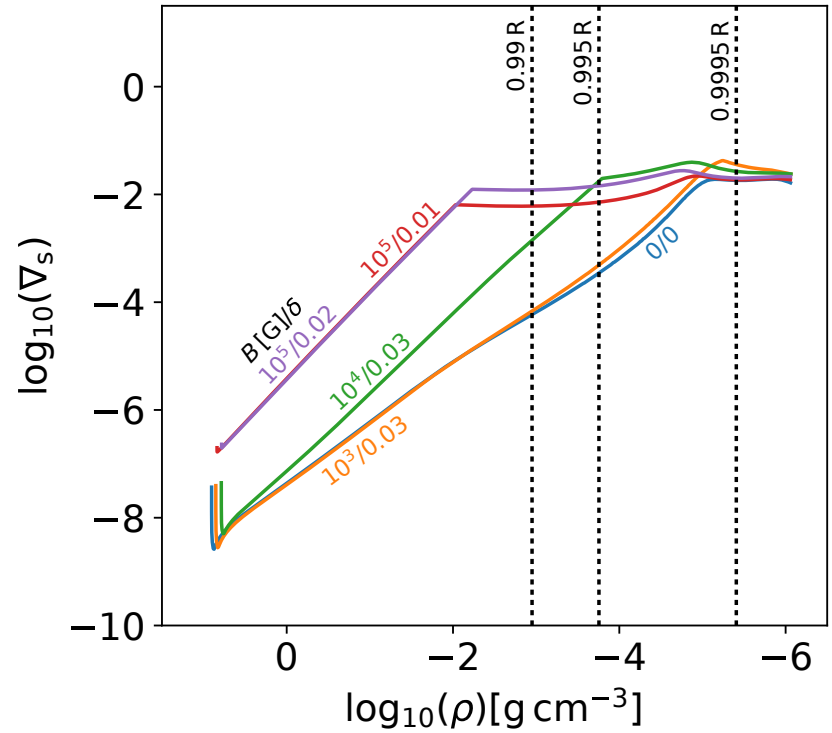

(a)

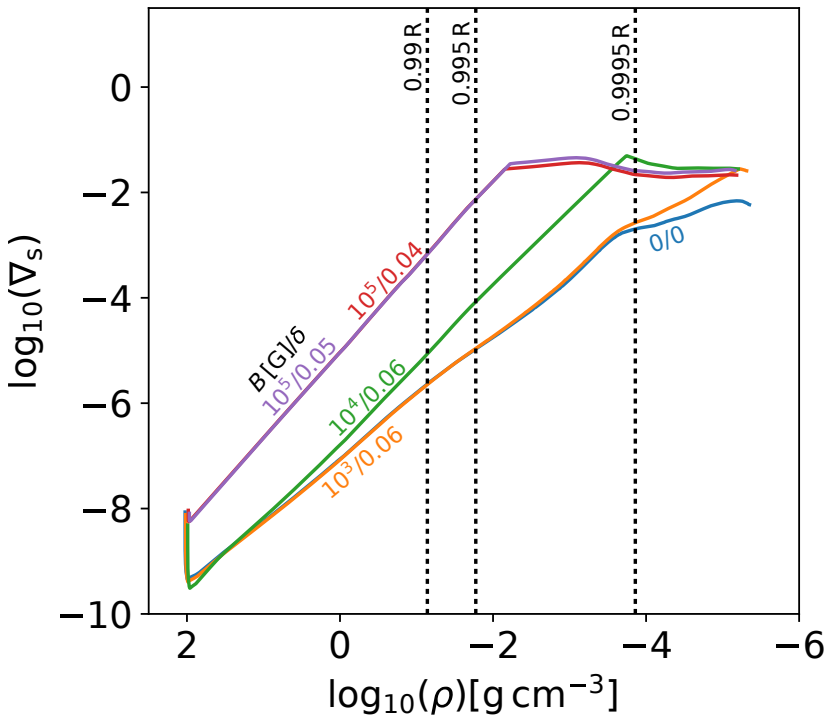

(b)

Figure 3.8: $\log_{10}(\nabla_s)$ as a function of $\log_{10}(\rho)$, for $0.3\,M_\odot$, (a) 10 Myr or (b) 1 Gyr, $\alpha_{\rm MLT} = 1.7$ stellar models at some combinations of $B_{\text{v-max}} = 10^3 - 10^5$ G and (a) $\delta = 0.01 - 0.03$ or (b) $\delta = 0.04 - 0.06$, including the unperturbed model. Increasing δ noticeably increases ∇_s where $B_v < B_{\text{v-max}}$, and increasing $B_{\text{v-max}}$ increases the depth at which δ noticeably increases ∇_s.

δ, the photospheric entropy $s_{\rm ph}$ decreases monotonically with increasing $B_{\text{v-max}}$; likewise at fixed $B_{\text{v-max}}$, increasing δ decreases $s_{\rm ph}$. In turn, $s_{\rm ad}$ is shown to increase strongly with δ, and to a lesser extent $B_{\text{v-max}}$. Pre-main-sequence stars with lower $s_{\rm ph}$ have higher $s_{\rm ad}$ for the reasons discussed in Section 3.2; hence, stars with higher $B_{\text{v-max}}$ and δ tend to have a higher $s_{\rm ad}$. On the main sequence, variations in $s_{\rm ad}$ are smaller, due to the self-regulation of the star through nuclear fusion. However, the differences in $s_{\rm ph}$ induced by changes in δ or $B_{\text{v-max}}$ are larger than in our fixed-$\alpha_{\rm MLT}$ models. A larger entropy contrast, as a result of higher superadiabaticity in the surface layers, produces small but noticeable changes in $s_{\rm ad}$. As in Sections 3.2 and 3.3, stellar structure is largely insensitive to the increasing $\nabla_{\rm s}$ in the deep interior; it responds more readily to an increased $\nabla_{\rm s}$ in the surface layers.

In Figure 3.10, we examine radius inflation calculated via $\Delta s_{\rm ad}$ (Equation (3.18)) as a function of the outputted radius inflation, showing good agreement for these MM14 models. For $\delta = 0.01 - 0.03$ models, we find $\Delta R/R_0 \lesssim 13\%$ ($R \lesssim 0.771\,R_\odot$) for our range of perturbed models at 10 Myr, and $\Delta R/R_0 \lesssim 2\%$ ($R \lesssim 0.292\,R_\odot$) at 1 Gyr. For $\delta = 0.04 - 0.06$ models at 1 Gyr, we find $\Delta R/R_0 \lesssim 6\%$ ($R \lesssim 0.302\,R_\odot$). Overall, we find greater changes in $s_{\rm ph}$ in these models than in the fixed-$\alpha_{\rm MLT}$ main-sequence models in Section 3.2.2, which is enough to slightly perturb $s_{\rm ad}$ from the value predominantly determined via nuclear fusion, producing small, yet noticeable, radius inflation. There is a slight divergence for our most-inhibited fully convective models, due to the increasing effective depth of the magnetic inhibition of convection. For those models, the asymptotic increase toward $s_{\rm ad}$ is reached at ever-increasing depth, thus our approximation $S_{\rm tot} \simeq s_{\rm ad} M$ becomes increasingly less accurate. Therefore, with increasing levels of radius inflation, the accuracy of using $s_{\rm ad}$ alone to determine the stellar radius decreases.

3.5 Combined Inhibition of Convection by Rotation and Magnetism

Both the S79 rotational and MM14 magnetic reformulations of MLT modify the superadiabaticity of a model. In the "magnetic" case, the superadiabaticity in the surface layers is noticeably increased between 0.99 and 0.995 R, and slightly increased from 0.995 R up to

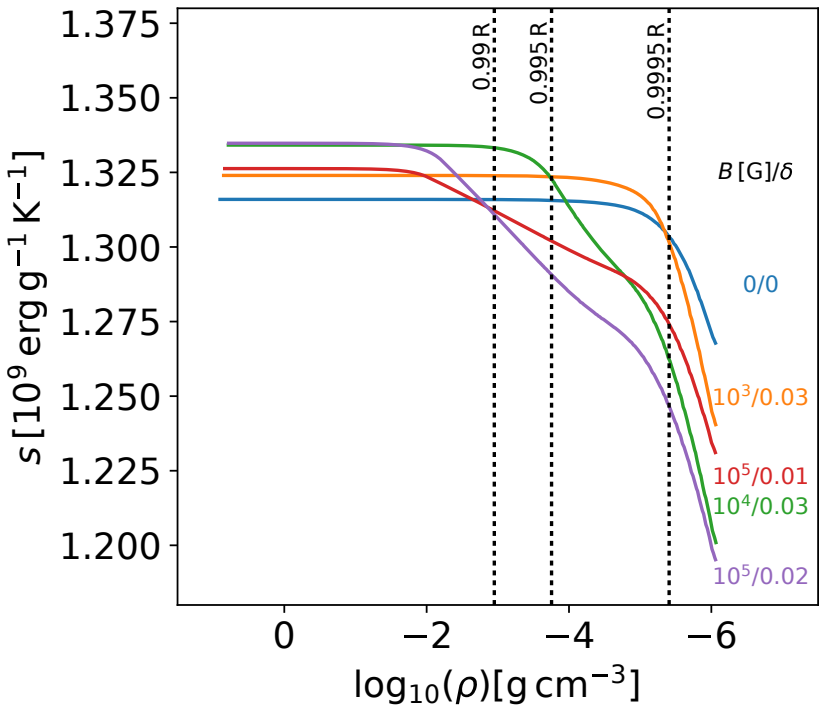

(a)

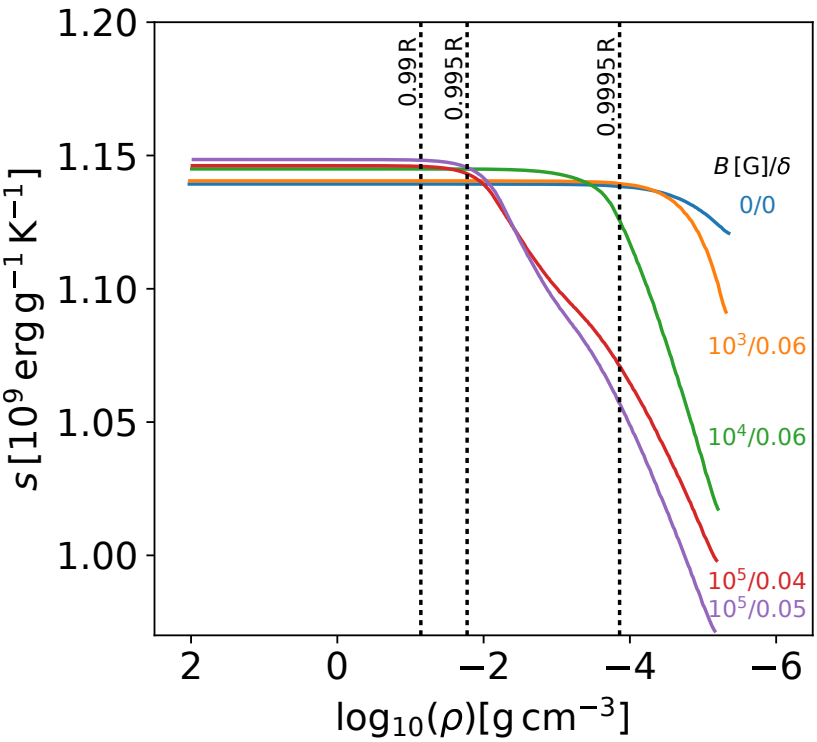

(b)

Figure 3.9: s as a function of $\log_{10}(\rho)$, for $0.3\,M_\odot$, (a) 10 Myr or (b) 1 Gyr, $\alpha_{\mathrm{MLT}} = 1.7$ stellar models at some combinations of $B_{\text{v-max}} = 10^3 - 10^5$ G and (a) $\delta = 0.01 - 0.03$ or (b) $\delta = 0.04 - 0.06$, including the unperturbed model.

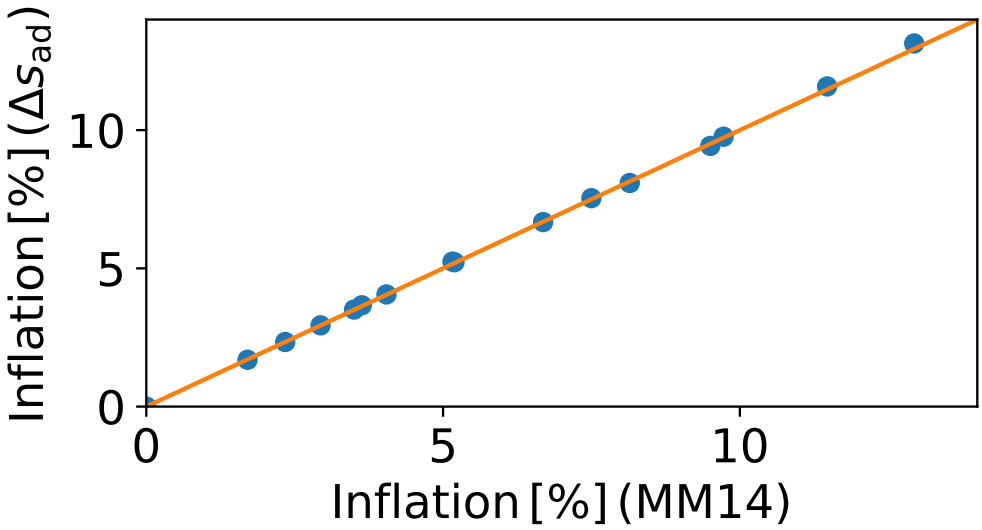

(a)

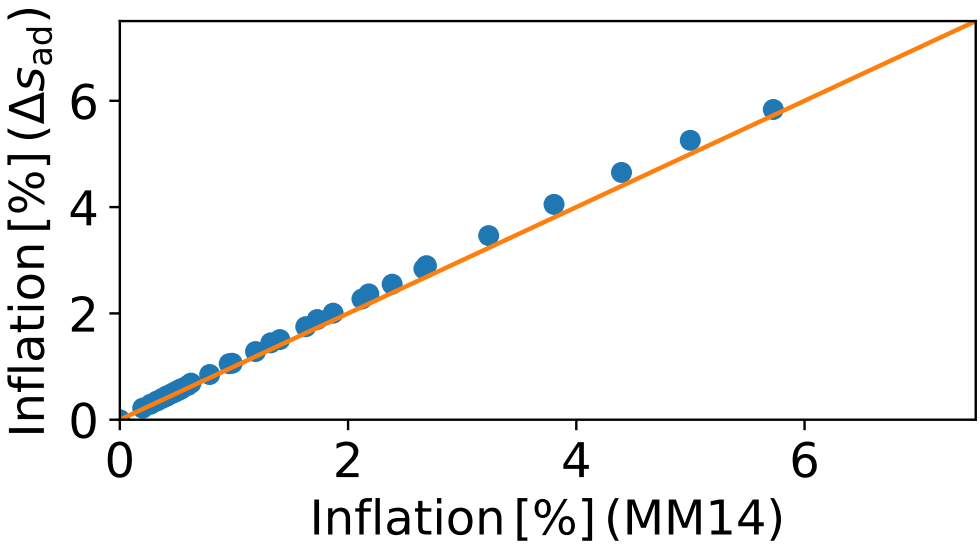

(b)

Figure 3.10: Radius inflation determined from $\Delta s_{\rm ad}$ via Equation (3.18) as a function of the outputted radius inflation from the MM14 models for $0.3\,M_\odot$, (a) 10 Myr or (b) 1 Gyr, $\alpha_{\rm MLT} = 1.7$ stellar models at all combinations of $B_{\text{v-max}} = 10^3 - 10^5$ G ($\Delta 1\ \log_{10}(\text{G})$) and (a) $\delta = 0.01 - 0.03$ ($\Delta 0.005$) or (b) $\delta = 0.01 - 0.06$ ($\Delta 0.005$). $y = x$ (orange) is plotted for ease of comparison.

the photosphere (see Figure 3.8). In the "rotating" case, there is a small difference in $\nabla_{\rm s}$ in the 0.99-0.995 R region, but negligible difference after this point up toward the photosphere (see Figure 3.7). Here, we briefly examine whether the *combination* of rotation and magnetism using these prescriptions could increase the radius of a model even further. To do so, we first modify the criterion for convection using the MM14 formulation, as in Section 3.4; the resulting model is then used as the "unperturbed" model for an application of the rotational formulation described in Section 3.3. Hence, the enhanced superadiabaticity near the surface in the magnetic models may be further increased by the rotation, with possible impacts on the structure. Of course, this is a very crude approximation; as noted in Section 3.1, the combined effects of rotation and magnetism may be considerably more complex than either simply rotation or magnetism acting alone, and these effects may not be additive (and indeed, in the case of the linear onset of convection, are not). Nonetheless we adopt it here as a first attempt at the problem.

In Figure 3.11, we plot $\log_{10}(\nabla_{\rm s})$ as a function of $\log_{10}(\rho)$, comparing a "magnetic rotating" $0.3\,M_\odot$, $\alpha_{\rm MLT} = 1.7$ stellar model at $\Omega = 20\,\Omega_\odot$, $B_{\text{v-max}} = 10^4\,$G, with $\delta = 0.03$ for 10 Myr and $\delta = 0.06$ for 1 Gyr, compared with the rotating-only case, the magnetic-only case, and the unperturbed model. We choose the most-perturbed model at each age to be $10^4\,$G in order to investigate the highest possible radius inflation attained by the addition of "rotational" effects at what we think is a realistic maximum field strength. At both ages, the superadiabaticity of our "magnetic rotating" model is higher than in the magnetic-only case by orders of magnitude within the deep convection zone, where convective velocities are low (i.e. Ro $\ll 1$). Closer to the surface, this difference diminishes (because Ro increases there).

We plot s as a function of $\log_{10}(\rho)$ in Figure 3.12 for our 10 Myr model. These changes in superadiabaticity are enough to produce a small change in $s_{\rm ad}$ for our pre-MS model. As a result of this, our 10 Myr "magnetic rotating" model is inflated by a further 1% compared to the magnetic-only case, giving $\Delta R/R_0 \simeq 10.5\%$ ($R \simeq 0.755\,R_\odot$). However, for our 1 Gyr model, there is negligible inflation, as the superadiabaticity is much lower throughout the surface layers compared to the pre-MS model, giving negligible changes in $s_{\rm ad}$. These results suggest that the combination of rotation and magnetism may indeed

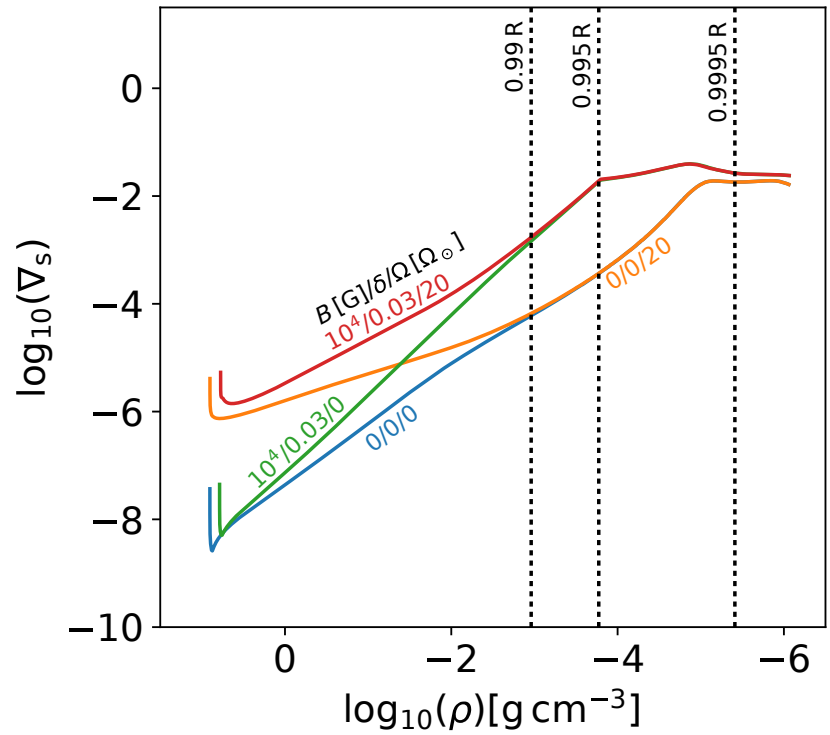

(a)

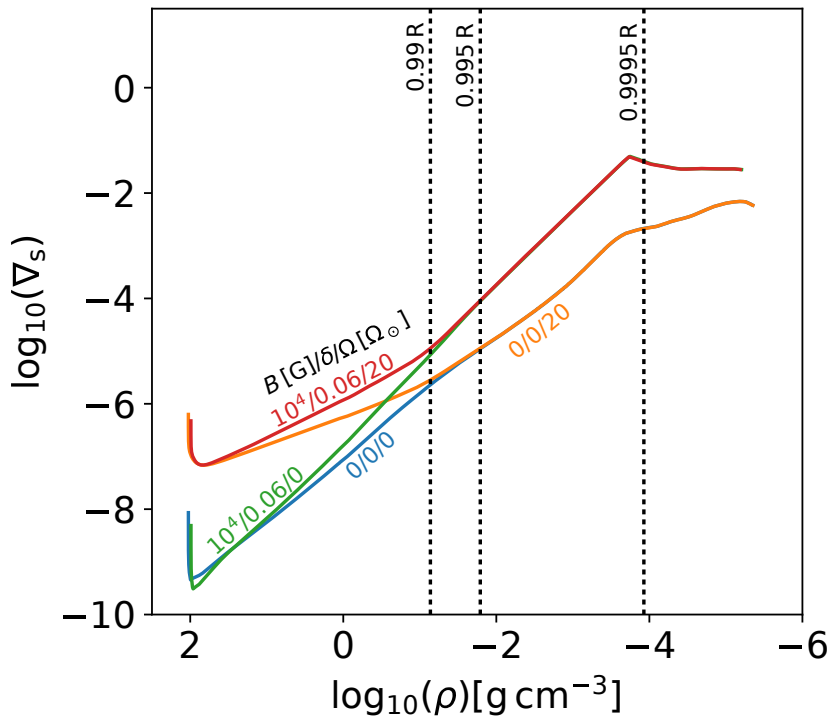

(b)

Figure 3.11: $\log_{10}(\nabla_s)$ as a function of $\log_{10}(\rho)$, for a $0.3\,M_\odot$, (a) 10 Myr or (b) 1 Gyr, $\alpha_{\rm MLT} = 1.7$ stellar model at $\Omega = 20\,\Omega_\odot$, $B_{\text{v-max}} = 10^4$ G and (a) $\delta = 0.03$ or (b) $\delta = 0.06$, including the rotating-only, magnetic-only, and unperturbed models.

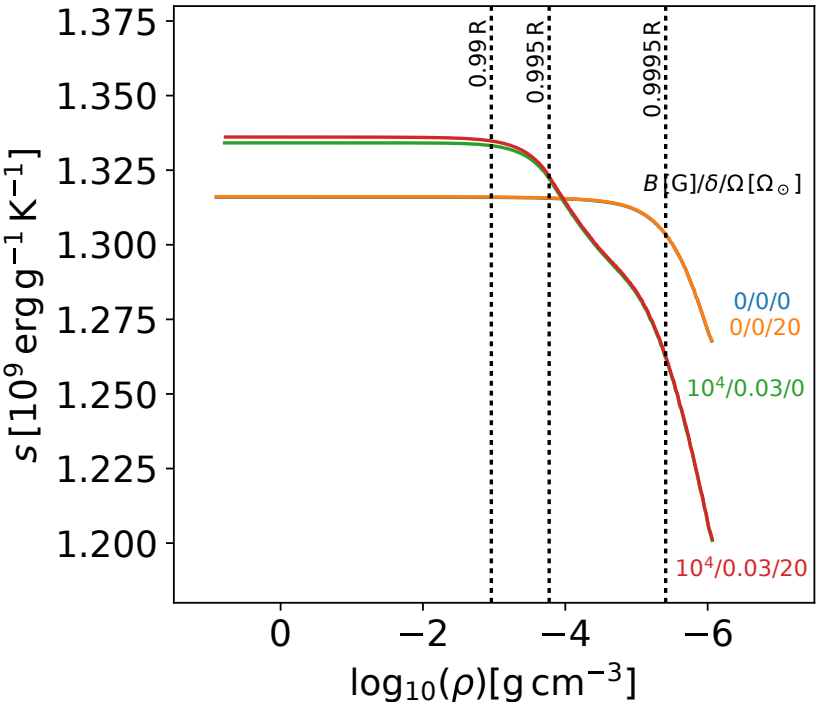

Figure 3.12: s as a function of $\log_{10}(\rho)$, for a $0.3\,M_\odot$, 10 Myr, $\alpha_{\rm MLT} = 1.7$ stellar model at $\Omega = 20\,\Omega_\odot$, $B_{\text{v-max}} = 10^4$ G, and $\delta = 0.03$, including the rotating-only, magnetic-only, and unperturbed models. The rotating-only case is near-identical to the unperturbed model.

further inflate the stellar radius, but the additional effect arising from rotation is only noticeable in the youngest models.

3.6 Depth-dependent $\alpha_{\rm MLT}$ as MLT Proxies for Rotation and Magnetic Fields

The structure of a 1D stellar model constructed with a modified version of MLT, like the rotationally or magnetically constrained versions described in Sections 3.3 and 3.4, cannot generally be duplicated by a model with a standard depth-independent $\alpha_{\rm MLT}$. The reason for this is straightforward: in the standard 1D models, $\nabla_{\rm s}$ throughout the stellar interior increases with decreasing $\alpha_{\rm MLT}$, whereas for the S79 and MM14 models, the inhibition of convection depends on parameters that vary with depth, i.e., Ro in the "rotating" case and δ in the "magnetic" case. It is not possible to mimic these effects with a standard depth-independent $\alpha_{\rm MLT}$, no matter its value. They can, however, be captured by models that include a depth-*dependent* $\alpha_{\rm MLT}$ ($\alpha_{\rm MLT}(r)$, hereafter), as described in this section.

Here, we provide explicit formulae linking a $\alpha_{\rm MLT}(r)$ profile to the rotationally and magnetically inhibited convection formulae of S79 and MM14 respectively. Our motivation for constructing such profiles is just that, in a given 1D stellar evolution code, it may be much more straightforward to input (or implement) an $\alpha_{\rm MLT}(r)$ profile than to modify the whole underlying MLT formulation. Knowledge of the precise correspondence between $\alpha_{\rm MLT}(r)$ and a particular depth-dependent theory of convective inhibition, arising from rotation, magnetism, or other effects, gives us the ability to model the non-standard 1D stellar structures arising from these effects without undue difficulty.

Models constructed with modified MLT formulations of the type and magnitude considered here can be regarded as perturbations at each depth to a fiducial unperturbed model. We write the perturbed model's $\nabla_{\rm s}$ as the unperturbed model's plus a given depth-dependent perturbation β:

$$\nabla_{\rm s} = \nabla_{\rm s_0} + \beta. \tag{3.30}$$

Thus any perturbation made to the superadiabaticity results in the modification of $ds/dr \propto \nabla_{\rm s}$, implying that the specific entropy will asymptotically converge to a different adiabat.

In Section 3.2.1, we found that a perturbed model's $\nabla_{\rm s}$ could be reproduced using the unperturbed model's and each model's $\alpha_{\rm MLT}$, i.e., Equation (3.7). By substituting Equation (3.7) into Equation (3.30), we find an approximate expression for $\alpha_{\rm MLT}(r)$ as a function of the unperturbed model's depth-*independent* $\alpha_{\rm MLT}$ and $\nabla_{\rm s}$, and the perturbation β:

$$\alpha_{\rm MLT}(r) \simeq \frac{\alpha_{\rm MLT_0}}{\left(1 + \frac{\beta}{\nabla_{\rm s_0}}\right)^{3/4}}. \tag{3.31}$$

We find that a $\alpha_{\rm MLT}(r)$ profile constructed using this expression allows us to reproduce virtually all of the radial variation of $\nabla_{\rm s}$ in both our 10 Myr and 1 Gyr non-standard "rotating" and "magnetic" stellar structure models. First, consider the case of the S79 "rotating" MLT formulation. We express Equation (3.25) in terms of $\alpha_{\rm MLT}(r)$ and the

unperturbed depth-independent $\alpha_{\rm MLT}$ using Equation (3.6):

$$\left(\frac{\alpha_{\rm MLT}(r)}{\alpha_{\rm MLT_0}}\right)^{-10/3} - \left(\frac{\alpha_{\rm MLT}(r)}{\alpha_{\rm MLT_0}}\right)^{-4/3} \simeq \frac{4}{41}\tau_{\rm c_0}^2\Omega^2. \tag{3.32}$$

Therefore, in the case of the S79 models, the depth-dependent perturbation can be expressed as

$$\beta \simeq \nabla_{\rm s_0}\left[\left(\frac{\alpha_{\rm MLT}(r)}{\alpha_{\rm MLT_0}}\right)^{-10/3} - \frac{4}{41}\tau_{\rm c_0}^2\Omega^2 - 1\right], \tag{3.33}$$

giving

$$\alpha_{\rm MLT}(r) \simeq \frac{\alpha_{\rm MLT_0}}{\left[\left(\frac{\alpha_{\rm MLT}(r)}{\alpha_{\rm MLT_0}}\right)^{-10/3} - \frac{4}{41}\tau_{\rm c_0}^2\Omega^2\right]^{3/4}}, \tag{3.34}$$

which must be solved iteratively.

We can mimic the "rotating" effects from the S79 MLT formulation in our 1D stellar structure models, solely using this $\alpha_{\rm MLT}(r)$ profile. We modify MESA to input $\alpha_{\rm MLT}(r)$ rather than the conventional fixed value and produce near-identical models to those produced using the S79 reformulation where we modified $\nabla_{\rm s}$. To demonstrate this, in Figure 3.13, we plot $\log_{10}(\nabla_{\rm s})$ as a function of $\log_{10}(\rho)$ for both our $\alpha_{\rm MLT}(r)$ and S79 stellar models, at 10 Myr and 1 Gyr; models constructed using the two techniques are indistinguishable here.

We can apply the same technique to mimic the effects of "magnetic" inhibition of convection via $\alpha_{\rm MLT}(r)$. In the case of the MM14 MLT formulation in the high efficiency convective regime, $\beta \simeq \delta/Q_0$, thus

$$\alpha_{\rm MLT}(r) \simeq \frac{\alpha_{\rm MLT_0}}{\left(1 + \frac{\delta}{Q_0\nabla_{\rm s_0}}\right)^{3/4}}. \tag{3.35}$$

We again input $\alpha_{\rm MLT}(r)$ into MESA and reproduce near-identical models to those produced using the MM14 reformulation. In Figures 3.14 and 3.15, we plot examples of $\log_{10}(\nabla_{\rm s})$ and s respectively as a function of $\log_{10}(\rho)$, produced by our $\alpha_{\rm MLT}(r)$ models and our MM14 models; excellent correspondence between the two model structures is

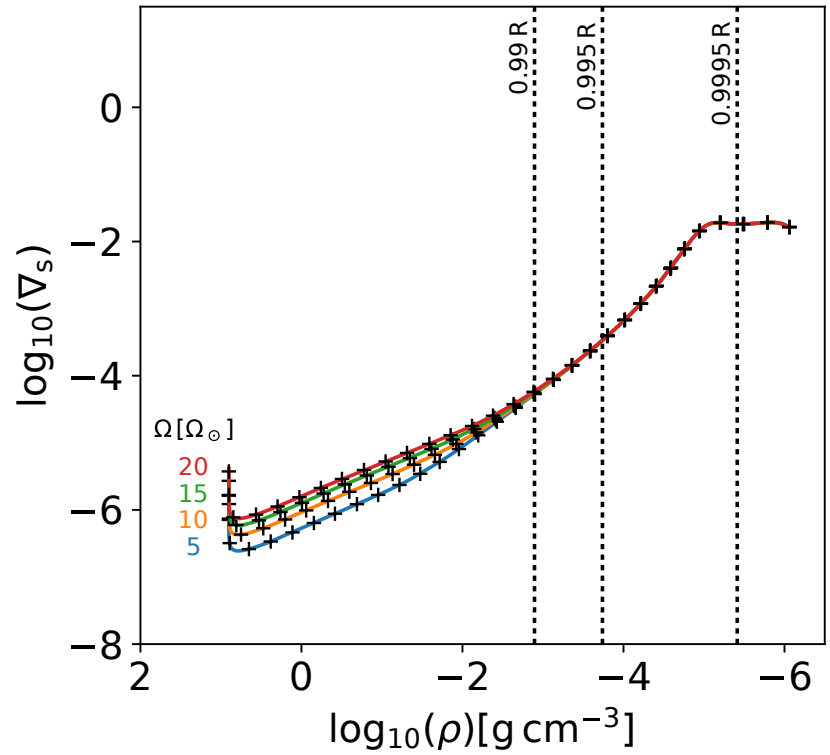

(a)

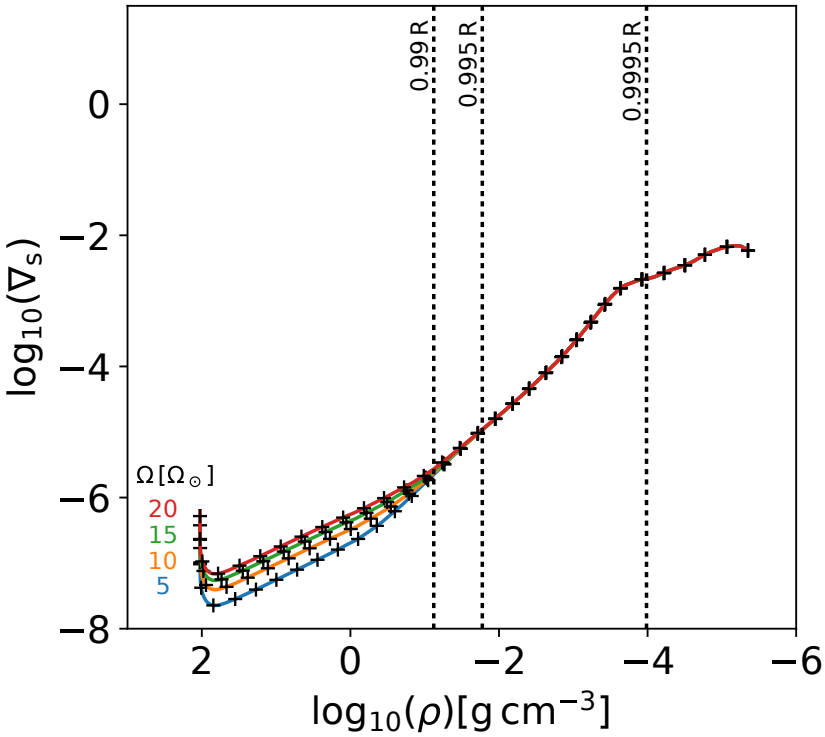

(b)

Figure 3.13: $\log_{10}(\nabla_s)$ as a function of $\log_{10}(\rho)$, comparing S79 "rotating" models and our $\alpha_{\rm MLT}(r)$ models (plus markers), for $0.3\,M_\odot$, (a) 10 Myr or (b) 1 Gyr, $\alpha_{\rm MLT} = 1.7$ stellar models at $\Omega = 5 - 20\,\Omega_\odot$ ($\Delta 5\,\Omega_\odot$).

evident.

In Figure 3.16, we examine radius inflation from our $\alpha_{\rm MLT}(r)$ models as a function of the radius inflation from our MM14 "magnetic" models, at both 10 Myr and 1 Gyr. They are in good agreement, with small divergences for our most-inhibited fully convective models, as in Section 3.4.2. As with the models discussed in Sections 3.3 and 3.4, this agreement is not just fortuitous: it stems from the fact that changes in the radii are linked to changes in $s_{\rm ad}$, which are well-described by our $\alpha_{\rm MLT}(r)$ profiles.

We also create an $\alpha_{\rm MLT}(r)$ expression for the combination of the magnetic and rotational reformulations of MLT (see Section 3.5), by treating $\alpha_{\rm MLT_0}$ in Equation (3.34) as the $\alpha_{\rm MLT}(r)$ profile for the magnetic prescription in Equation (3.35), which we will denote as $\alpha_{\rm MLT}(r)_B$, producing

$$\alpha_{\rm MLT}(r) \simeq \frac{\alpha_{\rm MLT}(r)_B}{\left[\left(\frac{\alpha_{\rm MLT}(r)}{\alpha_{\rm MLT}(r)_B}\right)^{-10/3} - \frac{4}{41}\tau_{\rm c_0}^2\Omega^2\right]^{3/4}}, \tag{3.36}$$

which must also be solved iteratively. In Figures 3.17 and 3.18, we plot $\log_{10}(\nabla_{\rm s})$ for both ages and s for 10 Myr respectively as a function of $\log_{10}(\rho)$, produced by a particular "rotating magnetic" model from Section 3.5 and our $\alpha_{\rm MLT}(r)$ model, including profiles from the equivalent rotating-only and magnetic-only cases; again, we see excellent correspondence between the two model structures.

In Figure 3.19, we plot $\alpha_{\rm MLT}(r)$ as a function of $\log_{10}(\rho)$ at both ages for the same model, to show the differences in the depth dependence of $\alpha_{\rm MLT}(r)$ for the rotating-only and magnetic-only cases. For the rotating-only case, $\alpha_{\rm MLT}(r)$ is constant and close to the unperturbed model value ($\alpha_{\rm MLT} = 1.7$) across a majority of the surface layers (implying negligible changes in stellar structure), and drops rapidly with depth in the deep interior where Ro $\ll 1$. For the magnetic-only case, $\alpha_{\rm MLT}(r)$ starts at a lower value at the photosphere, and drops sharply with depth in the surface layers (producing noticeable changes in stellar structure), rising again in the deep interior where δ drops rapidly.

In Section 3.2.2, we showed that it is possible to determine an explicit relation

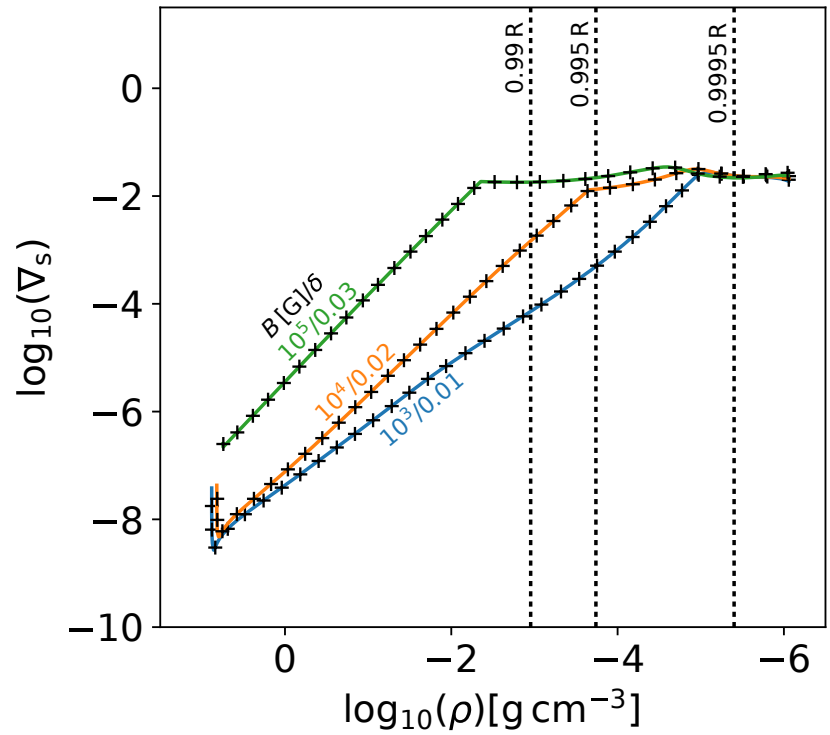

(a)

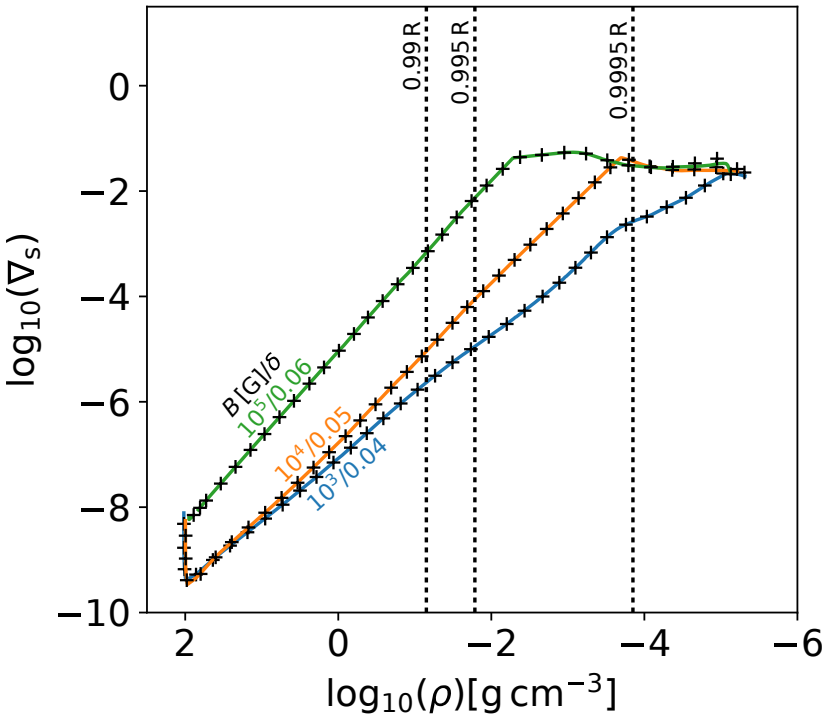

(b)

Figure 3.14: $\log_{10}(\nabla_s)$ as a function of $\log_{10}(\rho)$, comparing MM14 "magnetic" models and our $\alpha_{\rm MLT}(r)$ models (plus markers), for $0.3\,M_\odot$, (a) 10 Myr or (b) 1 Gyr, $\alpha_{\rm MLT} = 1.7$ stellar models at some combinations of $B_{\rm v\text{-}max} = 10^3 - 10^5$ G and (a) $\delta = 0.01 - 0.03$ or (b) $\delta = 0.04 - 0.06$.

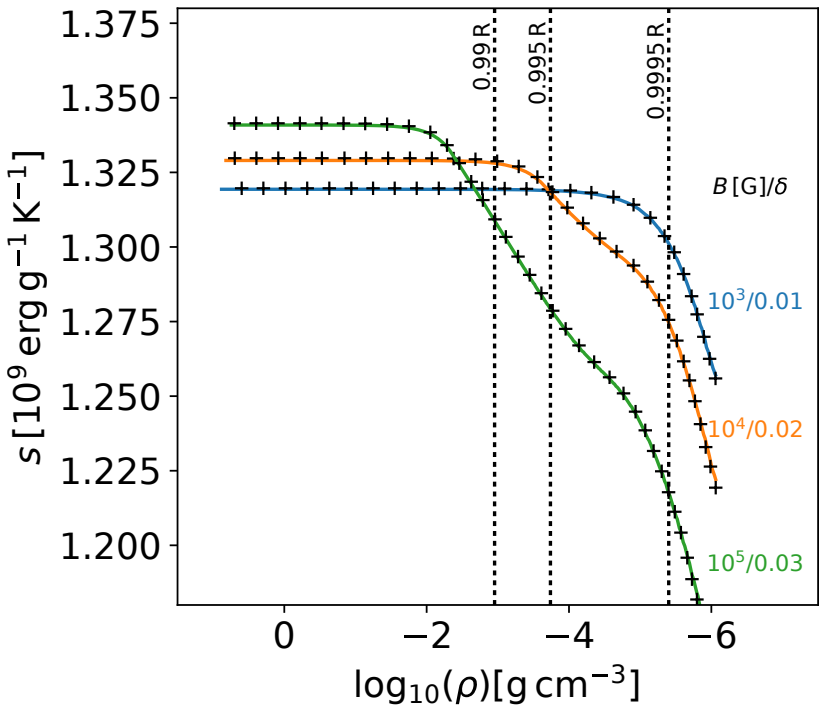

(a)

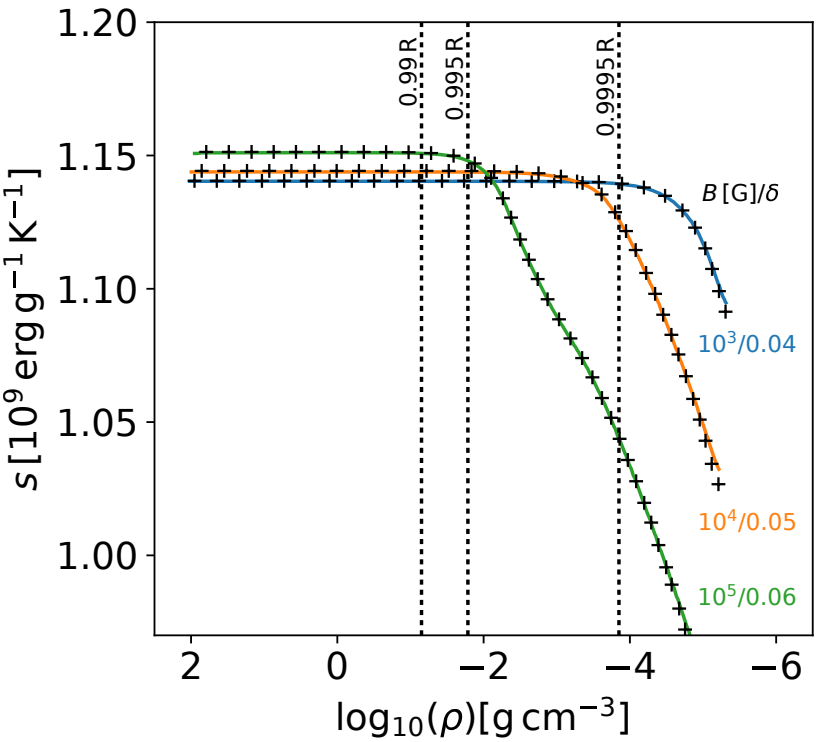

(b)

Figure 3.15: s as a function of $\log_{10}(\rho)$, comparing MM14 "magnetic" models and our $\alpha_{\rm MLT}(r)$ models (plus markers), for $0.3\,M_\odot$, (a) 10 Myr or (b) 1 Gyr, $\alpha_{\rm MLT} = 1.7$ stellar models at some combinations of $B_{\text{v-max}} = 10^3 - 10^5$ G and (a) $\delta = 0.01 - 0.03$ or (b) $\delta = 0.04 - 0.06$.

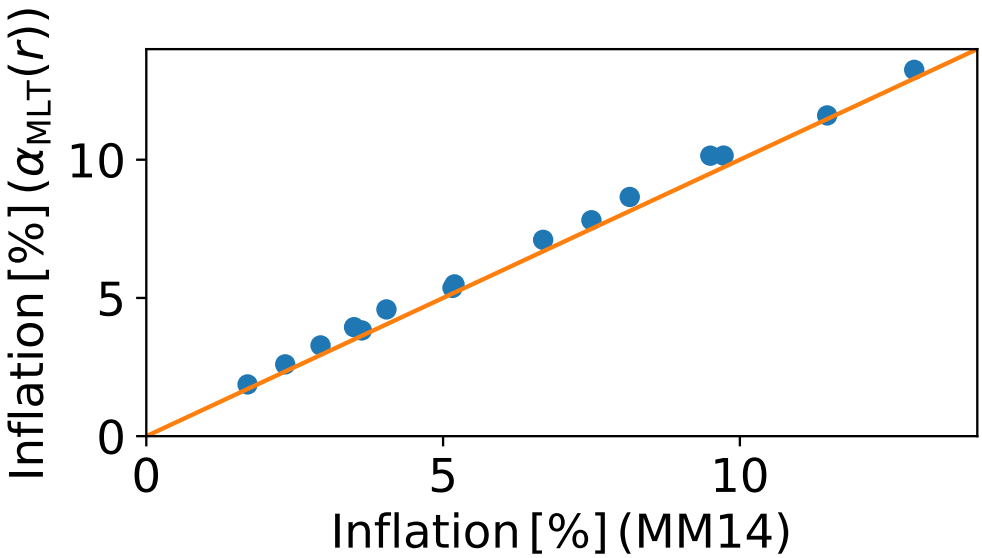

(a)

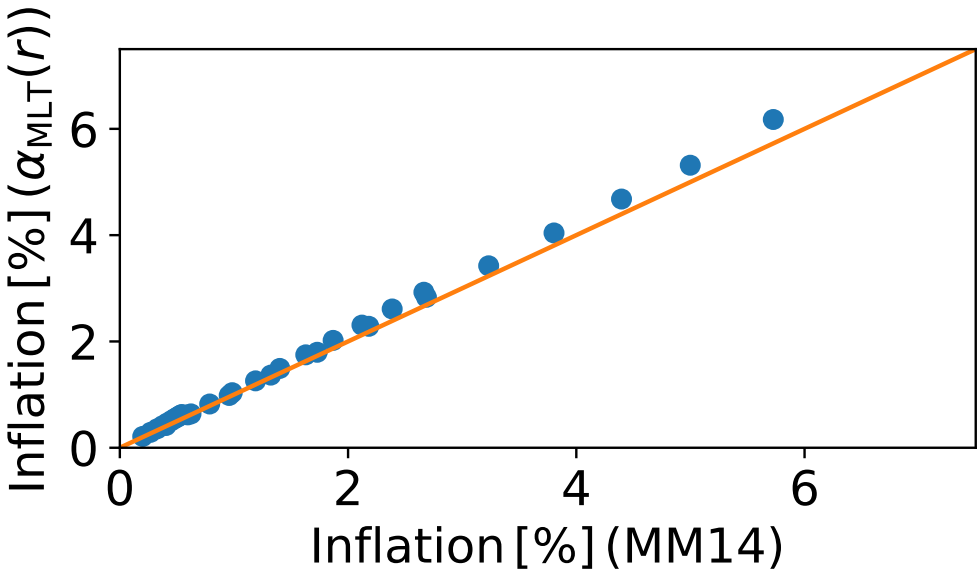

(b)

Figure 3.16: Radius inflation from our $\alpha_{\mathrm{MLT}}(r)$ models as a function of radius inflation from our MM14 models, for $0.3\,M_{\odot}$, (a) 10 Myr or (b) 1 Gyr, $\alpha_{\mathrm{MLT}} = 1.7$ stellar models at all combinations of $B_{\text{v-max}} = 10^3 - 10^5$ G ($\Delta 1 \log_{10}(\mathrm{G})$) and (a) $\delta = 0.01 - 0.03$ ($\Delta 0.005$) or (b) $\delta = 0.01 - 0.06$ ($\Delta 0.005$). $y = x$ (orange) is plotted for ease of comparison.

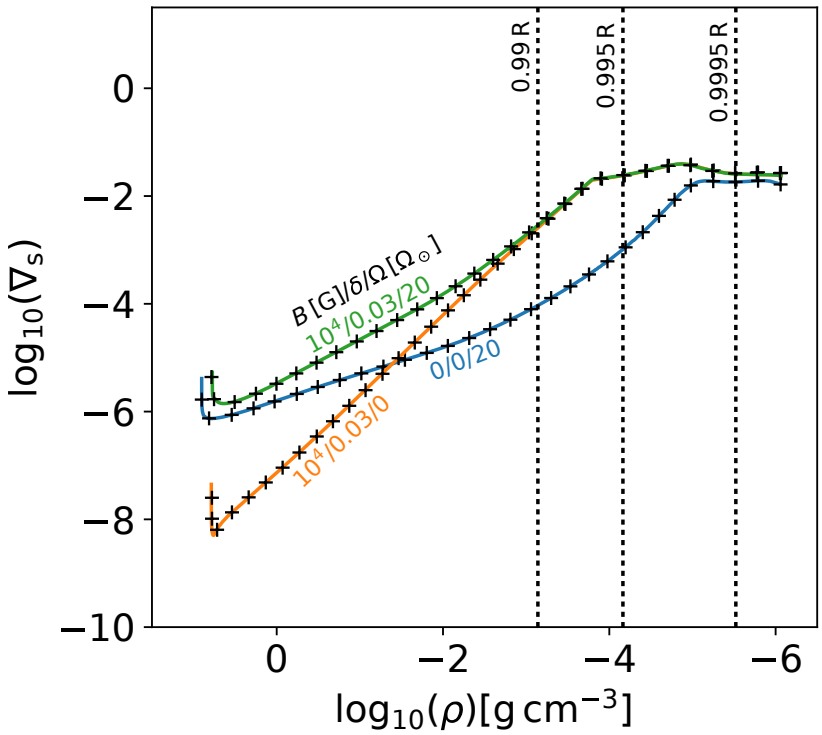

(a)

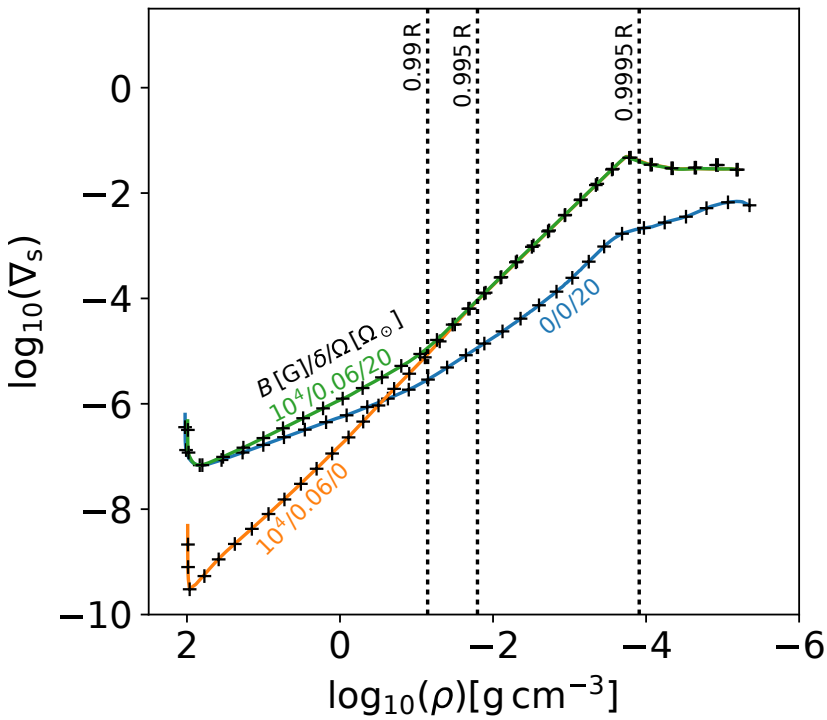

(b)

Figure 3.17: $\log_{10}(\nabla_s)$ as a function of $\log_{10}(\rho)$, comparing our $0.3\,M_\odot$, (a) 10 Myr or (b) 1 Gyr, $\alpha_{\rm MLT} = 1.7$ stellar model at $\Omega = 20\,\Omega_\odot$, $B_{\text{v-max}} = 10^4$ G, and (a) $\delta = 0.03$ or (b) $\delta = 0.06$, to our $\alpha_{\rm MLT}(r)$ model (plus markers). We include the rotating-only and magnetic-only cases for further comparison.

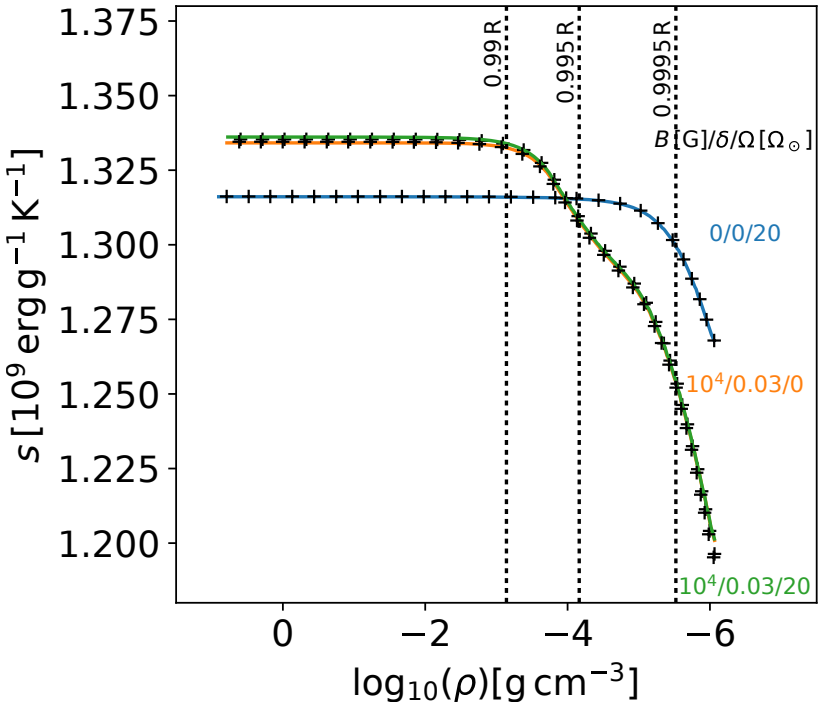

Figure 3.18: s as a function of $\log_{10}(\rho)$, comparing our $0.3\,M_\odot$, 10 Myr, $\alpha_{\rm MLT} = 1.7$ stellar model at $\Omega = 20\,\Omega_\odot$, $B_{\text{v-max}} = 10^4$ G, and $\delta = 0.03$, to our $\alpha_{\rm MLT}(r)$ model (plus markers). We include the rotating-only and magnetic-only cases for further comparison.

between $s_{\rm ad}$ and the depth-*independent* $\alpha_{\rm MLT}$ in standard 1D models. If this were possible in the depth-*dependent* case as well, it would allow us to provide analytical estimates of how $s_{\rm ad}$, and hence (via the formulae of Section 3.2.2) the overall stellar radius, responds to changes in the depth-dependent convective inhibition parameters in any given theory (e.g., δ in the MM14 formulation). Unfortunately, although we find that $s_{\rm ad} \propto \Delta s$ in all of our $\alpha_{\rm MLT}(r)$ models, it is no longer feasible to provide a simple analytical formula encapsulating the link between $s_{\rm ad}$ and $\alpha_{\rm MLT}(r)$. Essentially, this arises because we can no longer exclude $\alpha_{\rm MLT}(r)$ from the integral producing Δs in Equation (3.12): in the fixed-$\alpha_{\rm MLT}$ case for models with similar convective flux profiles, the integral associated with the high efficiency regime (excluding $\alpha_{\rm MLT}$ due to its depth independence) is near homologous between models, allowing a direct proportionality between Δs and $\alpha_{\rm MLT}$ (Equation (3.13)). However, in the $\alpha_{\rm MLT}(r)$ case, this is not possible as the integral is now weighted by $\alpha_{\rm MLT}(r)$ throughout the radial distribution; hence, in order to determine a change in $s_{\rm ad}$ between two models of differing $\alpha_{\rm MLT}(r)$, one must also have knowledge of all parameters in Equation (3.12) for the perturbed model, rather than just $\alpha_{\rm MLT}(r)$ and details of the unperturbed model.

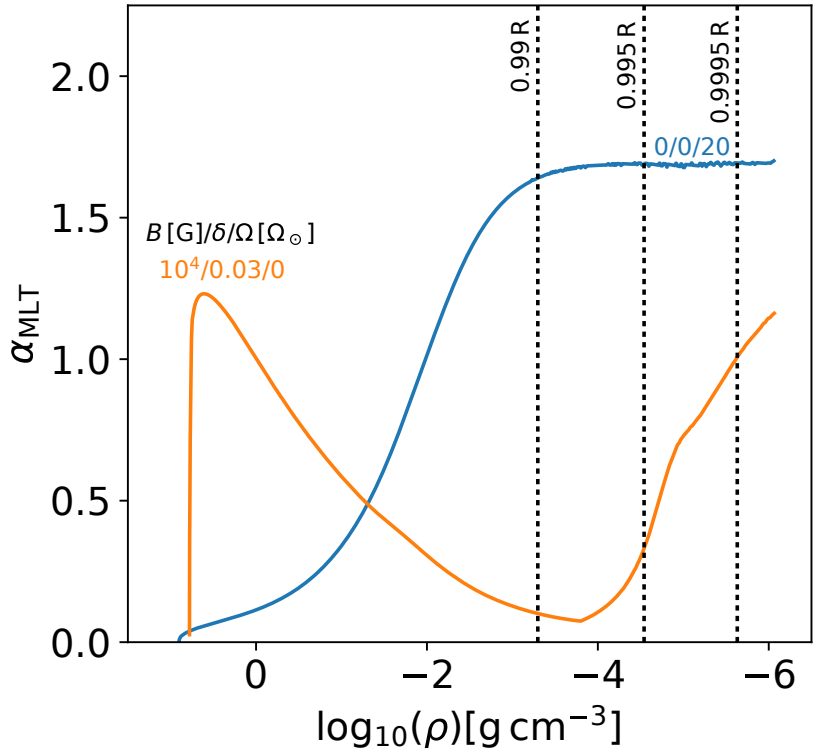

(a)

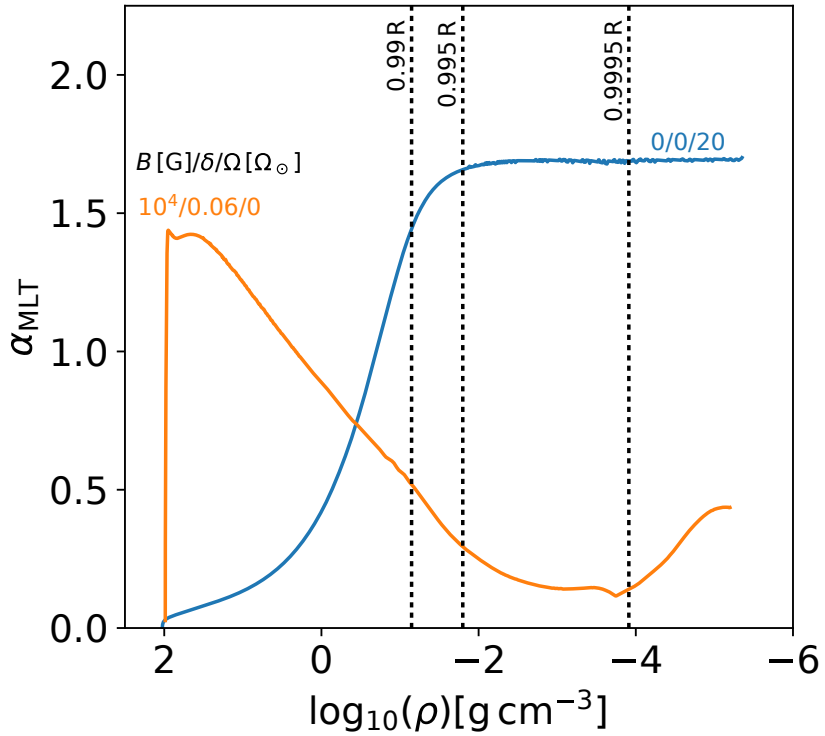

(b)

Figure 3.19: $\alpha_{\rm MLT}(r)$ as a function of $\log_{10}(\rho)$, for a $0.3\,M_\odot$, (a) 10 Myr or (b) 1 Gyr, $\alpha_{\rm MLT} = 1.7$ stellar model in the rotating-only case ($\Omega = 20\,\Omega_\odot$), and the magnetic-only case ($B_{\text{v-max}} = 10^4$ G, and (a) $\delta = 0.03$ or (b) $\delta = 0.06$).

3.7 Discussion and Conclusion

Rotation and magnetism both affect convection: the velocities, temperature gradients, and spatial structure that prevail in a magnetised, rotating flow are not generally the same as those that occur when rotation and magnetic fields are absent. In principle, the resulting changes in convective heat transport could affect the structure of stars or planets that host convection. Motivated by the observation that some low-mass stars appear to have larger radii than predicted by standard 1D stellar models, which parameterise the convective transport using MLT, several authors have suggested that rotation and/or magnetism may indeed be influencing the overall stellar structure. In this chapter, we have examined this issue using 1D stellar models that attempt to incorporate both rotational and magnetic effects in a highly simplified way, and compared our results to models constructed using a standard version of MLT (modified here to allow for a mixing length parameter $\alpha_{\rm MLT}$ that in some cases varies with depth). Below, we recapitulate our main findings and note some of their limitations.

The structure of a star may be regarded as a function of its entropy, so assessing the structural impacts of rotation or magnetism amounts to determining the role these play in modifying the star's entropy. In Section 3.2, we reviewed the links between entropy, convective efficiency, and stellar radii in "standard" 1D models, in which the mixing length parameter $\alpha_{\rm MLT}$ is assigned a depth-independent value that must be calibrated by comparison with observations. In these models, reducing the convective efficiency via a decrease in $\alpha_{\rm MLT}$ increases the temperature gradient required to carry an equivalent heat flux within the stellar interior. This translates into a larger entropy contrast between the photosphere and the deep interior for both pre-main-sequence and main-sequence models, which in turn influences the specific entropy attained in the deep interior (i.e., $s_{\rm ad}$) in an age-dependent fashion. We explicitly determine the radius inflation of a given model from the difference in $s_{\rm ad}$, with $\Delta \log R \propto \Delta s_{\rm ad}$. We also show how changes in the depth-independent $\alpha_{\rm MLT}$ are directly related to changes in the stellar radius, in a manner similar to that described by Christensen-Dalsgaard (1997) for solar-like stars.

One of our principal aims was to determine whether rotation alone could plausibly

modify the convective transport enough to change a fully convective star's radius by a noticeable amount. In Section 3.3, we considered a rotationally constrained version of MLT originally proposed by S79, and given renewed vibrancy by the recent analyses and simulations of Julien et al. (2012) and Barker et al. (2014). By implementing this theory directly into our 1D MESA models, we find that rotation has a negligible impact on the star's overall radius. This is because the radius is determined primarily by the interior adiabat, which in turn is established largely by layers near the stellar surface. These layers are almost completely uninfluenced by rotation at any plausible rotational velocity—that is, $\mathrm{Ro} \gg 1$ there because the convective velocity increases rapidly near the low-density photosphere—so rotation has little effect on s_{ad} and hence on the stellar radius, even though flows in the deep interior of the star *are* strongly affected by rotation. It is worth noting that if stars were instead well characterised by a single depth-independent Rossby number, rotation would (in at least some stars) be important everywhere, and would have a much more significant impact on the radius; it is primarily the depth variation of convective velocities that makes this impossible.

In Section 3.4, we argued that a particular prescription for incorporating the effects of magnetism into 1D stellar models, due to MM14, could be usefully analysed using the same techniques developed in Section 3.2. In particular, we note that the effect of varying magnetic fields in this model is to vary the entropy content of the deep interior; once this is known, the stellar radius is also determined, via the same formula developed in Section 3.2 (namely, Equation 3.18) for standard MLT models. In accord with MacDonald and Mullan (2017b), we find that *if* magnetic fields indeed influence convective transport in the manner assumed here, fields of a plausible strength (10^4 G or less) could noticeably "inflate" the stellar radius. This inflation is larger (by about a factor of two) in models at 10 Myr than in those at an age of 1 Gyr.

In Section 3.5, we showed that combining the rotational and magnetic reformulations of MLT, covered in Sections 3.3 and 3.4 respectively, can indeed "inflate" stellar radii by a further small amount. This demonstrates that the S79 rotation prescription is only effective at changing the stellar structure if the model is already "perturbed" by magnetism. The superadiabaticity throughout the stellar interior increases with magnetic

field strength; the effects of rotational inhibition can "feed" on this, increasing the superadiabaticity somewhat further and producing small structural differences in some cases. In our models, this additional effect is noticeable only on the pre-main-sequence.

Finally, in Section 3.6 we showed that both the rotationally and magnetically constrained versions of MLT explored in Sections 3.3 and 3.4, and the combination of these as shown in Section 3.5, can be duplicated by a "standard" MLT model in which the mixing length parameter $\alpha_{\rm MLT}$ is allowed to be depth dependent. We provide explicit formulae linking the radially variable $\alpha_{\rm MLT}(r)$ to the rotational and magnetic formulations of S79 and MM14 (Equations 3.34 and 3.35, respectively), and we show that models constructed using these $\alpha_{\rm MLT}(r)$ are indistinguishable from those directly employing the S79 or MM14 models. These formulae enable the computation of "magnetic" or "rotating" models, within the assumptions of the S79 or MM14 prescriptions, without modification of the mixing length formulation in a standard 1D stellar evolution code (though they do require that codes be capable of modelling non-constant $\alpha_{\rm MLT}$). We must caution, though, against taking these formulae as providing a *quantitatively* correct assessment of how rotation and/or magnetism affect the heat transport (and hence the structure of the star) at every depth; this is, in our opinion, unlikely to be the case, since the formulations on which it is based (namely those of S79 and MM14) have many potential shortcomings, as detailed below. We have derived and included these formulae mainly in order to illustrate *how* rotation and magnetism (in these prescriptions) could affect the structure of the star—namely, by modifying its specific entropy, just as $\alpha_{\rm MLT}(r)$ modifies the entropy in this depth-dependent MLT. The trends deduced here (regarding the relative efficacy of these mechanisms, for example, in objects of different ages) may well be *qualitatively* correct, even if the specific values of stellar radii, effective temperatures, etc., ultimately are not.

A principal limitation of our work is its reliance throughout on particularly simple models of how the rotation or magnetism affect the convective transport. In considering the effects of rotation on the structure, we effectively assumed that only the variation of ds/dr with Ω matters, and also that the rotationally constrained MLT of S79 adequately captures this variation; both assumptions are questionable. For example, the simulations

of Barker et al. (2014), which we cite as providing some numerical support for this scaling, effectively model only a single latitude near the pole (i.e., where rotation and the gravity vector are aligned); it is by no means clear that the same temperature scalings will hold at different latitudes. In general, rotation also introduces new anisotropy into the system (with motions increasingly aligned with the rotation axis in accord with the Taylor–Proudman constraint), implying that we might generally expect variations in the heat flux and/or entropy gradient with latitude. It is unclear how these latitudinal variations could best be represented in a 1D stellar model, which intrinsically assumes spherical symmetry. Similarly, the scaling of temperature or entropy gradients with rotation rate may well depend on latitude; indeed, latitudinal variations in these quantities are often present in spherical shell simulations of rotating convection (e.g., Browning et al. 2004; Raynaud et al. 2018).

It must likewise be acknowledged that the effects of magnetism on the flow, and hence on the stellar structure, are still uncertain. In general, they will depend on both the strength and the spatial morphology of the magnetic fields, which, in all the models quoted above and in our own work here, is not solved-for self-consistently as the outcome of a dynamo process, but instead must simply be imposed *a priori*. Models making different assumptions about the interior field strengths have yielded substantially different results. For example, the low-mass star models of Mullan and MacDonald (2001) explored fields of such strength ($\sim 100\,\mathrm{MG}$) that portions of the interior were rendered convective stable; this was motivated partly by the striking observational finding that the coronal heating efficiency of stars did not exhibit any clear break in behaviour at around spectral types M3–M4, where stars are (in standard non-magnetic models) predicted to transition from being partially radiative to fully convective (e.g., Fleming et al. 1993). Many of the other models noted above, including MacDonald and Mullan (2012) onward, have considered much weaker fields, which are probably more realistic (e.g., Browning et al. 2016). Meanwhile numerical simulations of the interiors of low-mass stars (Dobler et al. 2006; Browning 2008; Yadav et al. 2015) suggest that, in many cases, dynamos in these objects may yield fields that are approximately in equipartition with the convective kinetic energy density, rising above this in the most rapidly rotating cases (see, e.g., discussion in Augustson et al. 2017); the spatial structure of the fields is not yet certain, but is clearly influenced by the rotation

rate (e.g., Christensen and Aubert 2006; Browning 2008; Gastine et al. 2012; Yadav et al. 2015; Weber and Browning 2016; Aubert et al. 2017; see also discussions in Brun and Browning 2017). The 1D models considered here (and, for example, in MacDonald and Mullan 2017b) are at least broadly consistent with these constraints on the overall field strengths, but we have made no effort to mimic the interior radial profile of the field, or to capture aspects of its actual spatial morphology, which, in any event, are still uncertain.

The effects of the magnetism on heat transport are also somewhat unclear, but note, for example, that Yadav et al. (2016) find that convective heat transport is actually *enhanced* (relative to conductive transport) by the presence of magnetism in certain cases, in striking contrast to what is assumed in the MM14 formulation (or likewise that of Feiden and Chaboyer 2014, or in the reduced-$\alpha_{\rm MLT}$ models discussed here). Of course the simulations operate in parameter regimes far removed from those in actual stellar interiors, but they are nonetheless indicative of the sometimes surprising dynamics that can occur when convection, rotation, and magnetism interact in spherical domains.

More fundamentally, our models rely on the mixing length theory of convection, and on extremely simple atmospheric boundary conditions; both are crude approximations of the complex 3D transport occurring in these layers. Several authors have noted effects that are present in 3D convection but not easily captured in MLT (e.g., Canuto and Mazzitelli 1991; Meakin and Arnett 2007; Arnett et al. 2010; Currie and Browning 2017). Likewise, the role of the near-surface layers, where 3D convection coupled to radiative transport ultimately helps set the stellar adiabat, has lately been studied using simulations and theory (e.g., Tanner et al. 2014, 2016; Trampedach et al. 2014; Magic et al. 2015). It is beyond the scope of this chapter to provide detailed comparison between the effects induced by magnetism or rotation and those arising from all other effects not included in our modelling. However, it is worth noting that some of these effects must be clarified if a quantitative comparison between models and any specific observational data point is required. For example, variations in the surface atmospheric boundary condition and in metallicity, both fixed in our models, would modify the precise values of radius or effective temperature achieved at any given $\alpha_{\rm MLT}$, whether depth dependent or not (see, e.g., discussions in Tanner et al. 2014, 2016).

Overall, our results suggest that the effects on convection from rotation alone (if indeed it affects convection in the manner assumed here) cannot notably influence the overall structure of a fully convective star, but magnetism might. To have a substantial influence, the magnetism (or indeed any other agent that modifies the heat transport) must impact layers relatively close to the stellar surface, which largely establish the star's overall adiabat and hence its radius. These effects can be duplicated using standard MLT, but at the cost of allowing a depth-dependent $\alpha_{\rm MLT}(r)$ (intended to mimic the depth dependence of convective inhibition). In general, this may be difficult or impossible to calibrate using observations that probe the stellar surface alone. Further independent constraints on the form such depth-dependent convective inhibition must take—for example, by detailed comparison with 3D simulations incorporating rotation, magnetism, and radiative transport—may therefore be a prerequisite for truly predictive models of how magnetism affects the structure and evolution of these stars.

Chapter 4

Comparisons Between Mixing Length Theory and Simulations of Stellar Convection

4.1 Introduction

Fully convective stars are incredibly abundant: about 70% of the stars in our galaxy are M-dwarfs, and those with masses $\lesssim 0.35\ M_\odot$ have fully convective interiors (Chabrier and Baraffe 1997). We wish to better understand the interiors of these stellar objects, and the dynamic behaviour that exists within them. Unfortunately, it is difficult to observe the internal flows and magnetism directly; they might manifest at the surface, but many different effects combine in different ways (Brun and Browning 2017). To gain some complementary insights, we perform numerical simulations. The purpose of this chapter is to compare the dynamical behaviour realised in simulations of stellar convective flows to those in simple 1D stellar structure models, such as those we explored in Chapter 3. Recent studies have used 3D simulations of convection (e.g., Dobler et al. 2006; Browning 2008; Yadav et al. 2015), varying in complexity, in order to investigate these fully convective stars and their interior properties. These have shown that fully convective stars drive differential rotation in some cases, and that convective flow can be influenced by dynamo-generated

magnetic fields. In general, we are interested in investigating whether mixing length theory (MLT) of any kind provides a reasonable description of these dynamics. For example, the Stevenson (1979) reformulation of MLT (discussed in the previous chapter), later derived via simplified physical arguments by Barker et al. (2014), includes the effects of rotation on the convective heat transport of the stellar interior. A scaling law was derived between the average temperature gradient in the middle third of the domain and the rotation rate Ω, i.e., $-d\langle T\rangle/dz \propto \Omega^{4/5}$, in the rapidly rotating limit, which was supported by simulations in a localised (Cartesian) domain (Barker et al. 2014). However, in full 3D spherical-shell simulations of convection, the heat flow depends on many factors other than rotation, such as the shear, dissipative heating, magnetism, latitudinal-dependence, etc.; none of these effects are included in this scaling law, but could in principle radically alter it.

One way of characterising convection is via the specific entropy profile it establishes. Our previous chapter highlights the importance of entropy when considering the stellar structure. The adiabat of the specific entropy in the deep interior is dependent on the specific entropy contrast Δs between the adiabat and the value at the photosphere. As explored in Chapter 3, this adiabat largely determines the stellar radius in 1D stellar structure models. In a real star, Δs is set by the transition between convective to radiative transfer in the surface layers. There are additional effects that may influence this entropy contrast, such as rotation and magnetic fields. For example, the reformulation of MLT by MacDonald and Mullan (2014) implements the effects of magnetic fields on the convective heat transport by modifying the Schwarzschild criterion to include a magnetic inhibition parameter, which essentially depends on the profile of the vertical magnetic field strength. It was found that the effect of varying the magnetic field strength was to modify the specific entropy contrast of the star, changing the adiabat and thus inflating the stellar radius.

Ultimately, our aim is to gain an understanding of how rotation and magnetic fields affect the heat transport and structure of a star. This chapter establishes a trajectory toward this, but we must first understand how convection behaves in the absence of magnetism and rotation. Due to the physical effects notable in these 3D simulations, it is useful to perform local simulations of convection. Therefore, as a preliminary investigation, we

use local 2D "box in a star" simulations of convective flow in Cartesian geometry, using the anelastic approximation, and performed using the open-source pseudo-spectral code Dedalus (see Section 2.10). These local simulations allow us to look at different parameter regimes, isolate different effects, and examine highly turbulent flows. In Section 4.2, we investigate the dynamical behaviour of these simulations with changing density stratification, and the corresponding change in the properties of specific entropy.

Due to their artificial nature, local simulations are not fully indicative of real stars, so we turn to global 3D rotating hydrodynamic simulations of convective flow in Section 4.3. These simulations are performed in spherical geometry, using the anelastic approximation, with the open-source spherical-harmonic-based code *Rayleigh* (see Section 2.9). We investigate the dynamical behaviour of convection in these simulations, first by looking solely at the slowly rotating case, to get an understanding of how convection can vary just by changing the convective driving. We follow this by investigating how effective the "rotating" MLT reformulation of Stevenson (1979), or Barker et al. (2014), is at capturing the dynamical behaviour of fluid flow in more rapidly rotating 3D global simulations of convection. We discuss our overall findings in this chapter and conclude in Section 4.4.

4.2 Comparison with Local Simulations

In this section, we investigate the dynamical behaviour of convection in the absence of rotation and magnetism, using local "box in a star" 2D hydrodynamical simulations, modelled using Dedalus. All of the Dedalus simulations in this chapter are performed by solving the 2D hydrodynamical anelastic equations, under the Lantz-Braginsky-Roberts (LBR) approximation (detailed in Section 2.6.1), in a non-rotating Cartesian geometry, using a sine/cosine decomposition in the horizontal (no lateral heat flux), and the semi-implicit Crank-Nicolson Adams-Bashforth numerical scheme for time integration. In most cases, 192 grid points with dealiasing (128 modes) were used, but some used 384 grid points (256 modes) for higher resolution solutions. All of the variables used in the following investigation will be time averaged over a steady state temporal range.

4.2.1 Local Numerical Set Up

This description of the numerical set up largely follows the equivalent description in Currie and Browning (2017). These Dedalus simulations consider a hydrodynamic convective fluid in a 2D Cartesian domain of height d, with a polytropic background state. This is formulated for an ideal gas with polytropic index n, which gives the reference state for the temperature $\bar{T}$, density $\bar{\rho}$, and pressure $\bar{p}$ as

$$\bar{T} = \bar{T}_0(1 - \beta z), \tag{4.1}$$

$$\bar{\rho} = \bar{\rho}_0(1 - \beta z)^n, \tag{4.2}$$

$$\bar{p} = \mathcal{R}\bar{\rho}_0\bar{T}_0(1 - \beta z)^{n+1}, \tag{4.3}$$

respectively, where $\bar{T}_0$ and $\bar{\rho}_0$ are the bottom boundary values of the background temperature and density, respectively, $\mathcal{R}$ is the ideal gas constant, and $\beta = g/(c_{p,0}T_0)$, where g is the gravitational acceleration, and $c_{p,0}$ is the specific heat capacity (at constant pressure) at the bottom boundary. β is essentially the inverse temperature scale height, which can be used to measure the layer stratification (or number of density scale heights N_ρ):

$$N_\rho = -n \ln(1 - \beta d). \tag{4.4}$$

A polytropic, monatomic, adiabatic, ideal gas is assumed ($n = 3/2$).

In regards to boundary conditions, we are using 2D solutions, therefore $\boldsymbol{u} = (u, 0, w)$, and $\partial/\partial y \equiv 0$. Stress-free and impenetrable boundaries are employed at $z = 0$ and $z = d$:

$$w(z=0,d) = \left(\frac{du}{dz}\right)_{z=0,d} = 0. \tag{4.5}$$

At the bottom boundary, the flux is fixed (the source of heat flux into the domain):

$$F(z=0) = F_{\text{tot}}, \tag{4.6}$$

where F_{tot} is the total flux. At the upper boundary, specific entropy is fixed at

$$s(z=d) = 0, \tag{4.7}$$

and all heat flux must exit at the top via conduction. A flux-based Rayleigh number (see, e.g., Duarte et al. 2016) is also defined, which, roughly, measures the ratio of buoyancy driving to viscous and thermal dissipation:

$$\text{Ra}_F = \frac{gF_{\text{tot}}d^4}{c_{p,0}\bar{\rho}_0\bar{T}_0\nu\kappa^2}. \tag{4.8}$$

2D solutions allow for higher supercriticalities ($(\text{Ra}_F/\text{Ra}_{F,\text{c}})$, where $\text{Ra}_{F,\text{c}}$ is the value at which convection onsets) and N_ρ to be simulated.

Table 4.1 gives the input parameters used across all simulations, and Table 4.2 gives input parameters, and associated nondimensional parameters, that vary across simulations. All of these hydrodynamical simulations were performed until they reached a time-averaged statistical steady state.

4.2.2 Local Convective Flows and Energy Balances

First, we investigate the changes in convective structure of these local simulations, and the resulting energy balances, as we vary the density stratification (via N_ρ, using Equation (4.4)). Figure 4.1 illustrates the structure of convective flows across the 2D domain

Parameter	Value
$L_x : L_z$	1:1
n	1.5
g [cm s^{-2}]	2586
$\bar{\rho}_0$ [g cm^{-2}]	110

Table 4.1: Input parameters identical for all of the Dedalus simulations used in this chapter, where $L_x : L_z$ represent the aspect ratio of the domain, in x and z, respectively, $n(= 1.5)$ is the polytropic index for a polytropic, monatomic, adiabatic, ideal gas, g is the gravitational acceleration, and $\bar{\rho}_0$ is the density at the bottom boundary.

Model	N_ρ	d [10^{10}] [cm]	$c_{p,0}$ [10^7] [erg g^{-1} K^{-1}]	$\bar{T}_0$ [10^5] [K]	$\kappa = \nu$ [10^{12}] [cm^2 s^{-1}]	$F_{\rm tot}$ [10^{15}] [erg s^{-1} cm^{-1}]	Pr	$\log_{10}$ (Ra$_F$/ Ra$_{F,\rm c}$)
`L-Aa`	0.105	1.82	100	6.97	3.64	5	1	2.85
`L-Ab`	0.105	1.82	100	6.97	3.64	50	1	3.85
`L-Ac`	0.105	1.82	100	6.97	3.64	344	1	4.69
`L-Ad`	0.105	1.82	100	6.97	3.64	800	1	5.06
`L-Ae`	0.105	1.82	100	6.97	3.64	5000	1	5.85
`L-Ba`	0.706	0.46	9	3.48	3.64	10	1	2.28
`L-Bb`	0.706	0.46	9	3.48	3.64	100	1	3.28
`L-Bc`	0.706	7.28	36	13.93	3.64	0.34	1	4.43
`L-Bd`	0.706	7.28	36	13.93	5.00	10	1	5.48
`L-Be`	0.706	7.28	36	13.93	3.64	10	1	5.90
`L-Bf`	0.706	7.28	36	13.93	3.00	10	1	6.15
`L-Ca`	2.085	0.46	4.5	3.48	3.64	10	1	2.90
`L-Cb`	2.085	1.37	13.5	3.48	3.64	3.7	1	3.90
`L-Cc`	2.085	7.28	18	13.93	3.64	0.3	1	4.99
`L-Cd`	2.085	7.28	18	13.93	3.64	1	1	5.52

Table 4.2: Dimensional input parameters (that differ between simulations) and nondimensional parameters for the Dedalus local simulations, where d is the height of the domain, $c_{p,0}$ is the specific heat capacity (at constant pressure) at the bottom boundary, $\bar{T}_0$ is the background temperature at the bottom boundary, κ and ν are the kinematic viscosity and the thermal diffusivity, respectively, $F_{\rm tot}$ is the total flux, Pr$(= \nu/\kappa)$ is the Prandtl number (ratio of viscous to thermal diffusivity), and $\log_{10}$ (Ra$_F$/Ra$_{F,\rm c}$) is the logarithmic supercriticality, where Ra$_F$ is the flux-based Rayleigh number and Ra$_{F,\rm c}$ is the critical Rayleigh number (determined in Currie and Browning (2017) via a linear code).

for a snapshot of the $N_\rho = 0.105$ model `L-Ae`, showing the vertical velocity u and the horizontal velocity w. At the lower density stratification, the flow is similar to that of classic Rayleigh-Bénard convection in an unstratified medium, with near-symmetric upflows and downflows. Figure 4.2 show identical plots, but for the $N_\rho = 2.085$ model `L-Cd`, where the convective flow is more asymmetric about the mid-plane.

In these simulations, heat flux is transported through the domain, resulting in convection. The horizontally-averaged local energy balance for these simulations (Currie and Browning 2017) consists of the enthalpy flux

$$F_\mathrm{e} = \bar{\rho} c_p \langle w T' \rangle, \tag{4.9}$$

the kinetic energy (KE) flux

$$F_\mathrm{KE} = \frac{1}{2} \bar{\rho} \left\langle w |\boldsymbol{u}|^2 \right\rangle, \tag{4.10}$$

the conductive flux

$$F_\mathrm{cond} = -\kappa \bar{\rho} \bar{T} \left\langle \frac{ds'}{dz} \right\rangle, \tag{4.11}$$

and the viscous flux

$$F_\mathrm{visc} = -\left\langle \boldsymbol{u} \cdot \boldsymbol{\mathcal{D}} \right\rangle, \tag{4.12}$$

where $\bar{\rho}$ and $\bar{T}$ are the reference density and temperature, respectively, c_p is the specific heat capacity (at constant pressure), $\boldsymbol{u}$ is the vector velocity, w is the horizontal component of the velocity, T' is the temperature perturbation, ds'/dz is the specific entropy perturbation gradient, κ is the thermal diffusivity, and $\boldsymbol{\mathcal{D}}$ is the vector viscous stress tensor. The sum of these flux components must equate to the total flux F_tot, specified by the input parameters. The expression for conductive flux is an ansatz for sub-grid-scale convective motions that tend to isentropise the fluid.

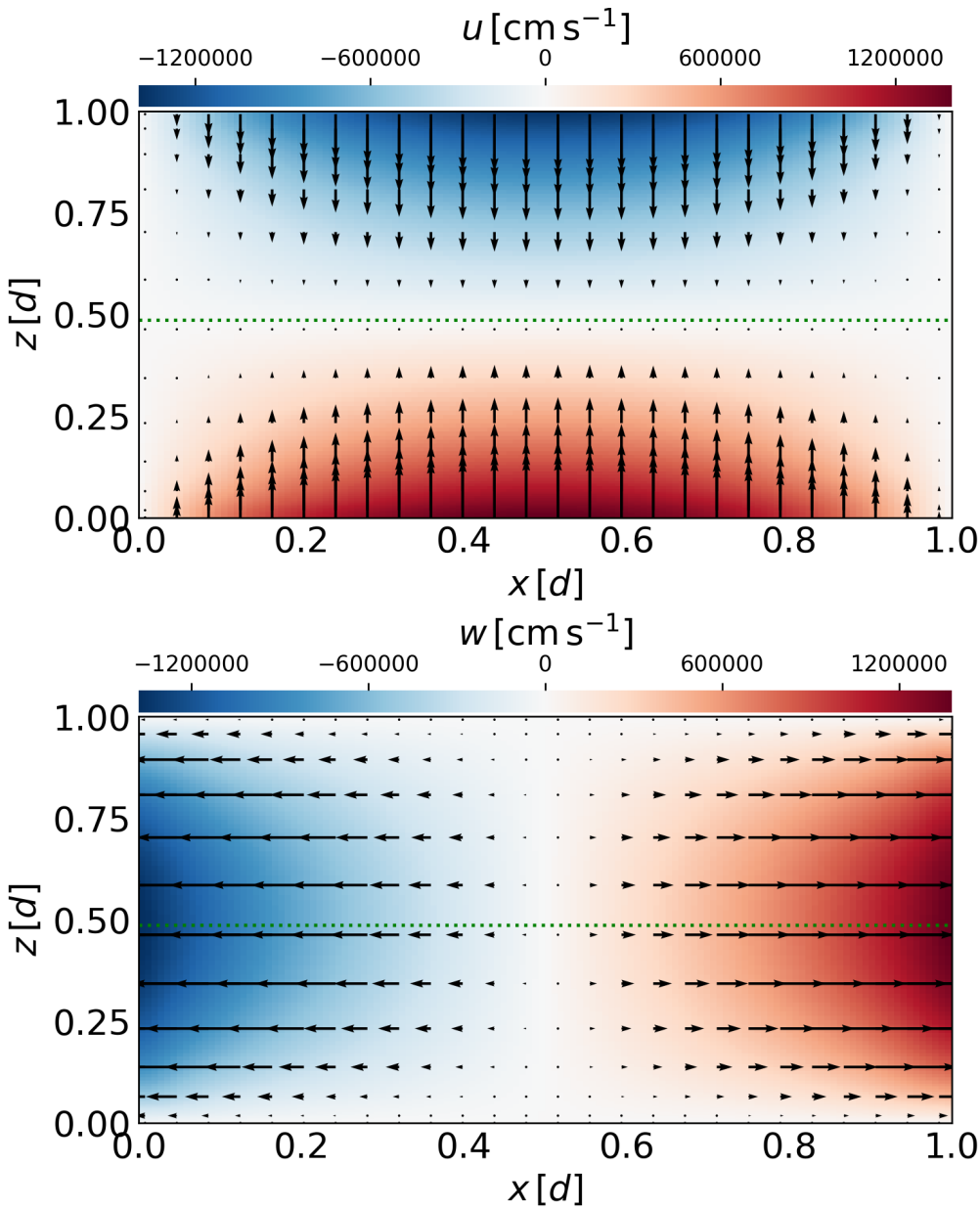

Figure 4.1: Convective flow of the $N_\rho = 0.105$ model `L-Ae`, showing velocity components u and w. Near-symmetric flow is shown, similar to that of classic Rayleigh-Bénard convection in an unstratified medium. The horizontal green dotted line indicates the point at which there is equal mass above and below, which is roughly at the mid-plane for this simulation.

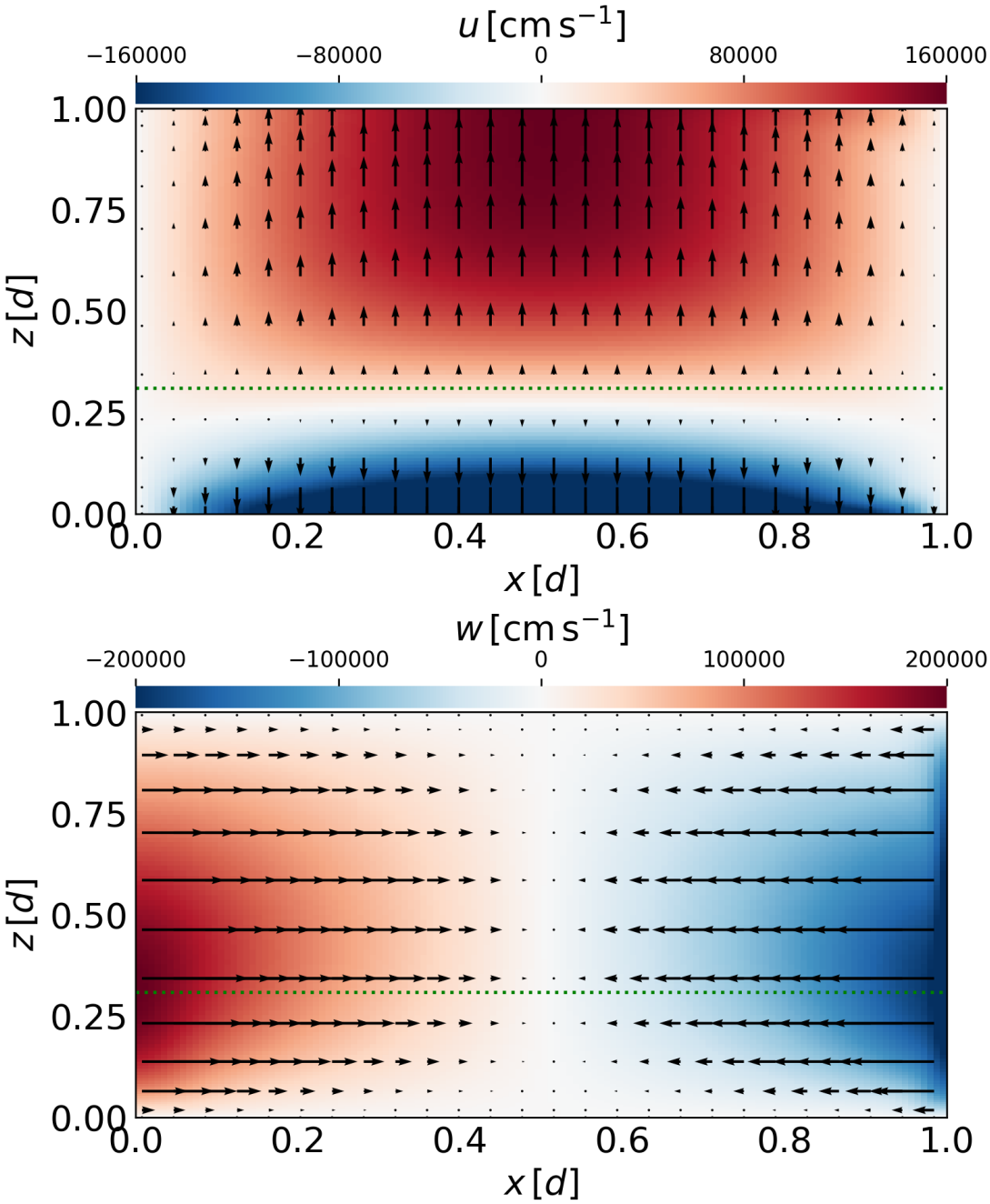

Figure 4.2: Convective flow for the $N_\rho = 2.085$ model `L-Cd`, showing velocity components u and w. Flow is becoming more asymmetric with increasing N_ρ. The horizontal green dotted line indicates the point at which there is equal mass above and below, which is closer to the bottom boundary compared to the lowest stratified case.

Energy balances for these local simulations of convection typically consist of an upward (positive) enthalpy flux, which carries the flux via convection, a downward (negative) KE flux, which is due to convective motions being asymmetric between upflows and downflows, an upward (positive) conductive flux, which forces the total luminosity to pass the upper boundary, and a viscous flux, which represents the total work done by surface forces (Currie and Browning 2017). This balance will vary with the density stratification. We demonstrate this by plotting the horizontally-averaged energy balances (expressed in luminosities) for the same supercriticalities in the previous figures: model `L-Ae` in Figure 4.3, and model `L-Cd` in Figure 4.4. At the lower density stratification, $F_{\mathrm{e}} \approx F_{\mathrm{tot}}$ in the bulk of the domain, carrying the heat flux upwards. F_{cond} is small throughout the domain, apart from at the boundaries, which allows for the imposed flux at the bottom boundary to be carried upward toward the upper boundary. We find that $F_{\mathrm{KE}} \approx 0$ at low density stratification, consistent with up-down symmetry of the flow in classic Rayleigh-Bénard convection in an unstratified medium. F_{visc} is also negligible at low density stratification. At $N_\rho = 2.085$, we see that F_{e} exceeds F_{tot} in the bulk of the domain, and F_{KE} becomes increasingly negative also, as the convective flow becomes more asymmetric with increasing density stratification. It is also no longer the case that $F_{\mathrm{tot}} \approx F_{\mathrm{conv}}$ for highly stratified domains; instead, it is found that $F_{\mathrm{tot}} \approx F_{\mathrm{conv}} + F_{\mathrm{other}}$, where $F_{\mathrm{other}} = F_p + F_{\mathrm{KE}} + F_{\mathrm{visc}}$, with F_p being the difference between F_{e} and F_{conv} (see Currie and Browning 2017). Near the bottom boundary, F_{cond} becomes slightly negative, and F_{KE} and F_{visc} increase: this is a result of a subadiabatic region forming as N_ρ is increased, which is illustrated in Section 4.2.3, and discussed in Section 4.4.

The conductive boundary layers in these simulations artificially mimic the transition between convective and radiative heat transfer in the surface layers of real stars, which sets up the specific entropy contrast. Thus, in the next section, we are motivated to investigate the specific entropy, and its gradient, as a function of the density stratification N_ρ.

4.2.3 Entropy in Local Simulations for Varying Density Stratification

The entropy content of a star is linked to the stellar structure (see, e.g., Stahler 1988). In a fully convective star, most of the interior lies at nearly constant specific entropy

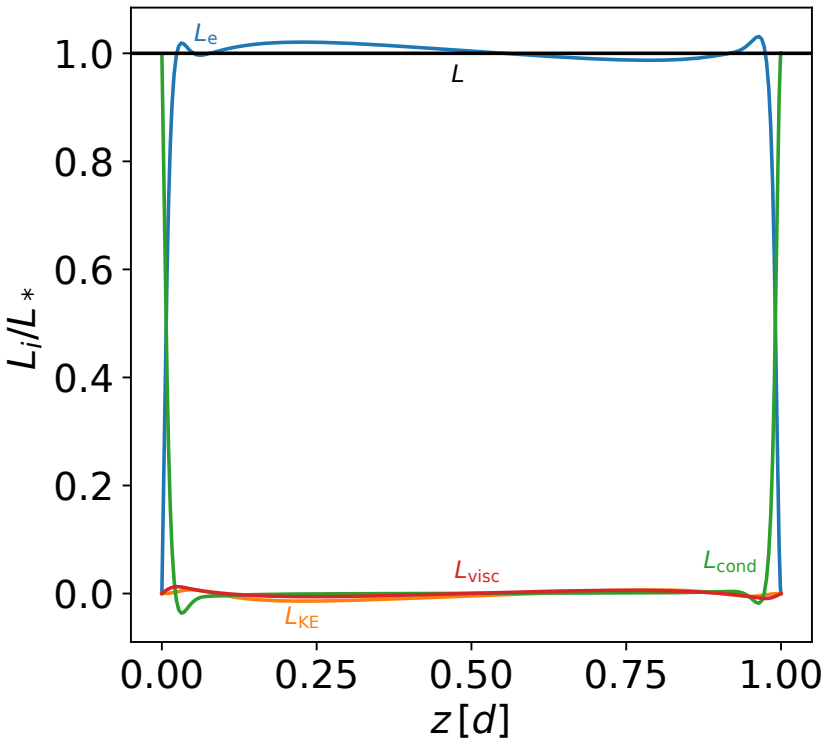

Figure 4.3: Horizontally-averaged energy balance profiles for model `L-Ae`. $F_{\rm tot} \approx F_{\rm conv}$ at low density stratification, analogous to classic Rayleigh-Bénard convection in an unstratified medium. $F_{\rm cond}$ is negligible apart from at the boundary layers. $F_{\rm visc}$ is negligible at low density stratification.

$s_{\rm ad}$, as the temperature gradient required to carry stellar flux upward is very close to the adiabatic value. A specific entropy contrast Δs is determined near the stellar surface, due to the interaction between convection and radiative transfer. This quantity fixes $s_{\rm ad}$ in the bulk of the domain, i.e., the adiabat, which effectively determines the stellar radius. This is how the specific entropy in 1D stellar structure models, which could be considered as a latitudinally-averaged quantity, is determined. However, in these local simulations of convection, this transition between convection and radiation does not exist; instead, conductive boundary layers are used to carry the remaining heat flux upward, which in turn sets up Δs.

In this section, we look at how the entropy content of these local simulations is influenced by the density stratification. Some of the changes in specific entropy, and its gradient, between simulations may be a result of boundary conditions and other simulation effects, but we investigate whether any changes are due to real physical changes in the domain. We start by looking at the dynamical behaviour of specific entropy at different

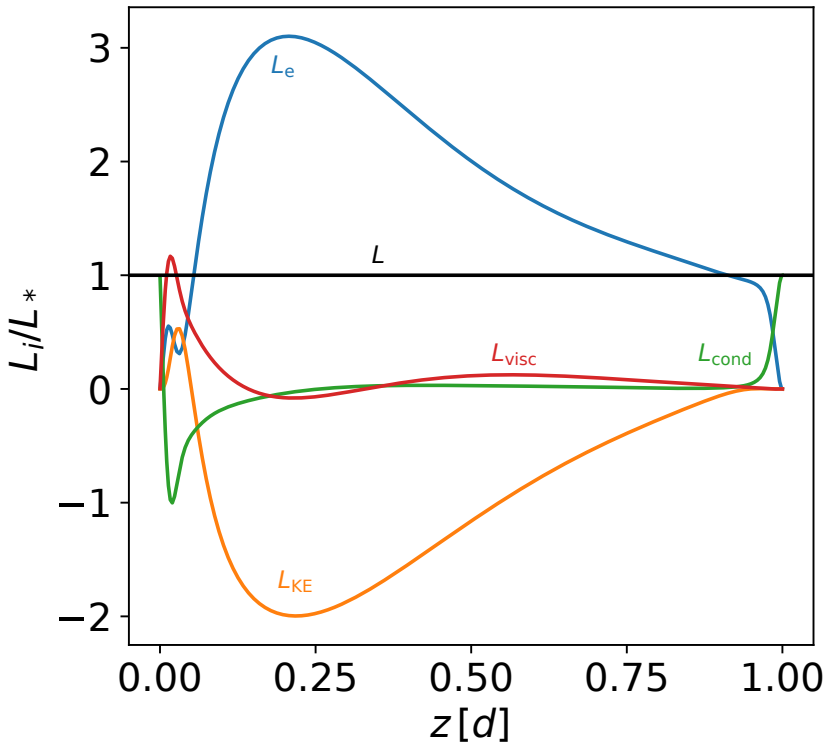

Figure 4.4: Horizontally-averaged energy balance profiles for model `L-Cd`. F_e and F_{KE} increase further in the bulk of the domain as N_ρ is increased. F_{cond} is negligible apart from at the boundary layers. F_{visc} is negligible, except for a peak at the bottom boundary (along with a peak in F_{KE} and dip in F_{cond}), as a result of a subadiabatic region forming.

density stratifications, as a function of the supercriticality $\mathrm{Ra}_F/\mathrm{Ra}_{F,\mathrm{c}}$. We normalise specific entropy by Δs_{cond}, which represents the specific entropy contrast in the case where all of the heat flux is transported via conduction, to illustrate how the entropy content of a simulation converges toward an isentropic state with increasing convective driving. As the upper boundary is set to zero by the boundary conditions, this is equivalent to the bottom boundary value. Using Equation (4.11), it can be shown that the horizontally-averaged specific entropy gradient for a fully conductive case is

$$\begin{aligned} \frac{ds_{\mathrm{cond}}}{dz} &= -\frac{F_{\mathrm{tot}}}{\kappa\bar{\rho}\bar{T}} \\ &= -\frac{F_{\mathrm{tot}}}{\kappa\bar{\rho}_0\bar{T}_0}\left(1-\beta z\right)^{-m+1}, \end{aligned} \tag{4.13}$$

therefore the conductive specific entropy contrast (by integrating the above, knowing $s_{\mathrm{cond}}(z=d)=0$, and setting $z=0$) can be expressed as

$$\Delta s_{\mathrm{cond}} = \frac{F_{\mathrm{tot}}}{\kappa\bar{\rho}_0\bar{T}_0}\frac{1}{\beta m}\left[(1-\beta d)^{-m}-1\right]. \tag{4.14}$$

In Figure 4.5, we plot the horizontally-averaged normalised specific entropy $s/\Delta s_{\mathrm{cond}}$ as a function of normalised depth for all the $N_\rho = 0.105$ simulations. The profiles are markedly different from those realised in our 1D stellar structure models in Chapter 3. From the bottom boundary upward, $s/\Delta s_{\mathrm{cond}}$ drops from its initial value and converges onto an approximate "adiabat" for that particular simulation, before dropping to zero at the upper boundary. As the supercriticality increases, $s/\Delta s_{\mathrm{cond}}$ in the bulk of the domain decreases, converging to an isentropic state. We also explore this for our highest density stratification, $N_\rho = 2.085$, in Figure 4.6. Analogous to the $N_\rho = 0.105$ case, $s/\Delta s_{\mathrm{cond}}$ in the bulk decreases as a function of the supercriticality, but the profiles themselves differ near the bottom boundary. With increasing supercriticality, $s/\Delta s_{\mathrm{cond}}$ initially increases with height and actually exceeds the bottom boundary value. At first glance, this result is surprising. However, this is tied to the presence of subadiabatic regions that we discuss below in Section 4.4. These may be due to physical effects, but may also be somewhat

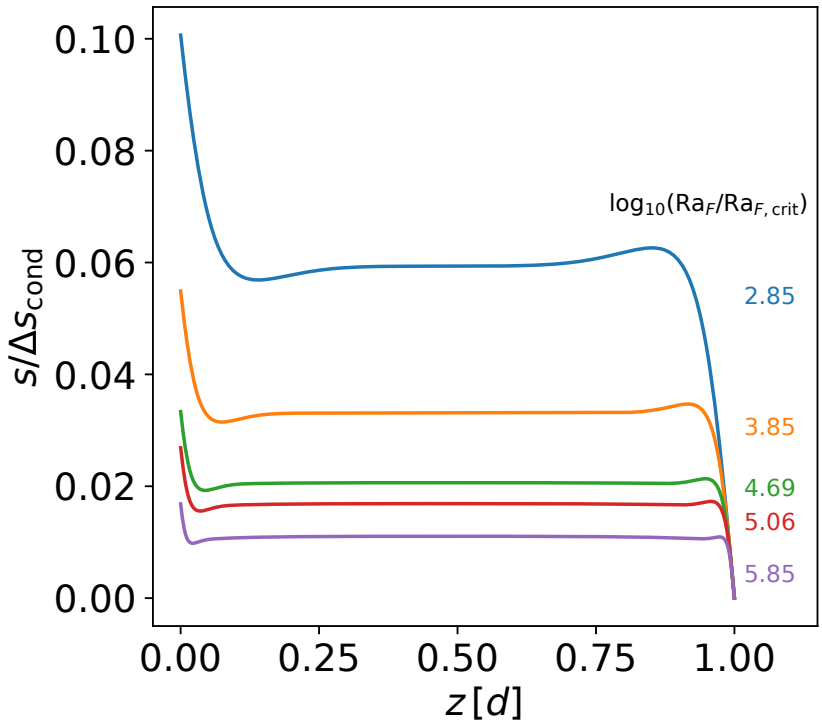

Figure 4.5: Horizontally-averaged $s/\Delta s_{\rm cond}$ as a function of normalised depth, for $N_\rho = 0.105$ 2D local convective simulations at different supercriticalities. The profile initially drops from the bottom boundary value and falls onto an approximate "adiabat", before dropping to zero at the upper boundary. The profile in the bulk of the domain decreases with increasing supercriticality, converging toward an isentropic state.

artificial in origin. One possible effect may be due to the amount of viscous dissipation in these simulations, which increases for more supercritical, highly stratified cases (Currie and Browning 2017). These stable layers result in a higher adiabat for a given supercriticality, when compared to the lowest stratified case.

The specific entropy profile is a function of both the imposed boundary conditions, but also real physical effects. To demonstrate this, we consider the specific entropy gradient ds/dz, which is related to the specific entropy contrast Δs (hence the inner boundary specific entropy s_0):

$$\Delta s = \int_d^0 \left(\frac{ds}{dz}\right) dz \equiv s_0. \tag{4.15}$$

Using Equations (4.6) and (4.11), it can be shown that the specific entropy gradient value fixed at the bottom boundary $(ds/dz)_{z=0} (= (ds'/dz)_{z=0}$, as $\bar{s}$ is isentropic) is

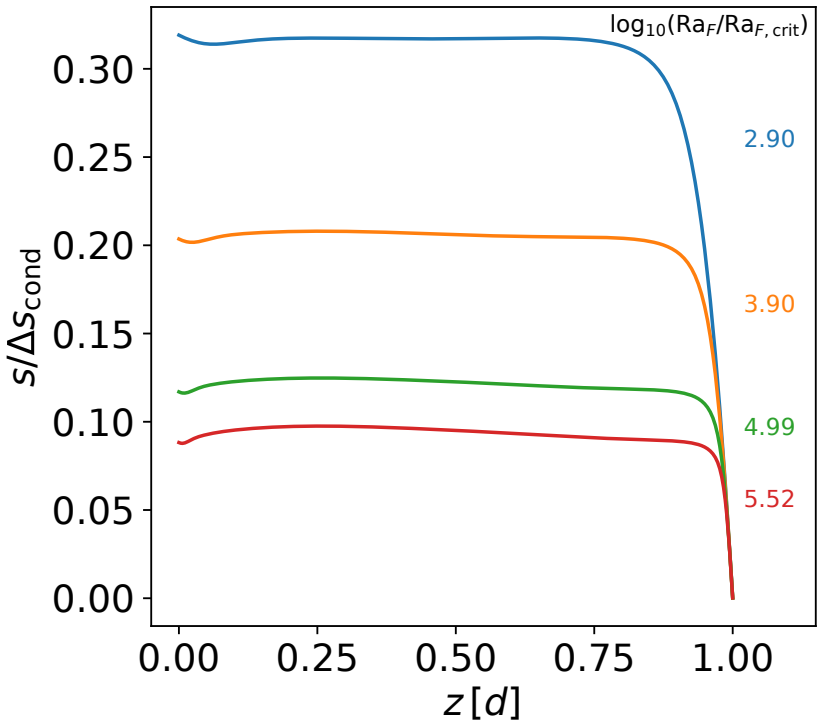

Figure 4.6: Horizontally-averaged $s/\Delta s_{\rm cond}$ as a function of normalised depth, for $N_\rho = 2.085$ 2D local convective simulations at different supercriticalities. Increasing supercriticality decreases $s/\Delta s_{\rm cond}$ in the bulk of the domain (as for the lowest stratified case), but increasingly exceeds the bottom boundary value as the supercriticality increases, due to a subadiabatic region forming near the bottom boundary.

$$\begin{aligned}\left(\frac{ds}{dz}\right)_{z=0} &= \left(\frac{ds'}{dz}\right)_{z=0} \\ &= -\frac{F_{\rm tot}}{\kappa\bar{\rho}_0\bar{T}_0},\end{aligned} \tag{4.16}$$

demonstrating that the absolute value of the specific entropy contrast Δs will depend, in theory, on both physical effects in the domain, but also on the imposed boundary conditions. In Figures 4.7 and 4.8, we plot the horizontally-averaged normalised specific entropy gradient $(ds/dz)(d/\Delta s_{\rm cond})$ as a function of normalised depth for all of the $N_\rho = 0.105$ and $N_\rho = 2.085$ simulations, respectively. For $N_\rho = 0.105$, $(ds/dz)(d/\Delta s_{\rm cond})$ is fairly isentropic in the middle third of the domain, but there are subadiabatic peaks ($(ds/dz)(d/\Delta s_{\rm cond}) > 0$) at each boundary (more so at the bottom boundary), which are likely a result of the imposed conductive boundaries. These subadiabatic regions increase with supercriticality, but also become more concentrated, as the bulk of the domain becomes increasingly isentropic. For the $N_\rho = 2.085$ case, the subadiabatic regions are larger

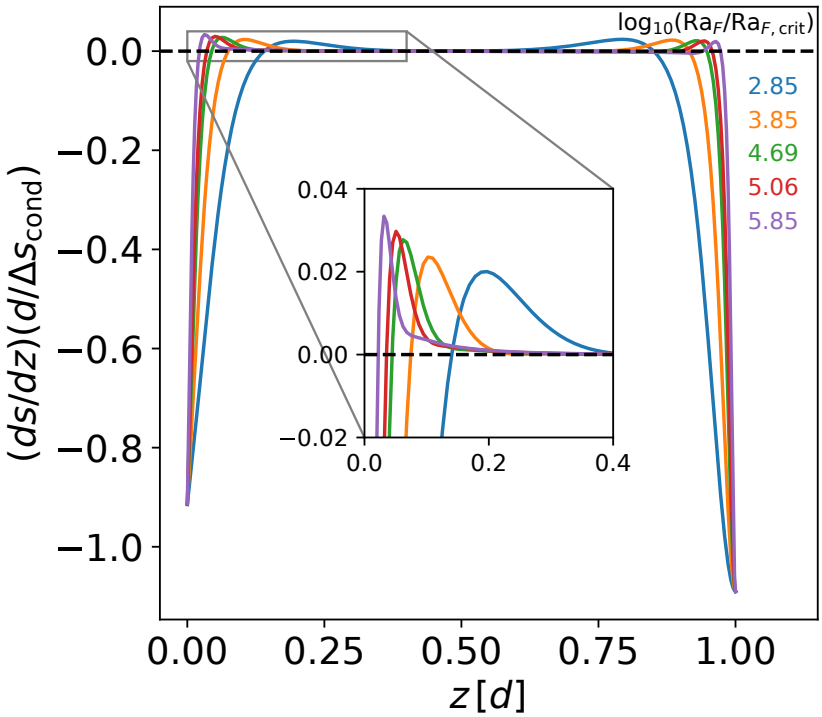

(a)

Figure 4.7: Horizontally-averaged $(ds/dz)(d/\Delta s_{\rm cond})$ as a function of normalised depth, for $N_\rho = 0.105$ 2D local convective simulations at different supercriticalities. There are sharp subadiabatic peaks at the bottom and upper boundaries, which increase in magnitude with increasing supercriticality. However, these become more concentrated at the boundaries as a function of supercriticality, as the bulk of the domain becomes increasingly isentropic.

in magnitude compared to the lowest stratified case, but are much more concentrated near the bottom boundary, suggesting that increased viscous dissipation may be partly responsible for these stable layers in highly stratified domains. Upper boundary effects are less noticeable with increasing density stratification.

The boundary conditions are clearly prevalent in these local simulations. We therefore look next at changes in average bulk properties, which are more likely to represent physical changes in the dynamical behaviour of convection. In Figure 4.9, we plot the horizontally-averaged normalised specific entropy value averaged over the middle third of the domain, $\langle s\rangle/\Delta s_{\rm cond}$, as a function of supercriticality. We see a decrease in $\langle s\rangle/\Delta s_{\rm cond}$ with increasing supercriticality at all density stratifications, which all appear to be converging toward an isentropic state. The overall value of $\langle s\rangle/\Delta s_{\rm cond}$ at the lower boundary, and hence within the interior as well, is then tending towards the fixed value at the cool upper boundary, that is towards $\langle s\rangle/\Delta s_{\rm cond} = 0$, implying a decrease in $\langle s\rangle/\Delta s_{\rm cond}$. For

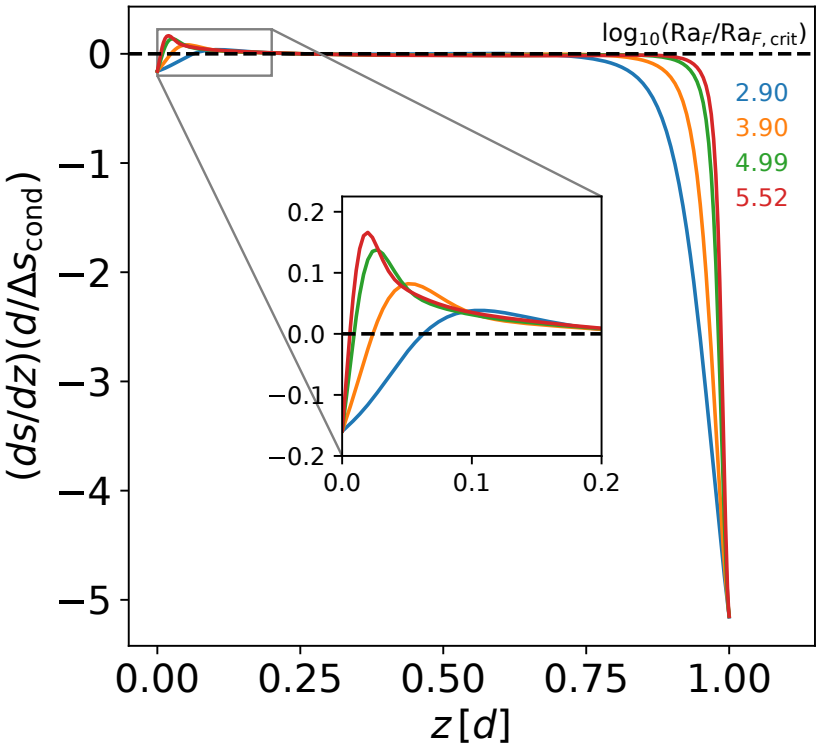

(a)

Figure 4.8: Horizontally-averaged $(ds/dz)(d/\Delta s_{\mathrm{cond}})$ as a function of normalised depth, for $N_\rho = 2.085$ 2D local convective simulations at different supercriticalities. With increasing supercriticality, simulations become increasingly subadiabatic at the bottom boundary. For a given supercriticality, these regions are more subadiabatic than the lowest stratified case, suggesting that these stable layers may be partly influenced by the increased viscous dissipation in highly stratified domains. However, these become more concentrated at the boundaries as a function of supercriticality, as the bulk of the domain becomes increasingly isentropic.

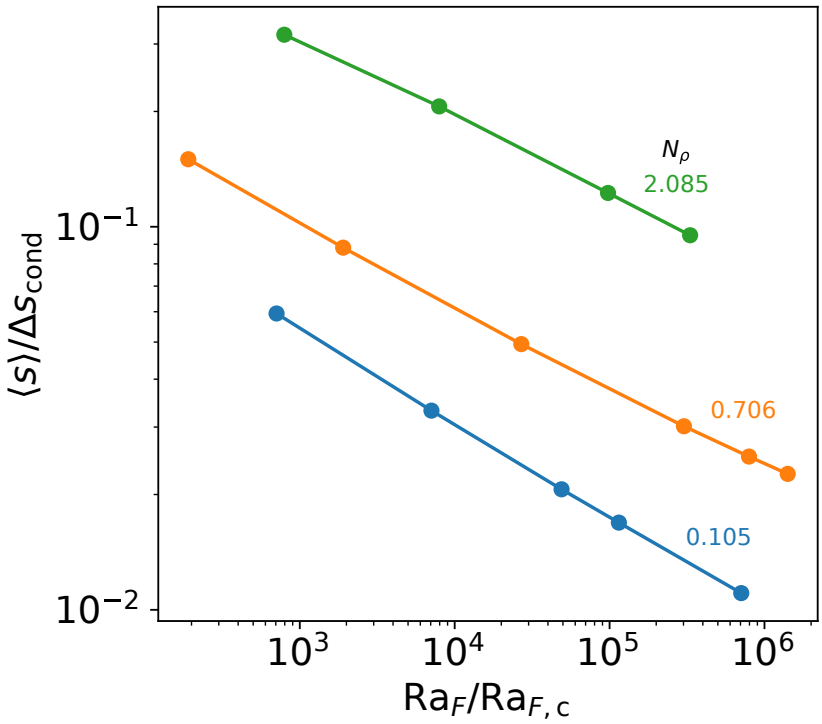

Figure 4.9: Horizontally-averaged $\langle s\rangle/\Delta s_{\rm cond}$, as a function of $\mathrm{Ra}_F/\mathrm{Ra}_{F,\mathrm{c}}$, for all N_ρ. $\langle s\rangle/\Delta s_{\rm cond}$ decreases with increasing supercriticality, and at fixed supercriticality, increases with N_ρ. At all density stratifications, $\langle s\rangle/\Delta s_{\rm cond}$ appears to be converging toward their respective isentropic states as supercriticality increases, with a fixed interior entropy increasingly close to that of the upper boundary value.

a given supercriticality, $\langle s\rangle/\Delta s_{\rm cond}$ increases with N_ρ, suggesting that the isentropic state that it converges toward is dependent on the density stratification of the system, due to differences in the finite boundary layers (as a result of the increasing subadiabatic layer) with N_ρ. In Figure 4.10, we plot the middle-third average of the horizontally-averaged normalised specific entropy gradient $\langle ds/dz\rangle(d/\Delta s_{\rm cond})$ as a function of supercriticality. We see that $\langle ds/dz\rangle(d/\Delta s_{\rm cond})$ increases negatively as a function of supercriticality, and plateaus at high $\mathrm{Ra}_F/\mathrm{Ra}_{F,\mathrm{c}}$ (the $N_\rho = 2.085$ case appears to be in the process of saturating, following a similar pattern to the lower stratified cases). With increasing density stratification, $\langle ds/dz\rangle(d/\Delta s_{\rm cond})$ converges to increasingly negative values, suggesting that the bulk of the domain becomes more superadiabatic (on average). This is consistent with the finding that simulations at higher N_ρ sit on a higher adiabat, so a larger superadiabatic gradient is required to meet the upper boundary condition for specific entropy, i.e., $s(z = d) = 0$.

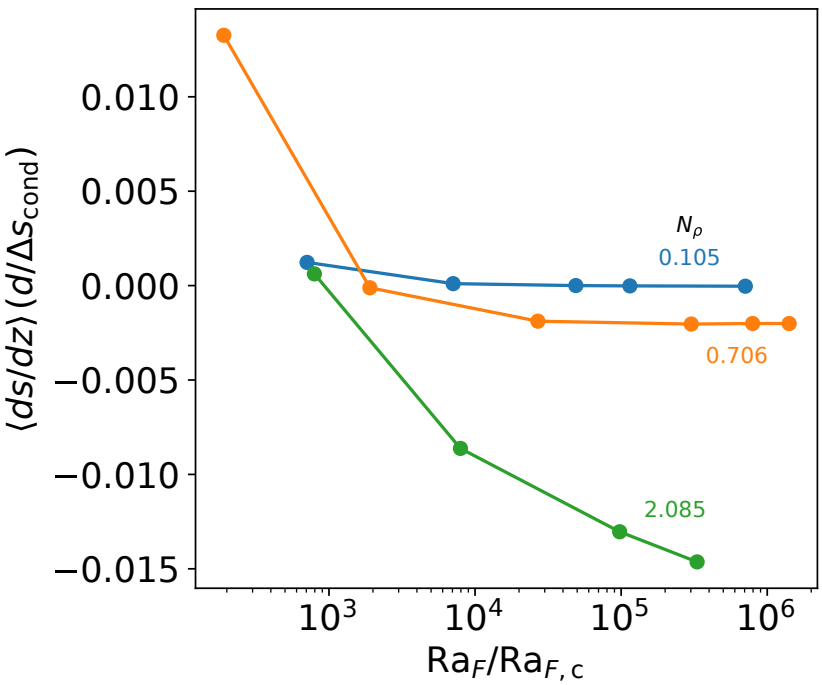

Figure 4.10: Horizontally-averaged $\langle ds/dz \rangle (d/\Delta s_{\rm cond})$, as a function of $\mathrm{Ra}_F/\mathrm{Ra}_{F,\mathrm{c}}$, for all simulations. $\langle ds/dz \rangle (d/\Delta s_{\rm cond})$ increases in magnitude with increasing supercriticality. There is an evident plateau of $\langle ds/dz \rangle (d/\Delta s_{\rm cond})$ for $N_\rho = 0.105$ and $N_\rho = 0.706$ cases, with $N_\rho = 2.085$ appearing to be still in the process of approaching a similar (lower) plateau as supercriticality increases. The bulk of the domain appears to become more superadiabatic as a function of N_ρ, which is required to bring a higher adiabat value down to $s = 0$ at the upper boundary.

4.3 Comparison with Global Simulations

In this section, we investigate the dynamical behaviour of convection as a function of rotation rate, and compare findings with those predicted via MLT. All of the *Rayleigh* simulations in this chapter are performed by solving the 3D hydrodynamic anelastic equations of motion under the Lantz-Braginsky-Roberts (LBR) approximation (see Section 2.6.1), in a rotating spherical geometry, using a semi-implicit pseudo-spectral approach (see Section 2.7.2). All of the variables used in this investigation are time averages over a steady state temporal range.

4.3.1 Global Numerical Set Up

The *Rayleigh* simulations in this chapter consist of a polytropic background state, provided by the anelastic benchmark suite of Jones et al. (2011). The polytropic background state is formulated by considering a thick convective shell surrounding an interior mass M_i, with a gravitational acceleration profile $g(r) = GM_i/r^2$. For an adiabatically stratified, polytropic domain, we define the background density $\bar{\rho}$, temperature $\bar{T}$, and pressure $\bar{p}$. The outer boundary background values for these variables are expressed as

$$\bar{\rho}_o = \bar{\rho}_i \left(\frac{\zeta_o}{\zeta_i}\right)^n, \tag{4.17}$$

$$\bar{T}_o = \bar{T}_i \left(\frac{\zeta_o}{\zeta_i}\right), \tag{4.18}$$

and

$$\bar{p}_o = \bar{p}_i \left(\frac{\zeta_o}{\zeta_i}\right)^{n+1}, \tag{4.19}$$

respectively, where $\bar{\rho}_i$, $\bar{T}_i$, $\bar{p}_i$ are the inner boundary values of density, temperature, and pressure, respectively, and n is the polytropic index. ζ is the radial variation of the reference state:

$$\zeta = c_0 + c_1 \frac{H}{r}, \tag{4.20}$$

where $H = r_o - r_i$ is the thickness of the shell (r_o and r_i are the outer and inner boundary radii, respectively), and c_0 and c_1 are

$$c_0 = \frac{2\zeta_o - \beta - 1}{1 - \beta}, \tag{4.21}$$

and

$$c_1 = \frac{(1+\beta)(1-\zeta_o)}{(1-\beta)^2}, \tag{4.22}$$

respectively. $\beta = r_i/r_o$ is the aspect ratio of the shell. Thus, ζ_o and ζ_i are

$$\zeta_o = \frac{\beta + 1}{\beta \exp\left(N_\rho/n\right) + 1}, \tag{4.23}$$

and

$$\zeta_i = \frac{1 + \beta - \zeta_o}{\beta}, \tag{4.24}$$

respectively, where $N_\rho = \ln\left(\bar{\rho}_i/\bar{\rho}_o\right)$ is the number of density scale heights. Centrifugal forces are neglected, because at the rotation rates considered in these simulations, these are much smaller than the overall gravitational force.

Stress-free and impenetrable boundary conditions are adopted, thus the radial component of velocity at these boundaries are

$$\begin{aligned} v_r(r = r_i, r_o) &= \left(\frac{d(v_\theta/r)}{dr}\right)_{r=r_i,r_o} \\ &= \left(\frac{d(v_\phi/r)}{dr}\right)_{r=r_i,r_o} \\ &= 0. \end{aligned} \tag{4.25}$$

At the inner boundary, the radial specific entropy gradient is set to

$$\left(\frac{ds}{dr}\right)_{r=r_i} = \left(\frac{ds'}{dr}\right)_{r=r_i} = 0, \tag{4.26}$$

therefore there is no diffusive entropy flux across this boundary. At the outer boundary, the specific entropy is set to

$$s(r = r_o) = 0. \tag{4.27}$$

The functional form of the internal heating Q profile in *Rayleigh* is solely dependent upon the background pressure profile:

$$Q(r, \theta, \phi) = \alpha \left(\bar{p}(r) - \bar{p}_o\right), \tag{4.28}$$

where α is a normalisation constant chosen such that

$$L_* = 4\pi \int_{r_i}^{r_o} Q(r) r^2 \, dr, \tag{4.29}$$

where L_* is the stellar luminosity, and $\bar{p}(r)$ is the mean pressure at a given point r. The thermal energy flux $F(r)$ required to be transported via convection and conduction across a spherical surface at radius r is then

$$F(r) = \frac{1}{r^2} \int_{r_i}^{r_o} Q(r') r'^2 \, dr'. \tag{4.30}$$

The choice of N_ρ influences the internal heating profile, with heating becoming more focussed near the inner boundary with increasing N_ρ (Featherstone and Hindman 2016). We finally define a flux-based Rayleigh number (see, e.g., Featherstone and Hindman 2016) as a measure of the convective driving in these simulations (a rough measure of the ratio of buoyancy driving to viscous and thermal dissipation):

Parameter	Value
N_r	256
N_θ	768
M_i [g]	4.345×10^{31}
$\bar{\rho}_i$ [g cm^{-3}]	75.543
c_p [erg g^{-1} K^{-1}]	3.5×10^8
n	1.5
N_ρ	4.0
r_i [cm]	5×10^9
r_o [cm]	$1.96 \times 10^{10} \equiv R_\odot$
L_* [erg s^{-1}]	$3.846 \times 10^{33} \equiv L_\odot$

Table 4.3: Input parameters identical for all of the *Rayleigh* simulations used in this chapter, where N_r and N_θ are the number of radial and θ points in the domain, respectively, M_i, ρ_i, and r_i are the mass, density and radius at the inner boundary, respectively, c_p is the specific heat capacity (at constant pressure), n is the polytropic index, N_ρ is the number of density scale heights, r_o and L_* are the radius and luminosity at the outer boundary, respectively, and $R_\odot$ and $L_\odot$ are the solar radius and luminosity, respectively.

$$\mathrm{Ra}_F = \frac{\tilde{g}\tilde{F}H^4}{c_p\tilde{\bar{\rho}}\tilde{\bar{T}}\nu\kappa^2}, \tag{4.31}$$

where g is the gravitational acceleration, F is the imposed heat flux, H is the height of the domain, c_p is the specific heat capacity (at constant pressure), $\bar{\rho}$ and $\bar{T}$ are the reference state density and temperature, respectively, ν and κ are the kinematic viscosity and the thermal diffusivity, respectively, and the tilde represents a global average of the given variables.

Table 4.3 gives the input parameters used for all of the simulations, and Table 4.4 gives the input parameters that vary across the simulations, and the associated nondimensional parameters. All of these hydrodynamic simulations were performed until they reached a statistical steady state. Viscosities and diffusivities in these simulations are considered to be eddy viscosities and diffusivities (see Section 2.6.2), resulting in much larger values compared to those found in the Sun. In the upper part of the convection zone in the Sun, $\kappa \sim 10^5$ cm s^{-1} and $\nu \sim 1$ cm s^{-1} (Miesch 2005), whereas in these simulations, $\kappa \sim 10^{12}$ cm s^{-1} and $\nu \sim 10^{11}$ cm s^{-1}. Despite these differences, some of these simulations reach a state in which the amplitude of convective motions is effectively independent of κ and ν, as shown in Section 4.3.2.

Model [$\Omega_\odot$]	Ω [cm^2 s^{-1}]	κ_o [10^{12}] [cm^2 s^{-1}]	ν_o [10^{11}]	Pr	Ek [10^{-3}]	Ra$_F$ [10^6]
`G-Aa`	0.25	1.2	4	$0.\dot{3}$	2.89	1.40
`G-Ab`	0.25	1.5	5	$0.\dot{3}$	3.61	0.71
`G-Ac`	0.25	1.8	6	$0.\dot{3}$	4.33	0.41
`G-Ad`	0.25	2.4	8	$0.\dot{3}$	5.77	0.18
`G-Ae`	0.25	3.6	12	$0.\dot{3}$	8.66	0.05
`G-Af`	0.25	4.8	16	$0.\dot{3}$	11.55	0.02
`G-Ag`	0.25	6.0	20	$0.\dot{3}$	14.43	0.01
`G-B`	0.50	1.2	4	$0.\dot{3}$	1.44	1.40
`G-C`	0.75	1.2	4	$0.\dot{3}$	0.96	1.40
`G-D`	0.90	1.2	4	$0.\dot{3}$	0.80	1.40
`G-E`	1.00	1.2	4	$0.\dot{3}$	0.72	1.40
`G-F`	1.10	1.2	4	$0.\dot{3}$	0.66	1.40
`G-G`	1.25	1.2	4	$0.\dot{3}$	0.58	1.40
`G-H`	1.50	1.2	4	$0.\dot{3}$	0.48	1.40
`G-I`	2.00	1.2	4	$0.\dot{3}$	0.36	1.40
`G-J`	4.00	1.2	4	$0.\dot{3}$	0.18	1.40

Table 4.4: Dimensional input parameters (that differ between simulations) and nondimensional parameters for the *Rayleigh* global simulations, where Ω is the rotation rate ($\Omega_\odot = 2.6 \times 10^{-6}$ s^{-1} is the solar rotation rate), κ_o and ν_o are the thermal diffusivity and kinematic viscosity at the outer boundary, respectively, Pr($\equiv \nu/\kappa$) is the Prandtl number (ratio of viscous to thermal diffusivity), Ek is the Ekman number (ratio of viscous to Coriolis forces), and Ra$_F$ is the flux-based Rayleigh number.

4.3.2 Global Convective Structures and Energy Balances

We start our investigation by looking at how the structure of convection, and the resulting energy balances, change as we modify the rotation rate in these simulations. Studies of rotating, stratified convective simulations have long shown that the structure of convection changes vastly with rotation rate (e.g., Gilman 1975; Gilman 1977; Gilman and Glatzmaier 1981; Gilman 1983; Browning et al. 2004; Miesch et al. 2008; Featherstone and Miesch 2015). Figure 4.11 illustrates the structure of convective flows at a single snapshot for the slowly rotating 0.25 $\Omega_\odot$ model `G-Aa`, showing the radial velocity v_r, the azimuthal velocity v_ϕ, and the specific entropy s, at both the deep interior (0.702 $R_\odot$) and near the surface (0.993 $R_\odot$). In this slowly rotating case, there are large scale convective cells, with asymmetries between the weak broad upflows (in red) and strong narrow downflows (in blue). Figure 4.12 shows these convective flows for the solar 1 $\Omega_\odot$ model `G-E`: there is still asymmetry between upflows and downflows, but the large scale convective cells are beginning to become smaller and stronger as rotation begins to dominate. The transition from a slow rotation "anti-solar" case, where flow at the pole rotates more rapidly than

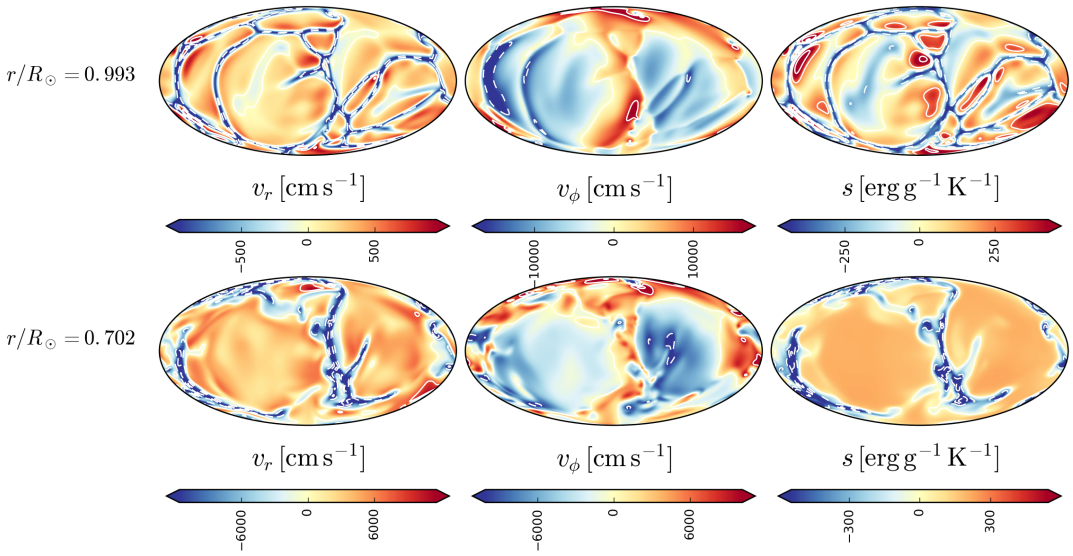

Figure 4.11: Shell slices of the 0.25 $\Omega_\odot$ model `G-Aa` near the surface (0.993 $R_\odot$) and in the deep interior (0.702 $R_\odot$) for radial velocity v_r, azimuthal velocity v_θ and specific entropy s. This simulation possesses an "anti-solar" profile, where flow at the pole rotates more rapidly than the equator. There are large convective cells present, and an asymmetry between weak broad upflows (red) and strong thin downflows (blue).

the equator, to a base rotation "solar-like" case, is apparent between these two rotation rates. Figure 4.13 shows these flows for the rapidly rotating 4 $\Omega_\odot$ model `G-J`: convective cells are beginning to align along the axis of rotation, in the form of "banana cells", which are comparable to the most unstable modes for the linear onset of convection in rapidly rotating spherical shells (see, e.g., Busse and Cuong 1977; Busse 1978). There is more isotropic downflow near the poles. These simulations have similar convective flow when compared to previous studies analysing M-dwarf convection: the upflow/downflow asymmetry is a common feature of convection in domains at high density stratification (see, e.g., Nordlund et al. 2009), and the rotational influence on the pattern of convection (such as the shaping of "banana cells") has also been found in simulations of fully convective interiors (e.g., Browning 2008; Yadav et al. 2016).

As in the local simulations, convection results from heat flux being transported across the domain. By considering the total energy equation (see, e.g., Nordlund et al. 2009), one can define the different shell-averaged flux components that make up the energy flux balance of a simulation, consisting of the enthalpy flux

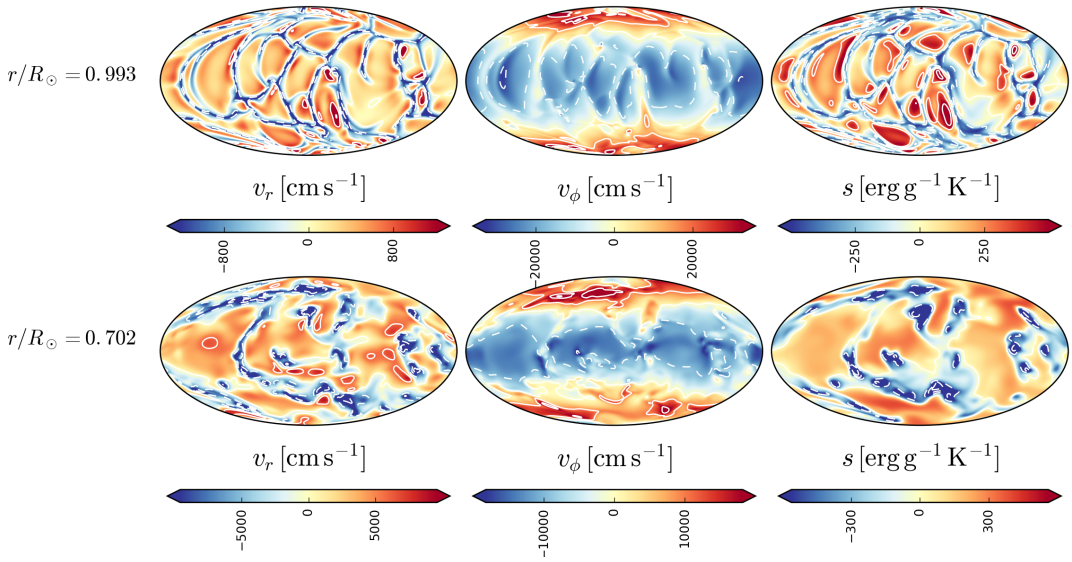

Figure 4.12: Shell slices of the 1 $\Omega_\odot$ model `G-E` near the surface (0.993 $R_\odot$) and in the deep interior (0.702 $R_\odot$) for radial velocity v_r, azimuthal velocity v_θ and specific entropy s. Convective cells are beginning to contract and become stronger, as rotation begins to dominate convection.

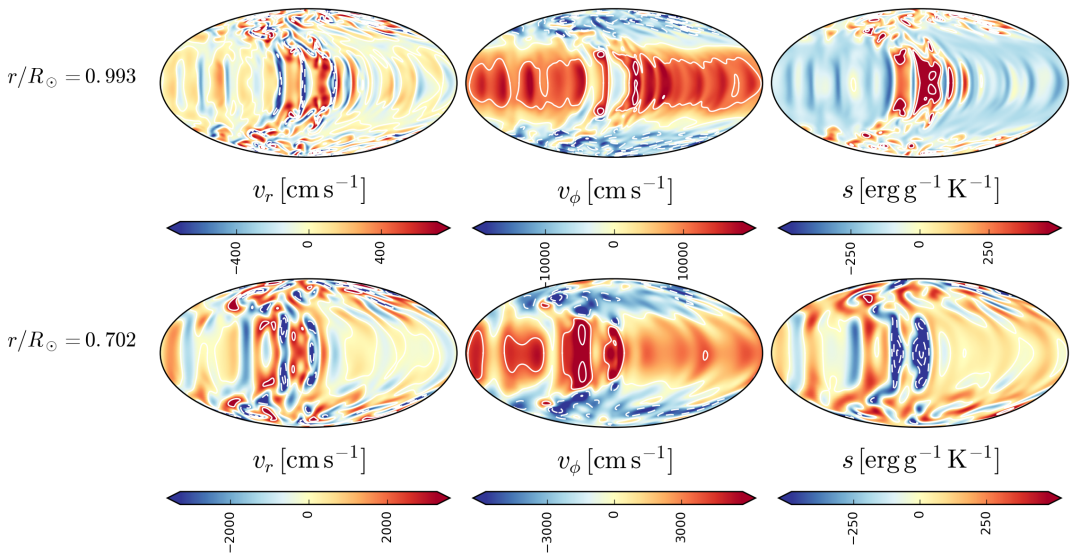

Figure 4.13: Shell slices of the 4 $\Omega_\odot$ model `G-J` 3D global convective simulation near the surface (0.993 $R_\odot$) and in the deep interior (0.702 $R_\odot$) for radial velocity v_r, azimuthal velocity v_θ and specific entropy s. Convective cells are taking on more of a "banana cell" pattern near the equator, as rotation further dominates convection.

$$F_{\mathrm{e}} = \bar{\rho} c_p \langle v_r T' \rangle, \tag{4.32}$$

the kinetic energy (KE) flux

$$F_{\mathrm{KE}} = \frac{1}{2} \bar{\rho} \left\langle v_r |\boldsymbol{v}|^2 \right\rangle, \tag{4.33}$$

the conductive flux

$$F_{\mathrm{cond}} = -\kappa \bar{\rho} \bar{T} \left\langle \frac{ds'}{dr} \right\rangle, \tag{4.34}$$

and the viscous flux

$$F_{\mathrm{visc}} = -\left\langle \boldsymbol{v} \cdot \boldsymbol{\mathcal{D}} \right\rangle, \tag{4.35}$$

where $\bar{\rho}$ and $\bar{T}$ are the reference density and temperature, respectively, c_p is the specific heat capacity (at constant pressure), $\boldsymbol{v}$ is the vector velocity, v_r is the radial component of the velocity, T' is the temperature perturbation, ds'/dr is the specific entropy perturbation gradient, κ is the thermal diffusivity, and $\boldsymbol{\mathcal{D}}$ is the vector viscous stress tensor. The sum of the above fluxes must equate to the net flux $F(r)$.

Analogous to the local simulations in Section 4.2.2, the typical energy balance of these global convective simulations consists of an upward (positive) enthalpy flux, a downward (negative) KE flux, and an upward (positive) conductive flux that forces the total luminosity to pass the outer boundary. The viscous contribution is negligible in all of these simulations, therefore is not included in these plots. The balance is dependent on the luminosity of the simulation, and also the rotation rate. Figure 4.14 shows the shell-averaged radial profiles of the energy balance components described above for model `G-Aa`. In this slowly rotating case, the enthalpy flux exceeds the total luminosity in the bulk of the simulation; the excess is balanced by a negative KE flux, which is due to the motions associated with convection being asymmetric between upflows and downflows. The conductive flux is small in the bulk of the simulation, but increases rapidly near the outer boundary to carry the flux outward. Figure 4.15 shows these profiles for model `G-E`: the enthalpy and KE flux both decrease slightly compared to model `G-Aa`, as rotation begins

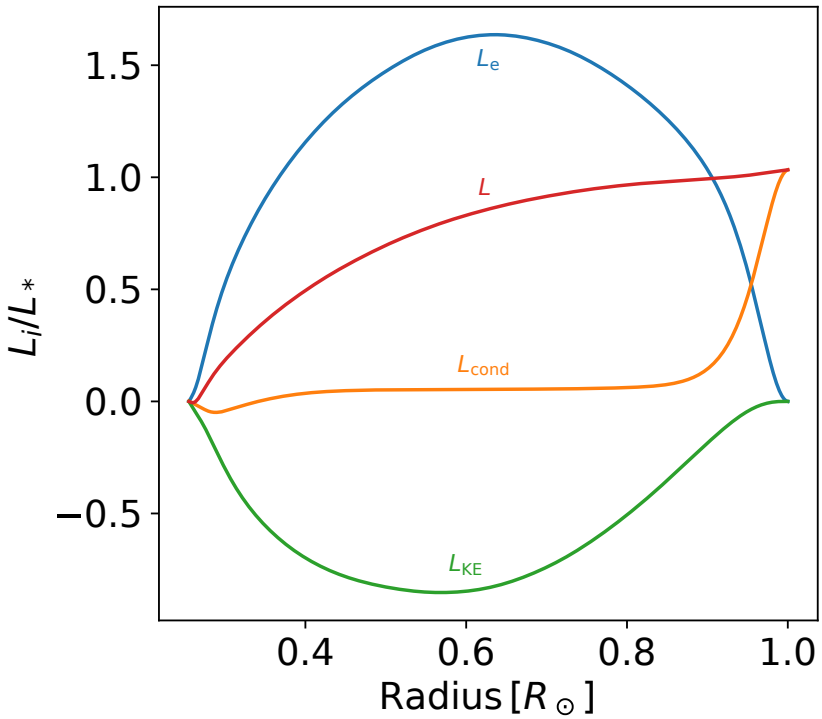

Figure 4.14: Shell-averaged energy balance profiles for model `G-Aa`. F_e exceeds the total flux in the bulk of the domain, which is balanced by F_{KE}, due to asymmetric convective flow. F_{cond} is negligible apart from at the upper boundary layer.

to dominate convection. This is even more evident in Figure 4.16 for model `G-J`, where the enthalpy and KE flux decrease substantially, causing the conductive flux to increase rapidly to carry the heat flux. These trends are largely in keeping with what is expected from analytical theory. As one increases the rotation rate, the critical Rayleigh number, $\mathrm{Ra}_{F,c}$, of a simulation, which is the value of Ra_F at which convection onsets, increases. Chandrasekhar (1953) showed analytically that $\mathrm{Ra}_c \propto \mathrm{Ek}^{-4/3} \propto \Omega^{4/3}$ for rapidly rotating convection, where Ek is the Ekman number (ratio of viscous to Coriolis forces). Therefore, at fixed Ra_F, the supercriticality ($\mathrm{Ra}_F/\mathrm{Ra}_{F,c}$), compared to the 0.25 $\Omega_\odot$ case, decreases with increasing rotation rate. This in turn tends to lead to less vigorous convection at more rapid rotation rates.

As with the local simulations, the conductive boundary layers mimic the transition between convective and radiative heat transfer in stars, which in turn sets up the specific entropy contrast. Therefore, we are motivated to investigate the specific entropy, and its gradient, as a function of rotation rate, in the next section.

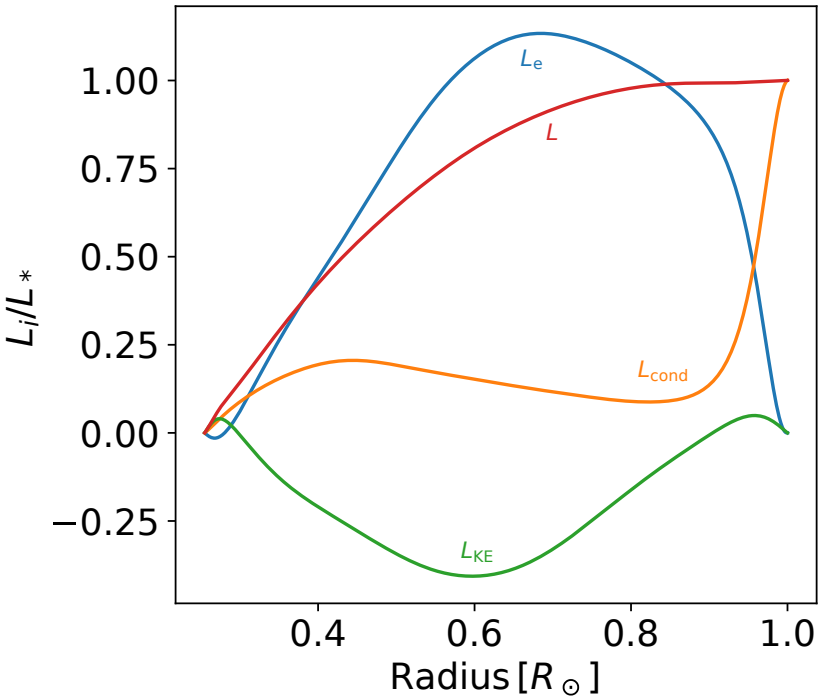

Figure 4.15: Shell-averaged energy balance profiles for model `G-E`. F_e and F_{KE} begin to decrease at this more rapid rotation rate, and F_{cond} is becoming non-negligible in the bulk of the domain, as rotation dominates over convection.

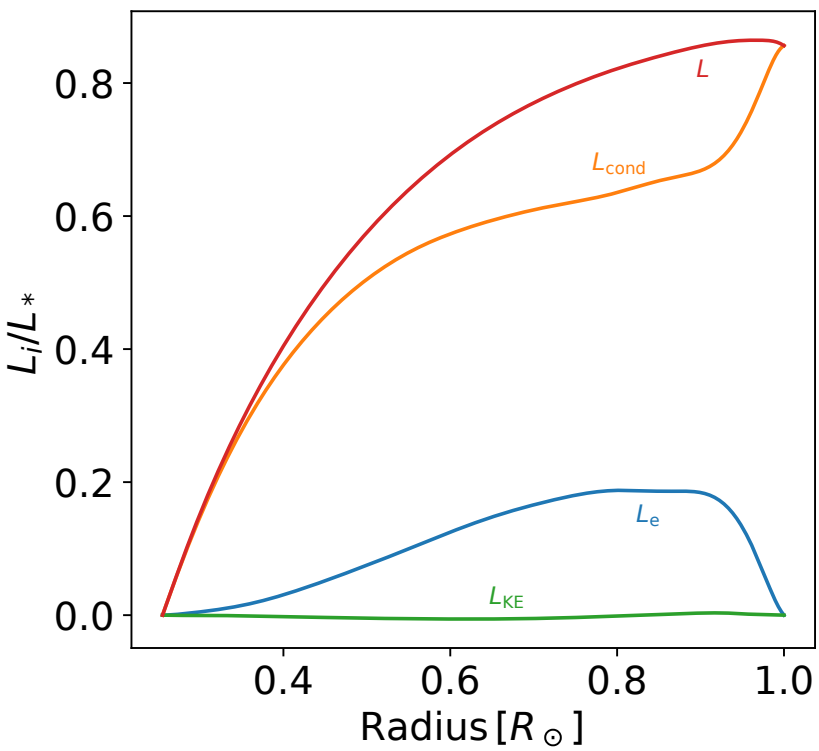

Figure 4.16: Shell-averaged energy balance profiles for model `G-J`. At this rotation rate, F_e and F_{KE} decrease substantially, thus F_{cond} increases to compensate.

4.3.3 Entropy in Global Rotating Simulations: Comparisons to Mixing Length Theory

In these global simulations of convection, the transition between convection and radiation does not exist as it does for real stars. In order to set up the specific entropy contrast Δs, we use conductive boundary layers to take over from the enthalpy flux and carry the remaining heat flux upward. In this section, we investigate how the specific entropy is modified in the presence of rotation for these global cases. Some of the changes in the specific entropy and its gradient will be caused by the imposed boundary conditions, but some will be representative of real physical effects. To help distinguish between these, we turn first to an analysis of the heat transport in the absence of rapid rotation, which provides some insight into boundary given effects, before turning to cases with rapid rotation rates.

In Figure 4.17, we plot the shell-averaged specific entropy s as a function of radius for the 0.25 $\Omega_\odot$ simulations with changing Ra_F. The profile shape is similar to that of our 1D stellar structure models in Chapter 3: the specific entropy asymptotically converges with depth toward the adiabat, s_{ad}. The outer boundary value of s is fixed at zero for all plotted simulations, as per our boundary condition. As one increases Ra_F, i.e., the convective driving of the simulation, the specific entropy profile converges to a more isentropic solution, i.e., $ds/dr \to 0$ in the bulk of the domain, and s_{ad} increases. s_{ad} is equivalent to the specific entropy contrast Δs in these simulations, as $s(r = r_o) = 0$. The entropy contrast Δs is directly related to ds/dr:

$$\Delta s = \int_{r_o}^{r_i} \left(\frac{ds}{dr}\right) dr \equiv s_{\mathrm{ad}}, \tag{4.36}$$

thus s_{ad} depends solely on the specific entropy gradient ds/dr.

We plot the shell-averaged specific entropy gradient ds/dr, and $\log_{10}(|ds/dr|)$ (to illustrate the bulk properties), as a function of radius for the same simulations, in Figure 4.18. The inner boundary ds/dr value is fixed at zero, and the absolute value at the outer boundary, $|ds/dr|_{r=r_o}$, increases with Ra_F. This is a result of the requirement

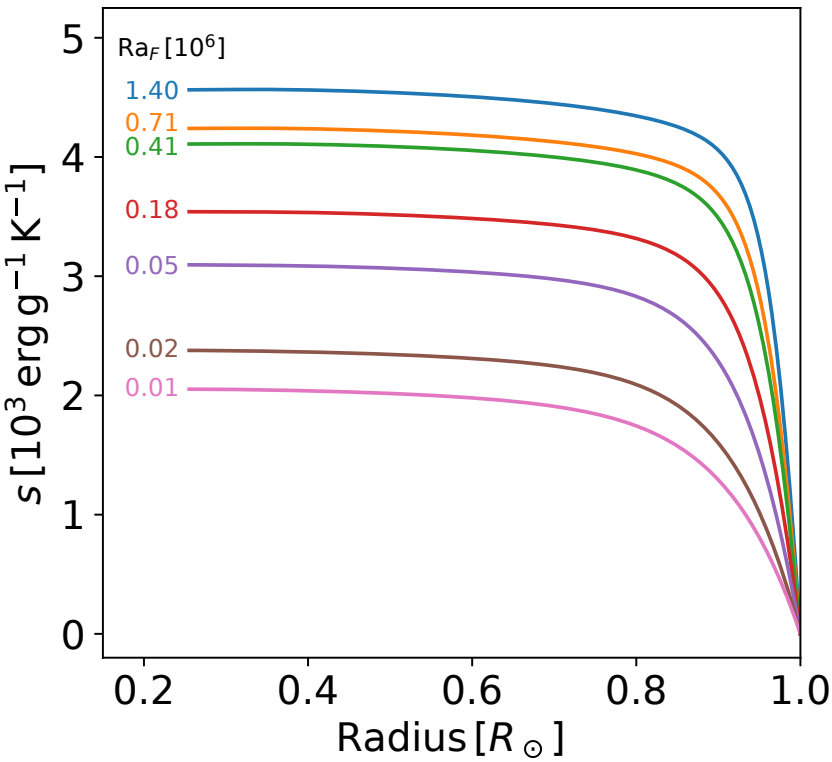

Figure 4.17: Shell-averaged s as a function of radius, for 0.25 $\Omega_\odot$ 3D global convective simulations at different Ra_F. Increasing Ra_F increases s_{ad}, i.e., the asymptotic value of specific entropy in the bulk of the domain.

that the heat flux per surface area leaving the outer boundary, which is carried by the conductive flux in this region, is equivalent to the defined stellar luminosity. Using Equation (4.34), $ds/dr (= ds'/dr$, because $\bar{s}$ is isentropic) at the outer boundary must equate to

$$\begin{aligned}\left(\frac{ds}{dr}\right)_{r=r_o} &= \left(\frac{ds'}{dr}\right)_{r=r_o} \\ &= -\frac{L_*}{4\pi r_o^2 \kappa \bar{\rho}_o \bar{T}_o},\end{aligned} \tag{4.37}$$

where $\bar{\rho}_o$ and $\bar{T}_o$ are the background density and temperature at the outer boundary. At constant L_* (as is the case for these simulations), it is evident that $|ds/dr|_{r=r_o} \propto \kappa^{-1}$, resulting in an increasing $|ds/dr|_{r=r_o}$ with increasing $\mathrm{Ra}_F \propto \nu^{-1}\kappa^{-2}$. We show this scaling with κ in Figure 4.19, demonstrating that our simulations are approximately in thermal balance. The behaviour of $|ds/dr|$ in the bulk of the domain also varies with Ra_F: on average, $|ds/dr|$ is lower at higher Ra_F in the bulk of the domain, as it becomes more

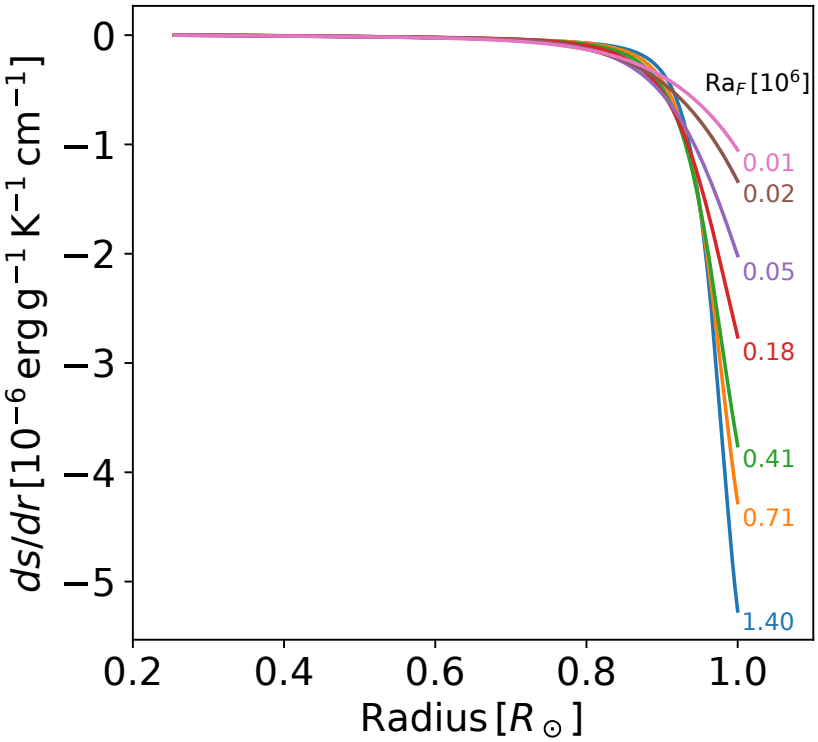

(a)

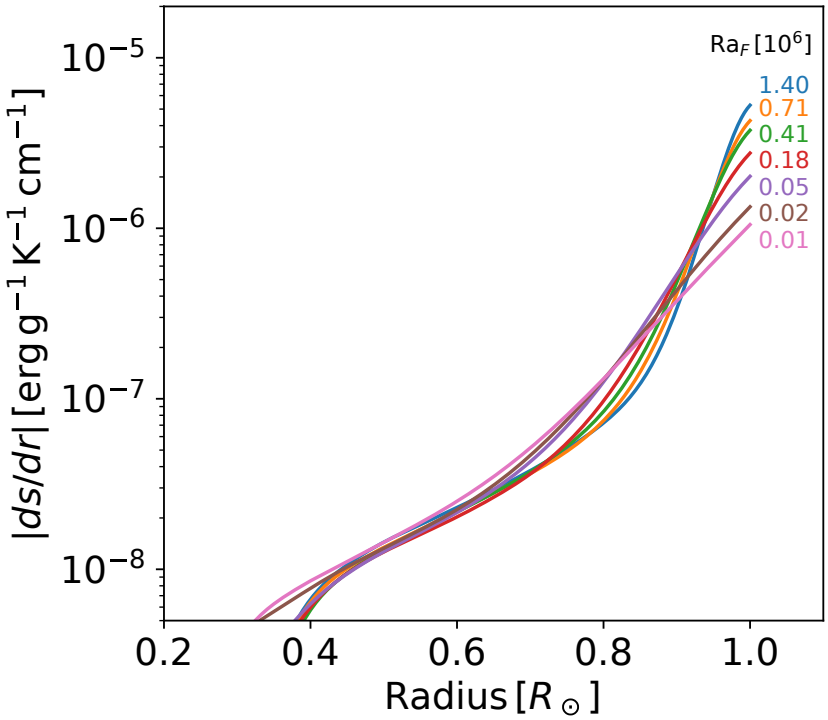

(b)

Figure 4.18: Shell-averaged (a) ds/dr, (b) $\log_{10}(|ds/dr|)$ as a function of radius, for 0.25 $\Omega_\odot$ 3D global convective simulations at different Ra_F. Increasing Ra_F increases $|ds/dr|$ at the outer boundary. In the bulk of the domain, $|ds/dr|$ (on average) is lower at higher Ra_F, converging toward a near-isentropic solution.

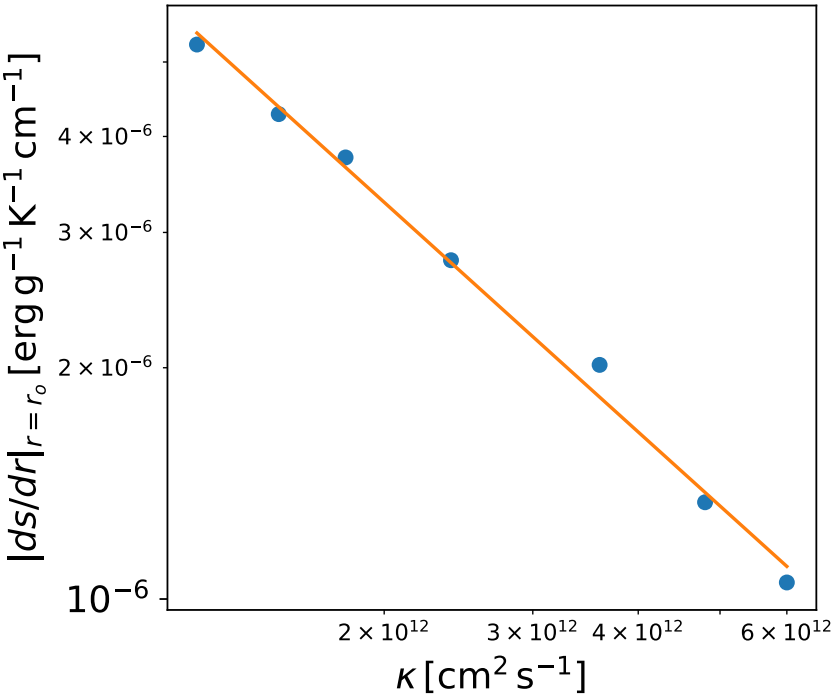

Figure 4.19: Shell-averaged $|ds/dr|_{r=r_o}$ as a function of κ, for 0.25 $\Omega_\odot$ 3D convective simulations at different Ra_F, where $|ds/dr|_{r=r_o}$ decreases with increasing κ (decreasing Ra_F). The orange line depicts $|ds/dr|_{r=r_o} \propto \kappa^{-1}$, demonstrating that this boundary condition is solely dependent on κ, for simulations at fixed luminosity.

isentropic. As Ra_F increases, the specific entropy contrast Δs increases, and the radial domain at which the specific entropy profile remains near-isentropic ($ds/dr \to 0$) increases, i.e., the specific entropy jump from the adiabat to the upper boundary value occurs closer to the upper boundary, resulting in a sharper drop at higher Ra_F.

As the profile of ds/dr is a function of both physical (in the bulk of the domain) and simulation effects (as a result of imposed boundary conditions), s_{ad} is also a function of both. To investigate this, we first looked at how the different properties of the specific entropy depend on Ra_F. In global simulations, we are limited to what value of Ra_F we can use, which means the adiabat may not be fully correct. As a result, we typically perform simulations at different Ra_F and attempt to find a scaling. In Figure 4.20, we show the globally-averaged KE to eventually plateau as a function of Ra_F for the 0.25 $\Omega_\odot$ cases, suggesting that convective flow properties will be similar as Ra_F increases further. In Figure 4.21, we plot s_{ad} as a function of Ra_F for the 0.25 $\Omega_\odot$ simulations. At higher Ra_F, s_{ad} appears to scale as $s_{\mathrm{ad}} \propto \mathrm{Ra}_F^{0.12}$, demonstrating that s_{ad} increases as the convective driving is increased. In Figure 4.22, we look at the shell-averaged $|ds/dr|$, averaged in the

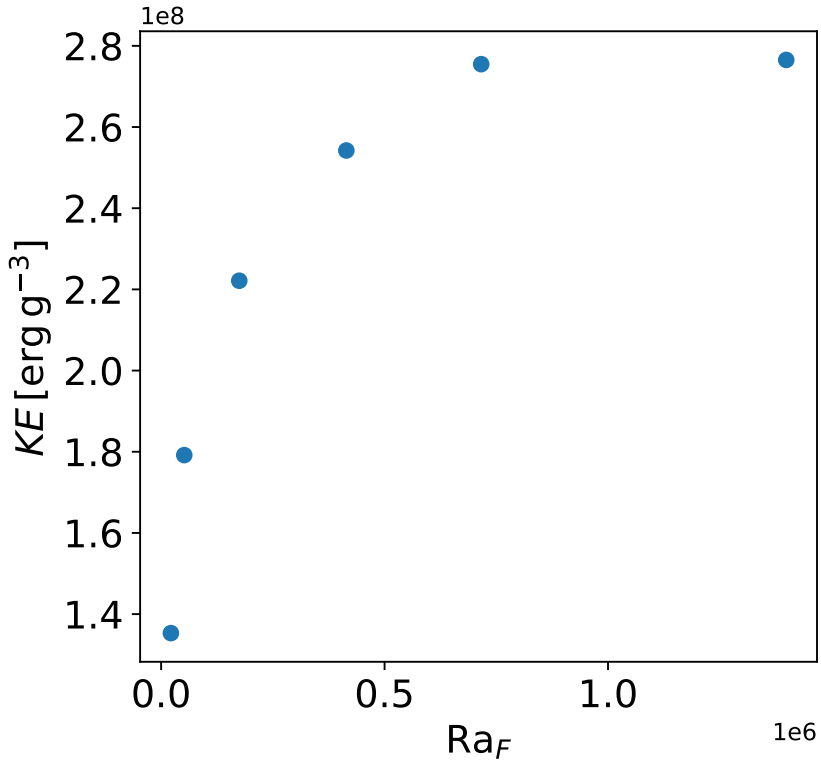

Figure 4.20: Globally-averaged kinetic energy as a function of Ra_F, for 0.25 $\Omega_\odot$ 3D global convective simulations. It appears to eventually plateau with increasing Ra_F, suggesting that properties of the convective flow will be similar at even higher Ra_F.

middle third of the domain (0.5-0.75 $R_\odot$), i.e., $|\langle ds/dr\rangle|$, as a function of Ra_F for the same models; we choose this value in order to capture more of the physical effects in the bulk of the domain, away from the imposed boundaries. This is analogous to Barker et al. (2014) using the average of the middle third value of $d\langle T\rangle/dz$ when scaling with rotation rate. At higher Ra_F, $|\langle ds/dr\rangle|$ appears to scale as $|\langle ds/dr\rangle| \propto \mathrm{Ra}_F^{-0.03}$, demonstrating that this middle-third value decreases with increasing Ra_F.

The supercriticality of the more rapidly rotating simulations for fixed Ra_F is lower than that for the lower rotation rates. Thus, as it may not be possible to determine the "correct" absolute entropy contrast Δs in these rotating simulations, we look at variations in the specific entropy gradient in the bulk of the domain to infer any possible Ω dependence. Using $|\langle ds/dr\rangle|$ allows easier comparison between simulations with changing rotation rate. In Figure 4.23, we plot the shell-average of $|\langle ds/dr\rangle|$ as a function of rotation rate, for all simulations at $\mathrm{Ra}_F = 1.40 \times 10^6$. The theoretical scaling of Barker et al. (2014), in terms of the specific entropy gradient rather than the temperature gradient,

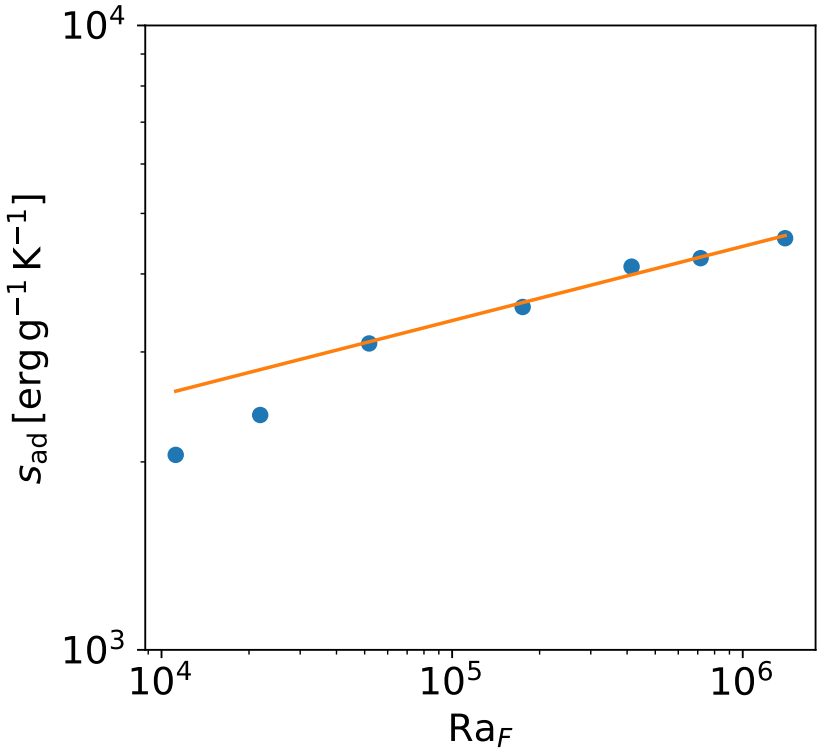

Figure 4.21: Shell-averaged $s_{\rm ad}$ as a function of Ra_F, for 0.25 $\Omega_\odot$ 3D global convective simulations. The orange line depicts $s_{\rm ad} \propto \mathrm{Ra}_F^{0.12}$, which describes the data well at high enough Ra_F.

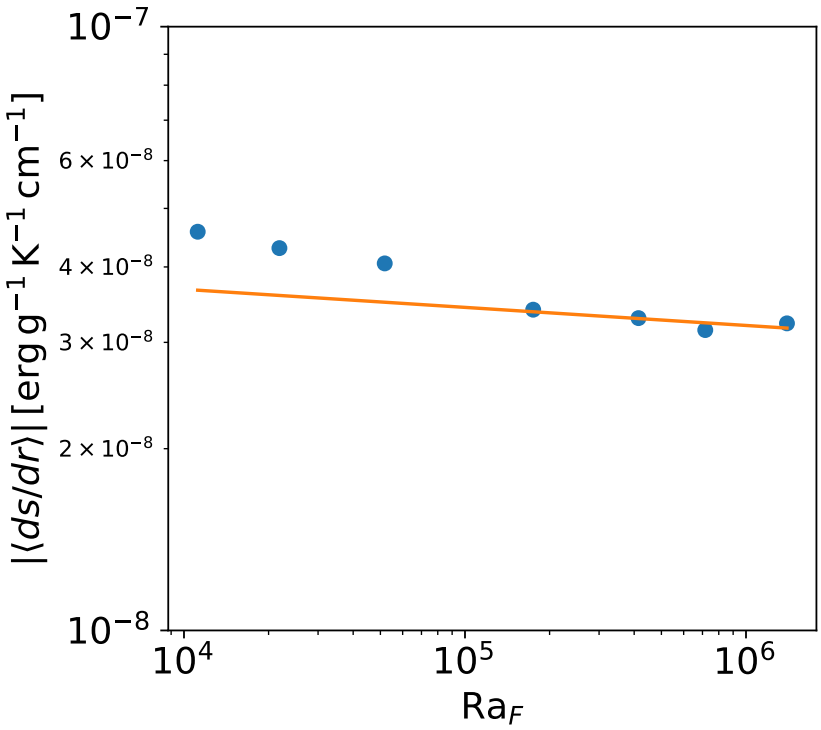

Figure 4.22: Shell-averaged middle-third average of the specific entropy gradient as a function of Ra_F, for 0.25 $\Omega_\odot$ 3D global convective simulations. The orange line depicts $|\langle ds/dr \rangle| \propto \mathrm{Ra}_F^{-0.03}$, which describes the data well at high enough Ra_F.

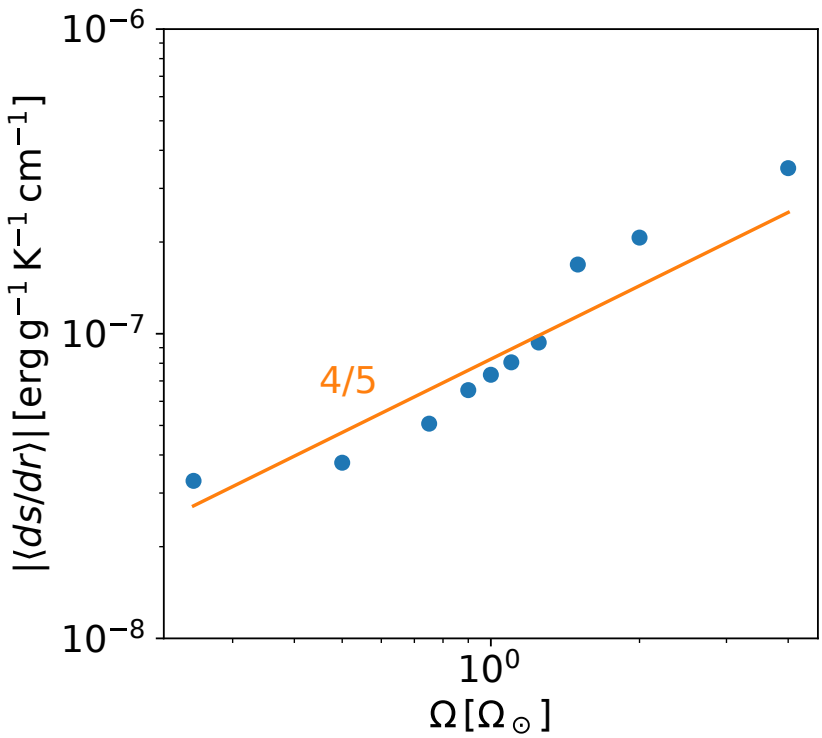

Figure 4.23: Shell-averaged $|\langle ds/dr\rangle|$ as a function of Ω, for fixed $\mathrm{Ra}_F = 1.40 \times 10^6$. For comparison, the orange line represents the scaling $|\langle ds/dr\rangle| \propto \Omega^{4/5}$. With increasing rotation rate, the supercriticality decreases; however, we still find the trend to be comparable to that of the scaling law mentioned.

i.e., $|\langle ds/dr\rangle| \propto \Omega^{4/5}$, is plotted in orange. The two agree remarkably well, despite the many effects present here (shear, latitude-dependence, etc.) that are not captured in the models of Barker et al. (2014), or in the previous theoretical work by Julien et al. (2012) and Stevenson (1979). This is a striking result, the implications of which are discussed in Section 4.4 below.

4.4 Discussion and Conclusion

The aim of this chapter is to gain a better understanding of how the heat transport and stellar structure is influenced by rotation, and determine whether mixing length theory (MLT) is capable of describing the dynamical behaviour of convection in these simulations. To investigate this, an understanding of how convection behaves for the non-rotating case is first required. We are motivated to compare the entropy content of these simulations, due to its strong links to the stellar structure (as explored in Chapter 3).

Because of the many physical effects present in 3D global simulations, such as shear, latitude, etc., we first look at how the dynamical behaviour of convective flow changes in 2D local "box in a star" simulations, in Section 4.2, as a function of the density stratification, in terms of changes in the specific entropy, and its gradient. Unfortunately, the artificial nature of this "local box" set up means it is hard to draw meaningful comparisons to MLT. The horizontally-averaged specific entropy profiles from these 2D simulations of convection have very different profiles to those found in our 1D stellar structure models in Chapter 3. For the lowest density stratification, approaching classic Rayleigh-Bénard convection in an unstratified medium, the specific entropy is fairly isentropic in the bulk of the domain as the supercriticality increases. However, with increasing density stratification (and supercriticality), regions near the bottom boundary become increasingly subadiabatic, affecting the entropy content of these simulations. This is a surprising result, considering that the enthalpy flux is positive throughout the bulk of the domain, even in the stably stratified region. The subadiabatic regions near the bottom boundary for these higher density stratifications may be why our profiles do not have a well-defined adiabatic trend, and even exceed the bottom boundary specific entropy in the bulk of the domain. The development of a subadiabatic layer has been found in previous studies of convective simulations (e.g., Korre et al. 2017; Käpylä et al. 2017). In Käpylä et al. (2017), for example, their local Cartesian hydrodynamic simulations of overshooting convection appear to have a substantial subadiabatic region in the lower part of the convection zone. They show it is possible for a subadiabatic layer to produce an upward enthalpy flux, because of downflows bringing low entropy material from the upper boundary to the region below, thus they conclude that convection is nonlocal in these calculations. They demonstrate that there may be a non-gradient term neglected in the mean-field enthalpy flux expression, called the Deardorff flux (e.g., Deardorff 1966), which is described as a counter-gradient flux. This term remains positive, independent of the sign of the specific entropy gradient, and is suggested to be the possible dominant contribution to the enthalpy flux in such layers.

If the subadiabatic layer turns out to be a real physical effect, it would suggest that fully convective stars aren't actually fully convective. In stars similar to the Sun, the dynamo generating the magnetic field is thought to occur due to shearing at the tachocline,

where the radiative core transitions into the convective envelope, as a result of differential rotation (Spiegel and Zahn 1992). Fully convective stars are assumed to not have a tachocline, thus their dynamos are expected to greatly differ from the solar-like case. However, many authors have allegedly found the rotation-activity relationship to follow the same correlation in both solar-like and low-mass fully convective stars (e.g., Mohanty and Basri 2003; Reiners and Basri 2008; Reiners et al. 2009; Browning et al. 2010; Wright et al. 2011; McLean et al. 2012; Newton et al. 2017). A subadiabatic region in these fully convective stars may help explain this lack of change at the boundary of full convection. These subadiabatic layers may have a physical origin, linked partly to the increasing amount of viscous dissipation in these simulations, as a function of supercriticality and density stratification (Currie and Browning 2017). However, they may also be somewhat artificial in origin, due to our imposed specific entropy gradient at the bottom boundary (see Equation (4.16)), rather than fixing $(ds/dz)_{z=0} = 0$ and using a heating function. The hard lower wall, which forces descending convective flows to decelerate, likely also plays a role in the vicinity of the boundaries. Thus, we turned to analysing bulk properties of the domain, namely the middle-third average of the specific entropy (and its gradient), which is normalised by the specific entropy contrast for a fully conductive case. We find that the normalised specific entropy converges toward an isentropic state as a function of supercriticality, for all density stratifications. However, the adiabat that it converges toward is an increasing function of density stratification, as a result of the increasing subadiabatic boundary layers driving the specific entropy upward in the bulk of the domain; this demonstrates that these layers influence properties in the bulk of the domain.

As these local simulations are generally not fully indicative of real stars, we turn to full 3D global simulations. These simulations have caveats of their own, but they allow us to include more realistic physical effects in the modelling of convection. In Section 4.3, we look at how the dynamical behaviour of convective flow changes in 3D global simulations as a function of rotation rate, by investigating how the specific entropy, and its gradient, change as a result. The shell-averaged specific entropy profiles from these 3D simulations of convection have a similar profile to those found in our 1D stellar structure models in Chapter 3. However, in these global calculations, Δs is also a function of shear flow, latitude, and other effects. In these simulations, the specific entropy gradient at the upper

boundary is fixed by the thermal diffusivity κ (for fixed stellar luminosity L_*). The radial component of the motion, which is essentially the convective flow, is forced to zero at the upper boundary (impenetrable wall). This results in the convective flux dropping to zero within this region, thus the conductive flux grows to compensate. As a result, the specific entropy gradient will (negatively) grow near the boundary in order to drive 1 L_* of luminosity out of the upper boundary to maintain a steady state, thus setting the specific entropy contrast. Therefore, Δs has nothing to do with the photospheric properties of a star in these simulations, but is rather a result of the driving of flux near the boundary.

By looking at the absolute middle-third average of the specific entropy gradient, $|\langle ds/dr \rangle|$, we encapsulate more of the physical effects on the convective flow, rather than simulation effects due to the imposed boundary conditions. This quantity is shown to scale with Ra_F in the slow rotator case (0.25 $\Omega_\odot$) at high enough Ra_F. We also investigate how $|\langle ds/dr \rangle|$ changes as a function of rotation rate. Our simulation data is consistent with the scaling law previously derived for rapidly rotating convection, namely $|\langle ds/dr \rangle| \propto \Omega^{4/5}$. This was predicted in the MLT formulation of Stevenson (1979), the asymptotic analysis of Julien et al. (2012), and supported by the local layer simulations of Barker et al. (2014). We are aware that it is not a perfect fit, possibly due to the supercriticality decreasing with rotation rate at fixed Ra_F, and a variety of different physical effects, such as shear and latitudinal-dependence. However, the approximate correspondence with $|\langle ds/dr \rangle| \propto \Omega^{4/5}$ is still striking.

Overall, we have shown that the heat transport is influenced by rotation rate in global simulations of convection, and that comparisons with MLT can be made to estimate the dynamical behaviour of these convective flows. Whether or not this has a noticeable impact on the stellar structure of a star is not yet clear. As found in Chapter 3, the "rotating" MLT reformulation of Stevenson (1979), or Barker et al. (2014), are unable to produce noticeable changes in the stellar structure of these 1D models. This is because the stellar radius in these models is primarily determined by the adiabat at which the star lies, which in turn is established by the specific entropy contrast resulting from the transition from convective to radiative heat transport in the surface layers. These layers are completely uninfluenced by rotation in our 1D models, as convective velocities increase

rapidly near the photosphere (Ro $\gg$ 1), resulting in rotation rate having a negligible impact on the adiabat, and hence on the stellar radius. The adiabat and specific entropy contrast in these global calculations are a function of the imposed boundary conditions, as well as physical effects, making direct comparison between these simulations and 1D stellar structure models difficult. However, as stated in the introduction, the ultimate goal is to understand how both rotation and magnetic fields can influence the heat transport of convection in these simulations and whether comparisons to MLT can be made, and we have established a future path toward this by first looking at non-rotating and rotating cases alone.

Chapter 5

The Conclusion

5.1 Concluding Remarks

In this thesis, we investigated how heat transport and stellar structure are influenced by rotation and magnetic fields, using 1D stellar structure models and reformulations of mixing length theory (MLT), 2D local simulations of convection, and 3D global simulations of convection. In particular, we examined how these effects can be regarded as a function of the entropy content of a star.

In Chapter 2, we discussed the numerical tools and computational methods used to perform these calculations. First, we introduced the magnetohydrodynamic (MHD) equations, which govern the dynamics of both the convective flow and the magnetic fields. We then introduced the 1D stellar equations, which (in the form taken here) assume spherical symmetry, hydrostatic equilibrium, and no magnetic fields, followed by a description of the criterion onset of convection, and a derivation of MLT. This was followed by a description of how the 1D stellar evolution code MESA, which we used to compute 1D stellar structure models in Chapter 3, applies these techniques. We then reverted back to the full MHD expressions, and discussed approximations to numerical methods, namely the finite-difference method and the (pseudo-)spectral method, and approximations to the MHD equations, including the anelastic approximation and the large-eddy formalism, typically used in simulations of convection. These methods allow the MHD equations to be solved in

a more tractable form, and allow for the investigation of flows in particular astrophysical environments. The practicality of some of these techniques were first tested in a simple 2D convection code we built, which was designed to model Rayleigh-Bénard convection. This was followed by brief descriptions of the convection codes used in Chapter 4, *Rayleigh* and Dedalus.

Motivated by the fact that observations of some low-mass stars appear to have larger radii than what is typically predicted by (pre-)main-sequence standard 1D stellar models, in Chapter 3, we incorporated two reformulations of MLT into our 1D stellar structure models, by Stevenson (1979) and MacDonald and Mullan (2014), to include rotational and magnetic effects, respectively. We gave a review of the links between entropy, convective efficiency, and stellar radii for standard 1D models, where the convective efficiency of a model is determined by a depth-independent MLT parameter $\alpha_{\rm MLT}$. Here, we provided formulae that link changes in $\alpha_{\rm MLT}$ to changes in the specific entropy in the bulk of the interior, and the stellar radius. We looked at how the "rotating" reformulation of MLT (Stevenson 1979) affects the stellar structure: we found rapid rotation effects to be negligible in these 1D models, because the adiabat at which the entropy lies in the bulk of the stellar interior is influenced mainly by the entropy contrast constructed in the surface layers, where convective velocities are rapid ($\mathrm{Ro} \gg 1$) and are thus unaffected by rotation. This was followed by looking at how "magnetic" reformulation of MLT (MacDonald and Mullan 2014) affects the stellar structure, using maximum magnetic field strengths $\sim 10^4$ G as supported by simulations (e.g., Yadav et al. 2015; Browning et al. 2016). Noticeable radius inflation was found in these cases, with pre-main-sequence models a factor of two more inflated than main-sequence models, where nuclear burning begins to strongly influence the adiabat (hence the stellar radius). As these reformulations of MLT essentially modify the superadiabatic gradient profile (and as a result, the specific entropy), we derive a depth-dependent $\alpha_{\rm MLT}$ that can be expressed in terms of the rotation rate or the magnetic field strength. This can be used to mimic the effects of these reformulations without the requirement of modifying the MLT formulation in MESA. We noted that these reformulations of MLT have their own limitations, and that this depth-dependent $\alpha_{\rm MLT}$ would be incredibly difficult to calibrate via observations. Further constraints on how convective heat transport is affected as a function of depth could be made using comparisons with

3D simulations of convection, which may provide further insight into how magnetism and rotation influence these stellar objects.

In Chapter 4, we made comparisons between MLT and simulations of convection, mainly by looking at the entropy content of these calculations. We looked at the dynamical behaviour of convection in 2D local simulations, produced using the Dedalus code, as a function of the density stratification, to first get an understanding of how convection behaves in the absence of rotation and magnetism. Profiles of horizontally-averaged specific entropy and its gradient are not particularly similar to those produced via 1D stellar structure models in the previous chapter. With increasing density stratification (and supercriticality), subadiabatic regions near the bottom boundary become more apparent, causing the specific entropy in the bulk of the domain to actually exceed the bottom boundary value. It is possible that this is a result of physical effects, such as the increased amount of viscous dissipation for more supercritical, highly stratified cases, but may also be partly artificial in origin, due to the imposed boundary conditions. We suggest that these subadiabatic regions affect the bulk properties of the specific entropy: the adiabat toward which the simulation converges increases with density stratification. Due to the artificial nature of local simulations, we then turn to 3D global simulations of convection, which can include more realistic physical effects, and investigate the convective behaviour, via the entropy content of the domain, as a function of rotation rate. Shell-averaged specific entropy profiles are similar to those in our 1D stellar structure models, but the entropy contrast between the bulk of the domain and the upper boundary is determined via conductive boundary conditions, rather than photospheric properties. To isolate these simulation effects, we looked at the middle-third average of the specific entropy gradient $|\langle ds/dr \rangle|$ as a function of rotation rate Ω, and our data is broadly consistent with the theoretical scaling relations of Stevenson (1979), Julien et al. (2012), and Barker et al. (2014), i.e., $|\langle ds/dr \rangle| \propto \Omega^{4/5}$.

5.2 Future Work

Overall, our findings show that rotation and magnetism are both important to consider when investigating the structure and heat transport of these astrophysical objects. In this section, we discuss potential directions in which the work of this thesis can be expanded.

Firstly, we wish to investigate whether dissipative heating effects could influence the stellar structure in 1D models, by looking further into how dissipation links to properties of convection and MLT. Currie and Browning (2017) explore the possibility of strongly stratified convective fluids having dissipative heating rates that exceed the luminosity carried by convection, which may modify the stellar structure, using 2D hydrodynamic local simulations of convection in a Cartesian layer under the anelastic approximation (identical to those used in Chapter 4). In standard models, the total heat flux F in the bulk of the convection zone is often assumed to be equivalent to the convective heat flux $F_{\rm conv}$. However, in strongly stratified cases, there is an additional flux term $F_{\rm other}$ to consider, i.e., the sum of kinetic energy, Poynting and viscous fluxes, that influences the local heating and cooling in the layer. This is a function of the dissipative heating rate, which itself increases with density stratification. Fundamentally, MLT provides an expression of how stellar flux is transported given a temperature (or entropy) gradient. To investigate the effects of dissipative heating, it is necessary to investigate whether changes in the specific entropy gradient as a function of density stratification in these 2D simulations are important enough to implement into 1D models. In Chapter 3, we derived a prescription that links the local superadiabaticity, hence the specific entropy gradient, to a depth-dependent $\alpha_{\rm MLT}$ profile. If there is non-negligible correspondence between dissipative heating and the specific entropy gradient, we could be closer to understanding how $\alpha_{\rm MLT}$ changes locally under these conditions, allowing us to implement these effects into our non-standard 1D models. Our work in Chapter 4 (e.g., Figure 4.10) provides preliminary indications of just such a link.

Secondly, we wish to continue other aspects of our investigation into MLT comparisons with simulations of convection. In Chapter 4, we plot the absolute middle-third average of the specific entropy gradient as a function of rotation rate, and find that the

trend is similar to that of the scaling law expressed in Barker et al. (2014). However, our simulations are not at fixed supercriticality with increasing rotation rate. In the future, we wish to perform simulations at fixed supercriticality (determining a critical Rayleigh number using a linear code, analogous to Currie and Browning 2017), and see whether these calculations change the relation between specific entropy gradients and rotation rate. Furthermore, we wish to look at how other physical effects can influence this scaling with rotation rate: in particular, we would like to investigate the influence magnetism has on heat transport in these simulations of convection. In Chapter 3, we demonstrate the influence that magnetic fields have on 1D stellar structure models, using the "magnetic" reformulation of MLT by MacDonald and Mullan (2014), which essentially modifies the onset of convection criterion. Thus, we are motivated to see if any MLT comparisons can be made to (rotating) magnetic simulations of convection, and whether magnetism indeed influences heat transport in a similar way to that outlined by MacDonald and Mullan (2014). We will also examine how magnetically dependent the rotating scaling law of Barker et al. (2014) is.

The suggested future work above only scratches the surface of potential extensions that could be made to the work outlined in this thesis. The increasing power of computers and ever-improving observations of such objects have allowed us to probe deeper into the dynamical behaviour within a stellar interior. Not only does it help determine the internal dynamics of stars, but it could also provide insight into the search for habitable exoplanets, which are affected by the properties of its host star.

5.3 Further Acknowledgements

This research has been supported by the European Research Council, from the European Union's Horizon 2020 research and innovation programme, under grant agreement No. 337705 (CHASM), and by a Consolidated Grant from the UK STFC (ST/J001627/1).

Various HPC resources have been used in this work: the DiRAC Blue Gene Q Shared Petaflop system at the University of Edinburgh, operated by the Edinburgh Parallel Computing Centre on behalf of the STFC DiRAC HPC Facility, and funded by BEIS National

E-infrastructure capital grant ST/K000411/1, STFC capital grant ST/H008845/1, and STFC DiRAC Operations grants ST/K005804/1 and ST/K005790/1; the DiRAC Complexity system, operated by the University of Leicester IT Services, which forms part of the STFC DiRAC HPC Facility, funded by BEIS National E-Infrastructure capital grant ST/K000373/1 and STFC DiRAC Operations grant ST/K0003259/1; the University of Exeter supercomputer, ZEN, which is a DiRAC facility jointly funded by the STFC, the large facilities capital fund of BEIS, and the University of Exeter; ISCA, the new University of Exeter supercomputer. We also acknowledge PRACE for awarding us access to computational resources, namely Mare Nostrum based in Spain at the Barcelona Supercomputing Center, and Fermi and Marconi based at Cineca in Italy.

We thank Isabelle Baraffe for her helpful comments on a draft of our publication to the Astrophysical Journal. We also thank the referee for a thoughtful review that helped to improve that publication.

A majority of the post-processing of work presented in this thesis makes use of the `NumPy` Python module (Van Der Walt et al. 2011), and figures were created using the `Matplotlib` Python module (Hunter 2007). 1D stellar structure models in Chapter 3 were produced using the MESA code (Paxton et al. 2011; Paxton et al. 2013; Paxton et al. 2015; Paxton et al. 2017) (see Section 2.5). 2D hydrodynamical simulations of convection in Chapter 4 were created by fellow group member Dr. Laura Currie (Currie and Browning 2017), using the Dedalus code (Burns et al. 2016). 3D hydrodynamical simulations of convection in Chapter 4 were created by fellow group member Dr. Felix Sainsbury-Martinez (Sainsbury-Martinez et al., In preparation), using the *Rayleigh* code (Featherstone and Hindman 2016).

Bibliography

Abbett, W. P., M. Beaver, B. Davids, et al. 1997. 'Solar Convection: Comparison of Numerical Simulations and Mixing-Length Theory.' ApJ 480 (May): 395–399.

Aerts, C., J. Christensen-Dalsgaard, and D.W. Kurtz. 2010. *Asteroseismology.* Astronomy and Astrophysics Library. Springer Netherlands.

Arakawa, A. 1966. 'Computational Design for Long-Term Numerical Integration of the Equations of Fluid Motion: Two-Dimensional Incompressible Flow. Part I.' *Journal of Computational Physics* 1 (August): 119–143.

Arnett, D., C. Meakin, and P. A. Young. 2010. 'Convection Theory and Sub-Photospheric Stratification.' ApJ 710 (February): 1619–1626.

Aubert, J., T. Gastine, and A. Fournier. 2017. 'Spherical convective dynamos in the rapidly rotating asymptotic regime.' *Journal of Fluid Mechanics* 813 (February): 558–593.

Augustson, K., S. Mathis, and A. S. Brun. 2017. 'Simple Scaling Relationships for Stellar Dynamos.' *ArXiv e-prints* (January).

Aurnou, J. M., M. A. Calkins, J. S. Cheng, et al. 2015. 'Rotating convective turbulence in Earth and planetary cores.' *Physics of the Earth and Planetary Interiors* 246 (September): 52–71.

Babcock, H. W. 1961. 'The Topology of the Sun's Magnetic Field and the 22-YEAR Cycle.' ApJ 133 (March): 572.

Baraffe, I., G. Chabrier, F. Allard, and P. H. Hauschildt. 1998. 'Evolutionary models for solar metallicity low-mass stars: mass-magnitude relationships and color-magnitude diagrams.' A&A 337 (September): 403–412.

Baraffe, Isabelle, Derek Homeier, France Allard, and Gilles Chabrier. 2015. 'New evolutionary models for pre-main sequence and main sequence low-mass stars down to the hydrogen-burning limit.' A&A 577, A42 (May): A42.

Barker, A. J., A. M. Dempsey, and Y. Lithwick. 2014. 'Theory and Simulations of Rotating Convection.' ApJ 791, 13 (August): 13.

Barnes, J. R., A. Collier Cameron, J.-F. Donati, et al. 2005. 'The decrease in differential rotation with decreasing stellar mass in a sample of young rapidly rotating main sequence stars.' In *13th Cambridge Workshop on Cool Stars, Stellar Systems and the Sun,* edited by F. Favata, G. A. J. Hussain, and B. Battrick, 560:95. ESA Special Publication. March.

Bassom, A. P., and K. Zhang. 1994. 'Strongly nonlinear convection cells in a rapidly rotating fluid layer.' *Geophysical and Astrophysical Fluid Dynamics* 76:223–238.

Bell, Cameron P. M., Tim Naylor, N. J. Mayne, R. D. Jeffries, and S. P. Littlefair. 2012. 'Pre-main-sequence isochrones - I. The Pleiades benchmark.' MNRAS 424 (August): 3178–3191.

Berta, Zachory K., Jonathan Irwin, David Charbonneau, Christopher J. Burke, and Emilio E. Falco. 2012. 'Transit Detection in the MEarth Survey of Nearby M Dwarfs: Bridging the Clean-first, Search-later Divide.' AJ 144 (November).

Böhm-Vitense, E. 1958. 'Über die Wasserstoffkonvektionszone in Sternen verschiedener Effektivtemperaturen und Leuchtkräfte. Mit 5 Textabbildungen.' *Zeitschrift für Astrophysik* 46:108.

———. 1992. *Introduction to Stellar Astrophysics,* 301. January.

Boyd, John P. 1989. *Chebyshev & Fourier Spectral Methods.* Springer-Verlag Berlin Heidelberg.

Braginsky, Stanislav I., and Paul H. Roberts. 1995. 'Equations governing convection in earth's core and the geodynamo.' *Geophysical and Astrophysical Fluid Dynamics* 79 (January): 1–97.

Brandenburg, Axel, and Kandaswamy Subramanian. 2005. 'Astrophysical magnetic fields and nonlinear dynamo theory.' *Physics Reports* 417 (1): 1–209.

Browning, M. K. 2008. 'Simulations of Dynamo Action in Fully Convective Stars.' ApJ 676 (April): 1262–1280.

Browning, M. K., A. S. Brun, and J. Toomre. 2004. 'Simulations of Core Convection in Rotating A-Type Stars: Differential Rotation and Overshooting.' ApJ 601 (January): 512–529.

Browning, M. K., M. A. Weber, G. Chabrier, and A. P. Massey. 2016. 'Theoretical Limits on Magnetic Field Strengths in Low-mass Stars.' ApJ 818, 189 (February): 189.

Browning, Matthew K., Gibor Basri, Geoffrey W. Marcy, Andrew A. West, and Jiahao Zhang. 2010. 'Rotation and Magnetic Activity in a Sample of M-Dwarfs.' *The Astronomical Journal* 139 (2): 504.

Brummell, N. H., N. E. Hurlburt, and J. Toomre. 1996. 'Turbulent Compressible Convection with Rotation. I. Flow Structure and Evolution.' ApJ 473 (December): 494.

Brun, A. S., and M. K. Browning. 2017. 'Magnetism, dynamo action and the solar-stellar connection.' *Living Reviews in Solar Physics* 14, 4 (September): 4.

Brun, A. S., M. S. Miesch, and J. Toomre. 2004. 'Global-Scale Turbulent Convection and Magnetic Dynamo Action in the Solar Envelope.' ApJ 614 (October): 1073–1098.

Burns, K. J., G. M. Vasil, J. S. Oishi, D. Lecoanet, and B. Brown. 2016. *Dedalus: Flexible framework for spectrally solving differential equations.* Astrophysics Source Code Library, March.

Busse, F. H. 1978. 'REVIEW: Non-linear properties of thermal convection.' *Reports on Progress in Physics* 41 (December): 1929–1967.

Busse, F. H., and P. G. Cuong. 1977. 'Convection in rapidly rotating spherical fluid shells.' *Geophysical and Astrophysical Fluid Dynamics* 8 (January): 17–41.

Calkins, M. A., K. Julien, S. M. Tobias, and J. M. Aurnou. 2015. 'A multiscale dynamo model driven by quasi-geostrophic convection.' *Journal of Fluid Mechanics* 780 (October): 143–166.

Canuto, C. 1988. *Spectral methods in fluid dynamics.* Springer series in computational physics. Springer-Verlag.

Canuto, V. M., and I. Mazzitelli. 1991. 'Stellar Turbulent Convection: A New Model and Applications.' ApJ 370 (March): 295–311.

Chabrier, G. 2003. 'Galactic Stellar and Substellar Initial Mass Function.' PASP 115 (July): 763–795.

Chabrier, G., and I. Baraffe. 1997. 'Structure and evolution of low-mass stars.' A&A 327 (November): 1039–1053.

Chabrier, G., J. Gallardo, and I. Baraffe. 2007. 'Evolution of low-mass star and brown dwarf eclipsing binaries.' A&A 472 (September): L17–L20.

Chandrasekhar, S. 1953. 'The Instability of a Layer of Fluid Heated below and Subject to Coriolis Forces.' *Proceedings of the Royal Society of London Series A* 217 (May): 306–327.

———. 1961. *Hydrodynamic and hydromagnetic stability.*

Charbonneau, Paul. 2010. 'Dynamo Models of the Solar Cycle.' *Living Reviews in Solar Physics* 7 (September).

Christensen-Dalsgaard, J. 1997. 'Effects of convection on the mean solar structure.' In *SCORe'96 : Solar Convection and Oscillations and their Relationship,* edited by F. P. Pijpers, J. Christensen-Dalsgaard, and C. S. Rosenthal, 225:3–22. Astrophysics and Space Science Library. December.

Christensen-Dalsgaard, J., W. Däppen, S. V. Ajukov, et al. 1996. 'The Current State of Solar Modeling.' *Science* 272 (5266): 1286–1292.

Christensen, U. R., and J. Aubert. 2006. 'Scaling properties of convection-driven dynamos in rotating spherical shells and application to planetary magnetic fields.' *Geophysical Journal International* 166 (July): 97–114.

Christensen, U. R., J. Aubert, P. Cardin, et al. 2001. 'A numerical dynamo benchmark.' *Physics of the Earth and Planetary Interiors* 128 (December): 25–34.

Clune, T. C., J. R. Elliott, M. S. Miesch, J. Toomre, and G. A. Glatzmaier. 1999. 'Computational aspects of a code to study rotating turbulent convection in spherical shells.' 25, no. 4 (April): 361–380.

Courant, R., K. Friedrichs, and H. Lewy. 1928. 'Über die partiellen Differenzengleichungen der mathematischen Physik.' *Mathematische Annalen* 100:32–74.

Cox, A. N., S. W. Hodson, and G. Shaviv. 1981. 'On the ratio of mixing length to scale height in red dwarfs.' ApJL 245 (April): L37–L40.

Cox, J. P., and R. T. Giuli. 1968. *Principles of stellar structure - Vol.1: Physical principles; Vol.2: Applications to stars.*

Currie, L. K., and M. K. Browning. 2017. 'The Magnitude of Viscous Dissipation in Strongly Stratified Two-dimensional Convection.' ApJL 845, L17 (August): L17.

D'Antona, F., and I. Mazzitelli. 1997. 'Evolution of low mass stars.' *Memorie della Societa Astronomica Italiana* 68 (January): 807–822.

Davies, G. R., W. J. Chaplin, W. M. Farr, et al. 2015. 'Asteroseismic inference on rotation, gyrochronology and planetary system dynamics of 16 Cygni.' MNRAS 446 (January): 2959–2966.

Deardorff, J. W. 1966. 'The Counter-Gradient Heat Flux in the Lower Atmosphere and in the Laboratory.' *Journal of Atmospheric Sciences* 23 (September): 503–506.

Deheuvels, S., R. A. Garcı a, W. J. Chaplin, et al. 2012. 'Seismic Evidence for a Rapidly Rotating Core in a Lower-giant-branch Star Observed with Kepler.' ApJ 756 (September).

Dittmann, J. A., J. M. Irwin, D. Charbonneau, et al. 2017. 'Discovery and Precise Characterization by the MEarth Project of LP 661-13, an Eclipsing Binary Consisting of Two Fully Convective Low-mass Stars.' ApJ 836, 124 (February): 124.

Dobler, W., M. Stix, and A. Brandenburg. 2006. 'Magnetic Field Generation in Fully Convective Rotating Spheres.' ApJ 638 (February): 336–347.

Dotter, Aaron, Brian Chaboyer, Darko Jevremović, et al. 2008. 'The Dartmouth Stellar Evolution Database.' *The Astrophysical Journal Supplement Series* 178 (September): 89–101.

Duarte, L. D. V., J. Wicht, M. K. Browning, and T. Gastine. 2016. 'Helicity inversion in spherical convection as a means for equatorward dynamo wave propagation.' MNRAS 456 (February): 1708–1722.

Eddington, A. S. 1926. *The Internal Constitution of the Stars.*

Falgarone, E., and T. Passot, eds. 2003. *Turbulence and Magnetic Fields in Astrophysics.* Vol. 614. Lecture Notes in Physics, Berlin Springer Verlag.

Featherstone, N. A., and B. W. Hindman. 2016. 'The Spectral Amplitude of Stellar Convection and Its Scaling in the High-Rayleigh-number Regime.' ApJ 818, 32 (February): 32.

Featherstone, N. A., and M. S. Miesch. 2015. 'Meridional Circulation in Solar and Stellar Convection Zones.' ApJ 804, 67 (May): 67.

Feiden, G. A. 2016. 'Magnetic inhibition of convection and the fundamental properties of low-mass stars. III. A consistent 10 Myr age for the Upper Scorpius OB association.' A&A 593, A99 (September): A99.

Feiden, G. A., and B. Chaboyer. 2012. 'Self-consistent Magnetic Stellar Evolution Models of the Detached, Solar-type Eclipsing Binary EF Aquarii.' ApJ 761, 30 (December): 30.

———. 2014. 'Magnetic Inhibition of Convection and the Fundamental Properties of Low-mass Stars. II. Fully Convective Main-sequence Stars.' ApJ 789, 53 (July): 53.

Ferguson, J. W., D. R. Alexander, F. Allard, et al. 2005. 'Low-Temperature Opacities.' ApJ 623 (April): 585–596.

Ferziger, J.H., and M. Peric. 2003. *Computational Methods for Fluid Dynamics.* Springer Berlin Heidelberg.

Fleming, T. A., M. S. Giampapa, J. H. M. M. Schmitt, and J. A. Bookbinder. 1993. 'Stellar coronae at the end of the main sequence - A ROSAT survey of the late M dwarfs.' ApJ 410 (June): 387–392.

Gastine, T., L. Duarte, and J. Wicht. 2012. 'Dipolar versus multipolar dynamos: the influence of the background density stratification.' A&A 546, A19 (October): A19.

Gastine, T., J. Morin, L. Duarte, et al. 2013. 'What controls the magnetic geometry of M dwarfs?' A&A 549 (January).

Gastine, T., J. Wicht, and J. Aubert. 2016. 'Scaling regimes in spherical shell rotating convection.' *Journal of Fluid Mechanics* 808 (December): 690–732.

Gillen, E., L. A. Hillenbrand, T. J. David, et al. 2017. 'New Low-mass Eclipsing Binary Systems in Praesepe Discovered by K2.' ApJ 849, 11 (November): 11.

Gilliland, Ronald L., Timothy M. Brown, Jørgen Christensen- Dalsgaard, et al. 2010. 'Kepler Asteroseismology Program: Introduction and First Results.' *Publications of the Astronomical Society of the Pacific* 122 (February): 131.

Gilman, P. A. 1977. 'Nonlinear Dynamics of Boussinesq Convection in a Deep Rotating Spherical Shell. I.' *Geophysical and Astrophysical Fluid Dynamics* 8 (January): 93–135.

———. 1983. 'Dynamically consistent nonlinear dynamos driven by convection in a rotating spherical shell. II - Dynamos with cycles and strong feedbacks.' ApJS 53 (October): 243–268.

Gilman, P. A., and G. A. Glatzmaier. 1981. 'Compressible convection in a rotating spherical shell. I - Anelastic equations. II - A linear anelastic model. III - Analytic model for compressible vorticity waves.' ApJS 45 (February): 335–388.

Gilman, Peter A. 1975. 'Linear Simulations of Boussinesq Convection in a Deep Rotating Spherical Shell.' *Journal of Atmospheric Sciences* 32 (July): 1331–1352.

Glatzmaier, G. 2013. *Introduction to Modeling Convection in Planets and Stars: Magnetic Field, Density Stratification, Rotation.* Princeton Series in Astrophysics. Princeton University Press.

Glatzmaier, G. A. 1984. 'Numerical simulations of stellar convective dynamos. I. The model andmethod.' *Journal of Computational Physics* 55 (September): 461–484.

———. 1985. 'Numerical simulations of stellar convective dynamos. II - Field propagation in the convection zone.' ApJ 291 (April): 300–307.

Gottlieb, D., and S.A. Orszag. 1977. *Numerical Analysis of Spectral Methods: Theory and Applications.* CBMS-NSF Regional Conference Series in Applied Mathematics. Society for Industrial / Applied Mathematics.

Gough, D. O. 1969a. 'The Anelastic Approximation for Thermal Convection.' *Journal of Atmospheric Sciences* 26 (May): 448–456.

———. 1969b. 'The Anelastic Approximation for Thermal Convection.' *Journal of Atmospheric Sciences* 26 (May): 448–456.

Gough, D. O., J. W. Leibacher, P. H. Scherrer, and J. Toomre. 1996. 'Perspectives in Helioseismology.' *Science* 272 (May): 1281–1283.

Gough, D. O., and R. J. Tayler. 1966. 'The influence of a magnetic field on Schwarzschild's criterion for convective instability in an ideally conducting fluid.' MNRAS 133:85.

Gough, D. O., and N. O. Weiss. 1976. 'The calibration of stellar convection theories.' MNRAS 176 (September): 589–607.

Grooms, I. 2015. 'Asymptotic behavior of heat transport for a class of exact solutions in rotating Rayleigh-Bénard convection.' *Geophysical and Astrophysical Fluid Dynamics* 109 (March): 145–158.

Hale, G. E., F. Ellerman, S. B. Nicholson, and A. H. Joy. 1919. 'The Magnetic Polarity of Sun-Spots.' ApJ 49 (April): 153.

Hansen, C. J., S. D. Kawaler, and V. Trimble. 2004. *Stellar Interiors: Physical Principles, Structure, and Evolution.*

Harvey, J. W., F. Hill, R. P. Hubbard, et al. 1996. 'The Global Oscillation Network Group (GONG) Project.' *Science* 272 (5266): 1284–1286.

Hathaway, D. H. 2015. 'The Solar Cycle.' *Living Reviews in Solar Physics* 12, 4 (September): 4.

Hathaway, David H., Thibaud Teil, Aimee A. Norton, and Irina Kitiashvili. 2015. 'The Sun's Photospheric Convection Spectrum.' *The Astrophysical Journal* 811 (2): 105.

Hayashi, C. 1961. 'Stellar evolution in early phases of gravitational contraction.' PASJ 13.

Hayashi, C., and R. Hoshi. 1961. 'The Outer Envelope of Giant Stars with Surface Convection Zone.' PASJ 13:442–449.

Herwig, F. 2000. 'The evolution of AGB stars with convective overshoot.' A&A 360 (August): 952–968.

Hunter, J. D. 2007. 'Matplotlib: A 2D graphics environment.' *Computing In Science & Engineering* 9 (3): 90–95.

Ireland, Lewis G., and Matthew K. Browning. 2018. 'The Radius and Entropy of a Magnetized, Rotating, Fully Convective Star: Analysis with Depth-dependent Mixing Length Theories.' *The Astrophysical Journal* 856 (2): 132.

Jackson, R. J., Constantine P. Deliyannis, and R. D. Jeffries. 2018. 'The inflated radii of M dwarfs in the Pleiades.' MNRAS 476 (May): 3245–3262.

Jones, C. A., P. Boronski, A. S. Brun, et al. 2011. 'Anelastic convection-driven dynamo benchmarks.' *Icarus* 216 (November): 120–135.

Julien, K., J. M. Aurnou, M. A. Calkins, et al. 2016. 'A nonlinear model for rotationally constrained convection with Ekman pumping.' *Journal of Fluid Mechanics* 798 (July): 50–87.

Julien, K., and E. Knobloch. 1998. 'Strongly nonlinear convection cells in a rapidly rotating fluid layer: the tilted f-plane.' *Journal of Fluid Mechanics* 360:141–178.

Julien, K., E. Knobloch, A. M. Rubio, and G. M. Vasil. 2012. 'Heat Transport in Low-Rossby-Number Rayleigh-Bénard Convection.' *Physical Review Letters* 109, no. 25, 254503 (December): 254503.

Käpylä, P. J., M. Rheinhardt, A. Brandenburg, et al. 2017. 'Extended Subadiabatic Layer in Simulations of Overshooting Convection.' ApJL 845, L23 (August): L23.

Kesseli, Aurora Y., Philip S. Muirhead, Andrew W. Mann, and Greg Mace. 2018. 'Magnetic Inflation and Stellar Mass. II. On the Radii of Single, Rapidly Rotating, Fully Convective M-Dwarf Stars.' AJ 155, 225 (June): 225.

King, E. M., S. Stellmach, and J. M. Aurnou. 2012. 'Heat transfer by rapidly rotating Rayleigh–Bénard convection.' *Journal of Fluid Mechanics* 691:568–582.

Kippenhahn, R., A. Weigert, and A. Weiss. 2012. *Stellar Structure and Evolution.* Astronomy and Astrophysics Library. Springer Berlin Heidelberg.

Kitchatinov, L. L., D. Moss, and D. Sokoloff. 2014. 'Magnetic fields in fully convective M-dwarfs: oscillatory dynamos versus bistability.' MNRAS 442 (July): L1–L4.

Korre, Lydia, Nicholas Brummell, and Pascale Garaud. 2017. 'Weakly non-Boussinesq convection in a gaseous spherical shell.' Phys. Rev. E 96, 033104 (September): 033104.

Kraus, A. L., S. T. Douglas, A. W. Mann, et al. 2017. 'The Factory and the Beehive. III. PTFEB132.707+19.810, A Low-mass Eclipsing Binary in Praesepe Observed by PTF and K2.' ApJ 845, 72 (August): 72.

Kupka, Friedrich, and Herbert J. Muthsam. 2017. 'Modelling of stellar convection.' *Living Reviews in Computational Astrophysics* 3, no. 1 (July): 1.

Lammer, Helmut, Herbert I. M. Lichtenegger, Yuri N. Kulikov, et al. 2007. 'Coronal Mass Ejection (CME) Activity of Low Mass M Stars as An Important Factor for The Habitability of Terrestrial Exoplanets. II. CME- Induced Ion Pick Up of Earth-like Exoplanets in Close-In Habitable Zones.' *Astrobiology* 7 (February): 185–207.

Lantz, S. R., and Y. Fan. 1999. 'Anelastic Magnetohydrodynamic Equations for Modeling Solar and Stellar Convection Zones.' *The Astrophysical Journal Supplement Series* 121 (March): 247–264.

Lantz, Steven Richard. 1992. 'Dynamical Behavior of Magnetic Fields in a Stratified, Convecting Fluid Layer.' PhD diss., CORNELL UNIVERSITY.

López-Morales, M. 2007. 'On the Correlation between the Magnetic Activity Levels, Metallicities, and Radii of Low-Mass Stars.' ApJ 660 (May): 732–739.

Lubin, J. B., J. E. Rodriguez, G. Zhou, et al. 2017. 'A Bright Short Period M-M Eclipsing Binary from the KELT Survey: Magnetic Activity and the Mass-Radius Relationship for M Dwarfs.' ApJ 844, 134 (August): 134.

Lydon, T. J., and S. Sofia. 1995. 'A Method for Incorporating the Effects of Large-Scale Magnetic Fields in the Study of Stellar Structure and Variability.' ApJS 101 (December): 357.

MacDonald, J., and D. J. Mullan. 2012. 'Precision modelling of M dwarf stars: the magnetic components of CM Draconis.' MNRAS 421 (April): 3084–3101.

———. 2013. 'Magnetic Effects and Oversized M Dwarfs in the Young Open Cluster NGC 2516.' ApJ 765, 126 (March): 126.

———. 2014. 'Surface Magnetic Field Strengths: New Tests of Magnetoconvective Models of M Dwarfs.' ApJ 787, 70 (May): 70.

———. 2015. 'Magnetoconvective models of red dwarfs: constraints imposed by the lithium abundance.' MNRAS 448 (April): 2019–2029.

———. 2017a. 'Apparent Non-coevality among the Stars in Upper Scorpio: Resolving the Problem Using a Model of Magnetic Inhibition of Convection.' ApJ 834, 67 (January): 67.

———. 2017b. 'Magnetic Modeling of Inflated Low-mass Stars Using Interior Fields No Larger than ∼10 kG.' ApJ 850, 58 (November): 58.

Magic, Z., A. Weiss, and M. Asplund. 2015. 'The Stagger-grid: A grid of 3D stellar atmosphere models. III. The relation to mixing length convection theory.' A&A 573, A89 (January): A89.

Malkus, W. V. R. 1954. 'The Heat Transport and Spectrum of Thermal Turbulence.' *Proceedings of the Royal Society of London Series A* 225 (August): 196–212.

Mann, A. W., G. A. Feiden, E. Gaidos, T. Boyajian, and K. von Braun. 2015. 'How to Constrain Your M Dwarf: Measuring Effective Temperature, Bolometric Luminosity, Mass, and Radius.' ApJ 804, 64 (May): 64.

Matsui, H., E. Heien, J. Aubert, et al. 2016. 'Performance benchmarks for a next generation numerical dynamo model.' *Geochemistry, Geophysics, Geosystems* 17 (May): 1586–1607.

McLean, M., E. Berger, and A. Reiners. 2012. 'The Radio Activity-Rotation Relation of Ultracool Dwarfs.' *The Astrophysical Journal* 746 (1): 23.

Meakin, C. A., and D. Arnett. 2007. 'Turbulent Convection in Stellar Interiors. I. Hydrodynamic Simulation.' ApJ 667 (September): 448–475.

Miesch, M. S., J. R. Elliott, J. Toomre, et al. 2000. 'Three-dimensional Spherical Simulations of Solar Convection. I. Differential Rotation and Pattern Evolution Achieved with Laminar and Turbulent States.' ApJ 532 (March): 593–615.

Miesch, Mark S. 2005. 'Large-Scale Dynamics of the Convection Zone and Tachocline.' *Living Reviews in Solar Physics* 2, 1 (April): 1.

Miesch, Mark S., Allan Sacha Brun, Marc L. DeRosa, and Juri Toomre. 2008. 'Structure and Evolution of Giant Cells in Global Models of Solar Convection.' ApJ 673, 557 (January): 557.

Moffatt, H.K. 1978. *Magnetic Field Generation in Electrically Conducting Fluids.* Cambridge Monographs on Mechanics. Cambridge University Press.

Mohanty, S., and G. Basri. 2003. 'Rotation and Activity in Mid-M to L Field Dwarfs.' ApJ 583 (January): 451–472.

Morales, J. C., I. Ribas, and C. Jordi. 2008. 'The effect of activity on stellar temperatures and radii.' A&A 478 (February): 507–512.

Morin, J., J.-F. Donati, P. Petit, et al. 2010. 'Large-scale magnetic topologies of late M dwarfs.' *Monthly Notices of the Royal Astronomical Society* 407 (4): 2269–2286.

Morin, J., E. Dormy, M. Schrinner, and J.-F. Donati. 2011. 'Weak- and strong-field dynamos: from the Earth to the stars.' *Monthly Notices of the Royal Astronomical Society: Letters* 418 (1): L133–L137.

Mullan, D. J., E. R. Houdebine, and J. MacDonald. 2015. 'A Model for Interface Dynamos in Late K and Early M Dwarfs.' ApJL 810, L18 (September): L18.

Mullan, D. J., and J. MacDonald. 2001. 'Are Magnetically Active Low-Mass M Dwarfs Completely Convective?' ApJ 559 (September): 353–371.

Newton, Elisabeth R., Jonathan Irwin, David Charbonneau, et al. 2017. 'The Hα Emission of Nearby M Dwarfs and its Relation to Stellar Rotation.' ApJ 834 (January).

Nordlund, Åke, Robert F. Stein, and Martin Asplund. 2009. 'Solar Surface Convection.' *Living Reviews in Solar Physics* 6, no. 1 (April): 2.

O'Mara, B., M. S. Miesch, N. A. Featherstone, and K. C. Augustson. 2016. 'Velocity amplitudes in global convection simulations: The role of the Prandtl number and near-surface driving.' *Advances in Space Research* 58 (October): 1475–1489.

Ogura, Yoshimitsu, and Norman A. Phillips. 1962. 'Scale Analysis of Deep and Shallow Convection in the Atmosphere.' *Journal of Atmospheric Sciences* 19 (March): 173–179.

Ossendrijver, M. 2003. 'The solar dynamo.' A&A Rev. 11:287–367.

Parker, E. N. 1993. 'A solar dynamo surface wave at the interface between convection and nonuniform rotation.' ApJ 408 (May): 707–719.

Paxton, B., L. Bildsten, A. Dotter, et al. 2011. 'Modules for Experiments in Stellar Astrophysics (MESA).' ApJS 192, 3 (January): 3.

Paxton, B., M. Cantiello, P. Arras, et al. 2013. 'Modules for Experiments in Stellar Astrophysics (MESA): Planets, Oscillations, Rotation, and Massive Stars.' ApJS 208, 4 (September): 4.

Paxton, B., P. Marchant, J. Schwab, et al. 2015. 'Modules for Experiments in Stellar Astrophysics (MESA): Binaries, Pulsations, and Explosions.' ApJS 220, 15 (September): 15.

Paxton, B., J. Schwab, E. B. Bauer, et al. 2017. 'Modules for Experiments in Stellar Astrophysics (MESA): Convective Boundaries, Element Diffusion, and Massive Star Explosions.' *ArXiv e-prints* (October).

Pizzolato, N., A. Maggio, G. Micela, S. Sciortino, and P. Ventura. 2003. 'The stellar activity-rotation relationship revisited: Dependence of saturated and non-saturated X-ray emission regimes on stellar mass for late-type dwarfs.' A&A 397 (January): 147–157.

Potekhin, A. Y., and G. Chabrier. 2010. 'Thermodynamic Functions of Dense Plasmas: Analytic Approximations for Astrophysical Applications.' *Contributions to Plasma Physics* 50 (January): 82–87.

Proudman, J. 1916. 'On the Motion of Solids in a Liquid Possessing Vorticity.' *Proceedings of the Royal Society of London Series A* 92 (July): 408–424.

Rast, Mark Peter. 2003. 'The Scales of Granulation, Mesogranulation, and Supergranulation.' *The Astrophysical Journal* 597 (2): 1200.

Raynaud, R., M. Rieutord, L. Petitdemange, T. Gastine, and B. Putigny. 2018. 'Gravity darkening in late-type stars. I. The Coriolis effect.' A&A 609, A124 (February): A124.

Reid, I. N., J. E. Gizis, and S. L. Hawley. 2002. 'The Palomar/MSU Nearby Star Spectroscopic Survey. IV. The Luminosity Function in the Solar Neighborhood and M Dwarf Kinematics.' AJ 124 (November): 2721–2738.

Reid, I. N., and S. L. Hawley. 2005. *New light on dark stars : red dwarfs, low-mass stars, brown dwarfs.*

Reiners, A., and G. Basri. 2008. 'Chromospheric Activity, Rotation, and Rotational Braking in M and L Dwarfs.' *The Astrophysical Journal* 684 (2): 1390.

———. 2009. 'On the magnetic topology of partially and fully convective stars.' A&A 496 (March): 787–790.

Reiners, A., G. Basri, and M. Browning. 2009. 'Evidence for Magnetic Flux Saturation in Rapidly Rotating M Stars.' *The Astrophysical Journal* 692 (1): 538.

Ribas, I. 2006. 'Masses and Radii of Low-Mass Stars: Theory Versus Observations.' Ap&SS 304 (August): 89–92.

Rogers, F. J., and A. Nayfonov. 2002. 'Updated and Expanded OPAL Equation-of-State Tables: Implications for Helioseismology.' ApJ 576 (September): 1064–1074.

Sainsbury-Martinez, F., N. Featherstone, M. Miesch, and M. Browning. In preparation. 'Anelastic Models of Fully-Convective Stars: Differential Rotation, Meridional Circulation, and Residual Entropy.'

Saumon, D., G. Chabrier, and H. M. van Horn. 1995. 'An Equation of State for Low-Mass Stars and Giant Planets.' ApJS 99 (August): 713.

Scalo, John, Lisa Kaltenegger, Ant Gona Segura, et al. 2007. 'M Stars as Targets for Terrestrial Exoplanet Searches And Biosignature Detection.' *Astrobiology* 7 (February): 85–166.

Scharmer, Göran B., Boris V. Gudiksen, Dan Kiselman, Mats G. Löfdahl, and Luc H. M. Rouppe van der Voort. 2002. 'Dark cores in sunspot penumbral filaments.' Nature 420 (November): 151–153.

Schmidt, Sarah J., Suzanne L. Hawley, Andrew A. West, et al. 2015. 'BOSS Ultracool Dwarfs. I. Colors and Magnetic Activity of M and L Dwarfs.' *The Astronomical Journal* 149 (5): 158.

Schou, J., H. M. Antia, S. Basu, et al. 1998. 'Helioseismic Studies of Differential Rotation in the Solar Envelope by the Solar Oscillations Investigation Using the Michelson Doppler Imager.' ApJ 505 (September): 390–417.

Siess, L., E. Dufour, and M. Forestini. 2000. 'An internet server for pre-main sequence tracks of low- and intermediate-mass stars.' A&A 358 (June): 593–599.

Soderlind, Gustaf, and Lina Wang. 2006. 'Adaptive time-stepping and computational stability.' *Journal of Computational and Applied Mathematics* 185 (January): 225–243.

Spiegel, E. A., and J. -P. Zahn. 1992. 'The Solar Tachocline.' A&A 265 (November): 106–114.

Sprague, M., K. Julien, E. Knobloch, and J. Werne. 2006. 'Numerical simulation of an asymptotically reduced system for rotationally constrained convection.' *Journal of Fluid Mechanics* 551:141–174.

Stahler, S. W. 1988. 'Understanding young stars - A history.' PASP 100 (December): 1474–1485.

Stassun, K. G., K. M. Kratter, A. Scholz, and T. J. Dupuy. 2012. 'An Empirical Correction for Activity Effects on the Temperatures, Radii, and Estimated Masses of Low-mass Stars and Brown Dwarfs.' ApJ 756, 47 (September): 47.

Stauffer, John R., Lee W. Hartmann, Giovanni G. Fazio, et al. 2007. 'Near- and Mid-Infrared Photometry of the Pleiades and a New List of Substellar Candidate Members.' *The Astrophysical Journal Supplement Series* 172 (October): 663–685.

Stein, Robert F. 2012. 'Magneto-convection.' *Philosophical Transactions of the Royal Society of London A: Mathematical, Physical and Engineering Sciences* 370 (1970): 3070–3087.

Stellmach, S., M. Lischper, K. Julien, et al. 2014. 'Approaching the Asymptotic Regime of Rapidly Rotating Convection: Boundary Layers versus Interior Dynamics.' *Physical Review Letters* 113, no. 25, 254501 (December): 254501.

Stevenson, D. J. 1979. 'Turbulent thermal convection in the presence of rotation and a magnetic field - A heuristic theory.' *Geophysical and Astrophysical Fluid Dynamics* 12:139–169.

Strassmeier, Klaus G. 2009. 'Starspots.' *The Astronomy and Astrophysics Review* 17, no. 3 (September): 251–308.

Tanner, J. D., S. Basu, and P. Demarque. 2014. 'The Effect of Metallicity-dependent T-τ Relations on Calibrated Stellar Models.' ApJL 785, L13 (April): L13.

———. 2016. 'Entropy in Adiabatic Regions of Convection Simulations.' ApJL 822, L17 (May): L17.

Tarter, Jill C., Peter R. Backus, Rocco L. Mancinelli, et al. 2007. 'A Reappraisal of The Habitability of Planets around M Dwarf Stars.' *Astrobiology* 7 (March): 30–65.

Taylor, G. I. 1917. 'Motion of Solids in Fluids When the Flow is Not Irrotational.' *Proceedings of the Royal Society of London Series A* 93 (March): 99–113.

Terrien, R. C., S. W. Fleming, S. Mahadevan, et al. 2012. 'The Metallicity of the CM Draconis System.' ApJL 760, L9 (November): L9.

Timmes, F. X., and F. D. Swesty. 2000. 'The Accuracy, Consistency, and Speed of an Electron-Positron Equation of State Based on Table Interpolation of the Helmholtz Free Energy.' ApJS 126 (February): 501–516.

Torres, G. 2013. 'Fundamental properties of lower main-sequence stars.' *Astronomische Nachrichten* 334 (February): 4.

Torres, G., J. Andersen, and A. Giménez. 2010. 'Accurate masses and radii of normal stars: modern results and applications.' A&A Rev. 18 (February): 67–126.

Torres, G., and I. Ribas. 2002. 'Absolute Dimensions of the M-Type Eclipsing Binary YY Geminorum (Castor C): A Challenge to Evolutionary Models in the Lower Main Sequence.' ApJ 567 (March): 1140–1165.

Trampedach, R., R. F. Stein, J. Christensen-Dalsgaard, Å. Nordlund, and M. Asplund. 2014. 'Improvements to stellar structure models, based on a grid of 3D convection simulations - II. Calibrating the mixing-length formulation.' MNRAS 445 (December): 4366–4384.

Van Der Walt, S., S. C. Colbert, and G. Varoquaux. 2011. 'The NumPy array: a structure for efficient numerical computation.' *ArXiv e-prints* (February).

van Saders, Jennifer L., Tugdual Ceillier, Travis S. Metcalfe, et al. 2016. 'Weakened magnetic braking as the origin of anomalously rapid rotation in old field stars.' Nature 529 (January): 181–184.

Vitense, E. 1953. 'Die Wasserstoffkonvektionszone der Sonne. Mit 11 Textabbildungen.' *Zeitschrift für Astrophysik* 32:135.

Walkowicz, Lucianne M., Christopher M. Johns-Krull, and Suzanne L. Hawley. 2008. 'Characterizing the Near-UV Environment of M Dwarfs.' ApJ 677 (April).

Weber, M. A., and M. K. Browning. 2016. 'Modeling the Rise of Fibril Magnetic Fields in Fully Convective Stars.' ApJ 827, 95 (August): 95.

Weiss, A., W. Hillebrandt, H.-C. Thomas, and H. Ritter. 2004. *Cox and Giuli's Principles of Stellar Structure.*

Wright, Nicholas J., Jeremy J. Drake, Eric E. Mamajek, and Gregory W. Henry. 2011. 'The Stellar-activity-Rotation Relationship and the Evolution of Stellar Dynamos.' *The Astrophysical Journal* 743 (1): 48.

Yadav, R. K., U. R. Christensen, J. Morin, et al. 2015. 'Explaining the Coexistence of Large-scale and Small-scale Magnetic Fields in Fully Convective Stars.' ApJL 813, L31 (November): L31.

Yadav, R. K., T. Gastine, U. R. Christensen, L. D. V. Duarte, and A. Reiners. 2016. 'Effect of shear and magnetic field on the heat-transfer efficiency of convection in rotating spherical shells.' *Geophysical Journal International* 204 (February): 1120–1133.

Zang, Thomas A., Steven E. Krist, and M. Yousuff Hussaini. 1989. 'Resolution requirements for numerical simulations of transition.' *Journal of Scientific Computing* 4, no. 2 (June): 197–217.

Zeeman, Dr. P. 1897. 'VII. Doublets and triplets in the spectrum produced by external magnetic forces.' *The London, Edinburgh, and Dublin Philosophical Magazine and Journal of Science* 44 (266): 55–60.

Index